



HAL
open science

Polarimetric detection of endo-clutter UAV in a low-grazing geometry

Milan Rozel

► **To cite this version:**

Milan Rozel. Polarimetric detection of endo-clutter UAV in a low-grazing geometry. Data Analysis, Statistics and Probability [physics.data-an]. Université Paris-Saclay, 2023. English. NNT : 2023UP-AST147 . tel-04498082

HAL Id: tel-04498082

<https://theses.hal.science/tel-04498082>

Submitted on 11 Mar 2024

HAL is a multi-disciplinary open access archive for the deposit and dissemination of scientific research documents, whether they are published or not. The documents may come from teaching and research institutions in France or abroad, or from public or private research centers.

L'archive ouverte pluridisciplinaire **HAL**, est destinée au dépôt et à la diffusion de documents scientifiques de niveau recherche, publiés ou non, émanant des établissements d'enseignement et de recherche français ou étrangers, des laboratoires publics ou privés.

Polarimetric detection of endo-clutter UAV in a low-grazing geometry

*Détection polarimétrique de drone endo-clutter en
incidence rasante*

Thèse de doctorat de l'université Paris-Saclay

École doctorale n°580 : sciences et technologies de l'information et de la
communication (STIC)

Spécialité de doctorat: Sciences du traitement du signal et des images
Graduate School : Sciences de l'ingénieur et des systèmes. Référent : Faculté des
sciences d'Orsay

Thèse préparée dans l'unité de recherche **Électromagnétisme et radar (Université
Paris-Saclay, ONERA)**, sous la direction d'**Hélène ORIOT**, directrice de recherche et le
co-encadrement de **Pierre BRUNEEL**, ingénieur de recherche.

Thèse soutenue à Paris-Saclay, le 26 octobre 2023, par

Milan ROZEL

Composition du jury

Membres du jury avec voix délibérative

Stéphanie BIDON Professeure, ISAE-SUPAERO, Université de Toulouse, France	Présidente
Laurent FERRO-FAMIL Professeur, ISAE-SUPAERO, Université de Toulouse, France	Rapporteur & Examineur
Marco MARTORELLA Professeur, Microwave and Integrated Systems Labora- tory, University of Birmingham, Royaume-Uni	Rapporteur & Examineur
Philippe FORSTER Professeur des universités, Université Paris Nanterre, France	Examineur
Fadela KABECHE Ingénieure de recherche, Direction générale de l'armement (DGA) - Ministère des Armées, France	Examinatrice

Titre: Détection polarimétrique de drone endo-clutter en incidence rasante

Mots clés: Polarimétrie, Radar, Drone, Fouillis

Résumé : La miniaturisation de l'électronique embarqué a permis le développement de drones de petites tailles et d'un large marché civil pour ces drones. La simplicité d'utilisation et le bas coût de ces drones en font des outils redoutables pour des personnes ou organisations mal intentionnées. Dans ce contexte, les systèmes radar peuvent jouer un rôle important pour contrecarrer une attaque menée avec un ou plusieurs drones. Néanmoins, les drones volent généralement à faible vitesse et proche du sol. De plus, ils ont généralement une faible surface équivalente radar. Ces cibles posent donc des problèmes aux systèmes radar qui ont du mal à les différencier du sol.

Le but de cette thèse est d'améliorer les capacités de détection endo-clutter des drones en utilisant la polarisation. Nous présentons une méthode permettant d'étudier les propriétés du clutter terrestre polarimétrique. Nous proposons des méthodes de simulation permettant d'identifier le meilleur détecteur dans une scène avec un clutter changeant sur les axes temporel et spatial. Nous étudions les avantages des détecteurs polarimétriques par rapport aux détecteurs mono-polarimétriques à l'aide d'une méthode de comparaison des détecteurs qui permet de choisir le meilleur détecteur en fonction des propriétés du clutter.

Pour atteindre cet objectif, nous analysons les propriétés spatio-temporelles du clutter à l'aide des données d'une campagne de mesure radar en environnement semi-urbain. Cette campagne de mesure nous permet de mettre en exergue des propriétés importantes du clutter telles que : la non-réciprocité du clutter polarimétrique pour un radar dont les antennes de réception des différentes polarisations sont distinctes, l'existence d'un temps d'intégration Doppler optimisant la stabilité du clutter et une instabilité de la signature polarimétrique

du clutter. Nous proposons de modéliser l'évolution temporelle du clutter en utilisant conjointement, la distribution des valeurs propres de sa matrice de covariance, et, l'angle entre les matrices de covariances d'une même case clutter à deux instants différents. Cet angle est appelé "angle de désadaptation".

Dans une deuxième phase nous comparons un ensemble de détecteurs polarimétriques et mono-polarimétriques pour des détections endo-clutter. Pour cela :

- Nous étudions l'influence du rang efficace de la matrice de covariance du clutter - contrôlé par le temps d'intégration Doppler - sur les performances des détecteurs et montrons que la minimisation du rang effectif améliore les performances des détecteurs.
- Ensuite, nous étudions les effets de l'angle de désadaptation sur les performances des détecteurs en fonction du clutter sélectionné. Nous constatons que les détecteurs filtrant le clutter ont des performances qui diminuent avec l'intervalle de temps entre l'estimation des propriétés du clutter et la réalisation du test de détection, alors que les autres détecteurs ont des performances qui ne sont pas affectées par cet intervalle de temps.
- Enfin, nous montrons que les détecteurs polarimétriques sont plus adaptés aux détections de drones endo-clutter que les détecteurs mono-polarimétriques.

Les méthodes d'analyse que nous avons présentées permettent d'optimiser le temps d'intégration Doppler et peuvent être utilisées dans les systèmes radar pour déterminer, de manière adaptative, le meilleur détecteur, en fonction du clutter étudié.

Title: Polarimetric detection of endo-clutter UAV in a low-grazing geometry

Keywords: Polarimetry, Radar, UAV, Clutter

Abstract: In the past decades, Unmanned Aerial Vehicles have benefited from the miniaturization of electronic components, allowing for cheap and small drone designs, and allowing a rapid development of the civilian market. Unfortunately, due to their low cost, high availability and ease of use, these systems have become a tool of choice for malicious actors, and have become a force multiplier for such actors. In this context, radars can play a significant role in the effort to thwart an attack with one or several UAVs. However, UAVs usually fly at slow speed and close to the ground and have a low radar cross section, which makes them difficult to detect as radar systems may have troubles to differentiate them from the ground. This thesis aims at addressing this challenge with the use of polarization. In this thesis, we aim at improving endo-clutter detection of UAVs. We study the advantages of polarimetric detectors over mono-polarimetric detectors, proposing a method to compare the detectors and choosing the best performing one according to clutter's properties. In order to do so, we first analyse the spatio-temporal properties of polarimetric ground clutter thanks to a measurement campaign in semi-urban environment. This campaign outlines important properties of the clutter such as: the non-reciprocity of polarimetric clutter for quasi-monostatic radar with separated transmit and receive antennas, the existence of an optimal Doppler integration time and the instability of the clutter polarimetric signature with time. We propose to model the temporal evolution of the clutter using both the distribution of the eigenvalues of the covariance matrix and a measure of the mismatch angle between covariance matrices. Then, we implement a benchmark of polarimetric and mono-polarimetric detectors to assess the performances of endo-clutter detection under spatio-temporal varying clutters. We compare the robustness of the polarimetric detectors to choose

the best performing detector for a given clutter:

- First, we study the influence of the effective rank of the clutter - controlled by the Doppler integration time - on the performances of detectors and confirm that it is useful to minimize the effective rank of the covariance matrix to improve the detection performances.
- Then, we analyse the influence of the mismatch angle on the performances of the detectors using simulated clutter in order to select the best detector, for a given time varying clutter. It turns out that endo-clutter detectors based on clutter filtering depend on the time delay between clutter estimation and detection test, while other detectors are time independent. Furthermore, this study shows the sensitivity of the detector performances to the eigenvalue distribution of the clutter.
- Finally, we show a clear improvement with polarimetric detectors over single polarization detectors for endo-clutter detection of UAVs in a low grazing geometry.

From these results, we conclude that multi-polarimetric detectors enable better performances for endo-clutter UAV detections. In addition we present a metric to optimize the effective-rank of the clutter with by adjusting Doppler integration time to increase the detection performances. Then, we determine that the shorter the time interval is between the clutter estimation and the detection test, the higher performances are. These results give a clear plan for polarimetric detections of endo-clutter UAVs, minimizing effective rank and the time interval between estimation and detection. We conclude that simulation methods described in this thesis could be used in a radar system to adaptively estimate the best polarimetric detector for a given clutter cell and target.

Remerciements – Acknowledgements

Voici enfin le moment de boucler cette thèse ! Après seulement \approx 4 ans de travaux sur ma thèse, le manuscrit a enfin été rendu (et validé) et je suis enfin prêt à soutenir ! Aucune bonne thèse ne serait complète sans des remerciements.

Je vais tout naturellement commencer par mon encadrement de thèse.

Tout d'abord, Hélène, ma directrice de thèse qui aura fait preuve d'une grande patience avec moi. Un grand merci en particulier pour ton encadrement qui aura permis de canaliser la thèse et l'aura remise dans le droit chemin au moment où elle en avait le plus besoin. Merci aussi pour m'avoir aiguillé vers les bonnes personnes dans le département pour m'avoir permis de clarifier efficacement les points d'ombres persistants.

Ensuite, je remercie Philippe qui malgré ce que veux bien en dire l'école doctorale m'aura énormément encadré. Je pense en particulier aux nombreuses discussions que nous avons eues. Que ce soit des échanges en rapport direct avec la thèse, portant sur la lutte anti-drone, discussions auxquelles je n'ai pas réussi à rendre entièrement justice avec ma thèse ou encore des discussions plus générales, mais toutes aussi intéressantes les unes que les autres. Enfin merci d'avoir créé ce sujet de thèse si intéressant et si vaste.

Merci aussi à Pierre, qui m'aura permis d'avancer extrêmement vite sur le sujet compliqué à aborder qu'est le mismatch grâce à ses excellents conseils et de fructueux échanges. De nombreuses parties très concrètes (quasiment autant que du fromage... du jambon...) de ma thèse lui doivent énormément, que ce soit l'analyse du clutter polarimétrique ou les simulations des détecteurs. Enfin je le remercie pour ces moments que nous aurons pu passer (et continuons) à développer ensemble sur le radar HYCAM.

Enfin, même s'il n'a pas vraiment fait partie de l'encadrement (mais en vrai, si), je remercie ici Nicolas qui m'aura permis de découvrir le radar et l'unité quand je suis arrivé à l'ONERA et avec qui je partage une appétence toute particulière pour l'expérimentation (à quand la prochaine manip CORNET ?).

Je tiens aussi à remercier certains collègues qui bien que n'ayant pas participé à l'encadrement, ont particulièrement participé à ma formation lors de ma thèse ou qui m'auront particulièrement aidé sur un point de ma thèse.

Je remercie Fred pour m'avoir appris les bases des traitements radar lors de mon arrivé à l'ONERA en 2019 et pour avoir globalement toujours été de bonne humeur (ou du moins

prêt à l'être), de bon conseil et prêt à aider. Seul bémol il a probablement ramené le COVID en France, mais chuuuuuuut !!!

Merci à Olivier qui m'aura permis de mettre en place proprement mes simulations de détecteurs en prenant le temps de m'expliquer les tenants et aboutissants desdites simulations.

Enfin merci à Dodo qui m'aura expliqué des concepts de traitements radars un peu plus avancés quand j'ai eu le plaisir de partager le même "bureau" que lui. En outre, sa mauvaise foi légendaire couplée à son honnêteté sans faille (oui, oui c'est 100% compatible) sont toujours là pour égayer l'ambiance. Et pour qui aime l'ordre et le rangement il saura leur faire plaisir avec une visite de son bureau.

Je remercie aussi Fayin pour les bons moments passés, sa bonne humeur et pour gentiment servir de bêta-testeur à mes codes pythons. Et je lui souhaite bien évidemment une excellente fin de thèse ! Je remercie aussi mes collègues avec qui j'ai pris et je prends un grand plaisir à partager les pauses café du midi, dans la meilleure salle de pause de l'ONERA, Anil, Daniel et Jean-François, Jérôme (S), Sophie et Romain. Merci aussi à Jérôme (H) pour son aide avec le "nouveau" numériseur d'HYCAM, qui nous aura tant aidé. Un grand merci aussi à Sylvain pour son aide tout au long de la thèse et tous ses conseils. Je tiens aussi à remercier trois collègues qui ont quitté l'unité lors de ma thèse et que j'aurais eu le plaisir de rencontré et de cotoyer (trop brièvement), Jean-Paul, Jack et Maxime.

Enfin des mercis en pagaille aux collègues avec qui j'ai eu l'occasion de travailler et/ou de partager des discussions et des bons moments pendant la thèse, Mariliza, Abi, Hoa, Steve, Tanguy, Anthony, Pierre, Ba-Huy, Alec et Julien.

Je n'oublie pas non plus la cellule gestion du DEMR qui m'aura accompagné tout au long de ma thèse, en particulier Valérie, Sylvie, Isabelle, Laure et Sophie.

Des remerciements un peu particulier, puisqu'il concerne des collègues que je n'ai pas vraiment rencontré pendant ma thèse, mais avec qui j'ai eu le plaisir de travailler alors qu'elle n'était malgré tout à fait pas fini. Merci Michel, Valérie (B), Jean-Philippe, Axel, Laurent, Juanito et Vincent. Pour finir cette section concernant l'ONERA je remercie aussi la direction du département de m'avoir fait confiance en m'embauchant alors que ma thèse n'était entièrement terminée et à tous ceux qui m'ont soutenu et/ou appuyé dans cette démarche.

Enfin, j'ai une pensée à la mémoire d'Orian qui nous a quitté en 2020.

Je tiens aussi à remercier Nathalie Nihouarn, secrétaire de la faculté de physique d'Orsay pour m'avoir énormément aidé à toucher mes salaires d'enseignant vacataire, malgré des conditions d'obtention excessivement compliquées pour un salaire...

Je remercie aussi les différents enseignants, professeurs et maitres de stages qui m'auront

tant appris, et en particulier Baptiste Portelli, qui m'aura "propulsé" sur la voie de la physique.

Vous entrez maintenant dans la section dédiée à mes amis de plus ou moins longue date qui m'ont soutenu et aidé avant et pendant ma thèse et j'en suis sûr continuerons à le faire après ma soutenance.

Merci à mes anciens camarades de l'ENS et en particulier de la prépa agreg avec qui j'aurai partagé de nombreuses soirées jeux en distanciel pendant les longs mois du COVID.

Merci à mes occasionnels compagnons de jeux-vidéo Jean et Louis. Merci à Apolline pour ces nombreuses soirées parisiennes au bar. Merci aussi à Hakim et Oscar que je connais depuis si longtemps et avec qui j'ai toujours autant de plaisir à partager du temps ! Merci à Mohamed pour ces (très) longues conversations téléphoniques toujours rafraichissantes et intéressantes !

Merci à la "team Saint-Just" qui aura tenu contre vents et marées. Merci Pierre, Marc et Marc, au hLM, Hugo, Lucas et Martin.

Un très grand merci à Pio et Olivier pour votre soutien et votre amitié depuis toutes ces années.

Un très grand merci au Pr. Shadocko (qui n'est pas réellement professeur mais par souci de protection des sources je ne peux pas en dire plus) pour toutes ces magnifiques soirées de jeux (moins de traquenards qu'avant, il semblerait que la maturité nous gagne...) et tous ces beaux memes.

Et un grand merci au DOCTEUR Clément qui m'aura accompagné au quotidien tout au long de cette thèse, et que j'espère j'aurai réussi à soutenir autant qu'il m'aura soutenu pendant la thèse !

Pour finir, un grand merci à ceux qui dans ma famille m'ont soutenu, mes cousins, mes cousines, mes oncles, ma sœur, ma mère et mon père.

Je dédie cette thèse à la mémoire de mes deux grand-pères.

And Now for Something Completely Different !

Résumé en français

Lors du début du XXI^e siècle, les drones ont grandement bénéficié des progrès effectués dans le domaine de la miniaturisation des composants électroniques. Ces progrès ont permis le développement de drones de plus en plus petit et de moins en moins cher, permettant une croissance rapide d'un large marché civil. Malheureusement, leur nature bon marché et la facilité d'accès aux drones en fait des outils privilégiés pour les acteurs malveillants, démultipliant leurs capacités de nuisance. Les radars peuvent jouer un rôle prépondérant pour contrecarrer les attaques de drones. Toutefois, les drones volent généralement à des vitesses réduites et proche du sol, et ont de faibles sections équivalentes radar. Ceci fait des drones des cibles compliquées à détecter et en particulier difficile à distinguer du sol. Cette thèse a pour but de s'attaquer à cette problématique grâce à la polarisation des ondes radar. Dans cette thèse nous cherchons à améliorer les processus de détection des drones endo-clutters. Nous présentons une méthodologie permettant d'étudier les propriétés polarimétriques du clutter de sol. Nous proposons des métriques et des méthodes de simulation permettant d'identifier quel détecteur a les meilleures performances pour les détections dans un clutter aux propriétés polarimétriques fluctuantes et en incidence rasante. Nous étudions les avantages des détecteurs polarimétriques par rapport à leurs homologues mono-polarimétriques et proposons une méthode de comparaison des détecteurs qui permet de choisir le plus apte des détecteurs en fonction des propriétés du clutter. Nous analysons tout d'abord les propriétés polarimétriques spatio-temporelles du clutter de sol grâce à une campagne de mesure d'un environnement semi-urbain. Cette campagne permet de mettre en exergue des propriétés importantes du clutter de sol polarimétrique, tel que : la non-réciprocité du clutter de sol pour un radar terrestre quasi-monostatique dont les antennes d'émission et de réception sont différentes, l'existence d'un temps d'intégration Doppler optimisant les probabilités de détections et l'instabilité de la signature polarimétrique du clutter. Nous proposons un modèle d'évolution temporelle du clutter basé sur la distribution des valeurs propres des matrices de covariance du clutter et sur l'angle de désadaptation entre les matrices de covariance du clutter. Nous implémentons un ensemble de détecteurs polarimétriques et mono-polarimétriques pour estimer leurs performances pour des détections endo-clutters. Nous comparons la robustesse des différents détecteurs polarimétriques pour pouvoir choisir le plus efficace pour chaque clutter :

- Tout d'abord nous étudions l'influence du rang effectif du clutter – contrôlé par le temps d'intégration Doppler – sur les performances des détecteurs et nous confirmons que minimiser le rang effectif de la matrice de covariance du clutter sous test permet de maximiser les performances des détecteurs.
- Ensuite nous analysons l'influence de l'angle de désadaptation sur les performances des détecteurs pour pouvoir sélectionner le détecteur le plus adapté à chaque clutter polarimétrique. Cette méthode montre que les détecteurs dont le fonctionnement est basé sur le filtrage du clutter en utilisant sa matrice de covariance, sont plus sensibles à l'intervalle de temps entre l'estimation des propriétés du clutter et le test de détection

alors que les autres détecteurs y sont moins sensibles. De plus cette étude se concentre aussi sur l'impact des distributions de valeurs propres des clutters sous test sur les performances des détecteurs.

- Enfin nous démontrons un intérêt significatif des détecteurs polarimétriques par rapport aux détecteurs non-polarimétriques pour les détections de drones endo-clutters.

D'après ces résultats, nous pouvons conclure que les détecteurs multi-polarimétriques permettent d'obtenir de meilleurs résultats de détections sur les drones endo-clutters. De plus nous avons proposé des métriques permettant d'optimiser le rang effectif grâce au temps d'intégration Doppler, ce qui permet d'augmenter les performances des détecteurs. Ensuite, nous avons déterminé que la minimisation de l'intervalle entre le test de détection et l'estimation des propriétés du clutter permettait elle aussi d'augmenter les performances des détecteurs. Les résultats de cette thèse permettent d'établir un plan de d'action pour optimiser la détection de drones endo-clutters, à savoir, minimiser le rang effectif du clutter sous test, en ajustant le temps d'intégration Doppler, et l'intervalle de temps entre le test de détection et l'estimation des propriétés du clutter. Enfin nous suggérons qu'il est possible d'utiliser les méthodes de simulations présentées dans cette thèse dans un système radar de lutte anti-drone pour choisir de manière adaptative le détecteur le plus adapté pour chaque case de clutter.

Contents

1	Introduction	17
1.1	Threat posed by Unmanned Aerial Vehicle	17
1.2	Specific challenges to counter-UAV systems	18
1.3	Thesis goal and approach	19
2	Counter-UAV radar and review of the litterature	21
2.1	Polarimetric monostatic ground radar.	21
2.1.1	Monostatic surface radars	22
2.1.2	Polarimetric radar	30
2.2	Interactions between Radars and U n m anned A erial V ehicles (UAVs).	34
2.2.1	UAV radar signature	34
2.2.2	UAV classification	37
2.2.3	Counter-UAV radar systems and detection	39
2.2.4	Conclusion	40
2.3	Radar Clutter	40
2.3.1	General consideration on clutter	41
2.3.2	Sea Clutter	41
2.3.3	Land Clutter in Low-grazing Geometry	41
2.3.4	Low-grazing polarimetric surface clutter	42
2.3.5	Conclusion	42
2.4	Polarimetric Radar Classification Methods	42
2.4.1	Weather Radars	43
2.4.2	S ynthetic A perture R adar (SAR)	44
2.4.3	Conclusion	46
2.5	Detections	46
2.5.1	Framework and Mono-channel Detectors	46
2.5.2	Mono-channel detector	47
2.5.3	Multi-channel Detectors	50
2.5.4	Polarimetric Detectors	51
2.5.5	Conclusion	54
2.6	Detectors tested in this thesis	54
2.6.1	Framework	54
2.6.2	Classical and adapted polarimetric detectors	55
2.6.3	Mono-polarimetric detector	56
2.6.4	New detector, E igen V alue detector (EVa)	57

3	Outline of the thesis	59
3.1	Goals	59
3.2	Methods	59
3.3	Outline of the work presented	60
4	Experimental Study of the Polarimetric Clutter	61
4.1	HYCAM	61
4.1.1	HYCAM radar architecture	61
4.1.2	Radar configuration for the measurement campaign	66
4.1.3	Polarimetric radar characterization and calibration	67
4.2	Measurement campaign	73
4.3	Study of the low-grazing polarimetric clutter	74
4.3.1	Non-correlation of the cross-polarization channels in the presented configuration	74
4.4	Polarimetric Clutter Properties	79
4.4.1	Presentation of the studied clutter range cells	80
4.4.2	Covariance matrix estimation	82
4.4.3	Eigenvalues	83
4.4.4	Doppler integration time influence on the Sample Covariance Matrix (SCM)	84
4.4.5	Comparison between range and time estimated SCM	85
4.4.6	Eigenvalues time series for the selected clutter	87
4.4.7	Temporal stability of the polarimetric signature	90
4.4.8	Summary of the clutter range cell analysis	96
5	Evaluation of detectors for low-grazing endo-clutter detections	99
5.1	Detection framework	99
5.2	General Simulation Framework	101
5.3	Testing a detector with a Covariance Matrix Couple (CMC) and Signal to Clutter Ratio (SCR)	101
5.3.1	Testing a detector with a value of Θ and SCR	102
5.3.2	Assessing the P_{FA} - <i>threshold</i> and P_D - <i>threshold</i> from the set of detector test outcomes	102
5.3.3	Assessing the performances of detector for different values of Θ and different SCR	103
5.3.4	Global parameters of the radar data and detectors	103
5.4	Influence of the effective rank on the detectors	103
5.4.1	Simulation procedure	103
5.4.2	Simulation parameters	104
5.4.3	Simulation results	104
5.4.4	conclusion	105
5.5	Robustness of detectors with the covariance matrices mismatch	108
5.5.1	Generating the covariance matrix couples with mismatch	108

5.5.2	Simulation parameters	109
5.5.3	Results according to covariance matrix eigenvalue distributions	109
5.5.4	Conclusion	110
5.5.5	Assessing the best performing detector	110
5.5.6	Conclusion	115
5.6	Hybrid simulations	117
5.6.1	Working principle	117
5.6.2	Simulation parameters	118
5.6.3	Simulation results	118
5.6.4	Drawing conclusion from the hybrid simulations	126
6	Conclusions and perspectives	127
6.1	Summary	127
6.2	Perspectives	129
6.2.1	Polarimetric analysis of UAV radar signature	129
6.2.2	Further analyses of the polarimetric clutter	129
6.2.3	Perspectives for the polarimetric detectors	129
6.2.4	Counter-UAV radar perspective	130
	Appendices	131
A	Steering vectors	133
B	HYCAM Receive apertures	135
C	Link between CNR and maximum correlation rate	137
D	Noise analysis	139
D.1	Noise measurement	139
D.2	Consideration on the noise estimation with N samples	139
E	Relative angle between two matrices of identical eigenvalue distributions and identical eigenvectors	143
F	Resampling to favor mismatch angle of 0°	145
G	UAV signature extraction	147
H	Maximum Likelihood detector for unknown amplitude and steering vector for each look	151
	Bibliography	153

List of Acronyms

API	A pplication P rogramming I nterface. 66
ATC	A ir T raffic C ontrol. 51
AWG	A rbitrary W aveform G enerator. 25, 66
BORD	B ayesian O ptimum R adar D etector. 51
CA-CFAR	C ell A veraging CFAR . 48, 49, 51, 55, 56
CDF	C umulative D istribution F unction. 101
CFAR	C onstant F alse A larm R ate. 40, 47, 48, 49, 51, 53, 55, 56
CMC	C ovariance M atrix C ouple. 10, 100, 101, 102, 103, 104, 106, 107, 108, 109, 110, 117, 118, 145
CNR	C lutter to N oise R atio. 54, 75, 76, 78, 79, 80, 84, 85, 90, 93, 94, 96, 97, 98, 105, 137
CUT	C ell U nder T est. 46, 47, 48, 49, 51, 54, 59, 60, 80, 83, 86, 108
DBF	D igital B eam F orming. 25, 34
ECEF	E arth C entered - E arth F ixed. 147
EMD	E mpirical M ode D ecomposition. 38
Eva	E igen V alue detector. 9, 54, 57, 99, 103, 105, 108, 109, 110, 115, 117, 118, 123, 125, 126, 128, 129
FAR	F alse A larm R ate. 55, 101
FOD-CFAR	F irst O rders D ifferential CFAR . 49
GAN	G enerative A dversarial N etwork. 38
GLRT	G eneralized L ikelihood R atio T est. 52, 53, 56, 151
GO-CFAR	G reatest O f CFAR . 48, 49
IEEE	I nstitute of E lectrical and E lectronics E ngineers. 31
IF	I ntermediary F requency. 26, 27, 66
IMF	I ntrinsic M ode F unction. 38
LHCP	L eft H and C ircular P olarization. 31

LNA	Low Noise Amplifier. 25, 26, 66
LoS	Line of Sight. 74, 75, 77, 78, 88
MF	Matched Filter. 50, 51
MIMO	Multi-Input Multi-Output. 34, 39
ML	Maximum Likelihood. 52
NATO	North Atlantic Treaty Organization. 57
NG	Noncentral Chi-Square Gamma. 41
ONERA	Office National d'Études et de Recherches Aérospatiales. 20, 24, 65, 68
OS-CFAR	Ordered Statistics CFAR. 49
P-GLRT	Polarimetric GLRT. 151
P-SIRV	Polarimetric SIRV. 54, 99, 103, 105, 108, 109, 110, 125, 126
PRF	Pulse Repetition Frequency. 30, 33, 37, 67
PRI	Pulse Repetition Interval. 21, 25, 29, 30, 66, 130, 149
PST-GLR	Polarization-Space-Time domain Generalized Likelihood Ratio. 52, 53
RADAR	Radio Detection And Ranging. 21
RCS	Radar Cross Section. 19, 22, 24, 27, 34, 35, 36, 37, 39, 40, 42, 43, 127
RF	Radio Frequency. 25, 26, 66, 67
RHCP	Right Hand Circular Polarization. 31
Rx	receive. 64
SAR	Synthetic Aperture Radar. 9, 41, 42, 44, 54
SCM	Sample Covariance Matrix. 10, 50, 54, 57, 72, 80, 82, 83, 84, 85, 90, 91, 93, 94, 100, 109, 115, 117, 128, 139, 140, 141, 142
SCR	Signal to Clutter Ratio. 10, 41, 42, 56, 57, 86, 101, 102, 103, 104, 105, 106, 108, 109, 110, 111, 112, 113, 115, 117, 118, 123, 125, 126, 127, 128
SDR	Software Defined Radar. 61
SIMO	Single-Input Multi-Output. 66
SINR	Signal to Interference plus Noise Ratio. 38, 53
SIRV	Spherically Invariant Random Vector. 56
SNR	Signal to Noise Ratio. 25, 37, 38, 40, 42, 48, 50, 54, 68, 70, 123, 127, 149

SO-CFAR	S mallest O f CFAR . 48, 49
srML	s quare r oot M aximum L ikelihood. 54, 56, 57, 83, 99, 103, 104, 105, 108, 109, 110, 115, 117, 123, 125, 126
ST-GLR	S pace- T ime domain G eneralized L ikelihood R atio. 53
STAP	S pace T ime A daptive P rocess. 51, 53, 130
STO	S cience and T echnology O rganization. 57
SVD	S ingle V alue D ecomposition. 37, 38, 39
Tx	transmit. 63, 64, 68
UAV	U nmanned A erial V ehicle. 9, 17, 18, 19, 20, 21, 22, 24, 26, 28, 30, 32, 34, 35, 36, 37, 38, 39, 40, 42, 44, 46, 48, 50, 51, 52, 54, 56, 57, 58, 60, 61, 73, 74, 80, 99, 118, 127, 128, 129, 147, 148, 149
UHF	U ltra H igh F requency. 42
VHF	V ery H igh F requency. 42
VI	V ariability I ndex. 48
VI-CFAR	V ariability I ndex CFAR . 48
WGS	W orld G eodetic S ystem. 147

Chapter 1 | Introduction

This part gives a general introduction of this PhD thesis, contextualizes and explains the challenges raised by UAVs and drones for air surveillance radars. First, it presents the uses of UAVs and their different types. Then it briefly explains the specific challenges posed to counter-UAV radar systems. Finally, it reviews the main objectives of this PhD work.

1.1 . Threat posed by Unmanned Aerial Vehicle

The acronym UAV stands for Unmanned Aerial Vehicle, an aerial vehicle with no pilot onboard. It can either be remote-controlled by a human or pre-programmed to act on its own. UAS for Unmanned Aircraft System or drone are also used to designate a UAV. These terms cover reusable aircrafts, single use aircrafts and ordnance such as cruise missiles [*Unmanned aerial vehicle 2022*].

UAVs are used in both military and civilian domains. Today, military forces use UAVs in a wide range of applications, from reconnaissance to weapon launch platform, including smart ammunitions. These different missions are carried out by a range of UAVs, from ultra-light UAVs, weighing less than 20 grams such as the FLIR systems Black Hornet [*Black Hornet PRS Datasheet 2022*] (Figure 1.1a), to several tonnes UAV with very large wingspan such as the RQ-4 Global Hawk [*Northrop Grumman RQ-4 Global Hawk 2022*] (Figure 1.1c) or the Divine Eagle UAV [*SYAC UAV 2022*].

They come in various forms: with fixed wings (MQ-9 Reaper, Harfang, Bayraktar TB2, Shahed-136...), rotary-wings (MQ-8 Fire Scout, DJI Phantom (Figure 1.1b)) [Chaturvedi et al. 2019], flapping wings, hybrid configurations... While UAVs were first reserved to armies and state actors due to the high cost and weight of electronics required for flight control and radio transmission, the increased miniaturization and the access to cheaper, more powerful and energy efficient electronics have made UAVs affordable for civilian users. As their military counterparts, civilian UAVs have many applications. Cinematography, search and rescue operations, geo-scanning, transportation of payloads or hobby, are few of their applications [Yaacoub et al. 2020]. Because of their simple operation even for beginners, most civilian UAVs are rotary-wings aircrafts, typically multi-copters. The broad availability of the technologies to build both civilian and military UAVs means that drones are now widely used [Chaturvedi et al. 2019; Yaacoub et al. 2020].

UAVs are used in the context of warfare between opposing armies, as weapon carriers, weapons themselves or as intelligence gathering tools. If drones have been widely used since at least World War II [Keane and Carr 2013], their military use has sharply increased since the end of the cold war.

UAVs are also potent tools for malicious operators. Reports indicate that drones



(a) Black Hornet UAV, source: [Wikimedia.org](https://www.wikimedia.org)



(b) DJI Phantom used as improvised weapon carrier by the Islamic State in Iraq and the Levant, source: [Waters 2017](#)



(c) RQ-4 Global Hawk High Altitude Long Endurance (HALE) UAV, source: [Wikimedia.org](https://www.wikimedia.org)

Figure 1.1: Different drones, of various types and size, note the large size differences.

are used to smuggle drug, weapons and other illegal objects into prisons or across borders, or to plan prison breaks. Civilian drones are even used as weapons and weapon delivery systems by terrorists [[Waters 2017](#)]. Malice is not necessary for UAVs to be disruptive, for instance the Gatwick airport was paralyzed between the 19th and the 21st of December 2018 due to several reports of drone sighting near the airport's runway [[Shackle 2020](#)].

By their nature, these disturbances are extremely low-cost since they use drones available to the public, however, the cost of counter-UAV systems is, by essence, high as they need to counter a wide range of threats. This rapid evolution requires not only to adjust air defense systems but to re-think them, in order to address the specific challenges of UAVs.

1.2 . Specific challenges to counter-UAV systems

A wide range of counter-UAV systems exists, including optro-electronic, acoustic, and radar systems.

During World War II, radar systems have proven to be better suited to air surveillance and air defense applications than acoustic and optical surveillance systems, quickly replacing acoustic surveillance [[Acoustic mirror 2022](#)] and progressively replacing optical surveillance. This is due to the many advantages of radar. First, radar systems offer a very unique all weather day/night surveillance capability. Secondly, radars are able to

survey very large areas, whereas other systems have much more limited field of view. It is therefore natural to consider radars for counter-UAV systems.

However, as we will see in the following parts, radar systems also have several limitations when it comes to dealing with UAVs. A radar system ability to detect an object depends on the target's **Radar Cross Section (RCS)**. RCS is a measure of how much energy is reflected back to the radar receiver. The RCS of an object depends on several factors, such as, the size of the object, its geometry, its material composition and the wavelength used of the radar. All other factors being equal the smaller the object is, the smaller its RCS. Small size UAVs especially pose challenges since small targets usually have small RCS and are therefore more difficult to detect. In addition, they are cheaper and easier to operate than the previous generations of UAVs, which make them a very common potential threat. These small UAVs also fly close to the ground meaning that counter-UAV radars need to be deployed in a low-grazing geometry, which gives high ground clutter returns. Objects illuminated by a radar scatter some energy back to the radar receiver, it is also true for ground objects, such as terrain and buildings. The radar returns of these objects are called radar clutter and pollute radar measurements at low-grazing angle.

Radar systems also use the Doppler effect to separate targets according to their relative speed with the radar. This property is especially important to discriminate returns from static objects such as buildings, ground or trees from a UAV. As this discrimination uses only the speed of the object, it fails to detect static targets relative to the radar system. Unfortunately many drones have rotary-wings meaning they are able to hover and therefore are easily confused with static returns. Targets that have the same speed as the clutter are named endo-clutter targets, and can evade detections.

UAVs also pose further operating challenges, including:

- the similarity of the flight domain and the magnitude of the radar signature between birds and UAVs.
- the highly maneuverable nature of UAVs
- the short time available to react to a threat as UAVs can appear very close to the radar and a vast surveillance domain, often 360° coverage

All of these challenges should be addressed if one wants to ensure counter-UAV radar system robustness.

1.3 . Thesis goal and approach

Extensive works have been published on classification of UAVs, amongst different types of UAVs or even between UAVs and small objects like birds. These works have focused on classical classification methods as well as more novel methods based on machine learning, in particular neural networks. Many papers report classification results of multi-copter drones using the signature of the blades of the rotor, the so-called blade flashes [Kang et al. 2021]. This well-known phenomenon is and was previously used for manned jet aircraft identification, known under the term Jet Engine Modulation [Bell and Grubbs 1993; Research and Technology Organization and Sensors and Electronics Technology Panel 2004].

Some works address UAV detection both when they are static or having a relative movement towards or away from the radar. To achieve endo-clutter detections, many works focus on the micro-Doppler signature of the blade flashes, because even if the target is endo-clutter the signature of the blade flashes are separated from the clutter.

As radar signal modulation by blade flashes is widely used for adversarial target recognition of jet aircraft some modern jet fighter designs already implement some features that greatly diminish the effectiveness of this method, for instance S-shaped air inlet [Chung and Tuan 2021].

That is why we choose not to take the access to the micro-Doppler signature for granted. Some UAVs have either reduced or obfuscated blade signature (for instance the RQ-16A T-Hawk [Honeywell RQ-16 T-Hawk 2021] has concealed blades) for flight characteristics reasons or maliciously.

This PhD work studies how to improve the detection process of endo-clutter targets when their signature is non-specific and aims to design robust detection schemes for endo-clutter UAVs with little or no micro-doppler signatures. To achieve this objective, we need to increase the diversity of data processed by the radar system. This can be done by using frequency diversity and a larger signal bandwidth, a distributed radar systems (with several transmitters and/or receivers), a finer resolution or polarization. Here we study how to use the polarization of the radar to enhance the detection scheme of endo-clutter targets in a low-grazing geometry for a ground surveillance radar.

This study uses real-world data collected with ONERA's HYCAM radar as well as simulations based on the analyses of the polarimetric clutter properties. This thesis first covers a review of previous works on surveillance radar and drone detection, polarimetric radar and endo-clutter detection schemes. Then, we detail the experimental protocol and the measurement campaign. These measurements lead to analyses of the polarimetric properties of the ground clutter in a low-grazing geometry.

The final part is dedicated to detector simulations to test their performances. In this part we present a simulation method that takes into account the changing clutter properties. With this simulation method we test the effect on the performances of polarimetric detectors of some clutter properties. We test the impact of the rank of the clutter on the performances of the detectors.

Using the mismatch angle, a measure of the mismatch between covariance matrices of the clutter introduced in the previous part, we test the influence of a mismatch between the estimated polarimetric clutter and the clutter under the target. Finally we test the robustness of the performances of the detectors to an inadequate estimation of the clutter polarimetric properties and we assess the performances of each detector using hybrid simulation based on real-world data of both UAV and clutter. We conclude with a summary of the content of this thesis and provide perspectives for future work.

Chapter 2 |

Counter-UAV radar and review of the literature

Radar (From **RA**dio **D**etection **A**nd **R**anging (RADAR)) systems were developed during the first third of the XXth century and were massively used during World War II [*History of radar 2022*]. They had decisive influence in several campaigns, most famously the Battle of Britain. Nowadays, radars use radio waves to support multiple applications in defence and security domains. They are also used for civilian applications, for example radar imaging for remote sensing or automotive radar. This broad range of applications is due to their ability to detect targets beyond visual range, e.g regardless -almost- of daytime, weather condition and environments. Among these applications, air surveillance is probably the most notable. Air surveillance radar systems, for civilian or defence applications, implement detection algorithms tuned to specific operations according to the capabilities of the system. Radars use time to measure distance and frequency to measure speed thanks to the Doppler effect. In addition, during the second half of the XXth century, it appeared that the polarisation properties of the electromagnetic emissions could be used in radar systems to detect and classify objects [Giuli 1986].

The goal of this thesis is to study the interest of polarimetry for surface radar systems to improve the detection of targets embedded in complex environments, with a special focus on the detection of UAVs). We first present an overview of the past and current literature addressing different aspects of the UAV endo-clutter detections. The specificity of UAVs imposes strong constraints such as a low-grazing angle and strong parasitic returns from building and ground, and leads to the development of new radar systems and processing. The radar returns from sea, ground, buildings and other slow or immobile objects have specific properties that are then addressed. Finally, we focus on the detection theory and modern detection algorithms. The performances of these algorithms provide an important metric to assess benefits of a radar technology.

2.1 . Polarimetric monostatic ground radar.

In this part we describe the operating principle of a monostatic polarimetric ground radar. We start with the radar equation and explain some important aspects of ground radar systems, such as gain, transmitted power and wavelength. We then focus on the basics of radar signals and signal processing, by describing **P**ulse **R**epetition **I**nterval (PRI), pulse-compression and Doppler processing. Finally we introduce radar polarimetry and review the specific requirements imposes on radar systems' design.

2.1.1 . Monostatic surface radars

This part is dedicated to monostatic surface radar. We use the radar equation to show the influence of the antennas gain, wavelength and distance to the target on the received power as well as the influence of the target's "radar size" called **Radar Cross Section (RCS)**. We briefly discuss the relationship between antenna type and radar performances and introduce basic radar signal processing steps, from matched filter to coherent Doppler processing.

Radar basic principles

An active radar transmits electromagnetic waves through an antenna which propagate at the speed of light $c = 299,792,458 \text{ m} \cdot \text{s}^{-1}$ (in vacuum). When a target is illuminated by the radar, a fraction of the incoming electromagnetic wave is scattered toward the radar receiver. The delay between the transmission of the radar signal and the reception of the signal backscattered by the target provides the range the target. If either the radar or the target are moving, the frequency of the received signal is shifted compared to the transmitted wave, because of the Doppler effect. As this shift is proportionnal to the speed relative speed between the radar and the target, it allows the radar to measure its speed relative to the target.

Monostatic radars have collocated antenna(s), transmit and receive units. The transmit and receive units can either share the same antenna or use two different antennas. To understand how the transmit and receive units and antenna(s) interact with the target we refer to the famous radar equation [Skolnik 1970]:

$$P_r = P_t G_t \frac{1}{R^2} \sigma \frac{1}{R^2} G_r \frac{\lambda^2}{(4\pi)^3} \quad (2.1.1)$$

Where:

P_r	Received power	Receive side
G_r	Receiving antenna gain	
P_t	Transmitted power	Transmit side
G_t	Transmitting antenna gain	
σ	Radar cross – section	Scatter side
λ	wavelength	
R/R	Distance between the radar and the target	Forward and back propagation side

On the transmit side of the radar equation, P_t is the transmitted power, the quantity of energy transmitted by the antenna. It depends on the power amplification stage.

G_t is the transmit antenna gain, it measures how directive the antenna is. It is proportional to the surface of the focusing element of the radar. In this case we have: $G_t \propto S \frac{4\pi}{\lambda^2}$ with S being the surface of the focusing element, thus, according to the Fraunhofer diffraction theory, $G_t \propto \frac{4\pi}{\Theta_{alt}\Theta_{az}}$, with Θ_{alt} and Θ_{az} the beam width of the antenna aperture, respectively, in elevation and azimuth.

Figure 2.1 shows two different radars operating in L-Band (respectively around 1.3 GHz and 1.75 GHz), with respectively ~ 45 dB of transmission gain and ~ 20 dB. The difference of the beam width also illustrates the relationship between gain and the energy being "concentrated" as the SRE-M6 (Figure 2.1a) radar has $\Theta_{alt} = \Theta_{az} = 1.1^\circ$ and the "Œ il noir" radar (Figure 2.1b) $\Theta_{alt} = 45^\circ$ and $\Theta_{az} = 10^\circ$. A larger focusing element leads to a thinner beam, thus a more concentrated energy and a higher gain.



(a) SRE-M6 Radar, source: radar-tutorial.eu



(b) DRVC 1 A "Œil noir" Radar, source: chars-francais.net

Figure 2.1: Two L-band (1 to 2 GHz) radar, due to the size difference of their parabola they have vastly different antenna gains.



(a) GM400 "Ground Master" S-Band Radar phased array radar, source: [Wikimedia.org](https://www.wikimedia.org/)



(b) DRBV 15A "Sea Tiger" S-Band Radar radar with focusing parabola, source: radar-tutorial.eu

Figure 2.2: S-Band radars (2-4 GHz), phased-array radar and radar with a focusing parabola.

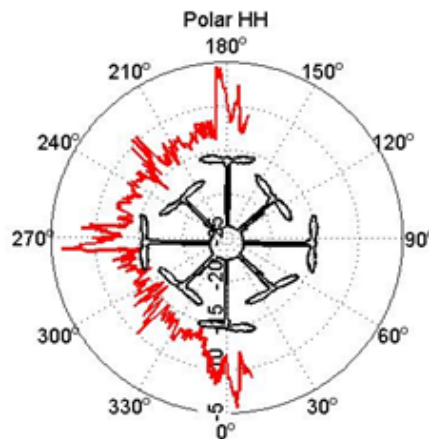


Figure 2.3: RCS of a UAV as a function of its aspect angle for a frequency band between 12 and 18 GHz. Source: **Office National d'Études et de Recherches Aérospatiales (ONERA)**, anechoic chamber measurements.

A radar with a focusing antenna has few or a single radiating elements at the focal point of the focusing antenna. The electromagnetic wave are focused by the parabola on these radiating elements, and the direction in witch the radar beam points depend solely on mechanical steering. By contrast, the phased array radar has a large number of radiating elements in its antenna. Figure 2.2a exhibits a phased array radar and Figure 2.2b a radar with a parabolic antenna.

After transmission, the waveforms propagate with respect to the beam pattern The term in R^{-2} comes from the conservation of energy and as the target gets further less and less energy reaches it.

σ is the **Radar Cross Section (RCS)** of the target. It is the fraction of energy the target reflects in the direction of the radar. The RCS is the surface of an equivalent metallic surface, which would reflect the same amount of energy as the target. As an example, $\sigma = 10 \text{ m}^2$ means that the target reflects as much energy back to the radar as a 10 m^2 metallic plate (within the far-field hypothesis). The RCS of a target depends on several factors:

- The aspect of the target relative to the radar receiver and transmitter
- The wavelength of the radar signal
- The nature of the target, such as its materials and shape

In the following, the RCS is expressed in dBsm (sm for squared meters), with $\sigma_{dBsm} = 10 \log_{10} \sigma_{m^2}$ to account for the fact that RCS value spans over many orders of magnitude. Figure 2.3 shows strong link between the RCS of a UAV and its aspect for a frequency band between 12 and 18 GHz.

When the electromagnetic wave hits the target it is scattered or reflected back in space and a portion propagates back to the radar, once more the conservation of energy introduces an additional R^{-2} factor.

G_r is the antenna reception gain. We can also model the power reflected by the target back to the receiver as a photon surfacic flux. Integrating over the receiving surface gives a photon flux, which translates to received power. The gain is proportional to

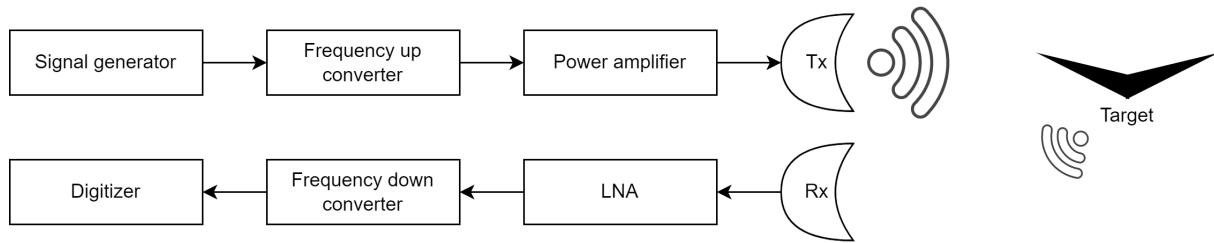


Figure 2.4: Radar working chart

the receiver surface. Once more, we can distinguish between antennas with a focusing element, for instance an antenna with a parabolic and one receiving element, and an antennas with several receiving elements. Non focused antennas also present an important drawback over antenna with a focusing element, namely the susceptibility to jammers. If a jammer is present off axis, a radar with parabolic antenna is not affected. A multi element antenna filters the jammer with **Digital Beam Forming (DBF)**, but the if jammer is strong enough to saturate the receivers it is impossible to filter it out and thus, it pollutes the signal of interest. However active array antennas provide a lot of advantages, amongst which, their versatile nature and their ability to operate several functionality at one (scanning, tracking, electronic warfare, etc).

Finally, P_r is the received power after all the steps. The signal received is altered by various noise. It can be noise from the environment, the antenna, the **Low Noise Amplifier (LNA)**, or from the rest of the radio frequency chain. When the noise comes from the **Radio Frequency (RF)** chain we call it noise factor (F), the quotient between the P_r and F , the noise from the LNA, gives us the instantaneous **Signal to Noise Ratio (SNR)**. The noise factor of the RF chain should be lower than the LNA noise factor, as the noise from the LNA is white noise, whereas the rest of the chain can have strongly colored noise. A colored noise has a nonflat spectrum, which means that the noise level varies with frequency.

Figure 2.4 shows a flowchart of the radar working principle as detailed above. The **Arbitrary Waveform Generator (AWG)** generates the signal transmitted by the radar. This flowchart is closely related to the radar system we use in the work presented. It should be noted that different radar design can be adopted, which might not follow the presented flowchart.

Radar signal

First generation radars transmitted high power pulses. This signal is repeated regularly with a time period named PRI and a pulse duration denoted τ in the following. τ only lasts a fraction of the PRI. For these radars the range resolution is given by τ [Skolnik 1970], as $\frac{c\tau}{2}$. It leads to the challenge, from a system perspective, to transmit high amount of energy in a very short time to guaranty detection and tracking performances of the system at relatively high resolution.

Instead of transmitting more and more power over shorter and shorter time period, coded waveform are used. The development of miniaturized electronics allows for the use of frequency-modulated waveform. With this waveform the range resolution is inversely proportional to the bandwidth of the waveform, B , and is written $\frac{c}{2B}$, as we show in the following.

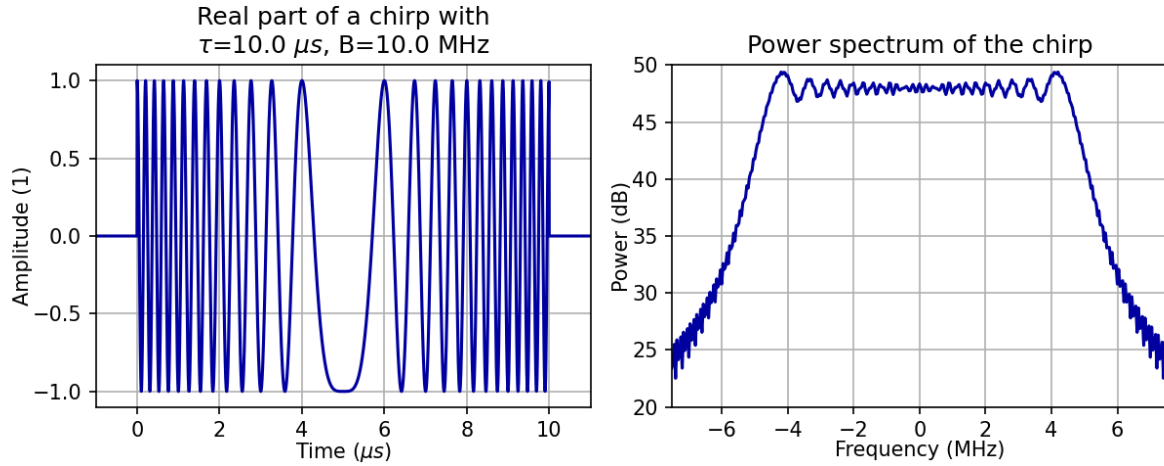


Figure 2.5: Chirp time serie and spectrum

The linear chirp is a widely used waveform (Figure 2.5 shows the real part and power spectrum of a chirp) in which the transmitted frequency is linearly swept from $f_c - \frac{B}{2}$ to $f_c + \frac{B}{2}$ over of duration τ . It can be expressed as:

$$s_{chirp}(t) = e^{2i\pi t(f_c + \frac{B}{2\tau}t - \frac{B}{2})} \quad (2.1.2)$$

With $0 \leq t < \tau$. Thus the transmitted signal becomes:

$$s_{transmitted}(t) = \begin{cases} s_{chirp}(t) & , 0 \leq t < \tau \\ 0 & , \tau \leq t < PRI \end{cases} \quad (2.1.3)$$

For implementation issues, the chirp is often generated around an **I**ntermediary **F**requency (IF) central frequency. Then it is transposed to the desired carrier frequency, in the **R**adio **F**requency (RF) domain. The signal then goes through power amplification, and is transmitted by the antenna. The waves travel in the space, hit different backscatters, and are partially reflected to the receive antenna. The received signal is filtered with a band-pass filter centered on the carrier frequency to reject out-of-band signals that would be amplified and then aliased. The signal is first amplified by a LNA, which adds thermal noise to the signal. We write the received signal as the sum of the different contributions of the scatterers and noise:

$$s_{received}(t) = \sum_{l=1}^L a_l e^{i\phi_l} s_{chirp}\left(t - \frac{2r_l}{c}\right) + a_{noise} e^{i\phi_{noise}} \quad (2.1.4)$$

With L being the number of scatterers and:

$$\langle a_{noise} \rangle^2 = \alpha k_B B_n T \quad (2.1.5)$$

Where α is the noise factor, k_B is the Boltzmann constant, B_n the used bandwidth and T the noise temperature. Figure 2.6 shows the echo from a target as well as the thermal noise illustrating equation 2.1.4. a_l is given by:

$$a_l = \sqrt{\frac{\sigma_l G_t G_r \lambda^2}{r_l^2 (4\pi)^2}} \quad (2.1.6)$$

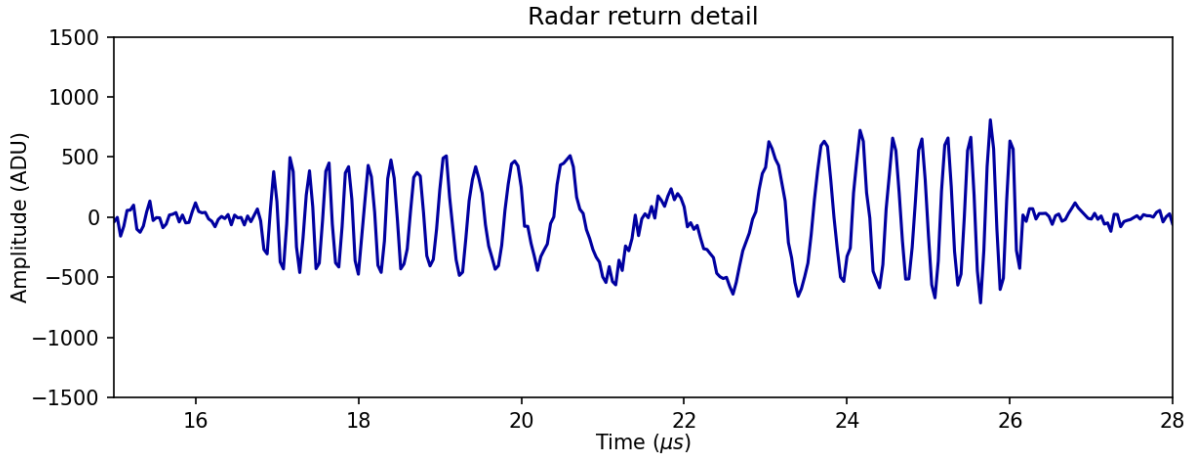


Figure 2.6: Radar signal showing the return from an airliner (Airbus A320).

where σ_l is the RCS of the backscatterer l and r_l its distance to the radar. ϕ_l is the intrinsic phase of the backscatterer.

The signal is down converted to an IF and digitized around this frequency. Lowering the working frequency limits the signal loss in the cable because higher frequency means a stronger power radiated by a cable, and the hardware for digitizing at lower frequencies is less constrained.

Pulse compression

Pulse compression is a cross-correlation of the received signal with a replica of the transmitted signal. The cross-correlation function between the signals s_0 and s_1 is given by:

$$\langle s_0, s_1 \rangle (t) = \int_{-\infty}^{+\infty} s_0^*(t') s_1(t - t') dt' \quad (2.1.7)$$

The pulse-compression is the cross-correlation between the transmitted signal and the received signal:

$$s_{pc}(t) = \langle s_{transmitted}, s_{received} \rangle (t) \quad (2.1.8)$$

The auto-correlation of the chirp is given by [Hein 2004]:

$$s_{chirp \text{ auto-correlation}}(t) = \langle s_{chirp}, s_{chirp} \rangle (t) = \tau \Lambda\left(\frac{t}{\tau}\right) \text{sinc}\left(Bt \Lambda\left(\frac{t}{\tau}\right)\right) e^{2i\pi f_c t} \quad (2.1.9)$$

With $\Lambda(x) = \max(1 - |x|, 0)$, the triangle function, $\text{sinc}(x) = \frac{\sin(x)}{x}$ the sinus cardinal function.

It is often approximated by:

$$s_{chirp \text{ auto-correlation}}(t) = \tau \text{sinc}(Bt) e^{2i\pi f_c t} \quad (2.1.10)$$

Figure 2.7 shows the auto-correlation of the chirp. We notice the sinus cardinal and its side lobes -13 dB below the main lobe and the first zeros at B^{-1} . It means that the range resolution is proportional to $\frac{c}{2B}$, and exactly $\frac{c}{2B}$ using the Rayleigh criterion for

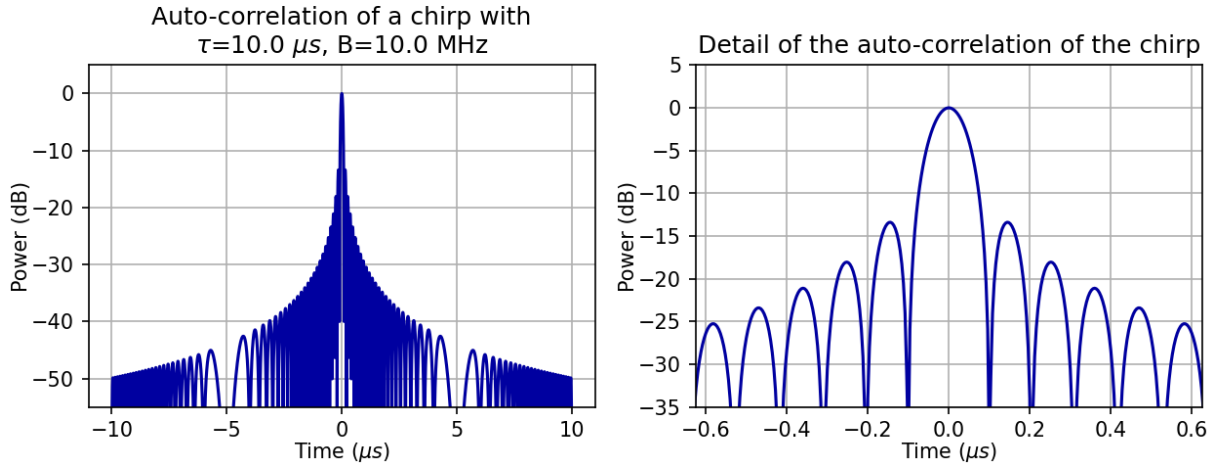


Figure 2.7: Chirp auto-correlation.

resolution [Lord Rayleigh 1879]. This proportionality relationship between bandwidth and range resolution is not specific to the chirp and holds true for every signal. The pulse-compressed signal of the backscatter l is written:

$$a_l s_{chirp \text{ auto-correlation}} \left(t - \frac{r_l}{2c} \right)$$

Thus, with 2.1.4 and 2.1.8 we can write s_{pc} :

$$s_{pc}(t) = \sum_{l=1}^L a_l s_{chirp \text{ auto-correlation}} \left(t - \frac{r_l}{2c} \right) + n' \quad (2.1.11)$$

With n' the noise component after pulse-compression. The total energy of transmitted by the chirp is $E_{trans} = P_{trans}\tau$ the same energy is conserved after pulse compression. As explained, the resolution after pulse compression is proportional to B the bandwidth. Thus, E_{trans} is measured over $1/B$, thus we have:

$$E_{trans} = P_{pc}/B = P_{trans}\tau \quad (2.1.12)$$

With P_{pc} the peak power after the pulse compression stage, thus we have $P_{pc} = P_{trans}\tau B$. The total power transmitted by the radar is $P_{eff} = P_{trans} \frac{\tau}{PRI}$ depending on the radar duty cycle $\frac{\tau}{PRI}$. P_{eff} is thus proportional to τ .

For a single frequency pulse radar the range resolution is proportional to $\frac{c\tau}{2}$ which means that increasing τ increases P_{eff} but degrades the range resolution. However, for a coded waveform with a bandwidth of B the range resolution is proportional to $\frac{c}{2B}$. The range resolution does not depend on τ which means that increasing τ increase P_{eff} but does not degrade the range resolution. The coded waveforms and pulse compression allows to decouple, the range resolution from the transmitted power, with range resolution being independent from τ .

Maximum unambiguous range and minimum measuring range

With a single antenna, a duplexer is used to separate the transmitter unit and receiver unit as the same antennas serves for both transmission and reception With two antennas, data recorded during the transmission of the radar is often discarded due to the

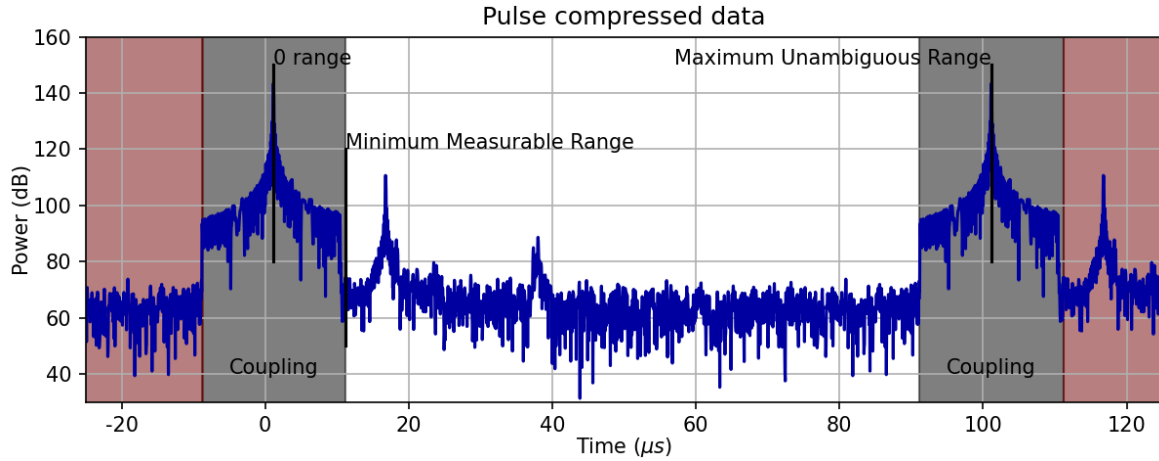


Figure 2.8: Radar signal after pulse-compression. There is an offset due to the propagation of the signal in the cables of the radar system.

coupling between the antennas. Despite the isolation between the antennas a large quantity of energy can go into the receiving antennas during the transmission. It often distorts the signal or masks it making its exploitation impossible. The distance $\frac{c\tau}{2}$ is therefore called the minimal measuring range and is the radar's blind spot.

The ambiguous range is defined by the PRI. Since the waveform is transmitted every PRI, a reflected signal traveling for $\delta t > PRI$ before getting back to the radar receiver cannot be distinguished from a signal travelling for $\delta t - PRI$. The distance $\frac{cPRI}{2}$ is called maximum unambiguous range. The radar has another blind spot between $\frac{c(PRI-\tau)}{2}$ and $\frac{cPRI}{2}$ which is the symmetric of the blind zone between 0 and $\frac{c\tau}{2}$. This blind spot is due to the coupling of the next pulse or the fact that the radar does not record this data.

Without dedicated waveforms management a radar can unambiguously detect targets between $\frac{c\tau}{2}$ and $\frac{c(PRI-\tau)}{2}$. This is illustrated in Figure 2.8.

Doppler processing

The radar system transmits a waveform at each PRI. We can separate the received signals in bursts of M pulses transmitted during $M \times PRI$ to do a coherent processing over this block of data organized along two axes. A short time axis corresponding to the delay between the emission of the waveform and the reception of the waveform and long time axis corresponding to the index of the pulse in the burst. The signal received by the radar can be written as:

$$s_{pc}(t, m) = \sum_{l=1}^L a_l s_{chirp \text{ auto-correlation}} \left(t - \frac{r_l(m)}{2c} \right) + n' \quad (2.1.13)$$

With the assumption that the backscatterers remain coherent during the burst, the pulse to pulse evolution of the signal in a burst allows the measurement of the Doppler effect on the signal. The Doppler effect is the name of the apparent shift of the signal frequency received from a moving object. The apparent frequency received by the radar, $f'_{c'}$, is related to the relative speed of the backscatterer toward the radar (v_{rel}) and can be approximated by:

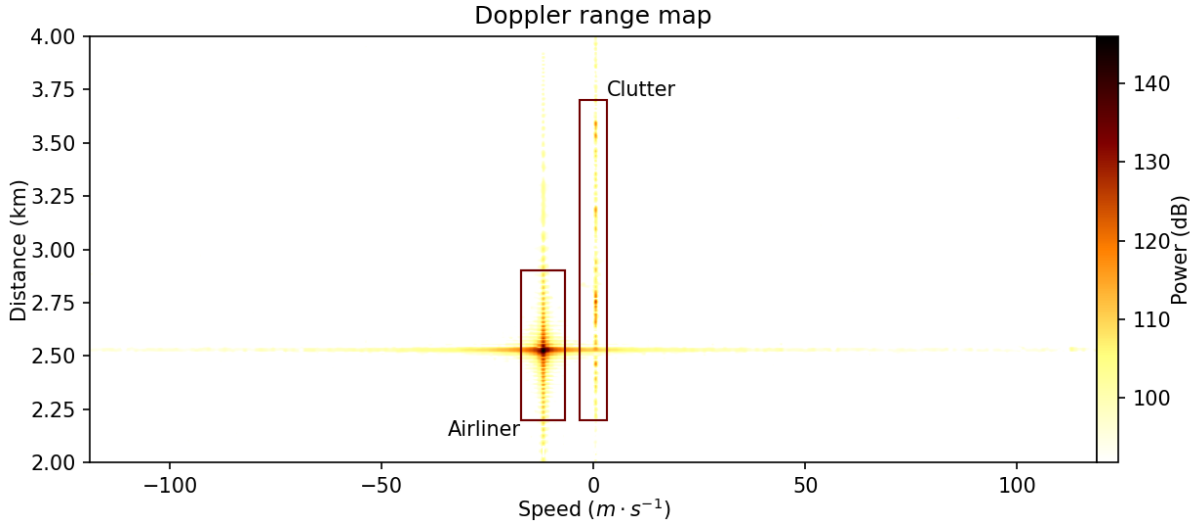


Figure 2.9: Example of Doppler range map of a radar signal with an airliner.

$$f'_c = f_c \frac{c - 2v_{rel}}{c} \quad (2.1.14)$$

For instance, by computing the discrete Fourier transform along the long time axis we filter the signal according to the relative speed of the backscatterer to the radar. The signal is organized along a range axis and a speed axis. We illustrate this with a Doppler-range map (Figure 2.9).

Since we emit the same signal every PRI we have a characteristic frequency of $PRF = PRI^{-1}$, **P**ulse **R**epetition **F**requency (PRF) stands for Pulse Repetition Frequency, we cannot measure shifts in frequency superior to the PRF without aliasing. Thus, the maximum unambiguous speed depends on the central pulse frequency and the PRI or PRF, as follows:

$$v_{amb} = \frac{PRF}{2f_c} = \frac{c}{4PRI \times f_c} \quad (2.1.15)$$

Defining waveforms is therefore a result of a compromise on the PRI since a long PRI leads to large unambiguous range measurement and low ambiguous speed measurement; conversely, a short PRI yields large unambiguous speed measurements and small ambiguous range measurements.

Figure 2.9 shows the Doppler range processing of the signal presented in Figure 2.6 and Figure 2.8. We see that for a speed of 0 m/s we have a signal; this signal is composed of the radar returns from objects that stand still, typically trees, buildings and terrain. This signal is called clutter in radar literature. In this figure, the airliner's signal is shifted due to its relative speed. In this example, the airliner was flying toward the radar at roughly $15 \text{ m} \cdot \text{s}^{-1}$ below the speed ambiguity, $\pm 120 \text{ m} \cdot \text{s}^{-1}$.

2.1.2 . Polarimetric radar

In this part we introduce the concept of polarization of the electromagnetic waves, using the Jones calculus formalism to describe it. We then discuss how a radar can measure polarization and how it constrains the radar system.

Polarization

Polarization is a property of waves, including electromagnetic waves. Polarization describes the direction of oscillation of a plane wave. The shape drawn in the polarization plane by the oscillations of the electromagnetic field defines the polarization state.

The three different shapes polarization can take are a line, an ellipse and a circle. The polarization state can be represented within a basis of two orthogonal vectors. Two different bases are often used, namely the circular basis and the linear basis.

In the orthogonal plane to the direction of propagation we define two axes x and y . A linear polarization means the shape drawn in the polarization plane is a line, and the circular polarization means the shape is a circle (see figure 2.10).

The first linear basis means we separate the polarization state into a linear combination of two linear and orthogonal polarization e.g. the **V**ertical (V) polarization, and the **H**orizontal (H) polarization. We mainly use linear polarization.

The circular basis decomposes the polarization state as a sum of circular polarization, **R**ight **H**and **C**ircular **P**olarization (RHCP) and **L**eft **H**and **C**ircular **P**olarization (LHCP). RHCP and LHCP describe in which way the circle is drawn. Two conventions exist: the **I**nstitute of **E**lectrical and **E**lectronics **E**ngineers (IEEE) convention states that LHCP is a polarization where the polarization rotates clockwise for an incoming wave whereas most physicists use the opposite convention.

The interaction between an electromagnetic wave and an object (a target) or a collection of objects (water droplets for instance) depends on its polarization. For instance, a sphere has the same signature whatever the polarization, but a dipole mostly reflects the polarization parallel to its orientation. Polarization of electromagnetic wave can also be affected by the propagation medium, and measuring the polarization from an emitted object or a propagation medium sometimes allows physicists to measure some of its properties, for instance [Mathys and Stenflo 1986] measures the magnetic field of distant stars thanks to the polarization of the received light.

Jones calculus is frequently used to describe polarization states [Collett 2005]:

$$J_0 = \begin{pmatrix} E_0 e^{i\phi_x} \\ E_1 e^{i\phi_y} \end{pmatrix} \quad (2.1.16)$$

With E_0 and E_1 amplitudes of the electric field along the x and y axes, ϕ_x and ϕ_y the phases of the oscillation projected along the x and y axes of the polarization plane. With this formalism $(1 \ 0)^T$ and $(0 \ 1)^T$ respectively describe H and V polarizations and $\frac{\sqrt{2}}{2}(1 \ i)^T$ and $\frac{\sqrt{2}}{2}(i \ 1)^T$ the two circular polarizations. Using this calculus any linear transformation can be expressed by:

$$MJ_0 = J_1 \quad (2.1.17)$$

where J_0 represents the incoming polarization state and J_1 the final polarization state and M the scattering or propagation matrix.

Polarimetric radar

In astronomy and more broadly in observational physics, sensors are usually receivers only. In this case there is only two polarizations (the two components of the Jones vector).

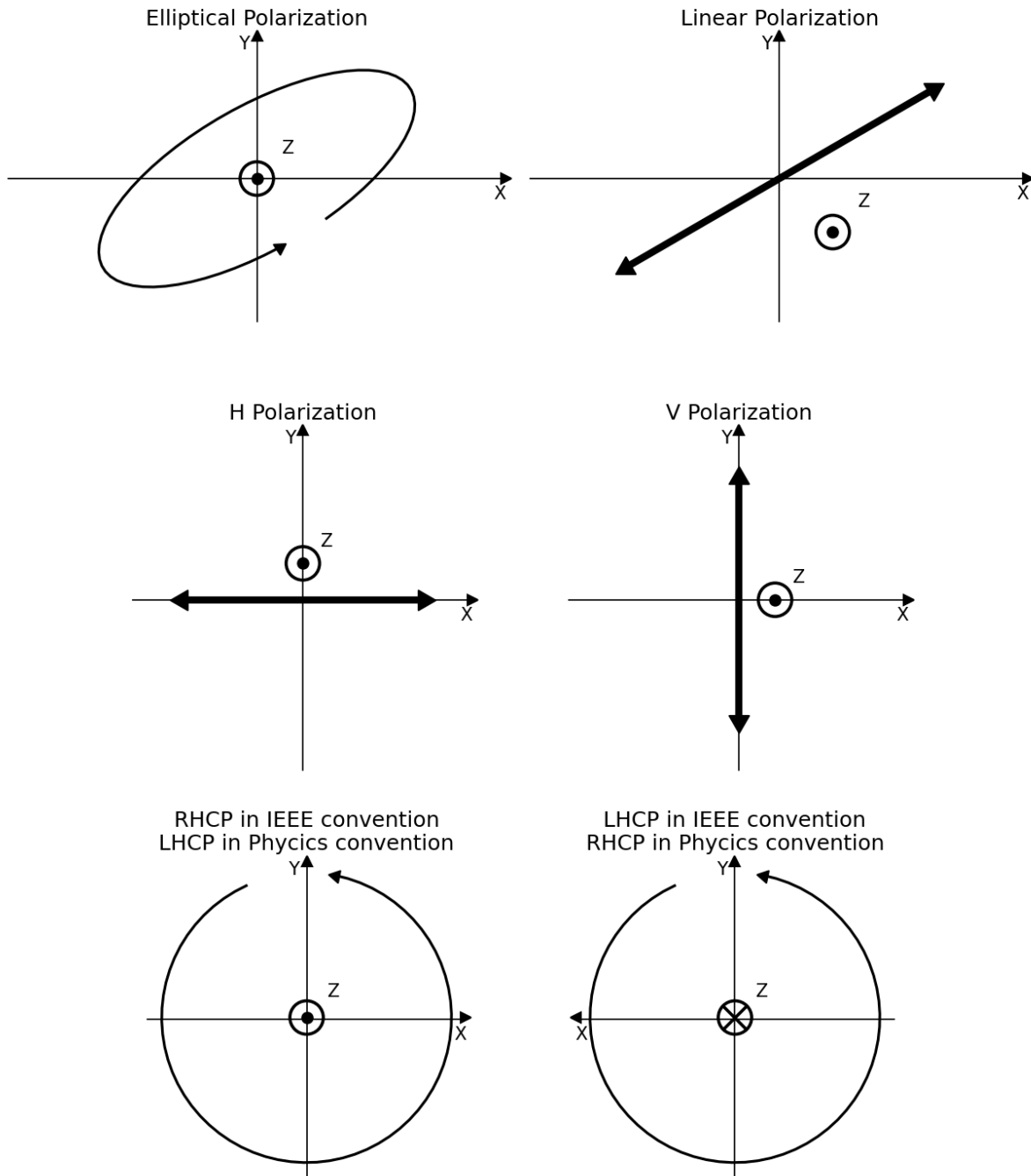


Figure 2.10: Example of polarizations, from top to bottom, arbitrary elliptical polarization and linear polarization, linear polarization basis and circular polarization basis.

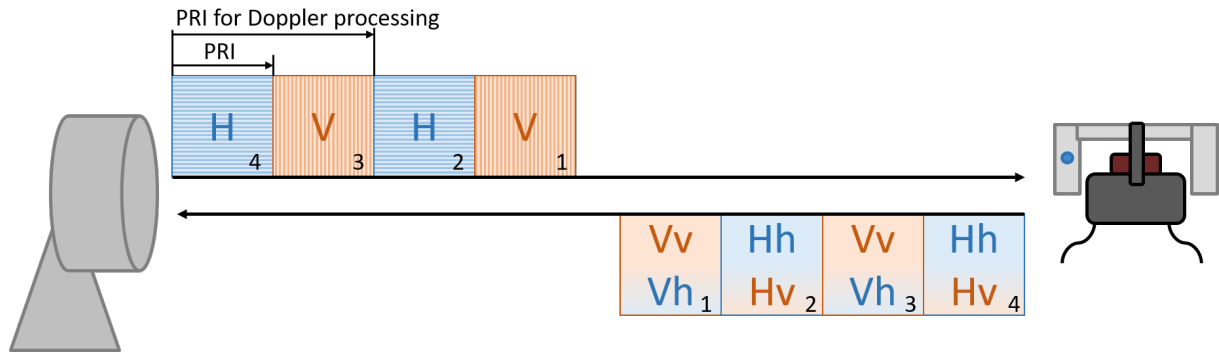


Figure 2.11: Usual transmit and receive scheme for a polarimetric radar.

In our case we use an active radar, which transmits and receives signal. The polarization of the received signal depends on the propagation and scattering process and on the transmitted polarization. To characterize our target we cannot rely only on the Jones vector measured, but we need to measure the backscattering matrix of the target that also depends on the transmitted signal 2.1.17:

$$M_p M_t M_p J_{Tx} = J_{Rx} \quad (2.1.18)$$

With J_{Tx} and J_{Rx} the transmitted and received polarization states for a single backscatterer, M_p is the propagation matrix of the medium in between the target and the radar, for the vacuum $M_p = \begin{pmatrix} R^{-2} & 0 \\ 0 & R^{-2} \end{pmatrix}$, with R the target distance to the radar, and finally M_t is the scattering matrix of the target:

$$M_t = S = \begin{pmatrix} S_{Hh} & S_{Vh} \\ S_{Hv} & S_{Vv} \end{pmatrix} \quad (2.1.19)$$

$S_{\alpha\beta}$ is the portion of α polarized electromagnetic wave that is reflected with a β polarization state. A polarimetric radar using linear polarizations can measure this scattering matrix. When emitting in the H polarization the radar measures S_{Hh} and S_{Hv} , when emitting in V polarization it measures S_{Vh} and S_{Vv} . According to the reciprocity principle, for a passive target we have $S_{Hv} = S_{Vh}$ [Tragl 1990].

As shown in Figure 2.11, radars often emit twice to measure completely the scattering matrix of the target, once in each polarization while receiving in both polarization simultaneously. It means that the PRF, and speed ambiguity are halved. The ambiguous range is unchanged.

Indeed, when the radar transmit a pulse in V polarization it starts receiving Vh and Vv polarization signals. It receives these signals up to a distance of $\frac{cPRI}{2}$, then the radar transmits a pulse in H polarization and start receiving Hh and Hv signals. The radar is still receiving Vh and Vv signals but this signals are coming from scatterers further than $\frac{cPRI}{2}$ whereas the signal in Hh and Hv are closer than $\frac{cPRI}{2}$. Because of conservation of energy, the R^{-4} factor in the radar equation, the Vh and Vv signals are a lot weaker than the Hh and Hv signals. Thus, we consider only the signal corresponding to the last polarization transmitted. So the maximum unambiguous range is linked to PRI , the time interval between the transmission of the H polarization and the V polarization. Furthermore, as the radar transmits only half of the time in a given polarization,

the transmitted power is effectively halved as well. These are the two main potential drawbacks of polarimetric surveillance radar.

Surveillance radar must be able to measure a wide range of speed as targets range from jet fighters to slow civilian airplanes; therefore, a lower speed ambiguity is not desirable, it can however be addressed by the radar by using additional processes and several different waveforms. The halved transmitted power can also be a drawback since it reduces the range of the radar by roughly 20% according to the radar equation 2.1.1.

To fully measure the scattering matrix we need at least 3 channels to the radar, a channel for Hh, Vv and Vh (or Hv) polarizations, increasing the system complexity. So far, this complexity has limited the use of fully polarimetric surveillance radars. However, polarization brings additional information about targets and the radar scene, thus it is used in some radar systems. We detail these uses in 2.4 and 2.5.4.

2.2 . Interactions between Radars and UAVs.

Since World War 2, radar is the main tool for air surveillance. As soon as UAVs became prevalent, the use of radar in a counter-UAV role have been studied. In this part, we review the literature addressing counter-UAV radars. Drones have a characteristic signature often exhibiting so-called micro-Doppler components, that are lower than the signature of the main body, which are used to detect and classify them. UAVs also require the radar system to operate in a low-grazing geometry as UAVs usually fly close to the ground, and defending against them necessitate monitoring large sectors at a time prompting the use **Multi-Input Multi-Output (MIMO)** radar using DBF.

2.2.1 . UAV radar signature

The first element to analyse when we consider a new target class is its signature. The signature of a target is defined as the RCS of this target as a function of aspect and frequency, and sometimes specific Doppler components.

The RCS of UAVs is a widely discussed topic with numerous articles in both journals and conferences. Most RCS measurements take place in anechoic chambers; it is also true for UAVs [Sedivy and Nemeč 2021]. The results discussed in the literature span over many frequency bands. For a consumer grade quadcopter, the maximum RCS reported in S-band, is around -19 dBsm, while in Ku-band the maximum RCS is around -9 dBsm for the same UAV [Li and Ling 2017; Patel, Fioranelli, and Anderson 2018a]. In C-band a RCS as high as -10 dBsm has been measured for a quadcopter. The lowest measured RCS are below -30 dBsm for certain frequencies (6.25 GHz and 7.5 GHz depending on the aspect of the UAV), with an average RCS -17 dBsm. An octocopter RCS has also been measured and its max RCS is around 0 dBsm and the minimum RCS always exceeds -16 dBsm [Herschfelt et al. 2017]. In [Sedivy and Nemeč 2021] X-band authors give RCS measurements for a variety of UAVs, the larger ones have RCS peaks between 0 and -10 dBsm, while smaller UAVs have RCS peaks between -15 and -12 dBsm. Finally in W-band smaller drones have a RCS peak between -15 to -5 dBsm, and mean RCS between -20 and -15 dBsm, whereas the bigger UAV has peak RCS going from -5 dBsm up to 2 dBsm and a mean RCS of -8 dBsm [Rahman and Robertson 2019]. These bands cover the low bands used in surveillance radar (L to X) as well as high bands preferred for classification as they grant better resolutions (Ku to W). Some of the measurements

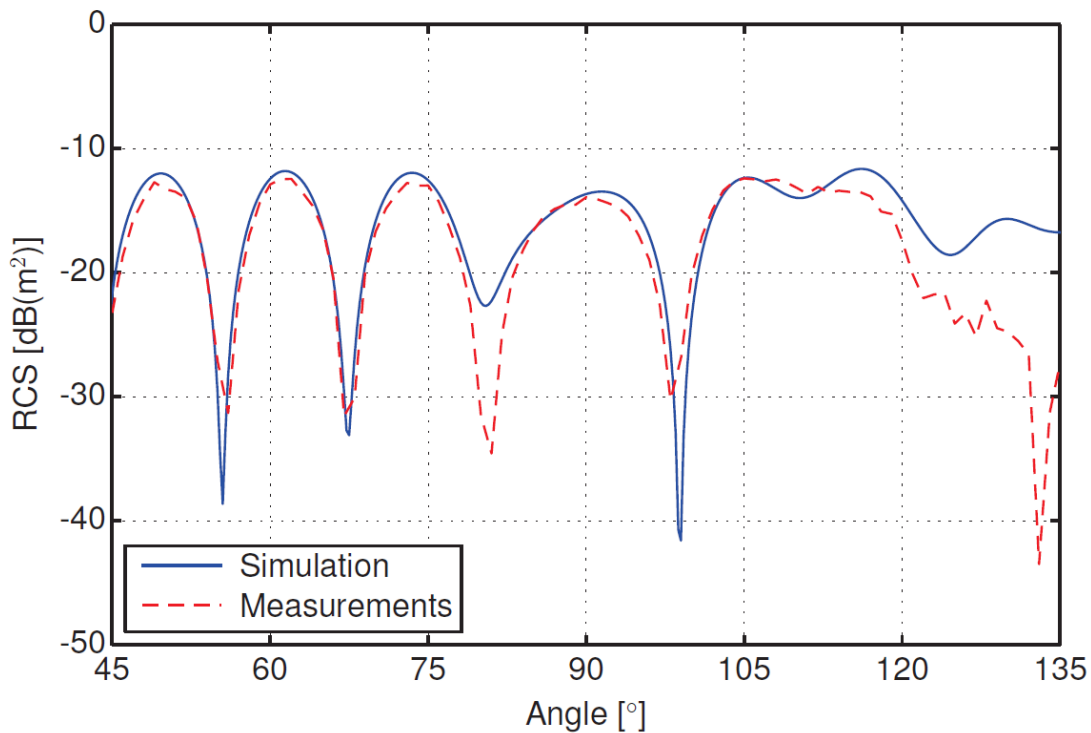


Figure 2.12: Comparison between the simulation results and measurements of DJI UAV. The angle is the angle between the transmit and receive antenna relative to the UAV. Figure from [Schroder et al. 2015]

take place with in-flight UAV [Sedivy and Nemeč 2021; Guay, Drolet, and Bray 2017].

There exists no unifying model, however, a substantial number of measurements are made on UAVs of commercial brands such as DJI [Sedivy and Nemeč 2021; Li and Ling 2017; Patel, Fioranelli, and Anderson 2018a; Rahman and Robertson 2019; Li et al. 2019; Herschfelt et al. 2017; Ezuma et al. 2022] (one of the leader on the civilian UAV market, models of this brand have been identified on warzones being used as makeshift weapon carriers [Death From Above 2017]). [Patel, Fioranelli, and Anderson 2018a] compiles the results of several previous articles in which drone signatures were measured, including [Schroder et al. 2015] in which the RCS of a DJI Phantom 2 drone is presented. It is also modelled as a core of pure copper being roughly shaped like the internal electronics of the UAV and an envelope of a dielectric material around this core to represent the plastic airframe of the UAV. This model and the measurement give similar results, as shown in Figure 2.12. The simulation results are not affected much by the dielectric permittivity chosen for the plastic airframe around the metallic core. In [Patel, Fioranelli, and Anderson 2018a], the RCS measured in the reviewed articles ranged from -30 dBsm for the small drones to -8 dBsm for the larger one.

When the measurements are made in anechoic chambers and compared to in flight measurements, authors find significant variations of RCS between the two configurations. In [Guay, Drolet, and Bray 2017] authors highlight for instance that the RCS was higher when the drone was flying (from 0 dB of difference up to RCS 6 dB higher). They suggest that the vibrations of the UAV during the flight prevent some of the destructive interferences.

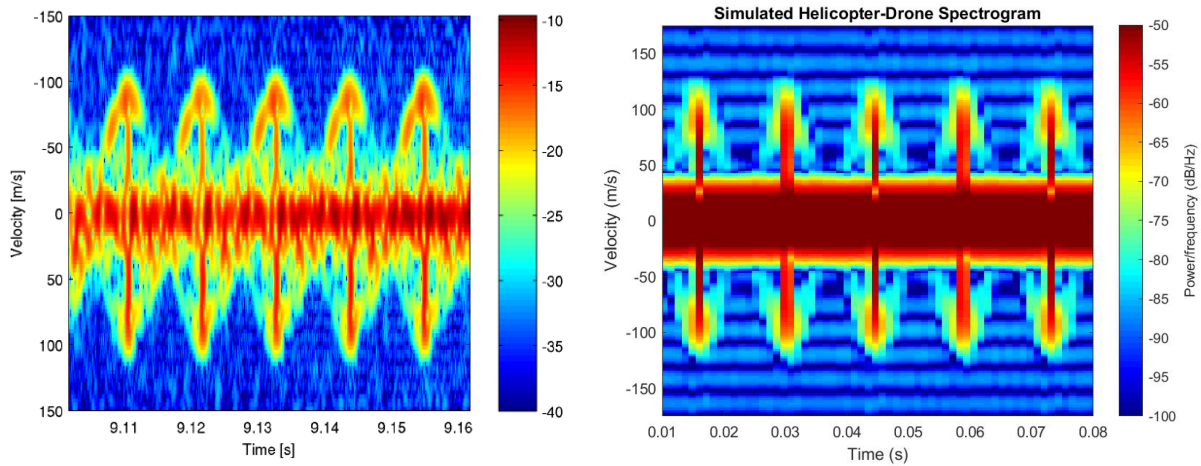


Figure 2.13: Measured and simulated spectrogram of a flying drone. We notice the blade flashes (every ~ 11 ms) and the returns from the propeller blade tip (the sine shaped returns). Source: [Leonardi, Ligresti, and Piracci 2022]

[Sedivy and Nemeč 2021] shows that assigning a single number to characterize the RCS of a UAV is an oversimplification and that the RCS should be characterized by its distribution as it varies sharply with the aspect of the UAV. [Rahman and Robertson 2019] compares the RCS distributions of UAVs in flight to birds in K and W bands. They show some differences in the RCS distributions of the UAV whether the UAV is in stationary flight or not. While hovering UAVs exhibit a lower standard deviation on their RCS distribution.

From this review, we conclude that UAVs have low RCS usually below -10 dBsm and often around -20 dBsm similar to 4++ and 5th generation fighters in frontal aspect (according to open source intelligence and estimations [Zikidis, Skondras, and Tokas n.d.]), which are notoriously hard to detect. Their RCS are also comparable to birds meaning that system designs geared toward UAV detection have to deal with birds, which evolve in the same flight domain as UAVs and are far more numerous.

Another feature of some UAV radar signatures is the presence of micro-Doppler, which is mainly due to the rotating parts. The blade flashes momentarily increase the RCS of the UAV when one or more of the propellers of the UAV are facing the radar. These RCS modulations give a very specific signature for multicopter UAVs. [Patel, Fioranelli, and Anderson 2018a], notes that the reviewed articles show that the blades' relative signal amplitude usually lay between -20 to -25 dB below the UAV main body signal amplitude, making their measurement in operational conditions challenging as outlined by [Khristenko et al. 2017]. Examples of these blade flashes and specific "Doppler" signature can be found in Figure 2.13 and in [Harmanny, Wit, and Cabic 2014; Ritchie et al. 2015; Ritchie et al. 2016; Schröder et al. 2016; Harman 2017].

For instance, if the RCS of a UAV is σ_{MB} , MB stands for Main Body, the RCS of its blades will be $\sigma_{Bl} \approx \sigma_{MB} - 24\text{dBm}$, Bl standing for "Blades", and we are able to detect that UAV at a maximum range of R_{MB} . Following 2.1.1 we write the equation:

$$CR_{MB}^4 = \sigma_{MB} \quad (2.2.1)$$

C is a constant that encapsulates the terms of the radar equation which are kept equal in this discussion, namely the wavelength, transmitted power, received power

and antenna gains. We have $\frac{\sigma_{MB}}{\sigma_{Bl}} = \frac{R_{MB}^4}{R_{Bl}^4}$ with R_{MB} the maximum range at which we can expect a reliable detection of the blades, and σ_{Bl} the RCS of the blades. Therefore we have $R_{Bl} = \frac{R_{MB}}{4}$, any signal processing on micro-Doppler signatures (be it classification or detection) requires the target to be 4 times closer to the radar. Signal processing relying on micro-Doppler is thus challenging to implement in operational context as [Khristenko et al. 2017] outlines. It needs to be emphasized that the typical RCS of small UAVs' propellers (in the lower range of measured RCS) is roughly the same as the RCS of sizeable insects [Zikidis, Skondras, and Tokas n.d.].

As already mentioned UAV signatures share some similarities with birds, thus their signature are often compared [Ritchie et al. 2016; Rahman and Robertson 2019]. [Ritchie et al. 2016] notes that the RCS of birds and UAVs are similar, but their Doppler signatures are quite different and suggest using such features to classify drones and birds. In [Rahman and Robertson 2019] the distributions of RCS of UAVs and birds are compared: even though the distributions exhibit some differences the authors consider this to be insufficient for classification purposes; and they suggest to use micro-Doppler for classification.

The influence of polarization for the blades signature is also investigated in [Ritchie et al. 2015], with simulations and experiments showing a lower return in Vv than in Hh polarization for a DJI Phantom drone. The micro-Doppler Hh signal was 30 to 40 dB lower than the main body signature according to simulations. The return in Vv could not be measured as the SNR of the Hh micro-Doppler signature was lower than 30 dB.

2.2.2 . UAV classification

Another important aspect of counter-UAV radars is their ability to classify drones, both classify them against other targets, and identify the model of UAV. One aspect of this classification is the differentiation between a drone and a bird, which are two target types that are in the same flight domains: close to the ground and usually moving slowly. The second aspect is the ability to differentiate between drone models. In [Patel, Fioranelli, and Anderson 2018a] some classification methods are reviewed.

Several methods to classify between UAVs and birds have been investigated. One of them relies on the RCS of the target. [Harmanny, Wit, and Cabic 2014] suggests that RCS can be used to discriminate between UAVs and birds as UAVs tend to have a larger RCS. Nevertheless they mention that this feature is not robust as it varies with the aspect of the target. [Ritchie et al. 2016] and [Rahman and Robertson 2019] confirm this and suggest to use other features such as the micro-Doppler signature.

While micro-Doppler signatures can be difficult to detect, as reported earlier, its implementation for classification against birds for instance is by far the most used feature for classification. Several methods exploit the Doppler signature but not all methods use the data in the same way.

Some articles analyse the micro-Doppler signature using spectrogram [Wit, Harmanny, and Molchanov 2014; Harmanny, Wit, and Cabic 2014]. This method requires a high PRF to measure the effects of the blade flashes. As stated in 2.1.1 the PRF defines the upper limit of the frequency to be observed. Thus, the PRF must be higher than $F_{Prop} \times N_{blades}$, with F_{prop} the propeller's frequency and N_{blades} the number of blades of the propeller. This method allows the discrimination between birds and UAVs. [Wit, Harmanny, and Molchanov 2014] uses a **Single Value Decomposition** (SVD) on the spectrogram to further quantize the micro-Doppler signature and shows that only a few

singular vectors carry most of the information (the SVD is the generalization of the eigenvalue decomposition to arbitrary matrices). [Kang et al. 2021] compares the spectrogram to the Doppler spectrum for classification, and outlines some drawbacks of using the spectrogram compared to the Doppler, notably its strong dependency on a clean measurement (clear of interference and with a good **Signal to Interference plus Noise Ratio** (SINR)) and its computational complexity. They show clear differences in both Doppler spectrum and spectrogram of birds and UAV thus enabling classification. [Oh et al. 2018] uses an **Empirical Mode Decomposition** (EMD) to classify different types of drones as well as to discriminate drones from birds. EMD is a decomposition of the signal into a sum of functions, which must satisfy some properties, they should form a basis that is orthogonal or nearly orthogonal. These functions are called **Intrinsic Mode Function** (IMF) and are computed from the dataset on which the EMD is performed. Their computation is a recursive process that is based on the envelope of the signal. The mean of the envelope of the signal is an IMF. The first IMF is removed from the signal and the envelope of the new signal is used to compute the next IMF. This recursive process is repeated until a stoppage criterion is reached and gives the IMF basis. This method gives good results for discriminating birds and drones as the correct identification rate is 99% (true positive rate), and no UAV is classified as bird with a rate above 2% (false negative rate). However this method doesn't seem to work as well for fixed wing UAVs as one of the two fixed wing UAVs tested is classified correctly only 58% of the time and is misclassified as an other fixed wing UAV 31% of the time, which shows the importance of micro-Doppler in the classifier.

In recent years, there has been a strong trend on using neural networks for classification, as it enables the discrimination of the models of UAV as well as birds and UAVs. [Kim, Kang, and Park 2017; Brooks et al. 2018; Rahman and Robertson 2020; Dale et al. 2021; Dale et al. 2022; Gérard 2022] show good performances of Neural Networks when it comes to classify drones and birds. It should be noted that [Dale et al. 2021] shows that the classification performances drop when the SNR gets low: the performances start to drop around a 35 dB SNR and some classifiers are unable to classify at 20 dB SNR (The SNR is measured after the Doppler processing in this case). [Dale et al. 2022] proposes to address this problem with data augmentation. [Gérard 2022] proposes to use **Generative Adversarial Network** (GAN) to augment the dataset. GANs are neural networks that take inputs to generate a new dataset resembling another dataset. [Gérard 2022] designed GANs that uses flight logs of UAVs to generate signatures for augmentation.

Another method for classification uses polarization, [Torvik, Olsen, and Griffiths 2016] for instance. They show true positive identification rate (the target is of a certain class and classified as such) superior to 98.8% for every of the 4 classes defined, UAV with carbon fiber blades, birds with flapping wings, UAV with plastic blades and gliding birds. The true positive rate for the UAV with carbon fiber blades is 100% which means that these targets are never misclassified (however some targets are misclassified as UAV with carbon fiber blades). They argue that in absence of substantial micro-Doppler signature for the target, polarization can be used in the classification process. Indeed the information carried by polarization remains when the frequency band, carrier frequency and dwell time are reduced to be more in line with operational radar standards.

Finally, work has been done on classification between loaded and unloaded drones. [Ritchie et al. 2017] outlines promising classification methods allowing a preliminary

assessment of the threat level of a drone thanks to the Doppler signature. The authors use the **Single Value Decomposition (SVD)** on the spectrogram of the Doppler data and achieve true positive rates of classification in excess of 95%.

2.2.3 . Counter-UAV radar systems and detection

UAV detection is the first topic to consider for a counter-UAV radar. As mentioned in part 2.1.2.1, UAVs have low RCS and specific flight behaviours. [Poitevin, Pelletier, and Lamontagne 2017] outlines that a radar system roughly needs 10 seconds to detect and establish an accurate track and 20 additional seconds for assessing the class of the target and the threat level of the UAV and eventually neutralizing the target. If the UAV is capable of travelling at $20 \text{ m} \cdot \text{s}^{-1}$ (a common speed for commercial drones), this processing time allows the UAV to travel 600 meters. It means that the minimum detection range should be at least one kilometre. Therefore, many operational counter-UAV radar systems usually operate in lower frequency bands, as shown in [Birch, Griffin, and Erdman 2015] and [*Radar Based Non-Cooperative Target Recognition (NCTR) in the Low Airspace and Complex Surfaces environments 2021*]. This includes L, S, C and X bands.

[Poitevin, Pelletier, and Lamontagne 2017] also outlines the need for counter-UAV systems to be able to cover a wide area, often having a necessary coverage as large as 360° . Thus, a frequent configuration for counter-UAV radar system is to use staring radars instead of scanning radars. A staring beam is a fixed large beam covering the whole radar surveillance zone allowing long integration time, while a scanning beam is a narrow beam covering the surveillance zone by being steered back and forth. [Herman 2015] describes a C-band radar and shows the different probability of detections as a function of range and operating mode of the radar with a scanning beam or a staring beam. He shows that depending on the target type staring radar performs better, staring radars especially give better tracking performances. Aveillant has developed L-band radars [Jahangir 2015; Jahangir and Baker 2016; Jahangir, Baker, and Oswald 2017; Gersone et al. 2018] for UAV detection with the ability to be used as staring radar. [Gersone et al. 2018] shows a potential drawback of staring radars for dealing with targets travelling perpendicular to the line of sight. The signal obtained with a standard Doppler processing is smeared both range and Doppler wise. The authors propose an alternative processing to address this problem.

MIMO radar systems (radar system with several independent transmitting and receiving elements able to emit orthogonal waveforms simultaneously) have large beams and use DBF which allows them to be in a staring radar configuration while providing a localisation ability. Thus, they are frequently used for counter-UAV radars. [Frankford et al. 2014] investigates the use of MIMO radar for the detection of UAVs and shows potential improvements of using MIMO radar instead of the phased array equivalent radar. [Klare, Biallowons, and Cerutti-Maori 2017; Biallowons, Klare, and Fuhrmann 2018] demonstrate the capabilities of the MIRA-CLE MIMO radar featuring a sparse antenna. This radar is able to have similar performances to its equivalent array antenna radar (with the synthetic antenna formed with MIMO processing).

There also exists UAV detection system that run passively, meaning that the radar does not emit the waveform and uses waveforms of the environment to make detections. For instance, [Schüpbach et al. 2017] reports UAV detections at up to 1.2 km using digital radio signal. It is reported a detection rate up to 36% for a probability of false alarm (the probability that a detection does not corresponds to a target) of 10^{-6} . [Poullin

2016] shows it is possible to use a passive radar using digital television signal to detect UAVs thanks to their blade flashes. [Poullin, Dorey, and Taylor 2022] shows this method can lead to passive detection of UAVs up to 10 km.

Many counter-UAV radar systems and classifiers implements standard detection algorithm of the **Constant False Alarm Rate (CFAR)** class for the detection step [Kwag et al. 2016; Drozdowicz et al. 2016; Hoffmann et al. 2016; Jahangir, Baker, and Oswald 2017; Aldowesh, Alnuaim, and Alzogaiby 2019; Martinez 2019; Morris and Hari 2021] which we describe in more detail in 2.5. However, some counter-UAV systems use more complex detection schemes. Specific detection schemes have been developed to address the need for a fine Doppler resolution. [Sun et al. 2019] describes the Iterative Adaptive Approach, which improves the Doppler resolution by iterating several frequency filters on the data. The iterative filters are used to remove more noise in the Doppler space; therefore, they allow the SNR of the UAV to increase after this processing, which leads to better performances for both classification and detection. They gain up to 7 dB for birds, and up to 4 dB of gain for UAVs.

2.2.4 . Conclusion

In this part, we have discussed the challenges associated with the detection and classification of UAVs. We outlined the low RCS of UAVs, in the range between -30 and -10 dBsm. We also showed the specificity of the signature of the copter type drones' blade flashes. The low RCS means that their signature is similar in terms of magnitude to the signature of birds which share the same flight domain and can be confused with UAVs. Therefore, the classification between UAVs and birds is essential. Measuring the blade flashes is often paramount for the classification of UAVs and bird as the vast majority of the methods use the micro-Doppler signature for classification. The flight domain of drones, close to the ground, at slow speed or even hovering, forces the radar to use a low-grazing geometry, which exacerbates the influence of clutter. This prevalence of clutter in the radar scenes makes the detection more difficult. The problem of endo-clutter detection of UAVs, is seldom addressed. One of the method used is to detect the blades exo-clutter signature instead of the endo-clutter signature of the main body. In our work we focus on the main body endo-clutter signature.

2.3 . Radar Clutter

As the previous part outlined counter UAV radar are forced to operate in a low-grazing geometry and deal with drones that fly at low speeds, thus, the clutter is an important feature of the radar scene. For UAV detection, clutter can be considered as the sum of all unwanted radar returns. Depending on the author, it includes only returns from stationary backscatterers, or even returns from objects part of the environment like cars or birds which can have very similar behaviour to actual targets of interests. For simplicity sake, in the following, clutter refers to stationary target returns (building, terrain, etc.), and quasi-stationary targets (vegetation). When clutter is studied in the next parts it might include targets such as cars and birds that happen to have null relative speed with the radar. The distributions of the clutter are usually heavy-tailed (unlike noise), thus they need a different model. Furthermore they have some form of temporal coherency as we detail.

2.3.1 . General consideration on clutter

As clutter is not a noise, but radar returns, it behaves differently in several ways. First it is coherent from pulse to pulse contrary to noise, this is called temporal coherency. It means that clutter has a specific Doppler signature. For a fixed ground radar, clutter will have a Doppler speed around $0 \text{ m} \cdot \text{s}^{-1}$ since it is composed of radar returns from immobile or slow moving objects (terrain, sea, buildings, trees, etc.). This temporal coherency has several consequences:

- Longer Doppler integration time does not change the **Signal to Clutter Ratio (SCR)**, since both the target and clutter are coherent.
- Higher transmitted power does not change the SCR.
- If the target and clutter have different speed (if the target is moving for instance), the clutter can be filtered out using its Doppler signature.

2.3.2 . Sea Clutter

Sea clutter is mostly caused by the swell of the sea and is not necessarily stationary. Sea clutter is usually modelled as a k-distributed random variable [Ward 1982]. Ward also outlines that the clutter is coherent from pulse to pulse which is not the case for the noise, which allows for a coherent integration that separates the clutter from the noise. [Ward, Baker, and Watts 1990] shows model based on the physics of the swell of the sea. He also proposes a temporal correlation of the complex monopolarimetric data (not relying only on the magnitude of the signal as usually done for sea clutter modelling). [Shnidman 1999] proposes a model for sea-clutter based on a modified Chi-square (χ^2) distribution, the **Noncentral Chi-Square Gamma (NG)**. This model provides the heavy tail behaviour expected while using the often used Chi-square distribution as underlying basis.

2.3.3 . Land Clutter in Low-grazing Geometry

Land clutter is more diverse than sea clutter and is therefore not modelled as easily as sea clutter. [Sekine et al. 1981] shows that this type of clutter can be modelled as a Weibull distributed random variable with parameters close to Rayleigh distribution. The article is based on measurements in low-grazing angle configuration (0.2° to 0.3°). [Shnidman 1999] states that log-normal and Weibull distributions fit well with ground clutter as they exhibit the same heavy tail properties that are observed for ground clutter. He proposes the NG distribution for land clutter as it relies on a physical model based on low number of backscatterers in resolution cells. Thus, it applies for applications where resolution cells are small such as high frequency radar or **Synthetic Aperture Radar (SAR)** (a technique we introduce in 2.4.2). It is not representative of our case, we detail in 4.1.2. In addition this model distribution allows for the modelling of speckle (high-resolution granular interferences). [Sayama and Sekine 2001] shows that cultivated lands are best modelled with Weibull, log-Weibull and K-distributions. They show that lowering the resolution (larger range cells) means less spread of the clutter distribution, as more backscatterers are included in the range cell and their contribution averaged. [Billingsley 2002] shows the dependency between the mean and median value of the clutter returns and the radar frequency. It should be noted that while the amplitude variations of the returns with frequency are largely monotonous,

some clutter types exhibit increase of RCS with frequency (for instance, urban clutter and farmland) and others decrease of RCS (for instance mountains) with frequency. He also shows that for high frequency radar (S-band and X-band) there is some seasonality of the mean clutter level, whereas in **Ultra High Frequency (UHF)**, **Very High Frequency (VHF)** and L-band the dependency is less or not pronounced. This is not only due to the smaller range resolution of the lower band but also due to the fact that smaller objects do not backscatter radar signal with large wavelength. For instance, a cultivated field changes with season, but a lower frequency radar will only be affected by the ground underneath the culture, and the ground doesn't change much from season to season. When range bins are well resolved in L-band, S-Band and X-band, the too high frequency shows a strong seasonality (up to +15 dB in late spring compared to winter) while the lower L-band shows little seasonality. [Davidson, Griffiths, and Ablett 2004] outlines that the estimation of the distribution of the clutter is not trivial due to the high variability between clutter cells.

2.3.4 . Low-grazing polarimetric surface clutter

[Ward, Baker, and Watts 1990] discusses the polarimetric signature of sea clutter. Hh returns show higher spikes than expected with the distribution used to model the sea clutter, with a duration of up to 2 seconds, while Vv polarisation returns are less spiky. It means that this burst of power are highly polarisation dependant. Sea clutter is usually heavier tailed in Hh than Vv .

[Moisseev et al. 2000] notes that the cross-polar to co-polar ratio is used to detect ground clutter in weather radar. This ratio tends to be higher in ground clutter than in meteorological targets. The correlation rate between Hh and Vv returns is also used since ground clutter has low correlation rates (under 0.8).

2.3.5 . Conclusion

This part outlines the differences between noise and clutter, namely the fact that clutter is coherent, and usually heavy-tailed. This means that endo-clutter detections are harder than exo-clutter detection: whereas a coherent integration allows for an increase of the target's signal while it keeps the noise at the same level, a coherent integration also increases the level of the clutter. In addition clutter returns are radar returns from backscatterers contrary to noise which means that SCR does not behave like SNR, as neither an increase in transmitted power nor a Doppler processing increases the SCR. To have better performances for endo-clutter detections we therefore have to use other sources of diversity such as polarization.

2.4 . Polarimetric Radar Classification Methods

Ground clutter proves to be a complex object that poses challenges to radar, as we mentioned the additional degrees of freedom brought by polarization are useful to characterize both environment and targets. The classification methods used in **Synthetic Aperture Radar (SAR)** imaging and weather radar informs us on the possibility brought by polarization.

2.4.1 . Weather Radars

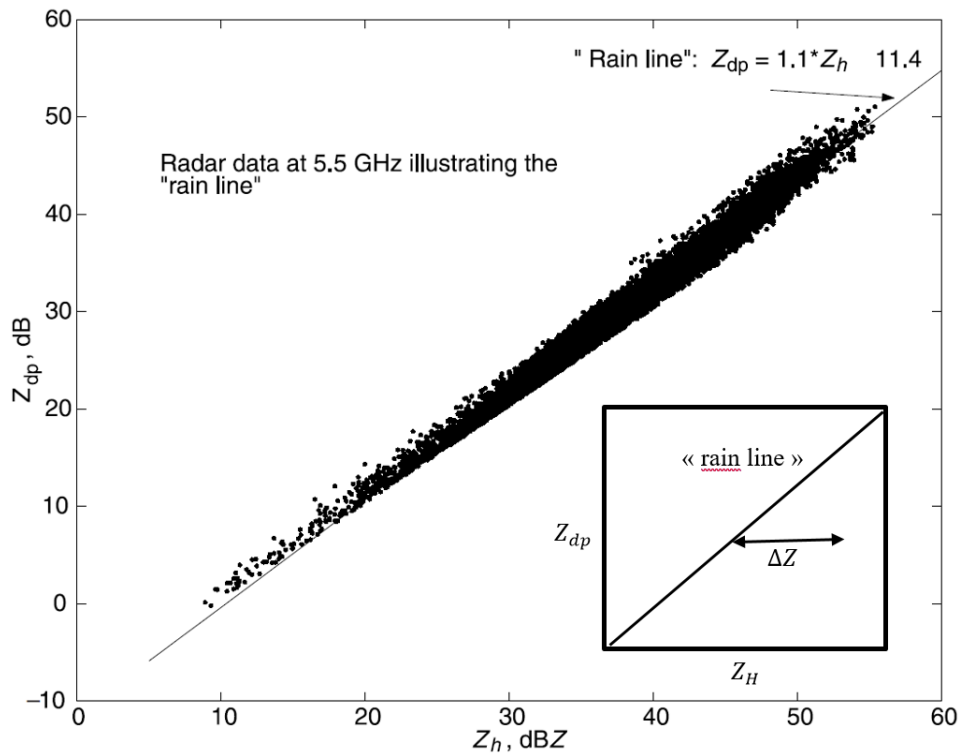


Figure 2.14: Plot of Z_{dp} as a function of Z_H showing the "rain line", source: [Bringi and Chandrasekar 2001]. We added the inset to show how ΔZ would manifest on a graph of the relationship between Z_H and Z_{dp}

Polarimetry enables weather radars to classify zones according to the rainfall rate. Authors of [Brandes, Ryzhkov, and Zrnich 2001] describe methods to measure the rainfall rate, with the specific differential phase (K_{dp}). K_{dp} is the rate at which the relative phase between H and V signal evolves. H and V polarized waves do not propagate at the same speed through a medium with non-spherical hydrometeors (water drops, hail, etc.). K_{dp} increases with the rainwater content [Sachidananda and Zrnich 1987].

Polarimetric radar also allows the classification of precipitations. [Ryzhkov and Zrnich 1998] proposes a classification of rain and snowstorm. The authors show that using K_{dp} as well as:

- Z_{dr} , the depolarization rate defined as the ratio between Hh and Vv channels in decibels,
- Z , the reflectivity factor (the "RCS" of a volume of hydrometeors),

allows the discrimination between rain and snow. [Schleiss et al. 2020] points out that polarimetric radar methods for estimating the rainfall rate do not exhibit any bias linked with the intensity of the signal received contrary to monopolarimetric methods. To obtain this result, authors compare measurements of rainfall rates obtained with monopolarimetric radar and polarimetric radar with measurements of ground rain gauges. In addition, the authors note that the performances obtained by the polarimetric radar are promising since they were not calibrated by ground rain gauges beforehand, contrary to the monopolarimetric radars.

Synthetic aperture radar

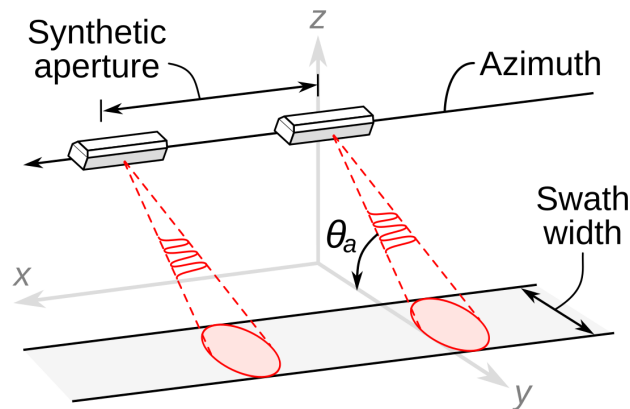


Figure 2.15: SAR working principle, it shows the synthetic aperture created by the movement of the radar. Source: wikimedia.org

Polarimetry also allows to classify between hail and rain [Tong et al. 1998] using the reflectivity in H , Z_H , and the difference reflectivity $Z_{dp} = 10\log(Z_H - Z_V)$, as Z_{dp} and Z_H are heavily correlated for rain forming the "rain line" (Figure 2.14). The signature of volumes of hydrometeors deviates from the "rain line" by ΔZ . The magnitude of ΔZ is linked to the ice fraction, f (the proportion of ice hydrometeors), with $f = 1 - 10^{-0.1\Delta Z}$ (See inset in Figure 2.14). [Liu and Chandrasekar 2000] shows that polarimetric data can be used to create a reliable classifier between hydrometeors type going from drizzle to large hail.

2.4.2 . Synthetic Aperture Radar (SAR)

SAR imaging uses the movement of a vehicle carrying a radar to create a virtual antenna larger than the physical antenna of the radar and therefore, achieve very fine resolution (Figure 2.15).

Airborne and spaceborne SAR are used to image large surfaces and polarimetry is used to classify and segment land patches with two classes of methods: some classifiers use the physics of backscattering mechanisms and others are based on empirical classifications coming from observations. One such classification methods uses the Pauli decomposition. With this decomposition of the scattering matrix based on the Pauli matrices, the scattering vector becomes:

$$\mathbf{X} = [\sigma_1, \sigma_2, \sigma_3]^T = \frac{\sqrt{2}}{2} [S_{Hh} + S_{Vv}, S_{Hh} - S_{Vv}, S_{Hv} + S_{Vh}]^T \quad (2.4.1)$$

Each element corresponds to a backscattering process:

- σ_1 corresponds to odd numbers of bounce scatterings (typically a sphere, trihedron or a plane surface),
- σ_2 corresponds to even numbers of bounce scatterings like a dihedron,
- σ_3 corresponds to the depolarizing process, corresponding to volumetric scatterers.

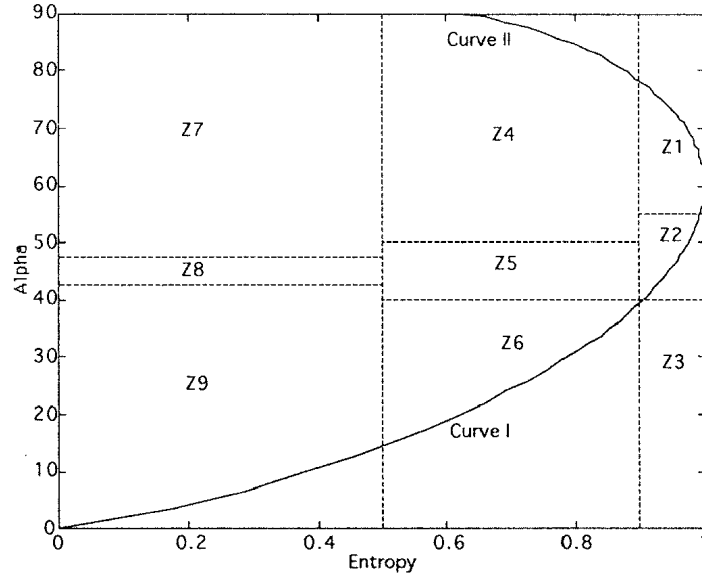


Figure 2.16: Different classes of the $H - \alpha$ decomposition [Cloude and Pottier 1997]. Curve I and II show the physical limit, points to the right of the curves are not physical.

[Cloude and Pottier 1996] discusses several polarimetric decompositions for classification. In [Cloude and Pottier 1997], a classification method based on the coherency matrix is discussed. The coherency matrix is:

$$C = \frac{1}{N} \sum_{i=1}^N X_i X_i^H \quad (2.4.2)$$

where X_i is the polarimetric radar data vector of one of N studied cells. This matrix is decomposed into eigenvalues λ_i with associated eigenvectors U_i . The entropy is defined as:

$$H = -\sum_{i=1}^3 p_i \log_3 p_i \quad (2.4.3)$$

with $p_i = \lambda_i / \sum_{j=1}^3 \lambda_j$, the anisotropy is defined as:

$$A = \frac{\lambda_2 - \lambda_3}{\lambda_2 + \lambda_3} \quad (2.4.4)$$

and finally the mean angle

$$\alpha = \sum_{i=1}^3 p_i \alpha_i \quad (2.4.5)$$

with α_i defined from the eigenvector U_i , with $U_i = [\cos(\alpha_i), \dots, \dots]$. This classification method uses 9 classes.

The classes are surfaces in the $H - \alpha$ space (shown in Figure 2.16), and represent, amongst other things, dihedral reflectors, random surfaces, random anisotropic scatterers, etc. The article shows the results obtained during two measurement campaigns: they seem to follow the physical model. This classification is often used to initialize unsupervised classification, for instance with machine learning methods.

[Freeman and Durden 1998] presents a classifier based on single and double bounce as well as a volumetric scattering decomposition and shows that this classifier gives good performances to distinguish between terrain types and even terrain state (for instance flooded or nonflooded terrain). Another decomposition based on the covariance matrix or coherency matrix such as the one proposed in [Yamaguchi et al. 2005]

propose to add other scattering mechanisms in the decomposition to better classify. [Yamaguchi et al. 2005] shows that this new component, the helical scattering process, is a useful component to discriminate between naturally occurring patches of land and urban areas. It also shows that modifying the volume scattering term is useful to better model the underlying scattering process and obtain a better classifier. This is an empirical approach to extend a physical classifier. To address the limitation of this model, [Yamaguchi et al. 2011] modifies the volumetric component of the decomposition, depending on the relative returns of the co-polar channels. This modification is made because, in light of new datasets the authors concluded that the physical model could be amended to classify more faithfully the patches, in more diverse measurement conditions. These results outline the risk of bias associated with the use of empirical models, that might later have to be corrected.

On the other hand, other classification methods do not use physical models to classify; they rely on observations to assess which combination of polarimetric parameters is better suited for a given task. For instance, [Wakabayashi et al. 2004] shows that polarimetric parameters allow a good classification of ice types. A relation exists between the Vv -to- Hh scattering ratio and the ice thickness.

2.4.3 . Conclusion

This part gives an overview of the classification methods that use polarimetric data, we outline that both for weather and imaging radar, polarimetric radar data to increases the accuracy of the measurements are creates new classification possibilities all together. Since the polarization is an asset for classification, the next part addresses radar detectors, and in particular, endo-clutter detection schemes on the one hand and polarimetric detection schemes on the other hand.

2.5 . Detections

2.5.1 . Framework and Mono-channel Detectors

Detecting a target may be the most important step in the radar processing chain as far as air surveillance is concerned. A radar detector is an algorithm (it can be either analogic or digital) able to take radar data and classify them between two states: target is present or target is absent. Given a vector of radar data \mathbf{X} in a given cell, the **Cell Under Test** (CUT), we write the following:

$$\begin{cases} h_0 : \mathbf{X} = \mathbf{n} + \mathbf{c} \\ h_1 : \mathbf{X} = a\mathbf{b} + \mathbf{n} + \mathbf{c} \end{cases} \quad (2.5.1)$$

With \mathbf{n} and \mathbf{c} respectively a noise vector and clutter vector, \mathbf{b} the target vector a is a scalar which. \mathbf{n} and \mathbf{c} represents both the power of the noise and clutter, as well as their structure along the different channels of the radar data, whereas \mathbf{b} represents the structure of the target radar data and a represents its magnitude. Here we do not consider the influence of interferences and/or jammers. h_0 and h_1 are the two hypotheses the detector must discriminate between. h_0 is the “no target” hypothesis and h_1 is the “target” hypothesis. Most detectors compute a value based on \mathbf{X} and compare it to a threshold, η_0 , the detection test is written:

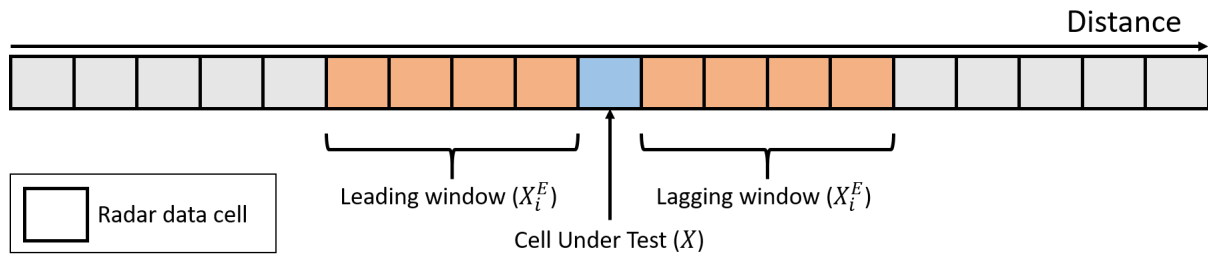


Figure 2.17: "Leading" and "lagging" windows in relation to the CUT.

$$f(\mathbf{X}) \underset{h_1}{\overset{h_0}{\leq}} \eta_0 \quad (2.5.2)$$

With $f(\cdot)$ a scalar valued function of the vector \mathbf{X} . Two important metrics for detectors are the probability of detection, P_D , and the probability of false alarm P_{FA} . P_D is the probability of detecting the target knowing the target is present (the true positive rate), while the P_{FA} is the probability to detect a target knowing none is present (the false positive rate).

A desirable property of radar is to have a **Constant False Alarm Rate (CFAR)**, meaning that for a given stable noise and clutter distribution the P_{FA} of the detector is constant. According to 2.5.2 lowering η_0 results in more detections, thus increasing the P_D and P_{FA} . Conversely increasing η_0 leads to lower P_D and P_{FA} . Fluctuations of the clutter or noise obviously impacts the P_{FA} . [Finn and Johnson 1968] proposes to adaptively change the threshold using secondary data. The secondary data is a set of scalar radar data not in the CUT, $\{X_i^E\}_{i \in [1, N]}$, the superscript E denotes that the associated variable is from the estimation dataset. Knowing the clutter and noise statistical distributions, we deduce the probability of false alarm thanks to the threshold. In [Finn and Johnson 1968] the threshold is dynamically adjusted to ensure a CFAR property, by using secondary data to estimate the variance of the clutter and noise distribution. We modify 2.5.2:

$$f(\mathbf{X}, X) \underset{h_1}{\overset{h_0}{\leq}} \eta \left(\{X_i^E\}_{i \in [1, N]} \right) \quad (2.5.3)$$

The $\eta(\cdot)$ function takes the secondary data and adjusts a threshold to ensure a constant false alarm rate. It is equivalent to having a fixed threshold with a $f(\cdot)$ function that adjusts the output levels with the secondary data and compares it to a fixed threshold as long as f output is in \mathbb{R}^{*+} . Under these assumptions 2.5.3 becomes:

$$f\left(\mathbf{X}, \{X_i^E\}_i\right) \underset{h_1}{\overset{h_0}{\leq}} \eta_0 \quad (2.5.4)$$

2.5.2 . Mono-channel detector

In [Finn and Johnson 1968], the data on which the detection test is made is scalar. The secondary data come from the range axis, from two windows, a "leading" one, with

data in range cells closer to the radar than the CUT and a "lagging" window, data further away from the radar than the CUT (Figure 2.17). The assumption is that the secondary data cells do not contain any target. Assuming the clutter and noise are normal distributed, the standard deviation of the clutter and noise distribution are computed using maximum likelihood estimator for zero-mean Gaussian noise:

$$\sigma = \sqrt{\frac{\sum_{i=1}^N |X_i^E|^2}{N}} \quad (2.5.5)$$

We have $\eta(\{\mathbf{X}_i^E\}_i) \propto \sigma$ and thus, $f(X, \{\mathbf{X}_i^E\}_i) \propto \frac{1}{\sigma}$. We have:

$$\frac{|X|^2 h_0}{\sigma^2} \underset{h_1}{\leq} \eta_0 \quad (2.5.6)$$

[Finn and Johnson 1968] shows that with this adaptive threshold, the probability of false alarm is independent from noise power. This detector is known as **Cell Averaging CFAR** (CA-CFAR) due to how the noise standard deviation is computed. This detector makes the assumption the secondary data are representative of the clutter or noise we want to be estimated in the CUT. This is an important drawback as this assertion does not necessarily hold, for instance, the presence of a target in the secondary data leads to a degraded P_D .

A solution to overcome this drawback is to censor the secondary data. It can be based on the raw output of the secondary data, or on more refined metrics such as variability index as we see next. Even though those methods are quite different they share a similar concept, as they both rely on cleaning the data entering in the estimation dataset to ensure they are representative of the noise and clutter under the target.

Greatest Of CFAR (GO-CFAR) [Hansen 1973] and **Smallest Of CFAR** (SO-CFAR) [Trunk 1978] are two detectors that address the shortcoming of the CA-CFAR. Each detector censors one of the aforementioned leading and lagging window. The GO-CFAR censors the smallest mean window. This detector is designed to ensure the P_{FA} does not increase in inhomogeneous environment. The SO-CFAR censors the highest mean window, and it prevents some decrease of P_D in multi-target or clutter edge scenarios. These detectors themselves have drawbacks outlined in [Weiss 1982]. Namely, the loss of P_D of GO-CFAR in multi-targets environment and an increased P_{FA} in clutter edge scenario for the SO-CFAR. The articles conclude that it is unlikely there exists an optimal CFAR algorithm for each and every case.

The authors of [Smith and Varshney 1997] propose the **Variability Index CFAR** (VI-CFAR) that measures the homogeneity of both the lagging and leading window by measuring the **Variability Index** (VI), $VI = 1 + \sigma^2/\mu^2$ with σ^2 the variance of the data and μ its mean value. Based on this value this detector switches between SO-CFAR, GO-CFAR and CA-CFAR. [Smith and Varshney 1997] shows that the detector behaves well in homogeneous environment as the CA-CFAR and is robust in the case of interfering target and clutter edge scenarios.

These four algorithms also have a cost of 1 dB as far as the effective SNR is concerned [Finn and Johnson 1968; Hansen 1973; Trunk 1978; Weiss 1982; Smith and Varshney 1997]. This cost comes from the evaluation of the noise with the secondary data. The noise and clutter estimation with secondary data cost SNR as it is not perfect (the

lower the amount of secondary data is the higher the loss is). Both SO-CFAR and GO-CFAR censors half of the secondary data. Instead of censoring half of the data some detectors first rank the secondary data to selectively censor only the highest value whichever the window it is in.

For instance the **Ordered Statistics CFAR** (OS-CFAR) [Blake 1988], ranks the secondary data and then censors a given percentage of the secondary data according to their value. Authors of [Blake 1988] show that the P_D losses of CA-CFAR in a multi-target environment are as large as 40% while in the same scenario the OS-CFAR detector only loses 5% of the P_D . However if enough secondary data is contaminated the OS-CFAR presents the same drawback as CA-CFAR as far as P_D loss is concerned. The underlying principle behind these detectors using scalar data, is to censor data that are not representative of the noise or clutter of the CUT.

More advanced detector adaptive censoring exist. For instance [Farrouki and Barkat 2005] and [Jiang, Huang, and Yang 2016] censor data according to its homogeneity. [Jiang, Huang, and Yang 2016] proposes an algorithm named **First Order Differential CFAR** (FOD-CFAR) that assumes that inhomogeneous data implies sharp variation in the secondary data, and adaptively censors the secondary data. In this detector, the secondary data are ranked according to their amplitude. The derivative of the ranked secondary data according to their index is computed. This derivative should be smooth for homogeneous data, conversely it means that if it exhibits peaks the data is not homogeneous. If the gradient crosses a certain threshold, the ranked data past the index of the peak are considered outliers and are censored. This type of detector avoids the under-censoring problems that the OS-CFAR class detectors can encounter. Authors show good performances of this type of detectors in terms of P_D in case of interfering targets even when interfering targets represents more than 25% of the secondary data, however the P_{FA} conservation in clutter edge environment are slightly lower than those of CA-CFAR and OS-CFAR.

Finally, some CFAR algorithms now use machine learning. For instance the Smart-CFAR described in [Carretero, Harmanny, and Trommel 2019] matches the performances of the CA-CFAR detector in homogeneous environment and drastically improves the P_D in clutter edge scenarios.

Some targets, including drones can be endo-clutter. Endo-clutter targets are targets which are "in" the clutter, it usually means they share a position and apparent speed with the clutter, by contrast exo-clutter targets which do not share its position or apparent speed with the clutter and therefore are "out" of the clutter. This has strong implications for the detectors, which therefore needs to be specifically designed for this case. Thermal noises usually has a normal distribution that does not vary much, spatially and temporally. This is different from clutter, which varies abruptly with respect to distance, is rarely Gaussian distributed but has a heavy tail distribution. To deal with endo-clutter targets, specific detectors are designed. [Schleher 1976] discusses the problems of detection in a Weibull distributed clutter. He shows that taking the linear value of the envelope of the signal of the input gives worse results than taking the logarithmic value and shows that the best performing detector is a binary detector, which has two thresholds. A first threshold to count how many "pre-detections" the detectors get. A pre-detection follows the same framework as previously described and is hypothesis h_1 in:

$$f(X_i) \underset{h_1}{\overset{h_0}{\leq}} \eta_0 \quad (2.5.7)$$

The pre-detection tests are run over for each X_i in the dataset under test $\{X_i\}_i$, this detection tests are identical to normal standard detection tests described above. These tests are repeated on n different realizations of the same range cell at different times. We obtain m pre-detections with n tests. The detection hypothesis is met if the number of "pre-detections", m , crosses the second threshold m_0 :

$$M \underset{h_1}{\overset{h_0}{\leq}} M_0 \quad (2.5.8)$$

This shows that applying a detection test on a previously processed data can lead to better performances than strictly relying on a single detection stage.

2.5.3 . Multi-channel Detectors

Another way to make detection in clutter is to filter out clutter by using data represented by vectors. These vectors contain informations about the physical process and characteristics of the targets and clutter. They must be estimated with care, ensuring the estimation is an accurate representation of these phenomena. In [Kelly 1986], Kelly proposes a detector based on the **Matched Filter (MF)**, to make detections in unknown Gaussian clutter. The MF test is written:

$$\max_S \frac{\|S^H R^{-1} X\|^2}{S^H R^{-1} S} \underset{h_1}{\overset{h_0}{\leq}} \eta_0 \quad (2.5.9)$$

S being a steering vector (see appendix A), X the measured vector and R being the known covariance matrix of the noise or clutter while the Kelly's detector written:

$$\max_S \frac{\|S^H \overline{R}^{-1} X\|^2}{S^H \overline{R}^{-1} S} \underset{h_1}{\overset{h_0}{\leq}} \eta_0 \quad (2.5.10)$$

With \overline{R}^E the estimated covariance matrix. In the next parts covariance matrices noted R denote known covariance matrices and covariance matrices noted \overline{R} denote estimated covariance matrices. Assuming a gaussian clutter as we do in the rest of this work, we use the **Sample Covariance Matrix (SCM)** estimator to compute \overline{R}^E :

$$\overline{R}^E = \frac{1}{N} \sum_i^N (X^{E_i}) (X^{E_i})^H \quad (2.5.11)$$

X^E_i are the data vectors used for estimating clutter properties and N is the number of data vectors used in the estimation. The author shows that the proposed detector performs worse than the MF (with SNR losses of 1 to 5 dB induced by the estimation of the covariance matrix), however it does not require any priori knowledge on the clutter or noise covariance matrix. As such, it can be used to adaptively detect targets in

unknown environment. It forms the basis of endo-clutter detectors when the clutter distribution is unknown. [Conte, Lops, and Ricci 1995] proposes a detector based on a prior knowledge of the covariance matrix and models the clutter as a compound Gaussian distribution. The proposed detection scheme works similarly to a CA-CFAR algorithm, but it gathers secondary data along the time axis in CUT. It allows this detector, contrarily to CA-CFAR, to keep its CFAR property even in a compound Gaussian environment. This detector outperforms a standard MF detector in case of a steady target in a K-distributed clutter. This comparison corresponds to a case in which Kelly's approach is valid (the covariance matrix can be and was estimated accurately) as the a priori knowledge of the covariance matrix is very important for proper operation of the detectors. Moreover, the standard detector does not retain a CFAR property contrary to the proposed detector. [Jay et al. 2003] proposes a detector, named **Bayesian Optimum Radar Detector (BORD)**, which exhibits a CFAR property independently of the underlying clutter distribution. The authors also exhibit similar detection performances to optimum K-distribution detector and optimum Student-t distribution detector respectively, for K-distributed and Student-t distributed clutter, which are the optimal detectors in those cases. This is based on modelling the clutter as a spherically invariant random process to model non-Gaussian process as a complex Gaussian distribution with the variance of this distribution being a positive random variable (the so-called texture of the clutter). Further work in [Pascal et al. 2004] confirms the CFAR properties from a distribution standpoint.

In airborne and spaceborne imaging radars the radar data vector \mathbf{X} usually contains both space and long-time information. Therefore, the covariance matrix and the detector tries to filter the clutter according to its Doppler and position, for instance in **Space Time Adaptive Process (STAP)** [Ward 1995].

Another way of detecting endo-target clutter is to discriminate the target thanks to its Doppler signature, as we mentioned in a previous part the case of UAVs with micro-Doppler signature is addressed in [Hoffmann et al. 2016]. [Duk, Rosenberg, and Ng 2017] also shows that for sea clutter the wavelet transform improves endo-clutter detections of small targets. The wavelet transforms allow the separation of the signal in different frequency sub-bands, and the author notes that the target is generally in a different frequency band from the clutter signal thus allowing for higher P_D .

2.5.4 . Polarimetric Detectors

The diversity provided by the polarization gives additional opportunities for detections. [Shrader 1973] shows that even early **Air Traffic Control (ATC)** radars used polarization to facilitate detections, as they note that of circular polarization reduced the signature of weather events by up to 20 dB, while only reducing the return of the targets (airliners) by 4 dB. This form of polarimetric detection shows that even monopolarimetric radars (using only one polarization) can take advantage of the polarimetric properties of the target and/or environment. The interest of multi-polarimetric radar was stressed as early as 1986 in [Giuli 1986], in which it is stated that polarization diversity offers additional abilities to make detections by increasing discrimination capabilities between disturbances and targets. This article notes that targets tend to have reduced cross-polar responses compared to the co-polar responses. The cross-polar signal is 4 to 14 dB lower than co-polar signal for linear polarization. On the contrary, for circular polarization cross-polar returns are 0 to 6 dB higher than the co-polar returns. It also

notes that the stability of the polarimetric signature is short for lower resolution radar as it is the sum of many different backscattering returns. The article also outlines the advantages of the monopolarimetric filtering based on prior knowledge of the disturbances. Such approach works for weather disturbances but can also be used to filter chaffs (metallic objects dropped by aircraft to disturb radar) and jamming as well. The article separates detectors in two classes of polarimetric detectors. The first class includes detectors which minimize the expected disturbance returns at emissions (as in [Shrader 1973]) by not emitting the polarization that will have high parasitic returns. The second class includes the detectors minimizing the returns of disturbances at the reception with a similar framework as the one presented in Kelly's detector, by filtering the parasitic returns afterwards. [Novak, Sechtin, and Cardullo 1989] presents several detectors using polarization. Some of the detectors deal with polarimetry only by using amplitude informations whereas others build upon the principle of the Kelly's detector.

Indeed this article presents the **Maximum Likelihood (ML)** detector, which is an adaptation of Kelly's detector with a fixed steering vector, this steering vector being the polarimetric data vector :

$$\left\| \mathbf{X}^H \overline{\mathbf{R}^E}^{-1} \mathbf{X} \right\| \begin{matrix} h_0 \\ \leq \eta_0 \\ h_1 \end{matrix} \quad (2.5.12)$$

It also presents the span, which is a detector based on the total polarimetric power. If \mathbf{X} the polarimetric is written, $\mathbf{X} = (x_{Hh}, x_{Hv}, x_{Vh}, x_{Vv})$, the span detector is:

$$\frac{|x_{Hh}|^2 + |x_{Hv}|^2 + |x_{Vh}|^2 + |x_{Vv}|^2 h_0}{\text{Trace}(\overline{\mathbf{R}^E}) h_1} \leq \eta_0 \quad (2.5.13)$$

[Park, Li, and Wang 1995] proposes a detector based on the **Generalized Likelihood Ratio Test (GLRT)** and Kelly's detector to use the polarization in addition to space-time diversity, by adding the polarization information to the measured vector and the covariance matrix estimation. The detector is called **Polarization-Space-Time domain Generalized Likelihood Ratio (PST-GLR)** and the test is written:

$$\frac{\left\| \mathbf{s}_1^H \overline{\mathbf{R}^E}^{-1} \mathbf{x}_p \right\|^2 h_0}{\mathbf{s}_1^H \overline{\mathbf{R}^E}^{-1} \mathbf{s}_1 \left(1 + \mathbf{x}_p^H \overline{\mathbf{R}^E}^{-1} \mathbf{x}_p \right) h_1} \leq \eta_0 \quad (2.5.14)$$

Where $\mathbf{s}_1 = (a_h \mathbf{s}, a_v \mathbf{s})^T$ with a_h being the polarimetric amplitude and phase of the target received in polarization h and a_v being the one received in v . \mathbf{s} is the space-time signature of the target (the same that is described in [Park, Li, and Wang 1995]). And \mathbf{x}_p is the data vector tested by the detector, with:

$$\begin{cases} h_0 : \mathbf{x}_p = (\mathbf{n}_h + \mathbf{c}_h, \mathbf{n}_v + \mathbf{c}_v)^T \\ h_1 : \mathbf{x}_p = (a_h \mathbf{s} + \mathbf{n}_h + \mathbf{c}_h, a_v \mathbf{s} + \mathbf{n}_v + \mathbf{c}_v)^T \end{cases} \quad (2.5.15)$$

With \mathbf{c}_x and \mathbf{n}_x are the clutter and noise space time signature for the x polarization (h or v). $\overline{\mathbf{R}^E}$ is obtained with a training dataset $\mathbf{x}_e, \mathbf{k} = (\mathbf{n}_{h,k} + \mathbf{c}_{h,k}, \mathbf{n}_{v,k} + \mathbf{c}_{v,k})^T$:

$$\overline{\mathbf{R}}^E = \sum_k \mathbf{x}_{e,k} \mathbf{x}_{e,k}^T \quad (2.5.16)$$

This detector shows better performances by around 8 dB of SINR compared to **S**pace-**T**ime domain **G**eneralized **L**ikelihood **R**atio (ST-GLR) (which is the same as STAP).

[Pastina et al. 2000] also proposes a polarimetric GLRT-based detector, and outlines the particular interest of adding cross-polar data for polarimetric detectors as man-made targets usually exhibit higher co-polar returns than natural targets. [De Maio and Ricci 2001] proposes a Polarimetric Adaptive Match Filter that builds on [Park, Li, and Wang 1995]'s PST-GLR. The test is written:

$$\frac{\mathbf{z}^H \mathbf{R}^{E-1} \mathbf{S} (\mathbf{S}^H \mathbf{R}^{E-1} \mathbf{S})^{-1} \mathbf{S}^H \mathbf{R}^{E-1} \mathbf{z} h_0}{(1 + \mathbf{z}^H \mathbf{R}^{E-1} \mathbf{z})} \underset{h_1}{\leq} \eta_0 \quad (2.5.17)$$

Using the same formalism as for the PST-GLR description, we have $\mathbf{S} = \begin{pmatrix} \mathbf{s} & \mathbf{0} \\ \mathbf{0} & \mathbf{s} \end{pmatrix}$ and:

$$\begin{cases} h_0 : \mathbf{z} = \mathbf{n} + \mathbf{c} \\ h_1 : \mathbf{z} = \mathbf{S} \mathbf{s}_1 + \mathbf{n} + \mathbf{c} \end{cases} \quad (2.5.18)$$

Which means that \mathbf{z} has the same data as \mathbf{x}_p but has dimension $2N$ instead of $N \times 2$ as \mathbf{x}_p (with N the dimension of the space-time data). and with $\mathbf{z}_{e,k}$ data from the training dataset:

$$\overline{\mathbf{R}}^E = \sum_k \mathbf{z}_{e,k} \mathbf{z}_{e,k}^T \quad (2.5.19)$$

The authors note that this implementation suffers no performance losses for realistic case (fluctuating target) against the PST-GLR described in [Park, Li, and Wang 1995]. In addition it represents a significantly lower computational load, which makes its use favorable for polarimetric detections.

[Yamaguchi 2002] describes a detector designed for a stepped frequency W-band radar (94 GHz) under the hypothesis that the decorrelation of the polarimetric clutter is more important than the decorrelation of the target. For each frequency of the stepped radar a measurement is made. The clutter suffers a larger decorrelation with the stepped frequencies than the target. The detector gives better results than the Log and Weibull CFAR detectors. However, we note that targets in the presented experiments are a trihedron and a dihedron, which are obviously more stable targets than drones. [De Maio, Alfano, and Conte 2004] adapts the GLRT to use polarization diversity and to take into account the non-Gaussian nature of the clutter, by modelling it as a compound-Gaussian distribution. The detectors presented are tested, and the authors show that they do not exhibit a strict CFAR property, but are robust to different clutter textures. Finally, the authors note that the real clutter data can exhibit covariance matrix mismatch between the matrix estimated with the secondary data and the actual covariance matrix of the clutter, and suggest further work on theoretical performance analysis of detectors in the presence of mismatch. [Meslot et al. 2016] studies the impact of polarization for ship detection in sea clutter; it shows the importance of dual polarization radars as the ideal polarization for detection varies with wind speed and grazing angle. In particular, it shows that using Vv polarization over Hh polarization

leads to a gain of 3 dB for the detection threshold for incoherent detection (without Doppler processing). With Doppler processing the gain is even more substantial, as gains of up to 5 dB can be made by using Vv polarization. Finally, [Bailey, Marino, and Akbari 2021] compares the use of a benchmark of polarimetric detectors for the detection of icebergs in the sea ice with a spaceborne SAR, and shows the importance of the cross-polar component in the performance of the detectors.

2.5.5 . Conclusion

This part has outlined the detection framework. First, we have addressed mono-channel detectors and how they deal with multiple targets scenarios as well as clutter edge scenarios. Then we have discussed endo-clutter detections and how multi-channel data are processed to suppress clutter. We outline the importance of the prior knowledge of the clutter data or its estimation as every endo-clutter detector requires knowledge of the properties of clutter. Finally we discuss polarimetric detections. Polarimetric detectors can use an a priori filtering, by not transmitting and/or receiving polarization which results in unfavorable SNR (For instance if the target does not have high RCS in Hh polarization but the clutter does the radar can avoid transmitting the H polarization or receiving h polarization). This technique requires an prior knowledge of the polarimetric scene and target, this knowledge being used during the design of the radar system. They can also use several polarimetric channel to increase data diversity and in similar way to endo-clutter detection filter out undesired signal.

The presented detectors rely on an estimation of the clutter properties to make detections. In particular multi-channel detectors rely on the prior knowledge or estimation of the covariance matrix representing the clutter to perform well.

2.6 . Detectors tested in this thesis

This part presents the detectors we use to assess the interest of polarization for the endo-clutter detection of UAVs. We present the framework of the detections and describe detectors from the litterature as well as adaptation of existing detector to the polarimetric case and a proposed detector which constitutes original work. These detectors constitute the benchmark of detectors we test in this thesis. We introduce the span, which is a classical detector described in [Novak, Sechtin, and Cardullo 1989], the **square root Maximum Likelihood (srML)**, an ad-hoc polarimetric adaptation of Kelly's detector [Kelly 1986] and the **Polarimetric SIRV (P-SIRV)** detector adapted ad-hoc from [Jay et al. 2003]. We introduce an additional detector, **EVa**, based on the eigenvalues of the SCM estimate of the CUT. We also propose an adaptation of the CA-CFAR detector [Finn and Johnson 1968] for the monopolarimetric detectors, using the time axis for clutter estimation instead of the range axis.

2.6.1 . Framework

As mentioned in 2.5, the goal of a detector is to convert mono or multi-channel data into a scalar to be compared with a threshold to assess whether or not a target is detected. Given a measured radar dataset $\{\mathbf{X}_i\}_{i \in [1, N]}$, the detectors we present aim at detecting a target in a clutter plus noise characterized by a covariance matrix \mathbf{R}^C , the clutter plus noise data is written: $\{\mathbf{X}_i^C\}_i \sim \mathcal{CN}(\mathbf{0}, \mathbf{R}^C)$. We use a high **Clutter to Noise Ratio (CNR)** hypothesis, meaning we do not model the clutter plus noise data has the

sum of data from the noise and the clutter but only as data from the clutter. We want to detect a target with a radar data written $\{\mathbf{X}^{UAV}_i\}_i$.

The detector hypothesis h_0 , target is absent, and h_1 , target is present is written:

$$\begin{cases} h_0 : \{\mathbf{X}_i\}_i = \{\mathbf{X}^C_i\}_i \\ h_0 : \{\mathbf{X}_i\}_i = \{\mathbf{X}^C_i + \mathbf{X}^{UAV}_i\}_i \end{cases} \quad (2.6.1)$$

$\mathbf{X}_i = \{x_{Hv,i}, x_{Vv,i}, x_{Hh,i}, x_{Hv,i}\}$, where X_i is the i_{th} polarimetric data vector, in the dataset of N polarimetric data vector under test. In the following \mathbf{X}^E denotes data used for the clutter estimation in the detector tests.

2.6.2 . Classical and adapted polarimetric detectors

In this part, we present polarimetric detectors found in literature and their adaptation to the polarimetric case. We also present an eigenvalue detector and mono-polarimetric detectors. This set of detectors constitute the basis for the benchmark of the performances to be performed in the following parts.

Span with multi-look

The span detector is an incoherent polarimetric detector. The span uses the sum of the power of the polarimetric channels to make detections. With the data vector $\mathbf{X} = (x_{Hh}, x_{Hv}, x_{Vh}, x_{Vv})$, the output of the span detector is:

$$span(\mathbf{X}) = |x_{Hh}|^2 + |x_{Hv}|^2 + |x_{Vv}|^2 + |x_{Vh}|^2 \quad (2.6.2)$$

In the same manner as CA-CFAR [Finn and Johnson 1968], we use previous data to adaptively change the output using the estimated clutter properties to keep the **False Alarm Rate (FAR)** under control. Therefore, the test is written:

$$\frac{\sum_i span(\mathbf{X}_i)}{\text{Trace}(\overline{\mathbf{R}^E})} = \begin{matrix} h_0 \\ \leq \eta_0 \\ h_1 \end{matrix} \quad (2.6.3)$$

Where η_0 is the detection threshold. The detector is analog to the classical description of the span detector [Novak, Sechtin, and Cardullo 1989]. This approach includes a multi-look, it consists in summing the output of the span detector for each \mathbf{X}_i , and using that as the scalar value used for the detection. We have several motivations for the multi-look: on the one hand, detectors implementing multi-look have been shown to be suited to endo-clutter detections as mentioned in a previous part (in [Schleher 1976]), and, on the other hand, some detectors of the benchmark intrinsically implement a multi-look, thus, a fair comparison between detectors need to include multi-look for every detector.

This span detector is identical to a CA-CFAR detector with a multi-look and the estimation of clutter properties over time instead of range. Thus, it preserves the same properties as a CA-CFAR detector, it is CFAR in homogeneous environment (homogeneous along the time axis, in this case).

srML with multi-look

The srML is based on the GLRT of the polarimetric data. This detector works by whitening the signal on which the detection test is performed according to the estimated covariance matrix of the underlying clutter:

$$\sum_i \sqrt{\mathbf{X}_i^H \mathbf{R}^E \mathbf{X}_i} \underset{h_1}{\overset{h_0}{\leq}} \eta_0 \quad (2.6.4)$$

square root Maximum Likelihood (srML), is named that way because it is based on the Maximum Likelihood detector for unknown steering vectors for each look, but instead of summing the power, the square-root of the power is considered, see appendix H

Spherically Invariant Random Vector (SIRV) with multi-look

SIRV detector makes the assumption the clutter data is SIRV, which means that $\mathbf{X}_i^C = \tau \mathbf{g}$, with $\mathbf{g} \sim \mathcal{CN}(\mathbf{0}, \mathbf{R}^E)$ is a random complex Gaussian variable and τ is a texture which is statistically independent from \mathbf{g} , with a different distribution. This detector is an adaptation of the GLRT detector to give the detector a CFAR property concerning the texture of the distribution of the clutter [Jay et al. 2003]. In a compound Gaussian distribution, the texture is the distribution compounded to the Gaussian distribution. It is written:

$$\sum_i \max \frac{\mathbf{S}^H \overline{\mathbf{R}^E} \mathbf{X}_i}{\mathbf{S} \sqrt{\mathbf{S}^H \overline{\mathbf{R}^E} \mathbf{S}} \sqrt{\mathbf{X}_i^H \overline{\mathbf{R}^E} \mathbf{X}_i}} \underset{h_1}{\overset{h_0}{\leq}} \eta_0 \quad (2.6.5)$$

The term $\sqrt{\mathbf{X}_i^H \overline{\mathbf{R}^E} \mathbf{X}_i}$ normalizes the results with respect to the filtered polarimetric power. Therefore, this detector should be sensitive only to the polarimetric signature of the target compared to the clutter, and ignore the relative power of the target compared to the clutter. However, SCR still plays a role, as low SCR implies the polarimetric signature of the target represent a lower proportion of the \mathbf{X}_i vector compared to the clutter.

2.6.3 . Mono-polarimetric detector

To these classical polarimetric detectors we add a mono-polarimetric detector. This detector is based on the same principle as the CA-CFAR previously described. Instead of using data of the range axis to evaluate the clutter level, we use data from the time axis.

$$\sum_i \frac{|x_{Pol,i}|}{|x_{Pol,i}^E|} \underset{h_1}{\overset{h_0}{\leq}} \eta_0 \quad (2.6.6)$$

We recall:

$$\mathbf{X}_i = (x_{Hh,i}, x_{Hv,i}, x_{Vh,i}, x_{Vv,i}) \quad (2.6.7)$$

$$\mathbf{X}^E_i = \left(x^E_{Hh,i}, x^E_{Hv,i}, x^E_{Vh,i}, x^E_{Vv,i} \right) \quad (2.6.8)$$

We use this detector as a benchmark of performances for detection with the polarizations $Pol \in \{Hh, Hv, Vh, Vv\}$. We use this detector on each of the four polarizations when we test the detectors on real data, to assess the interest of polarimetric detector.

2.6.4 . New detector, EVa

Finally, we introduce the EVa. It makes detection based on the eigenvalues of the SCM of the cells under test and the cells used for the estimation of the clutter. With the eigendecomposition of $\bar{\mathbf{R}}$ and $\bar{\mathbf{R}}^E$, we have $(\lambda_0, \lambda_1, \lambda_2, \lambda_3)$ and $(\lambda^{E_0}, \lambda^{E_1}, \lambda^{E_2}, \lambda^{E_3})$ respectively. The eigenvalues are sorted by magnitude. EVa consists in the following test:

$$\max_j \frac{\lambda_j}{\lambda^{E_j}} \frac{h_0}{h_1} \leq \eta_0 \quad (2.6.9)$$

This detectors aims at detecting change in the dominant backscattering process. The design philosophy of this detector is the following: for a clutter with a given set of eigenvalues the inclusion of a target in the same range cell will alter the eigenvalues. A target with low SCR might not be able to alter the highest eigenvalue much but should be able to alter the other eigenvalues especially if they are a lot lower than the highest one.

Preliminary tests of the srML, EVa and monopolarimetric detector (for the Hh polarization) on real UAV and clutter data from the measurement campaign described in 4.2 are in a NATO STO journal article [Rozel, Brouard, and Oriot 2022].

To use these detectors we have to determine several parameters. First, we need to determine Doppler integration time to extract the clutter data in which we intend to detect the UAVs. We want to determine this parameter while maximizing the performances of the detectors. We then need to determine how we choose the data used in the clutter estimation. We need to determine if it is better to use data in the same range cell but at different times as estimation data, or data from adjacent range cell at the same time as the detection test. We also need to quantify the mismatch between the dataset under test and the estimation data to quantify its effect on the detector performances. In this thesis we develop methods to choose these different parameters.

Chapter 3 | Outline of the thesis

3.1 . Goals

In this thesis we intend to propose a method to choose the best detector for endo-clutter detections of UAVs as a function of the encountered clutter. We propose to optimize the detection of endo-clutter UAVs taking into consideration:

- The type of detector used
- The Doppler integration time
- The mismatch between the estimated clutter covariance matrix and the clutter covariance matrix in the CUT

3.2 . Methods

In order to achieve these goals, we study the covariance matrices of real clutters obtained with a measurement campaign of a semi-urban environment. The presentation of the experimental setup and the measurement campaign is done in section 4.1 and 4.2.

First, we make the hypothesis that a clutter with covariance matrices that have a low rank are best suited for good detector performances. We confirm this hypothesis in section 5.4.

With this criterion, we determine that the estimation of the covariance matrix of a clutter cell is more accurate using samples from the clutter cell at different times instead of using samples from adjacent clutter cells at the same time. This analysis is presented in 4.4.5.

We then study the behaviour of the measured clutter, through its covariance matrix. We show that we can minimize the rank of the covariance matrices of clutter cells by adjusting the Doppler integration time (the results are presented in 4.4.4).

Then we propose to model the temporal behavior of the covariance matrices with:

- An eigenvalue distribution (see 4.4.6).
- An angle, called the mismatch angle, that characterizes the mismatch between a pair of covariance matrices of the same cell estimated at two different times. The mismatch angles measured are then linked to the time interval between the two clutter estimations and fitted with an exponential decay law (see 4.4.7).

Using this model, we are able to represent temporal clutter behaviors and analyze the performances of different detectors (in our case the detectors presented in section

2.6) for different clutter types. This analysis confirms that covariance matrices with low rank lead to good performances for polarimetric detectors (see section 5.4). They also confirm that a low mismatch angle between the estimated clutter and the clutter of the CUT leads to good performances (see section 5.5). However, the drawback of this method is that it does not take into account the polarimetric structure of the clutter. Instead it relies on random polarimetric structures for the estimated clutter and the clutter of CUT, by forcing this random polarimetric structures to correspond with a given mismatch angle. In order to overcome this drawback we perform hybrid simulations, more representative of the real clutter data (see section 5.6). We make simulations to measure the performances of the detectors with the time interval between clutter estimation and the detector test using measured clutter signature and measured UAV signature.

This simulation procedures provide a methodology for analyzing clutter and choosing the best polarimetric detectors and the best parameters for its operation.

Part of this work has been published in:

- Rozel, Brouard, and Oriot [2022](#): Publication related to preliminary tests of the polarimetric detectors on measured clutter data .
- Rozel et al. [2022a](#): Publication on the evaluation of the influence of the mismatch angle on the performances of the detectors.
- Rozel et al. [2022b](#): Publication related to the upgrade and automatization of the radar system used in this thesis.

3.3 . Outline of the work presented

The next parts are structured as follows:

- We present the measurement campaign on which we based the work of this thesis. We present the 3 clutters we study in this thesis and that provide a case study for our methodology
- We analyze the polarimetric clutter properties
- We make synthetic simulations of clutter to evaluate the performances of detectors and the influence of the eigenvalue distributions and mismatch angles on the performances
- We make hybrid simulations using measured clutters and UAV signature to test the influence of the time interval between the estimation and detection test on the performances of the detectors.

Chapter 4 |

Experimental Study of the Polarimetric Clutter

Since an accurate estimation of the environment properties is necessary for accurate detections, this chapter addresses several essential properties of the ground clutter in a low-grazing configuration. These properties are paramount to accurately assess the performances of polarimetric detectors.

In this chapter we present a measurement campaign on a UAV and semi-urban clutter and the radar used for this measurement campaign, HYCAM.

We then study the polarimetric properties of the low-grazing clutter. We first show that Hv and Vh polarization do not necessarily correlate if the receive elements for h and v polar are not perfectly colocated. We deduce that we have information on the 4 polarization channels instead of 3 in our polarimetric data vectors, this additional degree of freedom can be used to enhance the detection step. As clutter is extracted with Doppler processing, we introduce a metric to determine the optimal integration times.

As we use the time axis to estimate clutter properties and clutter composed of changing objects (vegetation, slow moving objects, etc.), their properties change and the estimated properties need to be updated. We introduce a metric to measure how clutter changes with time, and at which rate. By measuring this metric we derive a decay time of the clutter which can serve as a guide for determining the clutter estimation update time. Furthermore, we show a distinct advantage in using the time axis for clutter estimation, as it further reduces the introduced metric and provide a better description of the clutter than using the range axis for clutter estimation.

4.1 . HYCAM

4.1.1 . HYCAM radar architecture

HYCAM is a **Software Defined Radar** (SDR); it means that analog parts are reduced to a minimum. Each element of the transmitting antenna can emit an independent arbitrary waveform within the bandwidth constraints. On the receive side, beamforming is done digitally. This approach means the radar system is highly versatile, and can be used to test many aspects of the radar processing, such as detection and the effect of Doppler processing time on detections.

Figure 4.1 presents a flow chart of the radar architecture, each part is addressed in the following section.

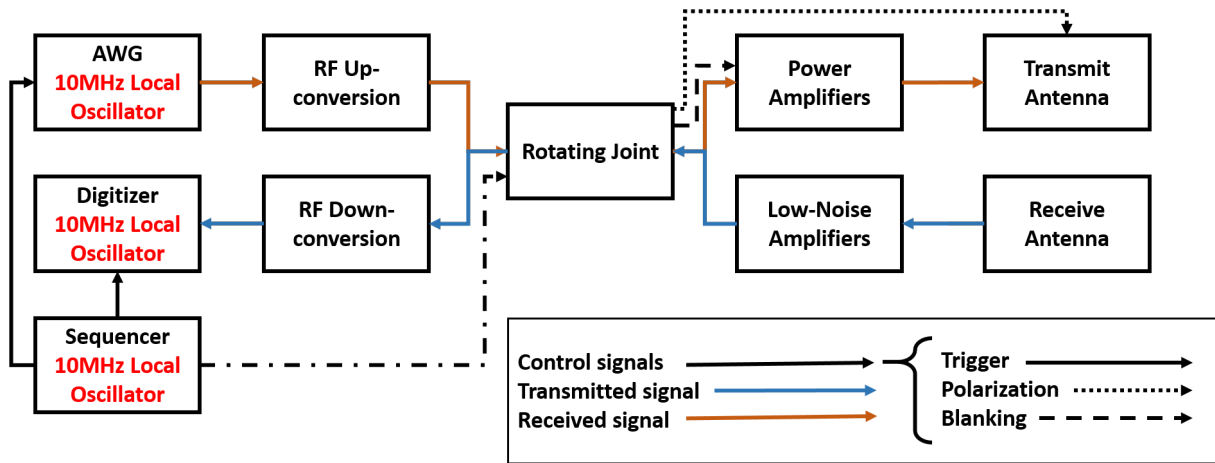


Figure 4.1: Flow chart detailing HYCAM architecture.

Antennas

HYCAM has two antennas mounted on a turret, a transmit antenna and a receive antenna (Figure 4.2). Both antennas are array antennas. The individual radiating element is a cross-shaped pair of perpendicular electrical dipoles slanted at 45° (See Figure 4.4). By shifting the phase of one of the dipole the transmitted polarization is changed (see figure 4.3).

The aperture of a single element is 120° in both azimuth and elevation. These elements are grouped in column of 32 elements. The spacing between two consecutive elements of a column is $\lambda/2$ and the spacing between two consecutive columns is $\lambda/2$, as shown in Figure 4.4.

Transmit antenna The transmit antenna is composed of 12 columns (Figure 4.5), which corresponds to a surface of 12×32 cross-shaped pair of dipoles. The smallest individually addressable unit is a column pair, each pair can transmit independently. Each pair has an aperture of 60° in azimuth and 4° in elevation. The full antenna azimuth aperture is 10° . The polarization of the transmitted can be controlled from pulse to pulse. The polarization is controlled by phase shifters. In the measurement campaign we transmitted the same waveform with all column pairs, alternating between polarization at each pulse.

Receive antenna The receive antenna has 16 independent columns, which corresponds to a surface of 16×32 cross-shaped pair of dipoles. The signal from each columns can be addressed in both polarizations in various combinations. (Figure 4.5).

Figure 4.6 shows two possible configurations for a group of 4 columns. In the single polarization configuration, each column returns the signal in one given polarization (h or v , h in the case presented Figure 4.6). Thus we have four independent signals, one for each column. In the multiple polarization configuration, for each column we receive the signal in both polarizations. Thus we have 8 different signals but only 4 output channels. Thus, we sum full column signal in pairs for each polarization. h signals from column C_0 and C_1 are summed together, and so are h signals from column C_2 and C_3 . The same is true for the v signals of these columns. The four channels contains the sum of the signals from $C_0 + C_1$ and $C_2 + C_3$ columns in both h and v polarizations.

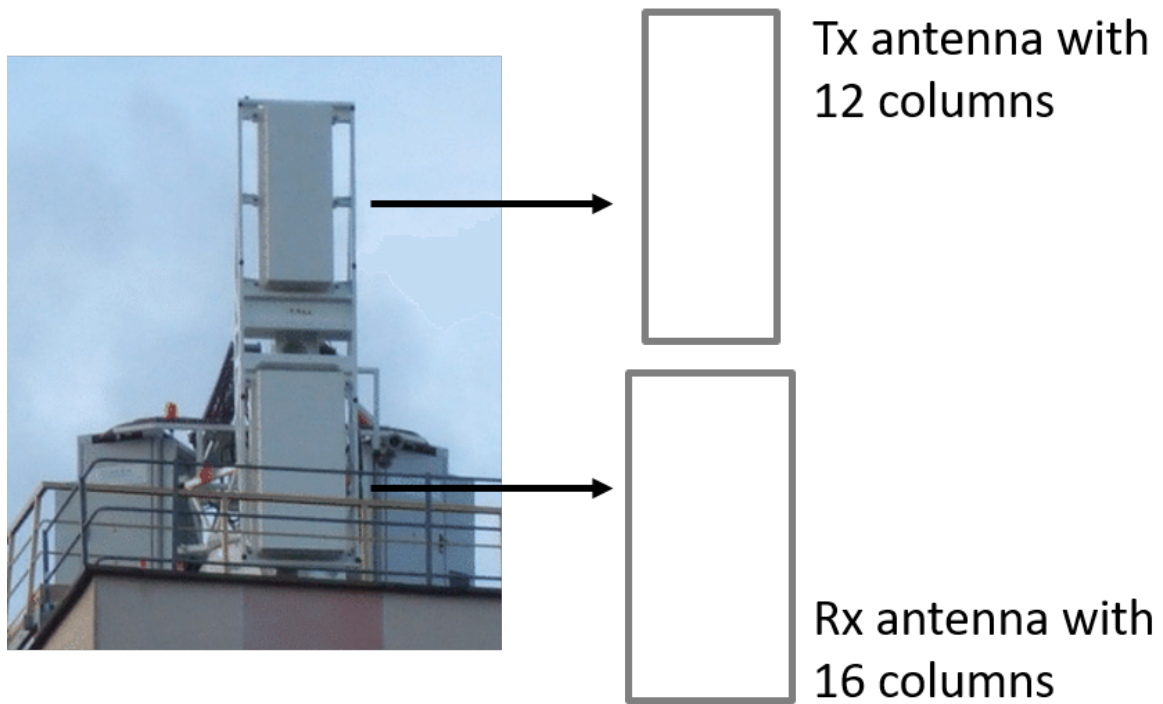


Figure 4.2: HYCAM radar and its two antennas

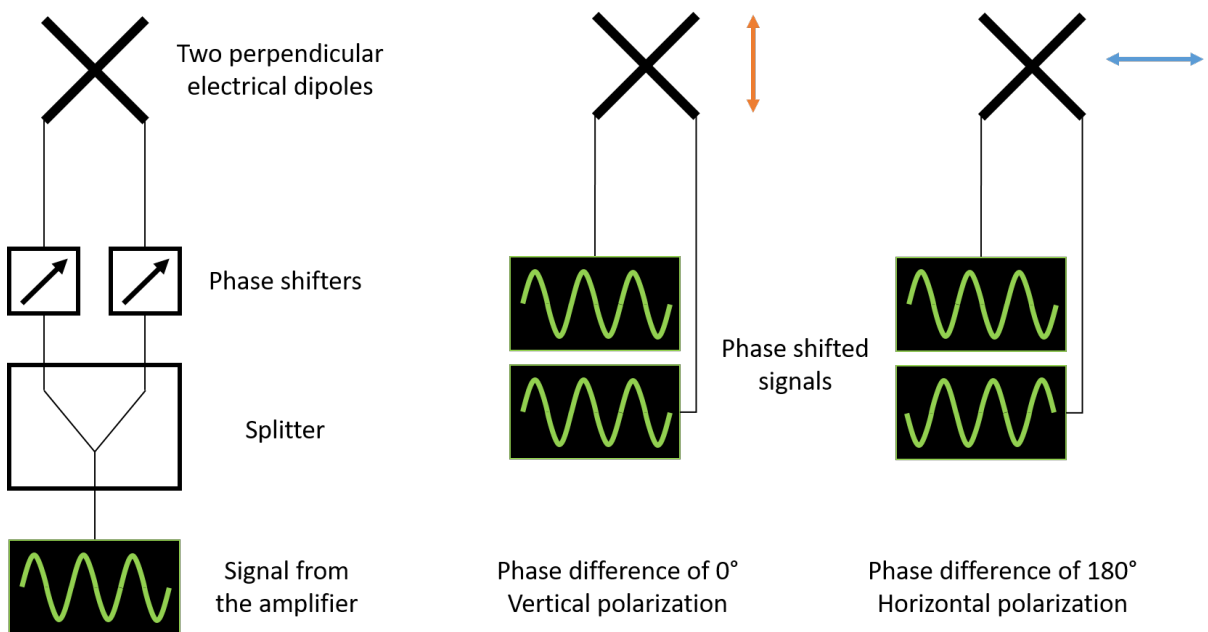


Figure 4.3: Description of an element of the transmit (Tx) antenna.

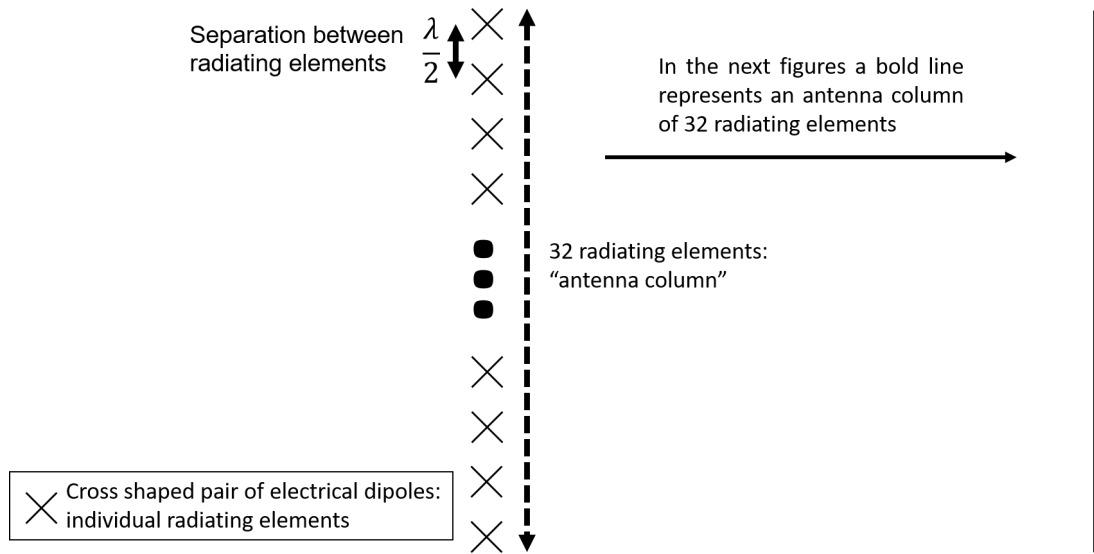


Figure 4.4: Radiating elements of the antennas and antenna columns.

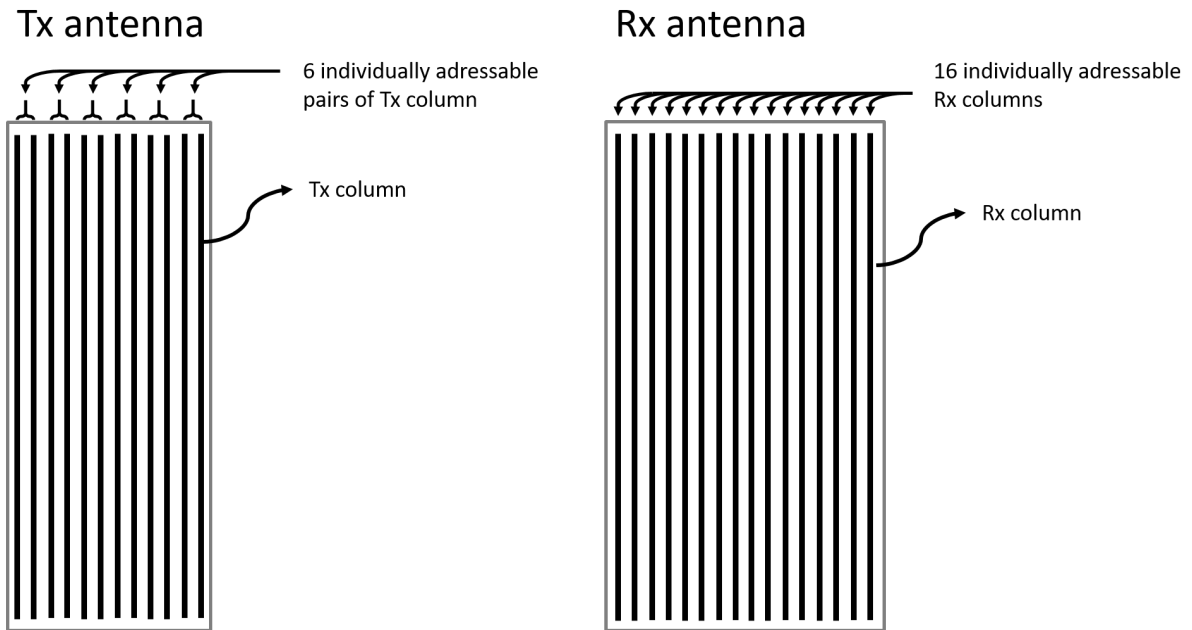


Figure 4.5: Columns of the Tx and receive (Rx) antennas

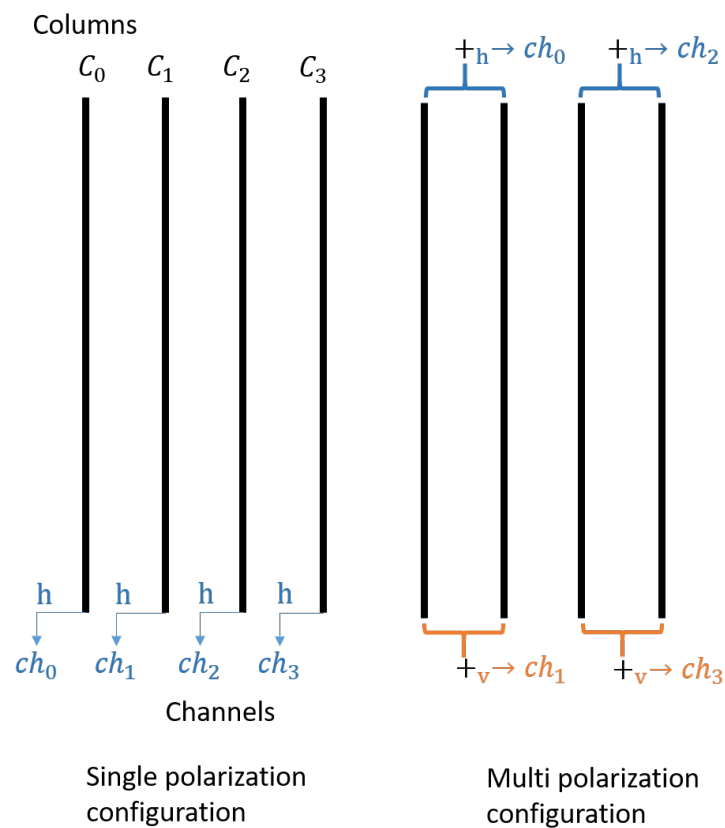


Figure 4.6: Monopolarimetric and fully polarimetric configuration of the receive antenna, we only show 4 columns for clarity. h designate the horizontal polarization and v the vertical polarization. ch_i designate the i^{th} channel.

The azimuth receive aperture for a single column is 120° and 60° for a column pair, the elevation aperture is 4° . The full antenna azimuth aperture is 8° .

In the multiple polarization configuration used in the following thesis we used the signal of 2 channels from configuration presented in figure 4.6. We used channel 0 and channel 3. This means that the antenna that receive the signal in h polarization is not colocated with the antenna receiving the v polarization. This means that there is a delay between the receive channels for off-axis targets that depends on the relative azimuth of the targets to the radar due to the 2λ distance between the receive channels.

Turret

The antennas of HYCAM are mounted on a turret with unlimited rotation in azimuth and elevation angles varying between -4° and 50° . This turret allows the radar to track targets with a given target designation. The radar is located in ONERA's Palaiseau research center on top of a 4-storey building meaning it has a panoramic view on the surrounding region, allowing for clutter measurements.

HYCAM has a rotating joint to pass the data through the turret.

Transmitted signal generation and amplification

The transmitted signal has a maximum bandwidth of 500 MHz around a central frequency of 3.15 GHz. We generate the transmitted signal with an AWG with 6 independent channels, one channel per column pair of the transmit antenna. The signal is generated in Intermediary Frequency (IF) around 1.5 GHz and transposed to the Radio Frequency (RF) around 3.15 GHz. The transmitted signal is then passed through the rotating joint of the turret to the power amplifiers. The radar has a peak output power of 700 W with a maximum duty cycle of 30%.

Digitizing the received signal

After reception, the radar signal is amplified by LNAs and then goes through the rotating joint to a RF down-converter, converting the signals center frequency from 3.15 GHz to the IF 1.5 GHz. Finally the signal is recorded on a 4-channel 12-bit digitizer able to accommodate the 500 MHz bandwidth.

Sequencer

To synchronize different parts of the radar, namely, polarization switching at transmission, power amplification blanking (to avoid transmitting noise when no signal is supposed to be transmitted), the AWG and the digitizer, HYCAM uses a sequencer. All these components use a common local oscillator to have a common reference frequency.

Control software

All of HYCAM components are controlled digitally. We created a new control software for the radar system that unifies the different components of the radar. The control software is able to control and monitor the turret. On the transmit side, the software can modify the waveforms transmitted by the AWG and the sequences used by the sequencer. On the receive side the software controls the digitizer, and its main parameters, such as sampling frequency, number of channels or acquisition time.

As the new control software controls both the transmit and receive side, it is able to prepare a measurement on all the devices and launch the measurement via the sequencer. The turret can automatically follow any target with appropriate target designation frames. This new control software coupled with the Opensky Network Application Programming Interface (API) was used to acquire automatically a large database of aircraft radar signatures as explained in a communication at the 10th Opensky symposium [Rozel et al. 2022b].

4.1.2 . Radar configuration for the measurement campaign

For the measurement campaign described in 4.2 we use a **Single-Input Multi-Output** (SIMO) waveform using the six transmit column pairs (meaning the same waveform is transmitted on all independent columns). Thus, the transmit azimuth aperture is 10° . We used a waveform with 10 MHz bandwidth, PRI of 100 μ s between the polar switching and a pulse duration τ of 10 μ s, alternating between transmitting H and V polarisation (See Figure 2.11 and Figure 4.7).

The maximum unambiguous range is then 15 km. The maximum unambiguous velocity depends on whether or not the waveform is polarimetric. In 2.1.2 we explained

that a fully polarimetric waveform (transmitting both polarizations successively) means the PRF is effectively divided by 2¹, therefore, the velocity ambiguity is also divided by 2. Thus, with a fully polarimetric waveform the velocity ambiguity is $\pm 120 \text{ m} \cdot \text{s}^{-1}$ and for the non polarimetric waveforms the velocity ambiguity is $\pm 240 \text{ m} \cdot \text{s}^{-1}$ because of the polarimetric PRF being half of the non-polarimetric PRF. The waveforms parameters are detailed in Table 4.1.

Parameter	Value
Carrier frequency	3.15 GHz
τ	10 μs
PRI	100 μs
Bandwidth	10 MHz
Sampling Frequency	25 MHz
Radar resolution	15 m
Range ambiguity	15 km
Velocity ambiguity	$\pm 120 \text{ m} \cdot \text{s}^{-1}$
Transmitted polarization	H, V
Coupling range	1500 m

Table 4.1: Parameters used in the measurement campaign.

As explained in 4.1.1, we used one pair of columns of the receive antenna for each polarization (using ch_0 and ch_3 in the configuration outlined in Figure 4.6): one in h polarization and the other in v polarization. These two receiving pairs are separated by two wavelengths, i.e., about 20 cm. As a result, Hv and Vh signals backscattered by a target off boresight of the radar will have different phases.

For each measurement, we made a calibration measurement using a transponder as described in 4.1.3.

With 10 MHz of bandwidth and with 10° transmit beam azimuth aperture, the range cell measures 15 meters and is $r \frac{10}{180} \pi \sim \frac{r}{7}$ wide, with r the range. For instance, at 3.5 km range, the range cell has a surface of roughly $9,000 \text{ m}^2$. This large surface area implies that a large number of backscatterers are present in one single clutter range cell. Thus, there is a high variability of the polarimetric signature from cell to cell.

4.1.3 . Polarimetric radar characterization and calibration

Characterization and calibration of the radar is essential. We need to ensure that the phase and amplitude between the different polarimetric channels is stable with time as the analyses we make in the next parts are based on the stability of the clutter signature. Furthermore, we want to ensure that the transfer function of the system does not depend on frequency, which means that the received signal is not distorted by the RF components. The knowledge of the transfer function also means we are able to compensate radar response in the received signal. We detail in this part the calibration and characterization procedure as well as the obtained results.

¹It is also possible to use orthogonal waveforms to emit both polarizations at the same time [Titin-Schnaider and Attia 2003], thus not altering the PRF

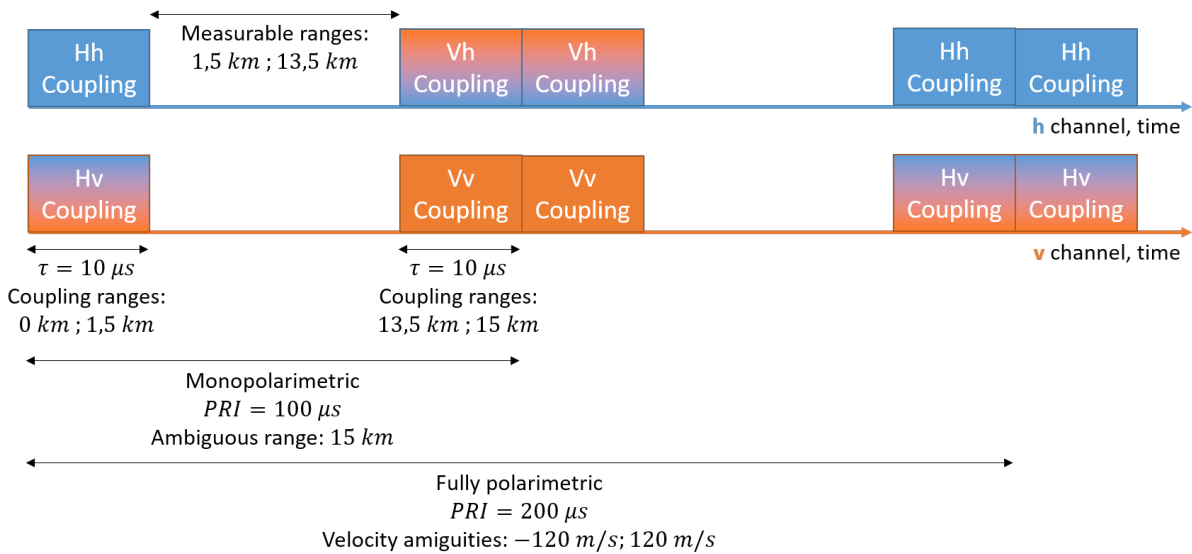


Figure 4.7: Description of the time sequences of data transmitted and received by the radar.

Using a transponder to characterize the radar

To characterize and calibrate HYCAM ONERA uses a transponder system. The transponder is equipped with two horn antennas. The transponder receives the radar signal through the receive horn antenna, then it amplifies the signal. Next the signal is fed in an optical fiber of 10 km to shift the position of the radar return (changing its relative position). This is important since the transponder is approximately 250 meters away from the radar, in the coupling domain which would degrade the measurement. At 10 km the clutter returns are far lower so it helps avoid disturbances in the measurement of the transfer function. In addition, the transponder also applies a phase ramp from pulse to pulse if the signal is strong enough. It simulates a moving target and reemits the signal toward the radar with the Tx horn antenna. The flowchart of the transponder is described in Figure 4.8.

It means the “target” is exo-clutter meaning the measurement of the returned power is not polluted by the clutter signal as shown in Figure 4.9.

The two horn antennas can be rotated to receive and transmit in a specific linear polarization. In our case we use the two horn antennas in a configuration in which they are rotated by 45° . According to the malus law [Collett 2005], the receive horn antenna receives in either H or V polarization with a reduced amplitude of -3 dB. Different configurations of the horn antennas are outlined in Figure 4.10, in particular the configurations with both antennas at 45° . This method allows for an accurate determination of the transfer function, moreover, it allows for the measurement of the relative amplitude and phase of the different polarimetric channels.

Measuring the transfer function. To compute the transfer function, we take a large number of consecutive waveforms received from the transponder. To increase the SNR on the measured radar data we want to sum these consecutive data. Integrating 1000 consecutive pulses gives a SNR of 80 dB of SNR. We align their phases before summing them. We use this method to avoid facing the off-grid problem when trying to

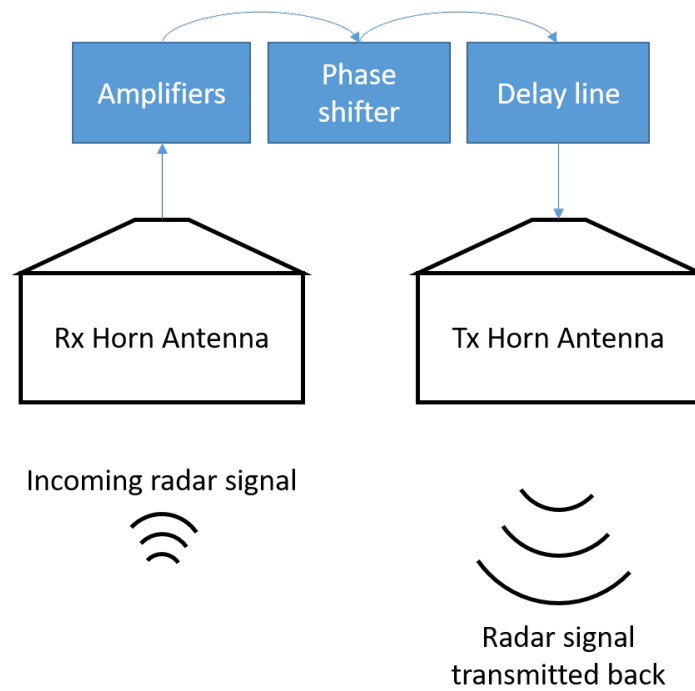
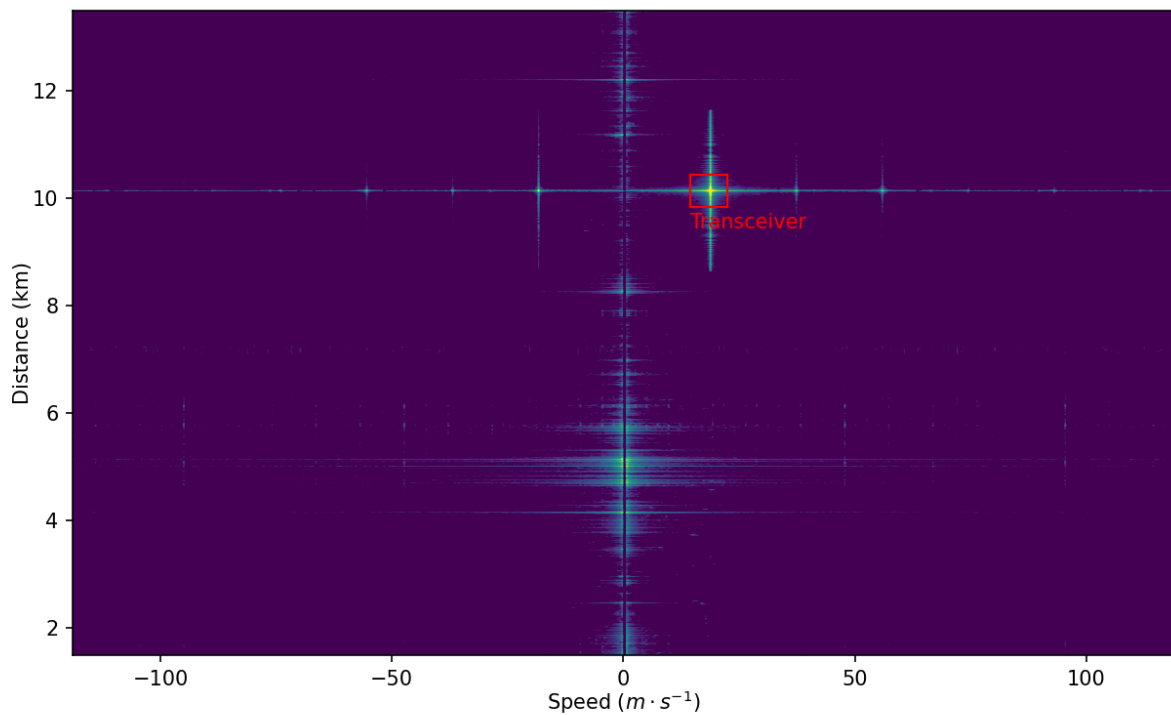


Figure 4.8: Transponder flow chart.

Figure 4.9: Doppler-range map with the transponder returns. Note the shift of $20 m \cdot s^{-1}$ on the Doppler-range map due to the phase shift (the Doppler artefacts on the transponder signals are due to a small default of the transponder).

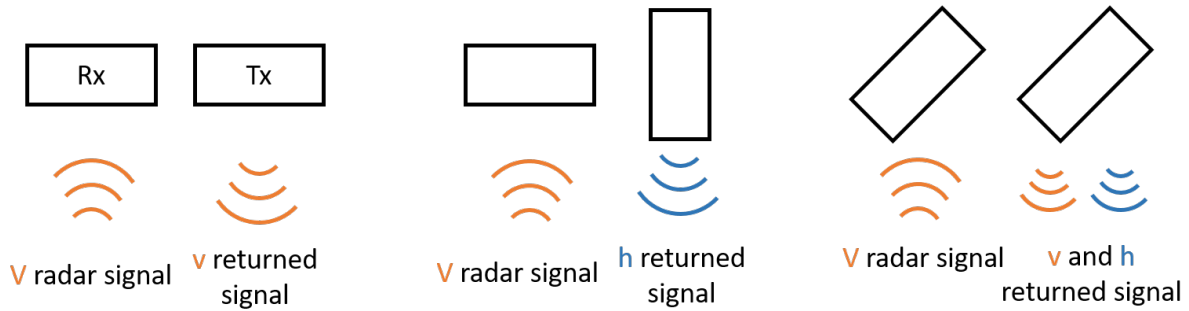


Figure 4.10: Several antenna configurations of the transponder.

measure the transponder response on the Doppler-range map. As we transmit chirps, we can use the fact that the phase of a chirp is a parabola. Thus, for each waveform a polynomial fit is performed to get the phase and correct it. Once the phases of the chirps are realigned, we take the mean of the measured chirps to estimate the “real” chirp. We use a Fourier transform on this chirp to get the received signal spectrum. By comparing the received signal spectrum to the spectrum of a perfect chirp we obtain the transfer function of the radar system.

Measuring the amplitude and phase stability between the polarimetric channels.

When the radar returns from the transponder are isolated we can measure the relative amplitude and phase between the channels. The transponder has, as any target, a backscattering matrix, \mathbf{S} , depending on the horn antenna configuration. For the configuration in which both horn antennas are oriented at 45° the backscattering matrix is [Sarabandi, Oh, and Ulaby 1992]:

$$\mathbf{S} = \begin{pmatrix} 1 & -1 \\ -1 & 1 \end{pmatrix} \quad (4.1.1)$$

It means that there will be a phase between the polarimetric channels due to the transponder, but this phase is independent with time. It allows us to check for the stability of the phase difference between the channels as well as to determine the systematic phase difference and the amplitude ratios between the channels.

HYCAM Calibration

We outlined a method for the calibration of polarimetric radars, we now apply this method to the HYCAM radar, we first measure the transfer function. We notice the theoretical and received chirps are different in Figure 4.11. This is to be expected, since the radar radio frequency chain is not perfect. The auto-correlation of the pulse compression gives the highest output possible (and thus the highest SNR), when the waveform used to compute the correlation is identical with the one emitted by the radar.

We see that the chirp power slightly varies across the band of interest for our measurement (less than 2dB over the 10 MHz under consideration). Which is confirmed by the transfer function (The ratio of the measured chirp spectrum and the theoretical chirp spectrum) shown in Figure 4.12, we notice that the amplitude variation in the bandwidth is less than 2 dB.

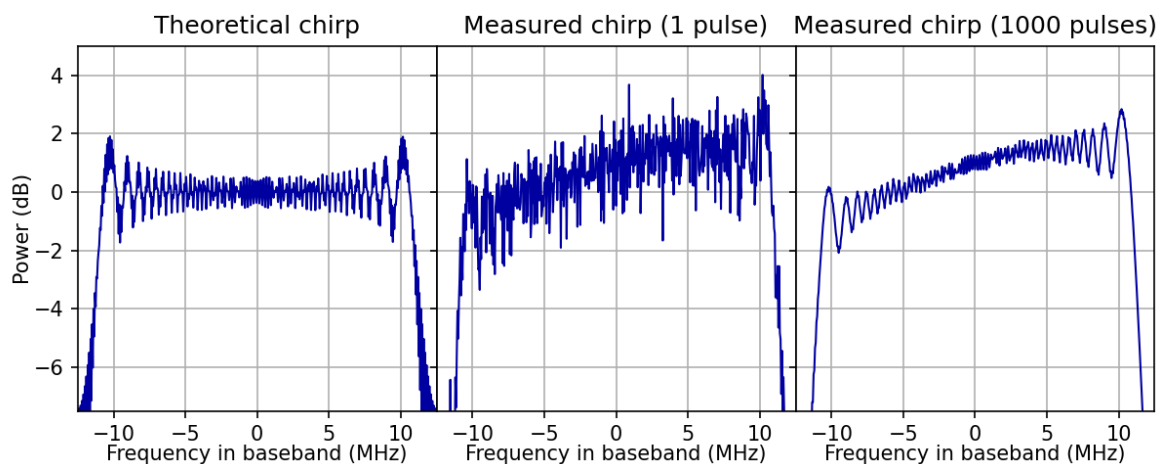


Figure 4.11: Comparison of the theoretical chirp (left), the chirp measured with 1 pulse (middle), and the chirp measured with a 1000 pulses (right) (Hh polarization). The chirp parameters are the following: 23 MHz bandwidth and a τ of 10 μs .

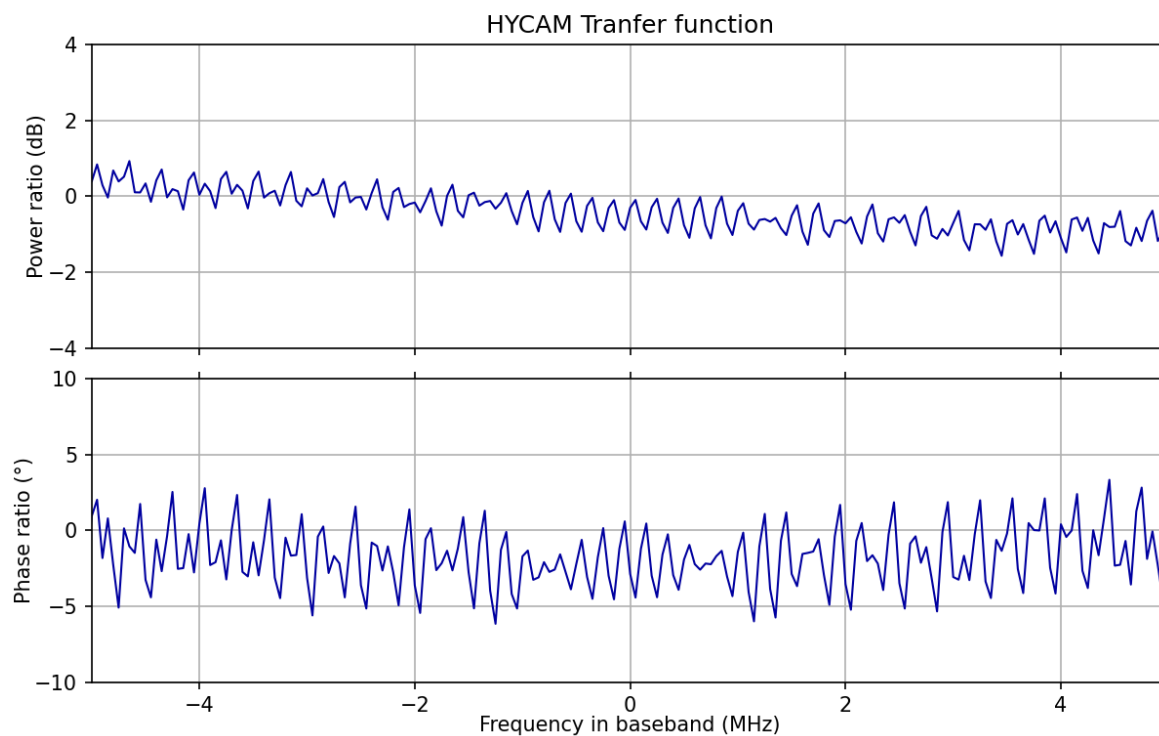


Figure 4.12: Transfer function of the HYCAM radar for the 10 MHz of the chirp used in this thesis.

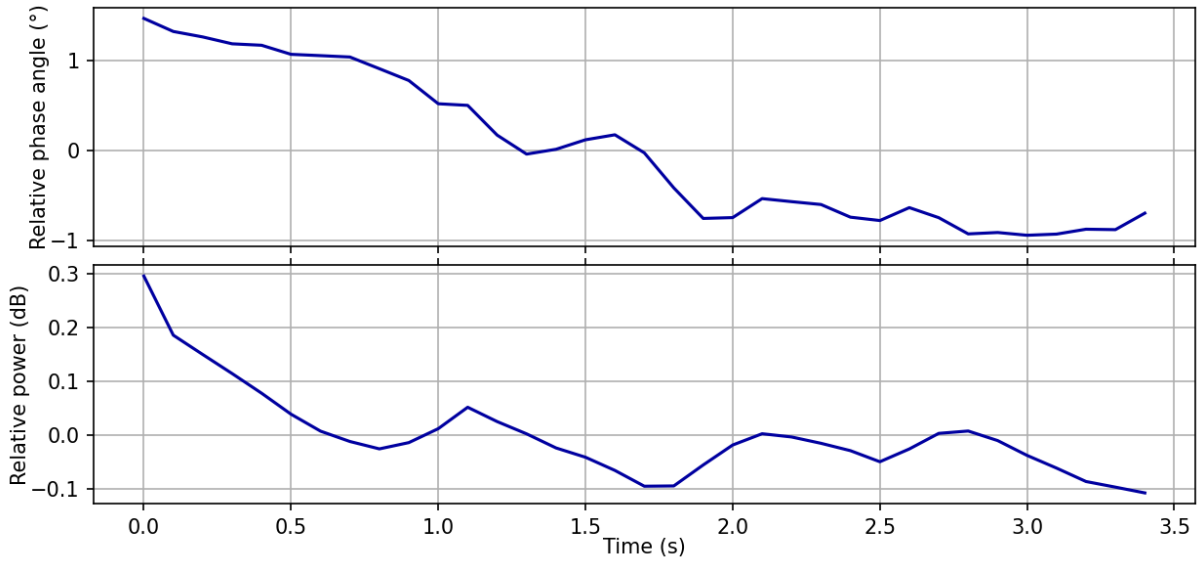


Figure 4.13: Relative phase and power between the Hh and Vv channels.

With the transponder with both horn antennas at 45° we measure the relative phase and amplitude between the co-polar channels Hh and Vv (see Figure 4.13). As the rest of our work takes interest only on the relative stability of polarimetric backscattering processes of the clutter, via the covariance matrices analysis on the time axis, it only necessitate that the amplitude and phase of the radar are stable during time.

It does not require for the ratio of the amplitudes to be equal to 1 or for the phase difference to be 0° .

As further analysis, we compute the polarimetric SCM of the data from the transponder (Figure ??) as follows:

$$\overline{\mathbf{R}_{trans}} = \frac{1}{N_t} \sum_t \mathbf{X}_t \mathbf{X}_t^H \quad (4.1.2)$$

with \mathbf{X}_t the polarimetric vector received from the transponder at a given time. This covariance let us estimate the phase and amplitude noise of the radar system. The normalized eigenvalues of this covariance matrix are $\{0 \text{ dB}, -41.4 \text{ dB}, -45.9 \text{ dB}, -76.5 \text{ dB}\}$. We are measuring one polarimetric state with the system (as all the polarimetric channels should be perfectly correlated), as such perfect system would have a rank 1 covariance matrix. In our case the interval between the first and second eigenvalue is -41.4 dB , which gives the sensitivity of the system for polarimetric measurements.

Conclusion

We provided a description of the radar system used in this thesis and a method to calibrate it. We have explained why the characteristics of the HYCAM radar are suitable for the polarimetric analysis we conduct in the next parts. Namely, the radar has both stable phase and power ratios between the different polarimetric channels, and we are able to measure data with a dynamic range of more than 40 dB between the dominant polarimetric backscattering process and the less intense polarimetric backscattering process.



Figure 4.14: Picture of the UAV used in the measurement campaign. The crown carbon fiber crown was not fitted on the UAV during the campaign.

4.2 . Measurement campaign

The measurement campaign was carried out with the Hycam radar and a UAV (Figure 4.14) with pre-defined flight patterns (Figure 4.16):

1. Two consecutive circles of 150 m of diameter with the UAV flying at $5 \text{ m} \cdot \text{s}^{-1}$
2. A 300 m length and 100 width hippodrome with its main axis pointing toward the radar with the UAV flying at $10 \text{ m} \cdot \text{s}^{-1}$
3. An hippodrome of length 250 m and width 50 m with its long axis pointing perpendicular to the aiming line of the radar with the UAV flying at $10 \text{ m} \cdot \text{s}^{-1}$
4. The drone hovering for 90 s

We chose these patterns to have a large variety of UAV positions in the range-Doppler space. The circles give us constant variation of both Doppler and range of the target. The hippodrome perpendicular to the line of sight of the radar represents a part of the trajectory in which the UAV has a very weak Doppler signature but is nonetheless flying at important speed. conversely, the hippodrome aligned with the line of sight of the radar gives the UAV a stable attitude (to hover UAVs make a lot of adjustments and thus change their attitude) and a large Doppler shift. The hovering phase gives us long phases of endo-clutter UAV signal. Figure 4.15 shows an example of flight log information projected on Google Earth's. We distinguish the two hippodrome trajectories and the circle. The blue line is the line of sight. The radar antenna aimed at the trajectory of the UAV.

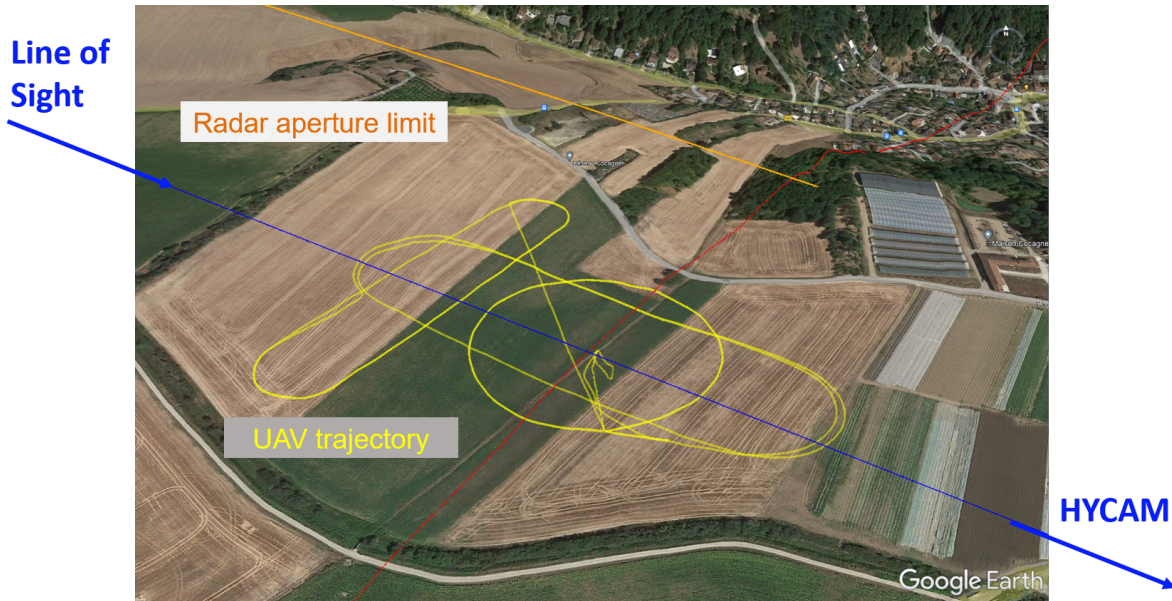


Figure 4.15: Projection of the trajectory of UAV on the map. Source : Google Earth

Figure 4.16 shows the surroundings, which is a typical semi-urban clutter. It features sparsely and densely forested areas and large fields. It also features roads, both oriented along the radar **Line of Sight** (LoS), with a Doppler signature for the cars, and perpendicular to the radar LoS meaning that the cars have Doppler signature similar to the clutter. Finally, the clutter also contains buildings either isolated or grouped in small towns.

4.3 . Study of the low-grazing polarimetric clutter

The data of this measurement campaign allows us to determine key quantities for the polarimetric signature of the clutter. We determine that in spite of reciprocity principle Hv and Vh returns are not fully correlated in most clutter cells, which is partially due to the use of 2 different elements to record Hv and Vh data, as we show with a simple model. We also establish an optimal Doppler processing time that minimize the degrees of freedom of our clutter. In addition, we carry out a space-time analysis of the clutter variations , with respect to received power and polarimetric signature. We also determine the existence of a decay time for the polarimetric signature of the low-grazing ground clutter.

4.3.1 . Non-correlation of the cross-polarization channels in the presented configuration

For any measurement with a colocated radar we expect correlated returns for Hv and Vh polarization because of the reciprocity principle. We show this is not the case in our experiment due to the geometry of the antenna and in our experiment.

Measure of the correlation of the cross-polarization channels

Given the reciprocity principle, $S_{Hv} = S_{Vh}$, the cross-polarization terms of the backscattering matrix are equal, we expect $X_{Hv} = X_{Vh}$, the cross-polarization returns from a

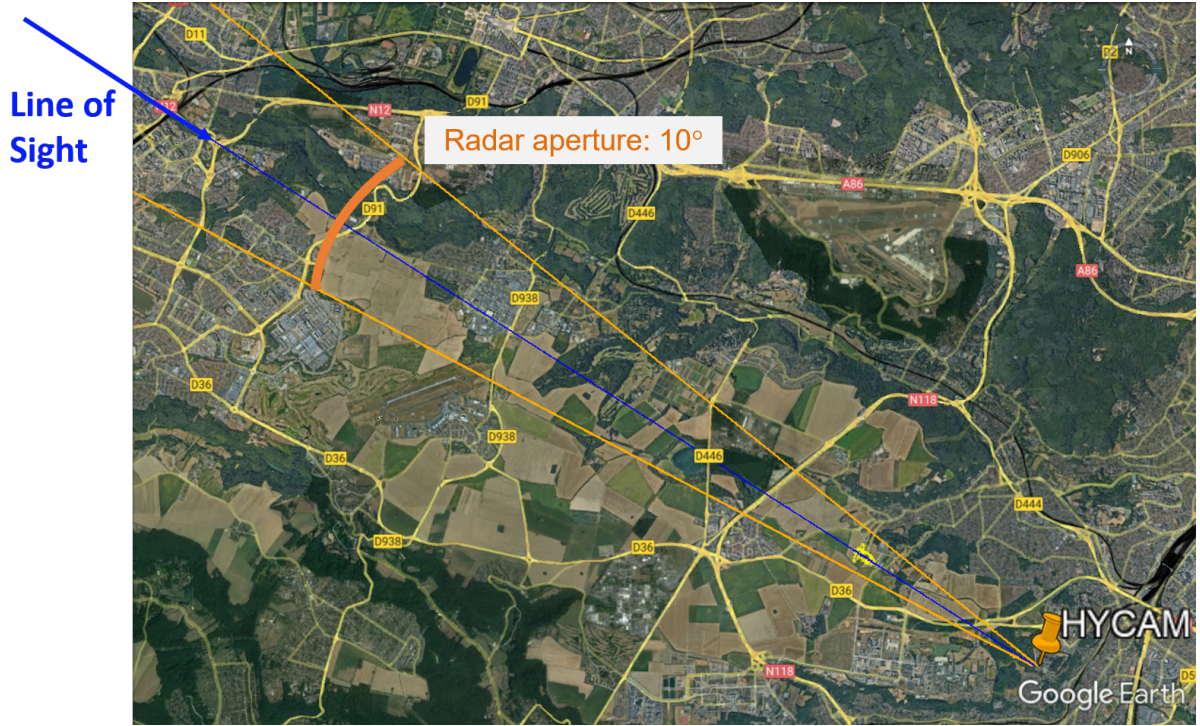


Figure 4.16: Map of the zone measured by the radar during the experiments, the orange lines represents the limit of the aperture of the radar and the blue line is the radar LoS.

given target are equal [Boerner et al. 1981]. However, we observe that for the clutter cells in our measurement campaign this relation is not verified (Figure 4.17). By defining the correlation rate for the clutter cell as:

$$\rho_{X_{Hv}X_{Vh}} = \frac{\sigma_{X_{Hv}X_{Vh}}}{\sqrt{\sigma_{X_{Hv}}^2 \sigma_{X_{Vh}}^2}} \quad (4.3.1)$$

With σ_{XY} and σ_X^2 respectively the estimated covariance between X and Y and estimated variance of X defined as follows:

$$\sigma_{XY} = \frac{1}{N} \sum_{i=1}^N (X_i - \bar{X})(Y_i - \bar{Y})^* \quad (4.3.2)$$

$$\sigma_X^2 = \sigma_{XX} \quad (4.3.3)$$

Where z^* is the conjugate of z . We compute the correlation along the time axis. The maximum expected correlation rate that we expect can be expressed as a function of the **Clutter to Noise Ratio** (CNR) on the X_{Hv} and X_{Vh} channels (see appendix C for demonstration).

$$\rho_{max} = \frac{\sqrt{CNR_{Hv} \times CNR_{Vh}}}{\sqrt{1 + CNR_{Hv}} \times \sqrt{1 + CNR_{Vh}}} \quad (4.3.4)$$

We estimate the CNR by making 128 consecutive Doppler-range maps with a 0.4 s integration time (Figure 4.18).

In Figure 4.18 cells with a speed of $0 \text{ m} \cdot \text{s}^{-1}$ represent the clutter and the cells with an arbitrary non zero speed (large enough to not be contaminated by the clutter) represent

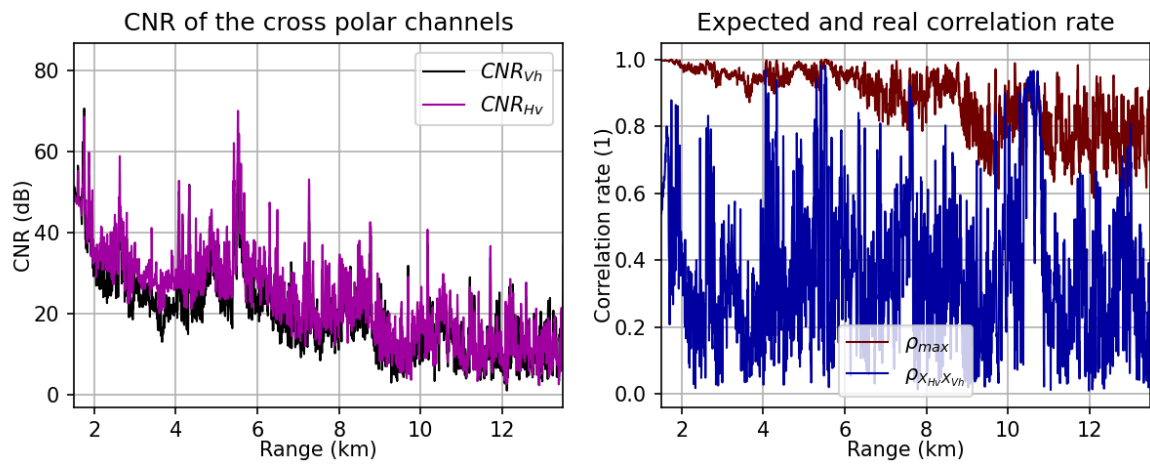


Figure 4.17: CNR (left) and expected (right, ρ_{max}) and measured correlation (right, $\rho_{X_{Hv}X_{Vh}}$) rate between Vh and Hv channels.

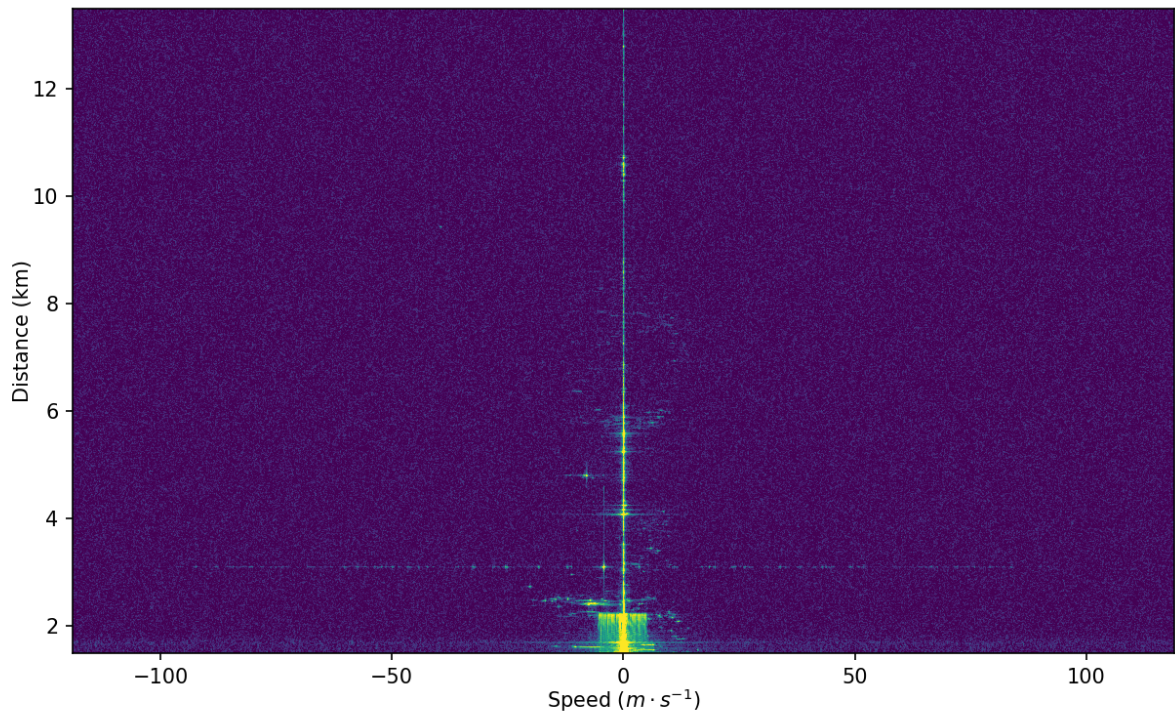


Figure 4.18: Doppler-range map. The clutter appears at $0 m \cdot s^{-1}$.

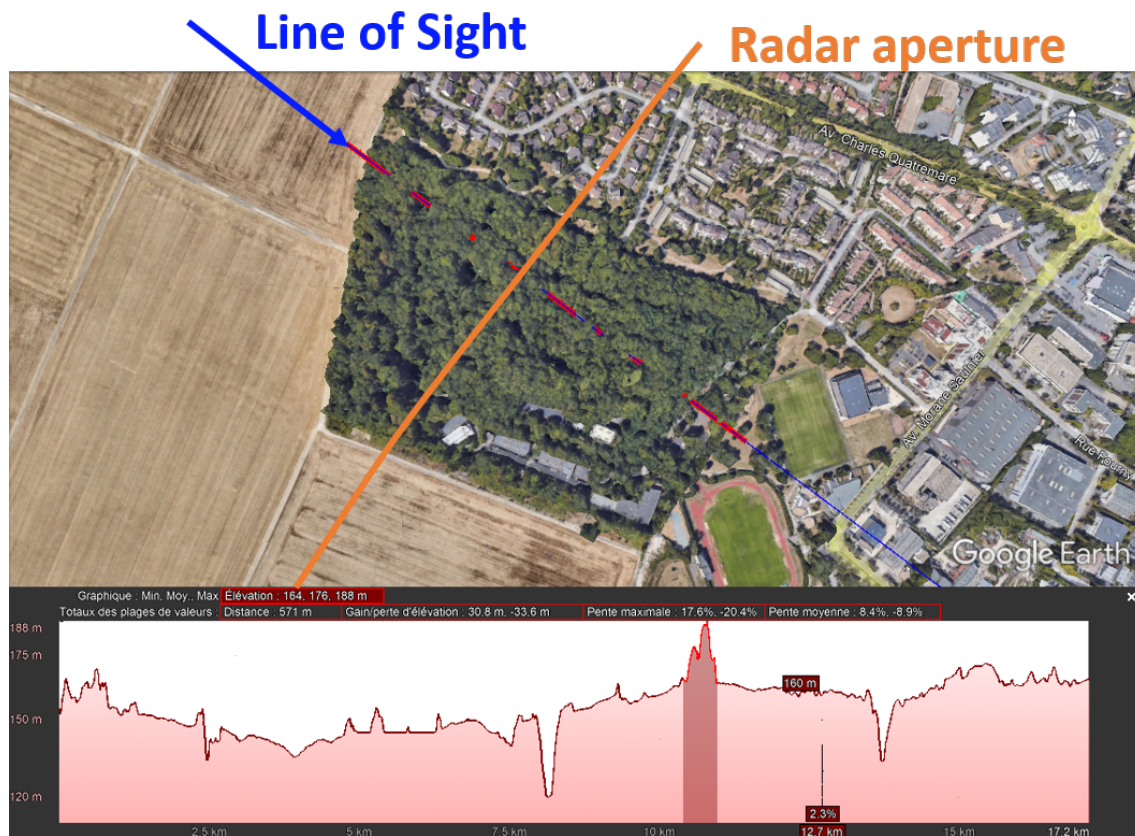


Figure 4.19: Height level along the radar LoS, and satellite image of the fort of Buc, outlined on the altitude profile. This range corresponds to a reciprocal clutter (correlation between H_v and V_h).

the noise (since there are no targets). We take the incoherent mean of the cells over time to get the noise and clutter power at each range. (Figure 4.17)

In Figure 4.17 we observe ρ_{max} and $\rho_{X_{H_v}X_{V_h}}$ as functions of range. We observe that the correlation rate is lower than the expected value except for rare range cells. This correlation should be ρ_{max} since $S_{H_v} = S_{V_h}$ except for noise. Amongst the exceptions, we notice a strong correlation between 10.5 km and 11 km.

Figure 4.19 shows that it corresponds to a small military fort. This fort is partially buried; however, it culminates 20 m higher than its surroundings with its trees. These trees are very densely packed. Furthermore, it is located in the center of the aperture, which mean that the amplitude received from this backscatterer is very similar for both antennas and the relative phase is close to 0° .

Modeling and simulation

To analyse this deviation from the expected values a simple clutter model was created. We run simulations to determine the radar returns of a unique range cell. In the said range cell at $r=10$ km we have N backscatterers spread over the aperture with $S = S_{H_v} = S_{V_h}$, the backscattering is given by:

$$S \sim \mathcal{CN}(0, 1) \quad (4.3.5)$$

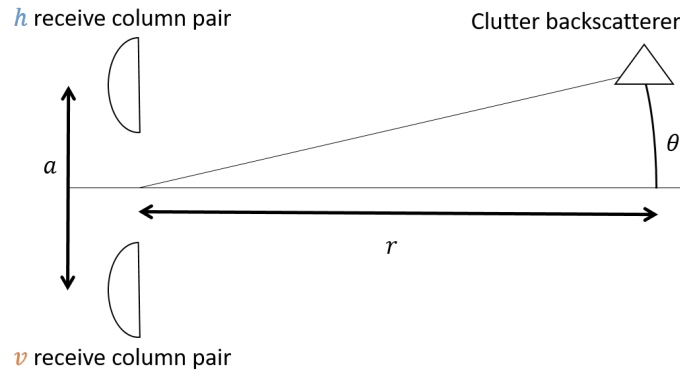


Figure 4.20: Drawing of the configuration of one clutter backscatterer.

$\mathcal{CN}(0, 1)$ is the complex normal distribution of mean 0 and variance 1. Each backscatterer is located at an angle θ away from the radar LoS, with:

$$\theta \sim \mathcal{U}(-\pi, \pi) \quad (4.3.6)$$

$\mathcal{U}(-\pi, \pi)$ is the uniform distribution between $-\pi$ and π .

We model the separation between the Hv and Vh phase centers (Figure 4.20) by applying a phase, $\phi(\theta)$, to the received power of the backscatterer and we apply a factor to take into account the radar transmit and receive apertures, $A_{Hv}(\theta)$ and $A_{Vh}(\theta)$ denoting respectively the v and h receiving element, A_{Xy} the product of the transmit aperture in X polarization and receiving aperture in y polarization. We then have following couple:

$$\begin{cases} X_{Hv} = S \times A_{Hv}(\theta) \times e^{i\phi(\theta)} + n_v \\ X_{Vh} = S \times A_{Vh}(\theta) \times e^{i\phi(-\theta)} + n_h \end{cases} \quad (4.3.7)$$

with n_x the noise that corresponds to the x polarization receive channel. The signal phase is then defined as:

$$\phi(\theta) = 2\pi \frac{-r + \sqrt{r^2 + \frac{a^2}{4} - ar \sin\theta}}{\lambda} \quad (4.3.8)$$

With $\lambda = 1 \cdot 10^{-1}$ m the wavelength of the carrier wave. To obtain $A_{Hv}(\theta)$ and $A_{Vh}(\theta)$, we measured the receiving aperture of HYCAM leading to the measurement presented in appendix B. By generating N sets (corresponding to N clutter cells) of M backscatterers we can estimate the signature of the N cells by the two antennas by coherently adding the backscatterer returns. We have:

$$\begin{cases} X_{Hv} = \sum_{i=1}^M S_i \times A_{Hv}(\theta_i) \times e^{i\phi(\theta_i)} + n_v \\ X_{Vh} = \sum_{i=1}^M S_i \times A_{Vh}(\theta_i) \times e^{i\phi(-\theta_i)} + n_h \end{cases} \quad (4.3.9)$$

We make an ergodic hypothesis, instead of measuring the correlation rate between the N iterations of the same clutter we measure the correlation rate between N sets of clutter cells measured in v and h polarizations.

Figure 4.21(a) shows the results of a 64 simulations with $M = 2048$ backscatterers, $N = 128$ clutter cells, $r = 10$ km, a separation between the pairs of column $a = 2\lambda = 20$ cm with varying CNR between -5 dB and 25 dB. The blue line is the average correlation

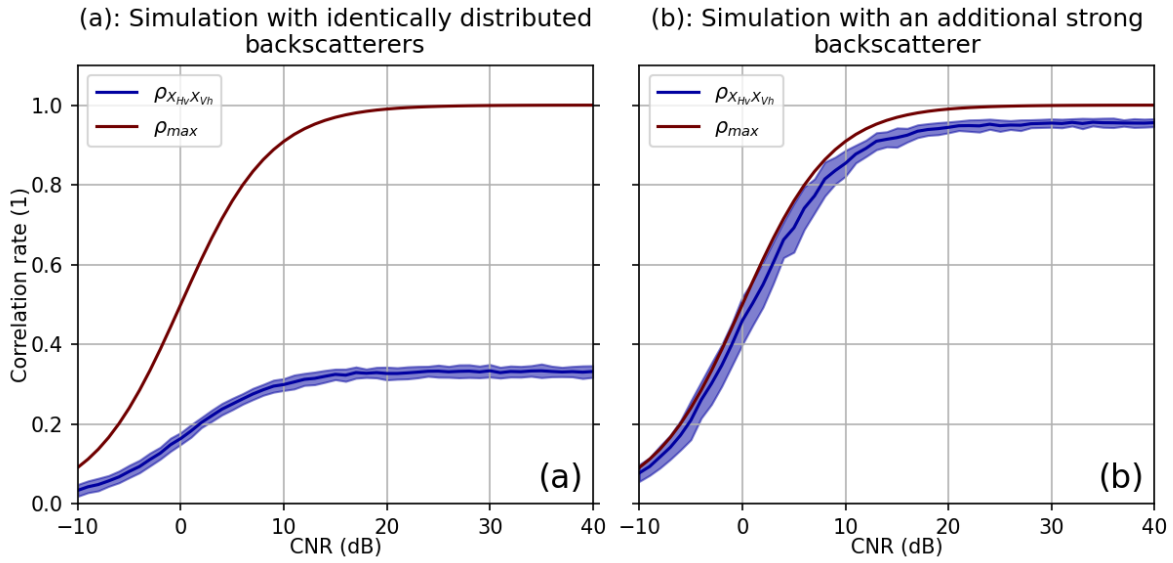


Figure 4.21: Theoretical correlation with the reciprocity principle and simulated correlation with the receiving pairs of columns separated by $2\lambda = 20$ cm with identically distributed backscatterers (a), and an additional strong backscatterer (10 dB above the other backscatterer) (b)

obtained with the simulations for each CNR and the outline is the standard deviation. The dark red line is the expected result for colocated antennas.

These results demonstrates that even though the reciprocity principle applies, the measured signature of the clutter for the Hv and Vh polarization do not necessarily correlate.

If we generate a stronger backscatterer in the center of the aperture (corresponding to the military fort at 10.5 km in our measurement), the correlation rate should go back up and be close to the theoretical maximum if the proposed model is valid considering the results observed on the real data (Figure 4.17). The Figure 4.21(b) shows the results of simulations with the same parameters as for Figure 4.21(a), with an additional backscatterer in the center of the aperture with a greater magnitude, $S = 10$ dBsm. These results confirms that with a strong backscatterer in the center of the aperture the correlation is close to the theoretical maximum.

Thus a semi-urban clutter with no dominant backscatterer can have different signatures for the Hv and Vh polarization. Hence, we consider the two cross polarization channels should bring an additional degree of freedom, which, when taken into account in the detection processing could result in better detection performances.

According to these results the measured polarimetric we consider in the following work is:

$$\mathbf{X} = \{X_{Vh}, X_{Vv}, X_{Hh}, X_{Hv}\} \quad (4.3.10)$$

4.4 . Polarimetric Clutter Properties

In order to improve performances of endo-clutter polarimetric detectors, we need to study polarimetric clutter properties. Since detectors require an estimation of clutter properties, we need to determine how to estimate polarimetric covariance matrix of

the clutter. The estimation should be as close as possible to the clutter in the CUT, as we suppose that cells closer to the CUT should be similar to the CUT, leading to better estimation of the clutter in the detection test, thus better performances. To make the estimation of the covariance matrix of a cell we need a dataset with N measurements of the cell at different times or N measurements of similar cells (surrounding the CUT). We need to choose how this estimation is done to better represent the clutter. If the clutter is perfectly stable with time the covariance matrix estimated along the time axis will be of rank 1 (if the covariance matrix is estimated on the range axis and the covariance matrix is stable with range it should also be of rank 1). Simulations conducted in 5.4 show that rank 1 matrices lead to better performances for polarimetric detectors.

Therefore, we try to minimize the rank of the covariance matrices. Thus, we choose the axis for the covariance matrix estimation that minimizes the rank of the covariance matrices obtained.

Then, we detail the properties of the polarimetric clutter using the covariance matrix formalism. We estimate the covariance matrices with SCM estimator and determine the Doppler processing time that also minimizes the rank of the covariance matrix.

We also define a decay time for the polarimetric signature of the clutter and postulate that we can partially decouple the polarimetric signature from the power of the clutter.

These tests serve the simulation establishing the performances of polarimetric detectors for endo-clutter UAVs we present in the final part.

4.4.1. Presentation of the studied clutter range cells

In this thesis, we illustrate our work on three different clutter range cells. These ranges are representative of different clutters we find in a semi-urban environment.

Farmland Clutter

The first clutter we study is farmland clutter located 3.54 km away from the radar. This clutter is composed almost exclusively of unharvested farmland (Figure 4.22). The CNR of this range cell is 14.5 dB for a 10 ms integration time.

Farmland and Road Clutter

The farmland and road clutter is characterized by a nearly tangential road to the radar meaning that during the measurement clutter will contain cars with a low radial velocity. The rest of the clutter is composed of unharvested farmland (Figure 4.23). The CNR of this range cell is 19.4 dB for a 10 ms integration time.

Urban Clutter

A third kind of clutter is composed of buildings which dominate signature of clutter in this range cell even though the other 2/3 are composed of woodland and farmland (Figure 4.24). The CNR of this range cell is 12.2 dB for a 10 ms integration time.

The properties of these three clutters which will be detailed in this chapter and are summed up in 4.4.8.

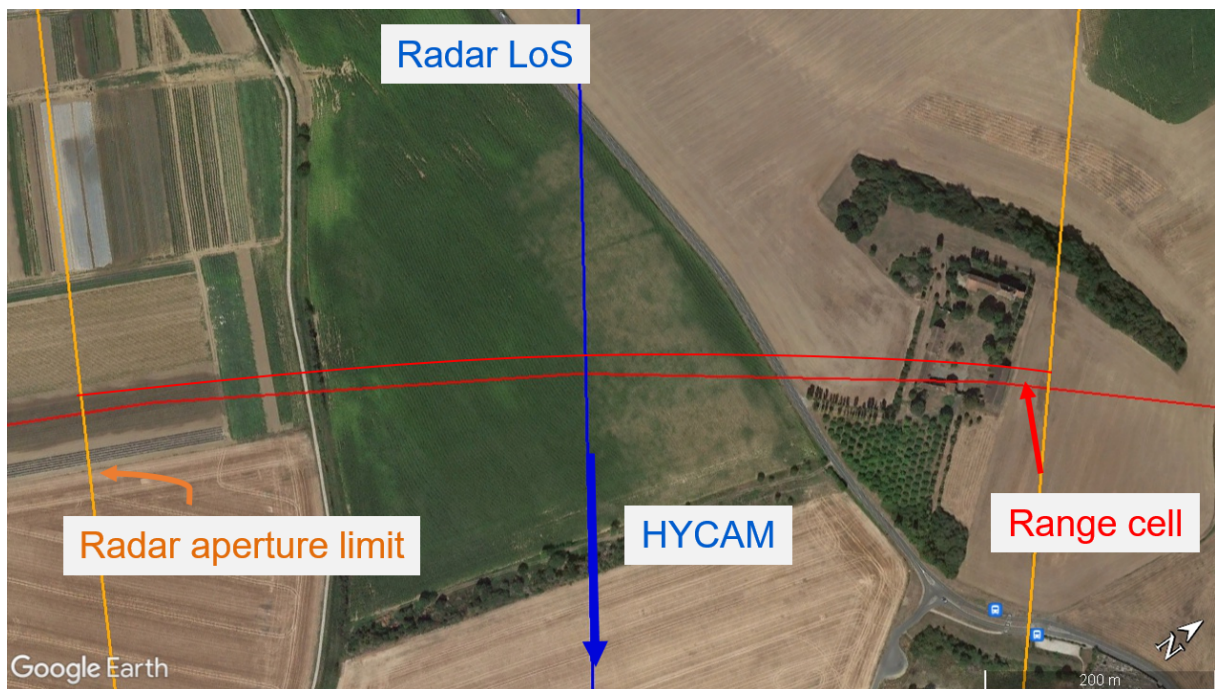


Figure 4.22: Map of the farmland clutter.

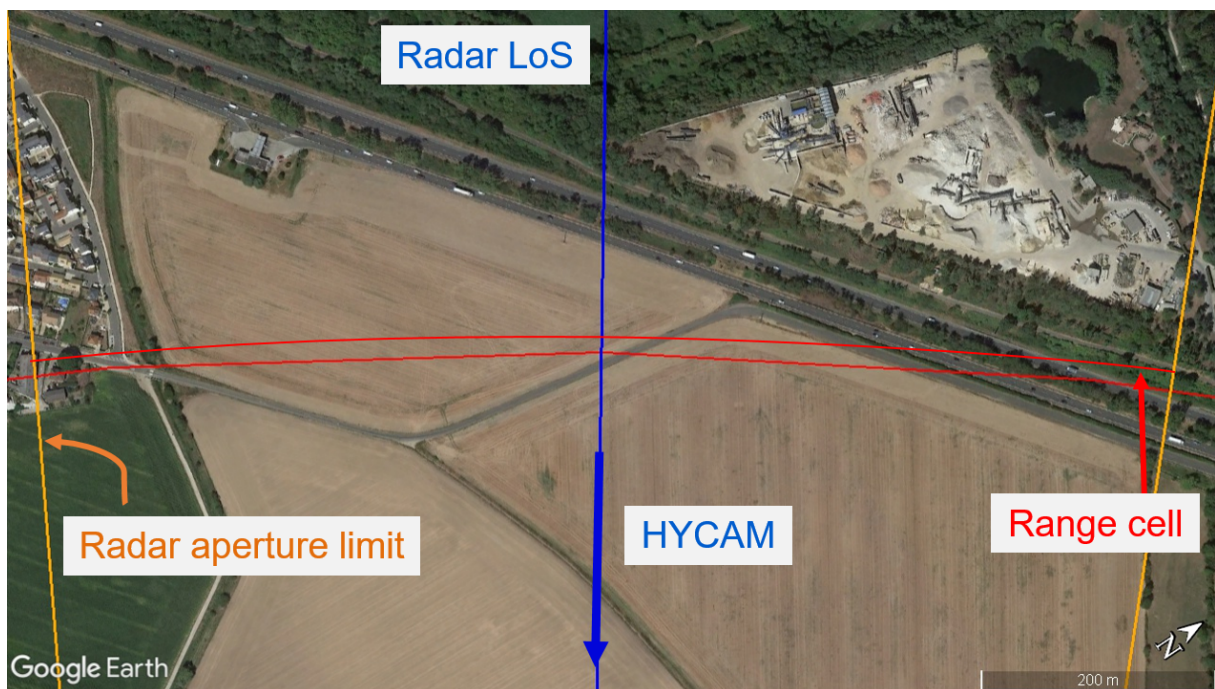


Figure 4.23: Map of the farmland and road clutter.

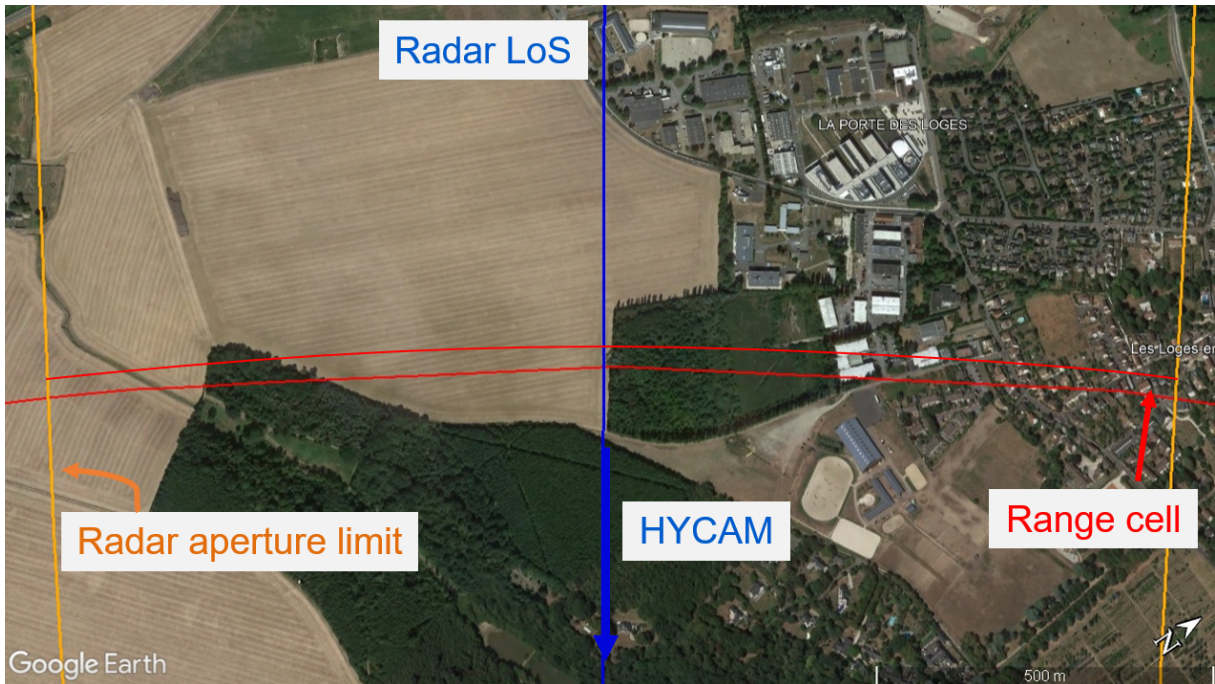


Figure 4.24: Map of the urban clutter.

4.4.2 . Covariance matrix estimation

We use the polarimetric covariance matrix to analyze the properties of the polarimetric clutter. After the Doppler-range processing we format each clutter cell as:

$$X(t, d) = \{X_{Hh}, X_{Hv}, X_{Vh}, X_{Vv}\} \quad (4.4.1)$$

with d and t respectively being the distance and time coordinates of the clutter cell. As emphasized previously, we use both X_{Hv} and X_{Vh} as they do not completely correlate. We compute an estimate of the covariance matrix, using the SCM. The SCM is averaged over the time axis as illustrated in Figure 4.25 as we justify in 4.4.5.

Each clutter cell contains a large number of different backscatterers, which means their polarimetric signature can strongly vary with distance. On the other hand, there

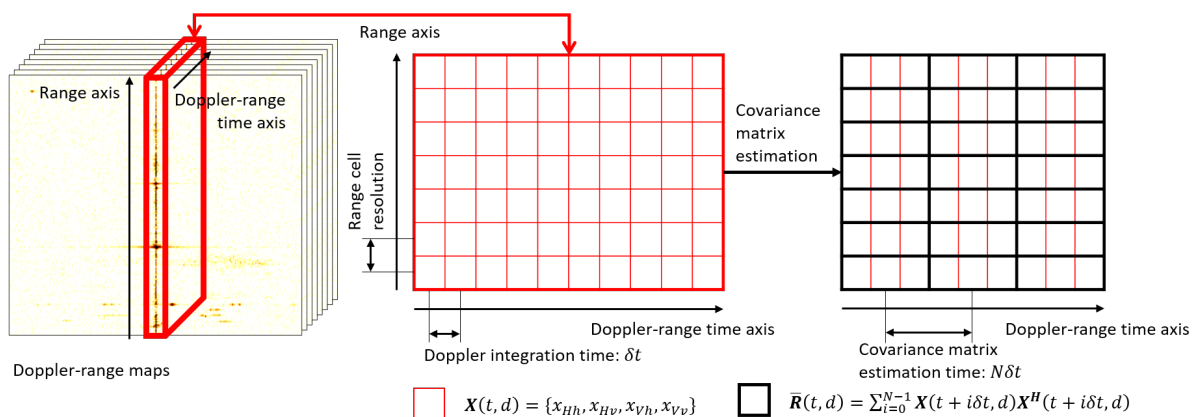


Figure 4.25: Estimation of the covariance matrix from the Doppler-range maps.

are few variations in the nature and number of backscatterers in a clutter cell during time (except the presence of target or rare phenomena). It means that the polarimetric signature should be more stable along the time axis than along the distance axis. The covariance matrix estimates is written:

$$\bar{\mathbf{R}}(t, d) = \frac{1}{N} \sum_{i=0}^{N-1} \mathbf{X}(t + i\delta t, d) \mathbf{X}^H(t + i\delta t, d) \quad (4.4.2)$$

4.4.3 . Eigenvalues

To characterize the covariance matrices we use the eigenvalue decomposition. We have:

$$\bar{\mathbf{R}} = \mathbf{U}^{-1} \mathbf{\Lambda} \mathbf{U} \quad (4.4.3)$$

$$\mathbf{L} = \text{diag} \{ \lambda_0, \lambda_1, \lambda_2, \lambda_3 \} \quad (4.4.4)$$

λ_i are the sorted eigenvalues and \mathbf{U} the eigenvectors basis. Each eigenvalue represents a set of backscattering processes and its power. An equal repartition of power between the eigenvalues means that no set of backscattering process is dominant during the time of analysis, whereas a concentration of power in a single eigenvalue mean that the backscattering processes are stable during the time of analysis. A 4x4 complex covariance matrix estimated with the SCM has 16 independent parameters; the eigenvalues reduce these 16 independent parameters to 4 and allows an analysis based on the stability of the clutter signature.

We characterize the covariance matrices by their rank as some detectors (srML for example) project the data from the CUT in the orthogonal subspace to the estimated clutter. Due to the rank-nullity theorem, the orthogonal subspace is larger as the rank of the covariance matrix is lower, thus the target is more likely to be in this orthogonal subspace.

The clutter return is a composition of several polarimetric backscattering processes shifting during the time of analysis. The rank of the SCM represents how much the polarimetric signature of the clutter changes during its estimation. To measure the rank of the SCM we introduce the eigenvalues' Shannon entropy [Shannon 1948]:

$$H = - \sum_{i=0}^{N_{chan}-1} p_i \log_{N_{chan}} p_i \quad (4.4.5)$$

with:

$$p_i = \frac{\lambda_i}{\sum_{j=0}^{N_{chan}-1} \lambda_j} \quad (4.4.6)$$

We introduce the effective rank as a useful metric for N_{chan} -channel coherent signals that, related with a finite number of parameters, to estimate dimension of the problem. [Roy and Vetterli 2007] shows:

$$r_{eff} = N_{chan}^S = \prod_{i=0}^{N_{chan}-1} p_i^{-p_i} \quad (4.4.7)$$

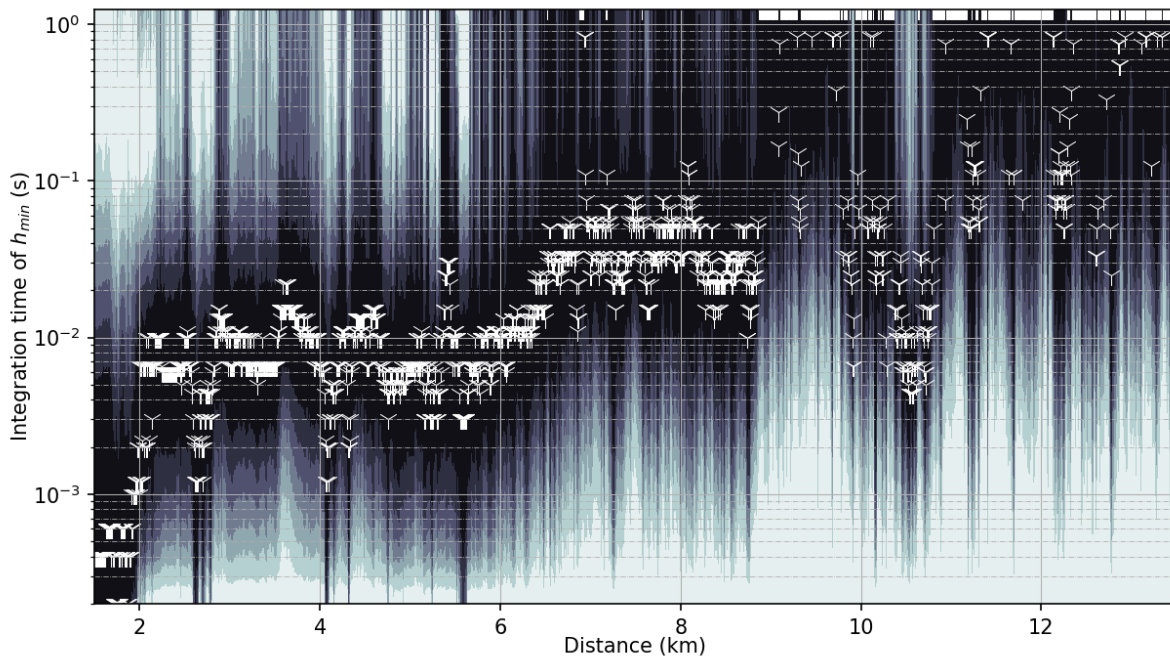


Figure 4.26: Mean effective rank over the duration of the measurement as a function of the range cell and the Doppler processing time, normalized for each range under consideration. Markers indicate the minimum effective range for each range cell.

We expect a low effective rank in range cells where the clutter polarimetric scattering mechanisms are stable with time. As we detail in 5.4, a low effective rank is conducive to high performance for the detectors based on the structure of the covariance matrix of the clutter.

4.4.4 . Doppler integration time influence on the SCM

We measure the effective rank as a function of the Doppler processing time. We apply Doppler processing on the data with different integration time ranging from 200 μs (no Doppler processing) to 1 s (Doppler processing over 5000 pulses). We compute the SCMs over these Doppler processed data with a fixed number of samples ($N = 20$). We measure the effective rank for each range cell and each integration time. We search local minima of the effective rank, as lower rank matrices means the clutter filtering problem has a lower number of degrees of freedom and thus, is easier to address. Figure 4.27 shows the effective rank as function of range and of the Doppler processing time. The dynamic is normalized at each range to emphasize the local minimum. Markers show minimum of the effective rank at each range. We observe that a Doppler processing time of the order of magnitude of 10^{-2} s seems to consistently minimize the effective rank for most ranges. At ranges inferior to 2 km, the radar is still receiving the signal from backscatters in near field and the signal is akin to radar coupling, meaning that this data is not representative of the clutter returns we expect. Returns from ranges further than 8 km suffer from a low CNR (Figure 4.17 and Figure 4.28b).

Figure 4.27 shows the minimum effective rank at each range. We see a high dispersion of value at further ranges, most probably due to the low CNR. The effective rank level at range closer than 9 km are all lower than 2, which suggests that clutter filtering

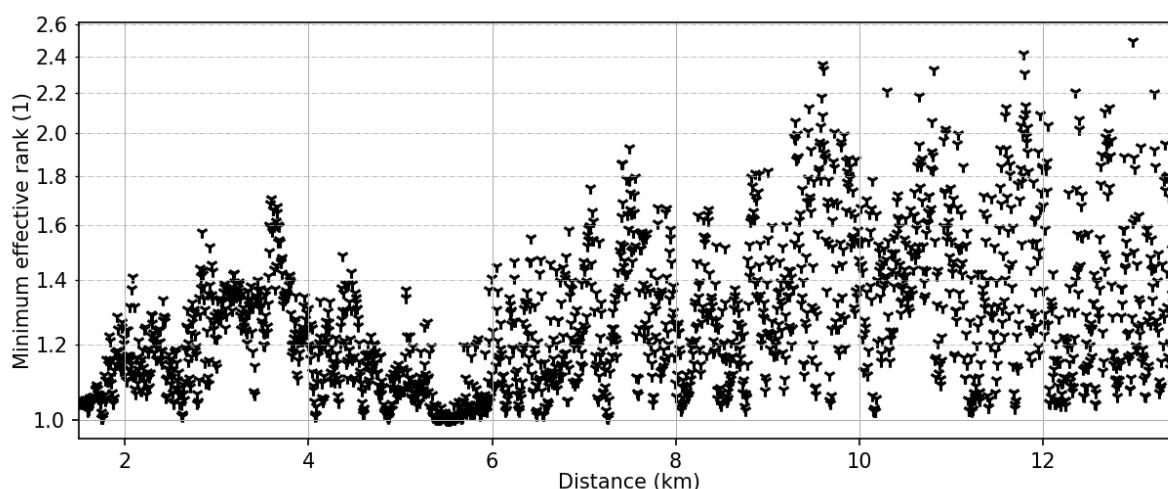


Figure 4.27: Minimum effective rank measured at each range.

works well at this ranges. In the next parts, we choose the integration time following three constraints:

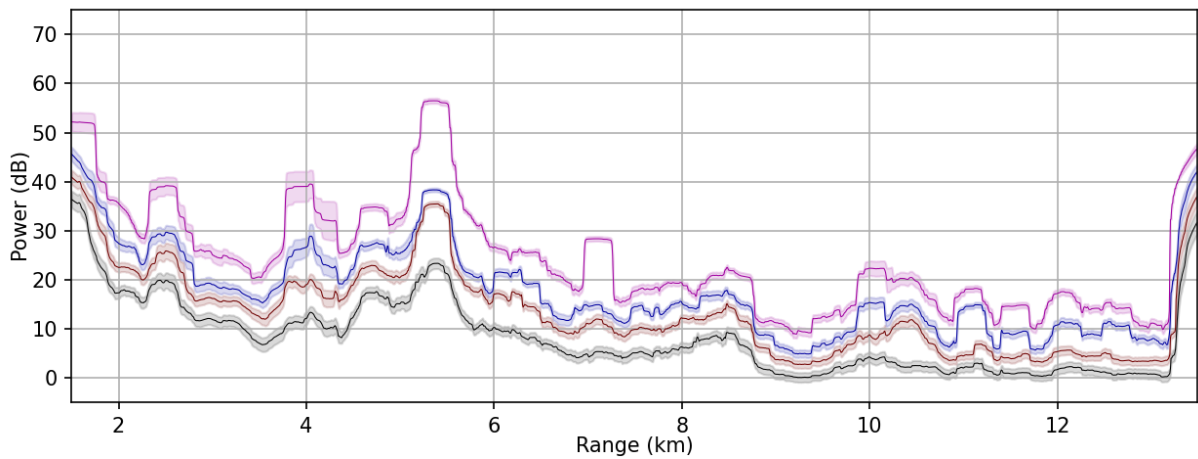
1. The Doppler integration and the estimation of the SCM must be long enough to ensure a sufficient CNR and an adequate estimation.
2. The total integration time should be short enough to be actionable, as an integration time too long masks rapid variations of the clutter and might be longer than the time the target spends in the clutter.
3. The integration time plays a role in the effective rank of the covariance matrix as discussed in 4.4.4 and we want to minimize this effective rank.

These computation enables an adaptive Doppler processing time, depending on the clutter cell under consideration.

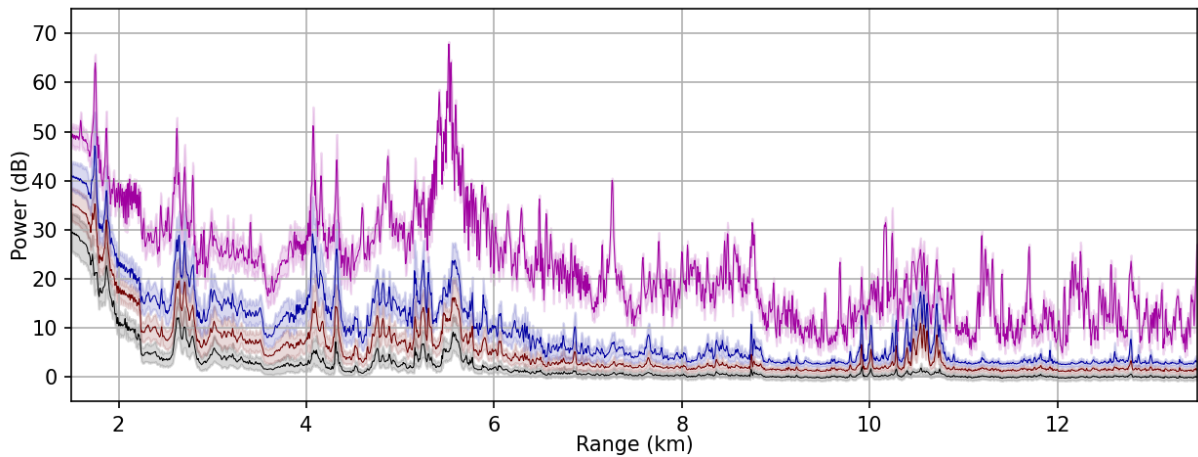
As we also want to keep our processing close to what can be achieved operationally, which means a common integration time for each range cell, even if the integration time doesn't minimize the effective rank at every ranges. The Doppler processing was computed over 10 ms (50 pulses long burst per polarization), and the SCM estimates over 50 samples. It means, each covariance matrix, and eigenvalue set, represent 500 ms of data. This Doppler processing time is the one chosen for every studied clutter cell in the following, except if specified otherwise. This value is a compromise between adequate estimation of the covariance matrix and a fast integration time to have a larger number of uncorrelated data to study (or in an operational context a faster refresh rate of the detector).

4.4.5 . Comparison between range and time estimated SCM

The clutter we study in this part exhibits several different behaviors. Figure 4.28a and 4.28b show the mean eigenvalue over time as a function of the distance for covariance matrices computed over the range axis (Figure 4.28a) and the time axis (Figure 4.28b). To compute the mean eigenvalues we compute covariance matrices of the clutter using a 10 ms Doppler processing time and 50 samples, for each range cell we have



(a) Covariance matrices computed over the range axis. The outlining shape shows the standard deviation of the log-distribution of the eigenvalues during time at each range.



(b) Covariance matrices computed over the time axis. The outlining shape shows the standard deviation of the log-distribution of the eigenvalues during time at each range.

Figure 4.28: Mean eigenvalues at each range

several covariance matrices. These matrices are diagonalized and we average their eigenvalues. The profile of the highest eigenvalue are similar, (with some plateaus in Figure 4.28a caused by the spatial averaging) however the lower eigenvalues are significantly different with the two averaging methods. The lower eigenvalues are significantly lower with the temporal averaging compared to the spatial averaging.

This leads to an overall higher effective rank when using spatial averaging as shown in Figure 4.29.

In addition we notice plateaus corresponding to high values, which means that high clutter signal will contaminate nearby cells. These plateaus reduce the SCR of the target in the CUT even if the target is not in a cell in which the clutter signal is strong, as long as a cell with high clutter signal is close to the CUT. The eigenvalues vary sharply with respect to range (as shown in Figure 4.28b), which means that clutter from one range cell to another can be very different. As clutter cells differ from range to range, we cannot estimate the polarimetric properties of a clutter cell by observing a neighboring cell, and prevents clutter estimations on range data. As two neighboring range clutter cells can have drastically different behaviors estimating the properties of one of these range

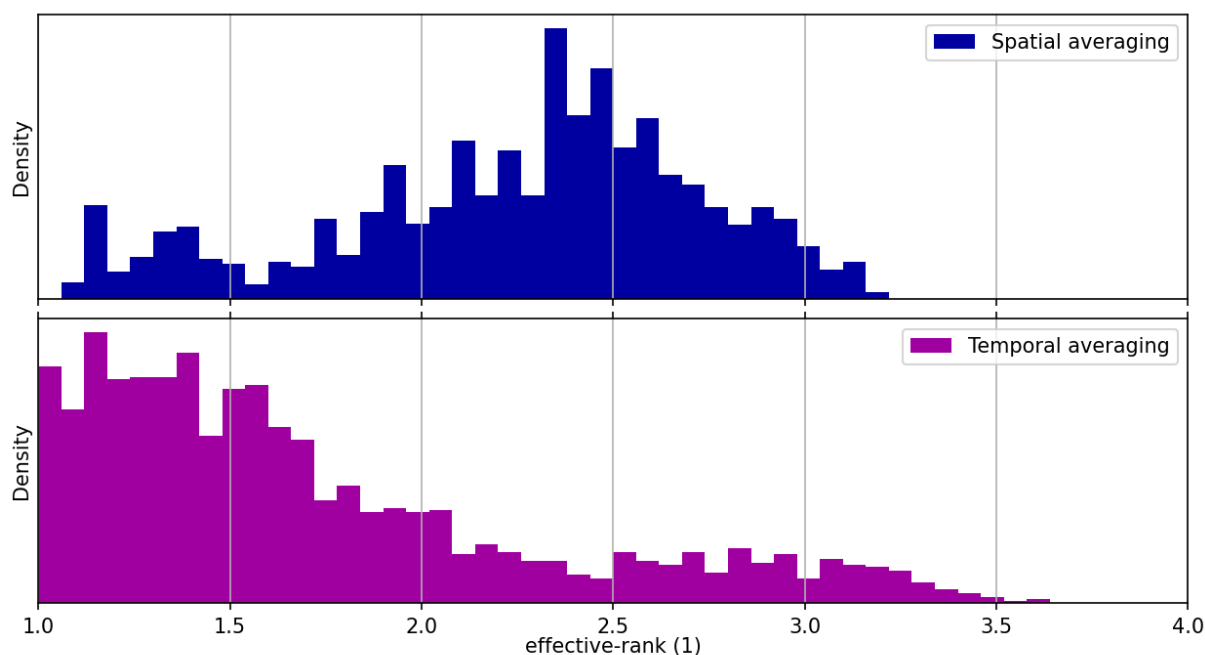


Figure 4.29: Histograms of the mean effective ranks using spatial and temporal averaging

cells with the other one is not possible. We cannot use spatial data for estimations so we focus on the time series of eigenvalues as we will use temporal data for estimations, as we outlined.

4.4.6 . Eigenvalues time series for the selected clutter

In this section we show the time series of the selected clutter and we study the distributions of these time series. We use these time series to characterize the clutter cells as they exhibit different properties for different range cells. Figure 4.30 shows the time series of the eigenvalues of the farmland clutter.

The distributions of the log-eigenvalues time series for the selected range cell are shown in relation to each others in Figure 4.31

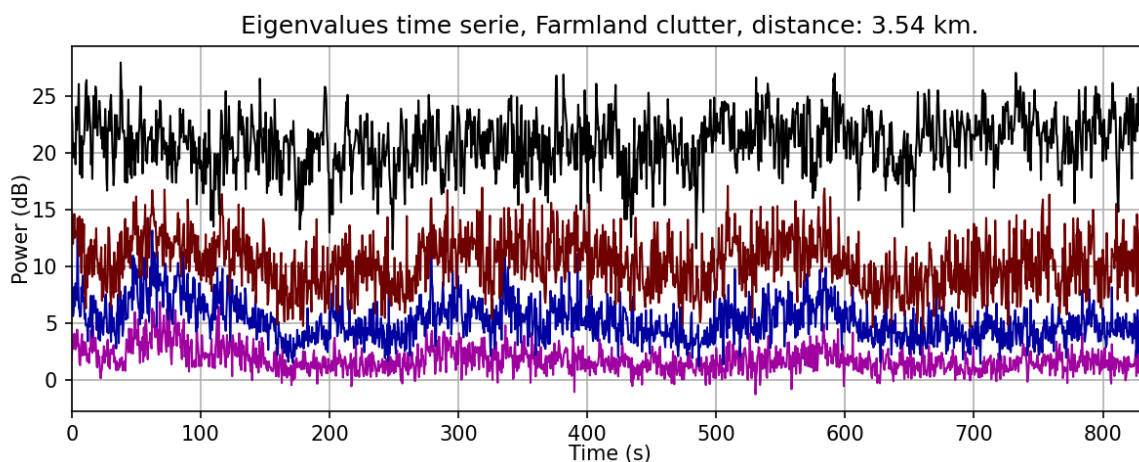


Figure 4.30: Eigenvalues time series of farmland clutter.

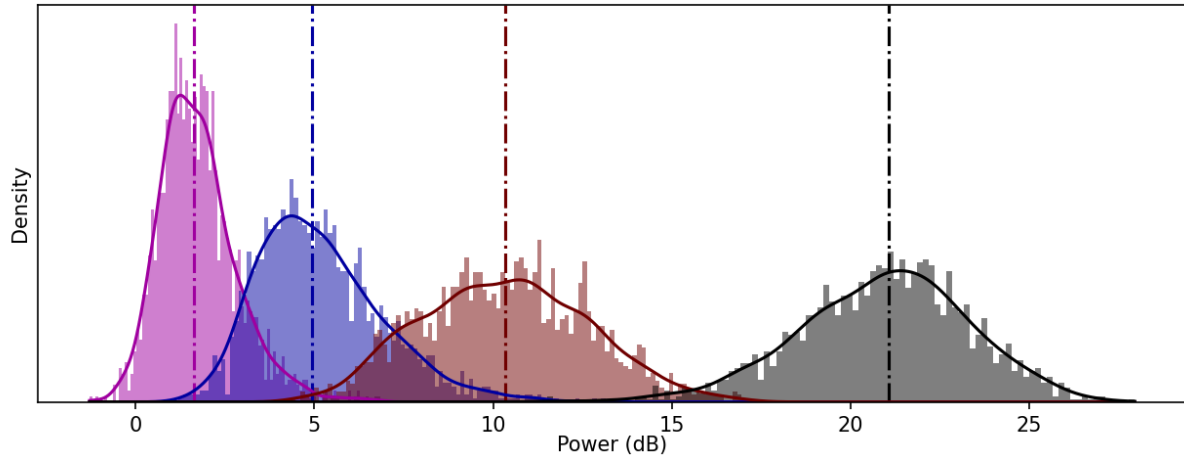


Figure 4.31: Eigenvalues time series distributions for the farmland clutter. The dashed line is the median of the distributions of the eigenvalues.

There is an overlap between the eigenvalue distribution meaning that the classification method based on the rank of the eigenvalue is limited as they can “switch” depending on the fluctuations. To better characterize the eigenvalue distribution we fit them with different distributions (Figure 4.32).

	1st Eigenvalue	2nd Eigenvalue	3rd Eigenvalue	4th Eigenvalue
Log-Normal	$1.3 \cdot 10^{-5}$	$3.4 \cdot 10^{-3}$	$2.0 \cdot 10^{-2}$	$4.3 \cdot 10^{-1}$
Exponential Weibull	$1.4 \cdot 10^{-5}$	$3.1 \cdot 10^{-3}$	$1.5 \cdot 10^{-2}$	$3.4 \cdot 10^{-1}$
Gamma	$1.4 \cdot 10^{-5}$	$3.3 \cdot 10^{-3}$	$6.4 \cdot 10^{-2}$	$8.2 \cdot 10^{-1}$
χ^2	$1.4 \cdot 10^{-5}$	$3.3 \cdot 10^{-3}$	$6.4 \cdot 10^{-2}$	$8.3 \cdot 10^{-1}$

Table 4.2: Sum square error for the distribution fit shown in Figure 4.32

Figure 4.32 shows the eigenvalue distributions fitted with a different distribution to approximate the eigenvalue distribution. The sum square error of each fitted distribution are given in Table 4.2. The log-normal distribution corresponds to a model used for the amplitude of non-polarimetric clutter [Shnidman 1999] and properly fits our eigenvalue distributions. Since no model exists for the polarimetric ground clutter in the geometry we consider, we assume the eigenvalues time series are lognormal distributed in the simulations of the following parts. We prefer the lognormal distribution on the exponential Weibull distribution as the lognormal distribution has fewer parameters.

Time series of urban clutter and road clutter show an important gap between the first and following eigenvalues. The road and farmland clutter time series are typical of low effective rank matrices with a dominant eigenvalue (15 dB above in Figure 4.33(a)). The road is nearly perpendicular to the radar LoS, which means that car passing by have low relative velocity and are endo-clutter. In Figure 4.33(b), we have urban clutter with one dominant eigenvalue. We expect a stable signature as building’s backscattering processes are stable with time, however this does not seem to be the case here, which is probably due to the fact that there are roads in the same clutter cell with traffic.

4.4.7 . Temporal stability of the polarimetric signature

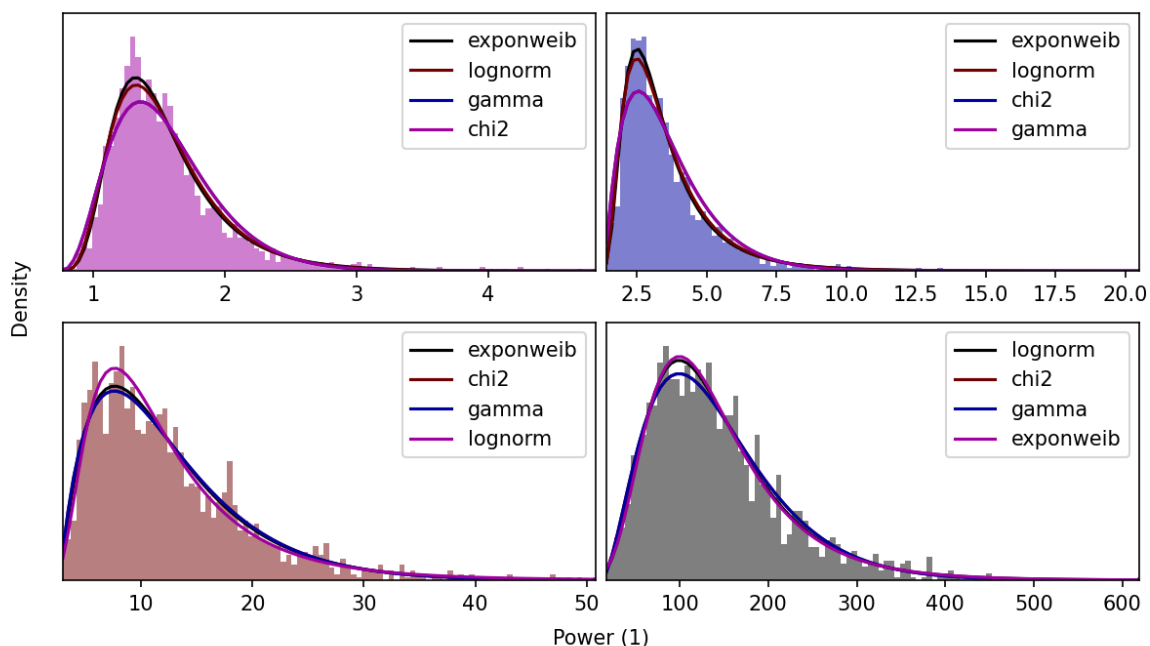


Figure 4.32: Distribution of the 4 eigenvalues time series of the farmland clutter (from left to right and top to bottom, the lowest to highest ranked eigenvalues distribution), fitted with a log-normal distribution.

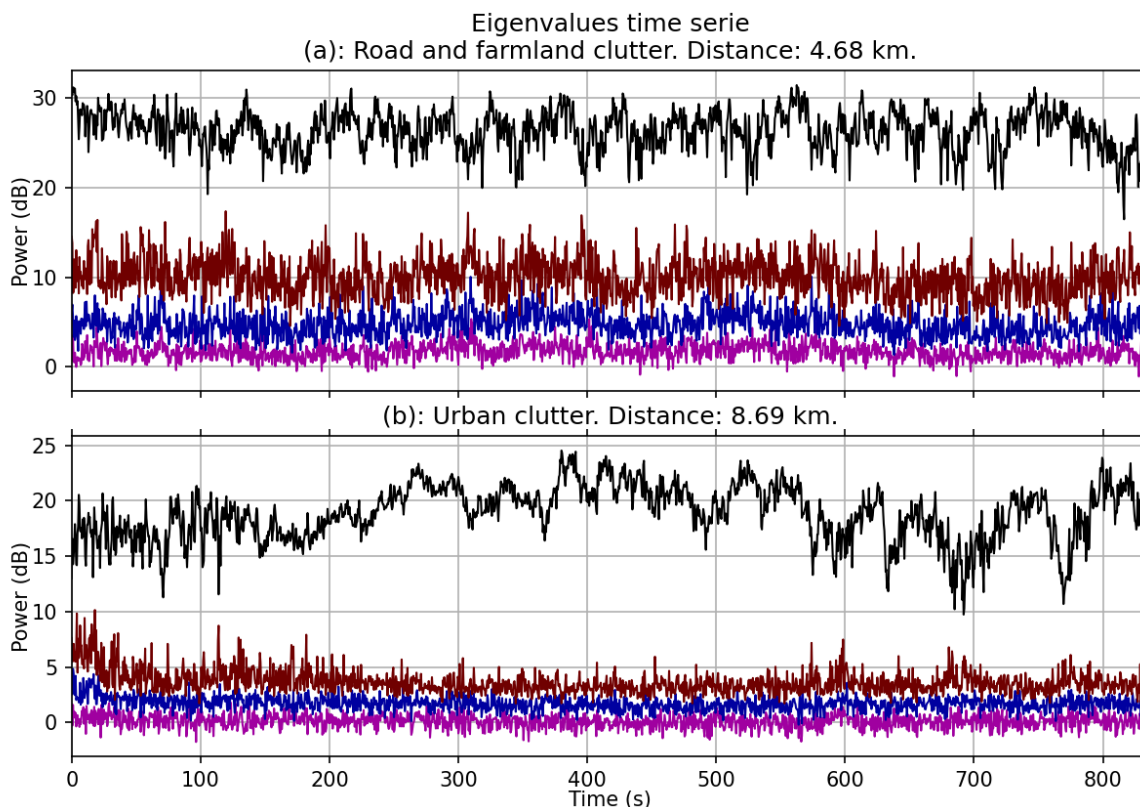


Figure 4.33: Eigenvalues time series at two additional ranges, (a) is road and farmland clutter and (b) is urban clutter.

The eigenvalues time series show that there is a tendency to have stable total clutter power and stable ratios between eigenvalues. We make the hypothesis that the eigenvalue temporal distributions are stationnary. We want to quantify the temporal stability of the clutter polarimetric stability to better model its evolution.

To further quantify the stability of the clutter we measure a distance between the covariance matrices of a same range cell according to their relative time point of estimation. With the hypothesis that the eigenvalues distributions are stable, we propose to use the angle between the matrices as distance measurement. This angle gives us a measure of the temporal stability. This measurement has a sampling rate limited by the Doppler integration time and the number of sample in the SCM estimation. In order to measure the temporal stability on a shorter time scale we modify the Doppler integration and the SCM estimation processes. Using no Doppler integration increases the sampling rate but reduces the CNR of the clutter cells and the values gives different mismatch angles. The range cells with the lower CNR exhibit lower mismatch angle, we hypothesize that this is due to the high proportion of noise in the clutter data. We explain that such behaviour is expected for covariance matrices containing mainly noise. We conclude that the mismatch angle model is valid for high CNR data, which is the case when the Doppler integration time is long enough. Finally we test the hypothesis that covariance matrix with low CNR behave similarly to noise matrices by measuring the impact of the number of samples in the SCM estimation. We expect that noise covariance matrices should have low mismatch if the number of samples of the estimation is high.

Mismatch angle

We define the mismatch angle as the angle between the two square matrices:

$$\cos\theta_{AB} = \frac{\langle \mathbf{A}, \mathbf{B} \rangle}{\|\mathbf{A}\| \|\mathbf{B}\|} \quad (4.4.8)$$

Using the canonical inner product for square matrices, $\langle \mathbf{A}, \mathbf{B} \rangle = \text{Trace}(\mathbf{A}\mathbf{B}^H)$ and $\|\cdot\|$ its associated norm. We call this quantity the mismatch angle; it aims at measuring the difference of polarimetric signature using the covariance matrices as an angle. For a given set of eigenvalues distributions, the mismatch angle depends almost only on the eigenvectors (see appendix E), which allows us to monitor the fluctuations of the polarimetric signature while ignoring the fluctuation of total clutter power. To assess the extent to which the signature of the clutter changes with time we use the mismatch angle, $\theta(t, t + \delta t)$.

$$\cos\theta(t, t + \delta t) = \frac{\langle \overline{\mathbf{R}}(t), \overline{\mathbf{R}}(t + \delta t) \rangle}{\|\overline{\mathbf{R}}(t)\| \|\overline{\mathbf{R}}(t + \delta t)\|} \quad (4.4.9)$$

With $\overline{\mathbf{R}}(t)$ the SCM estimate at time t . In the following we focus on the study of the cosine of the mismatch angle, $\cos\theta(t, t + \delta t)$, except if specified otherwise. We introduce:

$$D(t, \delta t) = \frac{\cos\theta(t, t - \delta t) + \cos\theta(t, t + \delta t)}{2} \quad (4.4.10)$$

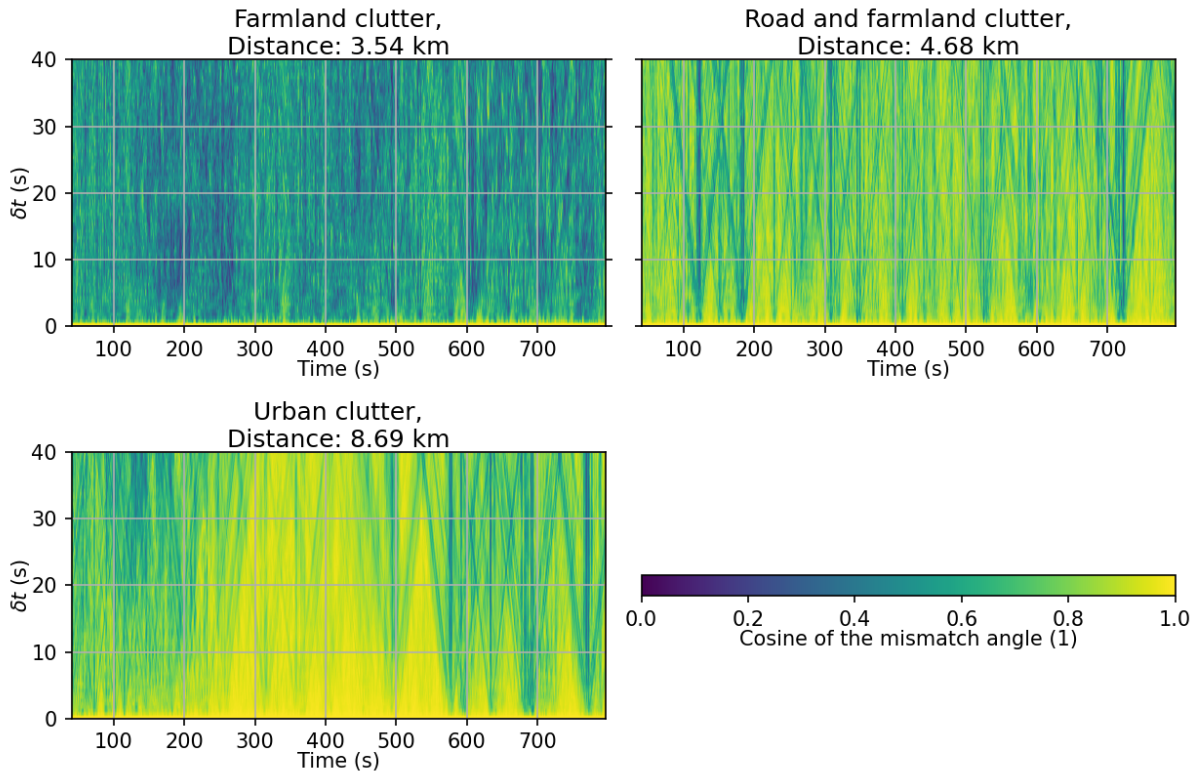


Figure 4.34: Plot of D for the 3 clutter. Lower D value means the clutter is less stable.

Which represents the mismatch between the SCM at time t and the SCMs at a distance of δt . A large D means the covariance matrix at t is misaligned with the matrices at time δt .

Figure 4.34 shows the mean cosine of the mismatch angle between a reference matrix measured at time t and the matrices measured at $t + \delta t$ and $t - \delta t$ (equation 4.4.10). The lower the value of the cosine, the higher the mismatch angle is and thus the higher the mismatch between the matrices is. Figure 4.34 shows that different range cells give vastly different results. For the farmland range cell, we notice the cosine of the mismatch angle gets to low values even for as for small δt , which means that the SCM of the clutter as this range tends to be unstable, despite the stability of eigenvalue distribution with time. It means that the polarimetric signature of the clutter changes with time. Similarly, we see an instable clutter signature for the farmland and road. In the same way, the urban clutter shows lower mismatch than the previous clutter, however, between 40 s and 200 s and 600 s and 800 s, there is a set of SCM, which have a strong mismatch for every δt .

We introduce:

$$\bar{D}(\delta t) = \frac{1}{N_t} \sum_t D(t, \delta t) \quad (4.4.11)$$

by averaging $D(t, \delta t)$ over the time axis.

To assess the typical time of the decay, we do an exponential fit on the data $\bar{D}(\delta t)$. We exclude the data point at $t = 0$ from the fit since there is no mismatch between two identical matrices. The gap between $\bar{D}(0)$ and $\bar{D}(t_0)$ can indicate that the sampling rate of $\bar{D}(\delta t)$ is too low to measure correctly the typical time of decay. In Figure 4.35(a) we

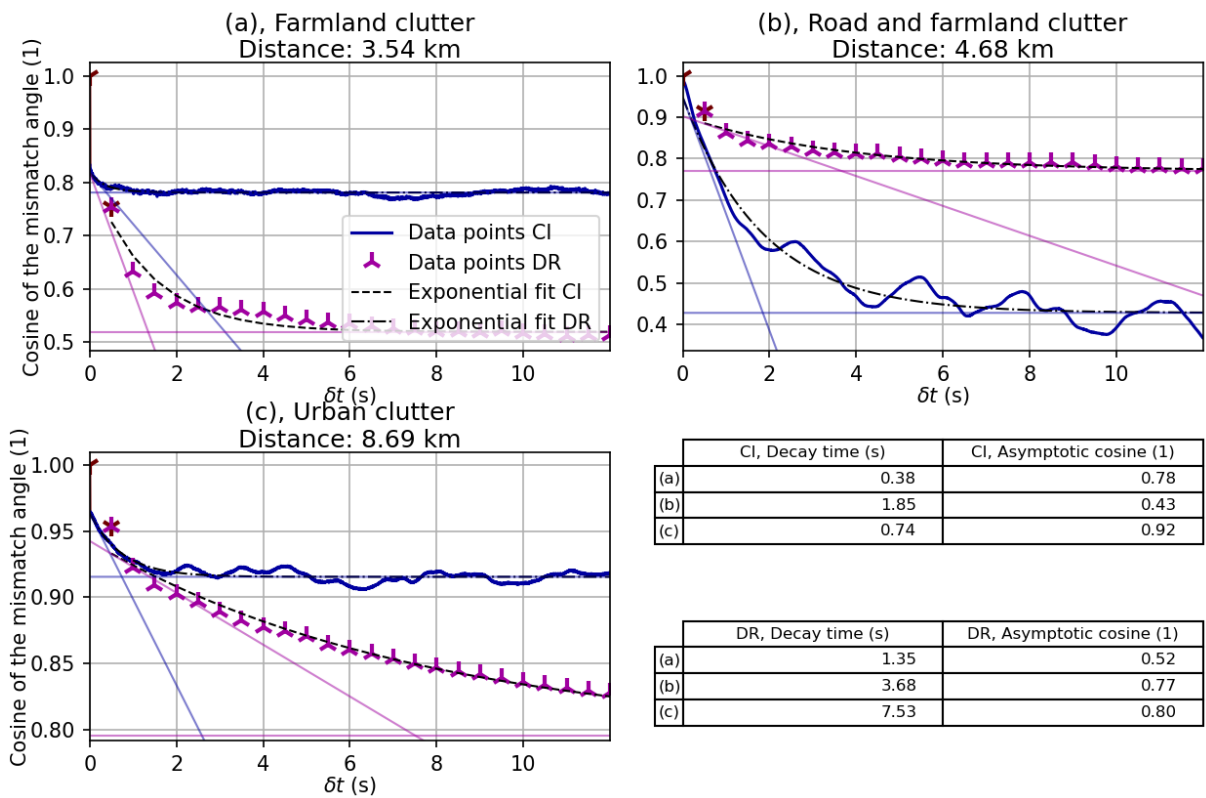


Figure 4.35: Mean of the decay of the cosine of the mismatch angle over the time axis. Here mean is shown for two different integration time, no integration (CI) and typical integration of 10 ms (DR).

observe a large gap between $\overline{D}(0)$ and $\overline{D}(t_0)$ for Doppler integrated data. The cosine of the mismatch angle starts at approximately 0.8 meaning that δt resolution is lacking to properly measure the decay time. However it is sufficient to observe a further decrease from 0.78 to 0.52 with a time constant of 1.35 s, this corresponds with the observation of low stability made with Figure 4.34(a). Figure 4.35(b) exhibits a similar decrease with the floor being higher at 0.77 and the initial drop is less pronounced and the decrease time is longer: 3.68 s. Finally, Figure 4.35(c) shows a long decay time of 7.53 s and a higher match during the time, which is expected for urban clutter and a higher floor at 0.8.

Influence of the Doppler integration time on the mismatch angle evolution

In order to increase the sampling rate, and measure the mismatch angle over shorter δt we compute $\overline{D}(\delta t)$ using the pulse-compressed data without any Doppler processing and we compute the SCMs over 20 samples. This means the SCMs use 4 ms of data. Since we do not use Doppler processing the CNR is reduced by 17 dB compared to an integration time of 10 ms: the farmland clutter stands around -3 dB, the urban clutter CNR stands around -5 dB, and the farmland and road clutter has a CNR around 2 dB.

Figure 4.35(b) shows that the behaviors of the farmland and road clutter are different between long and short integration times. The short time integration leads to higher mismatch (the dark blue line in Figure 4.35(b)), we make the hypothesis that it is due to the presence of the road and the clutter signature exhibits high frequency variations due to the cars, that are averaged by a longer integration time.

The farmland clutter and the urban clutter show lower mismatch without Doppler integration (the dark blue line in Figure 4.35(a) and Figure 4.35(b)). This behaviour typical of the decay for low CNR range cell. Indeed, if the CNR is lower, the proportion of noise in the covariance matrix is higher. Since the covariance matrix of the noise is written:

$$\begin{pmatrix} \sigma_v^2 & 0 & 0 & 0 \\ 0 & \sigma_v^2 & 0 & 0 \\ 0 & 0 & \sigma_h^2 & 0 \\ 0 & 0 & 0 & \sigma_h^2 \end{pmatrix} \quad (4.4.12)$$

With σ_x^2 the noise on the x reception channel, we expect the noise matrices to match when between each other if the noise is stationary. The SCM cell in which noise is important tends toward the value of equation 4.4.12 (see appendix D). This constant diagonal component added in clutter covariance matrix reduces the mismatch.

Influence of number of samples of the SCM estimate

The quality of the SCM estimation is linked to the number of samples used in the estimation. As noise matrices are identical in our measurements the source of mismatch between two noise matrices is the estimation quality. Thus, we expect the noise matrices to closely match if they are well estimated. This means the higher the number of sample we have the lower the mismatch angle should be. This means that for higher numbers of samples the match between the covariance matrices should be higher if there is a low CNR. A more accurate estimate leads to a higher match between the

noise covariance matrices. Meanwhile it should not modify significantly the match of clutter covariance matrices in which the CNR is high.

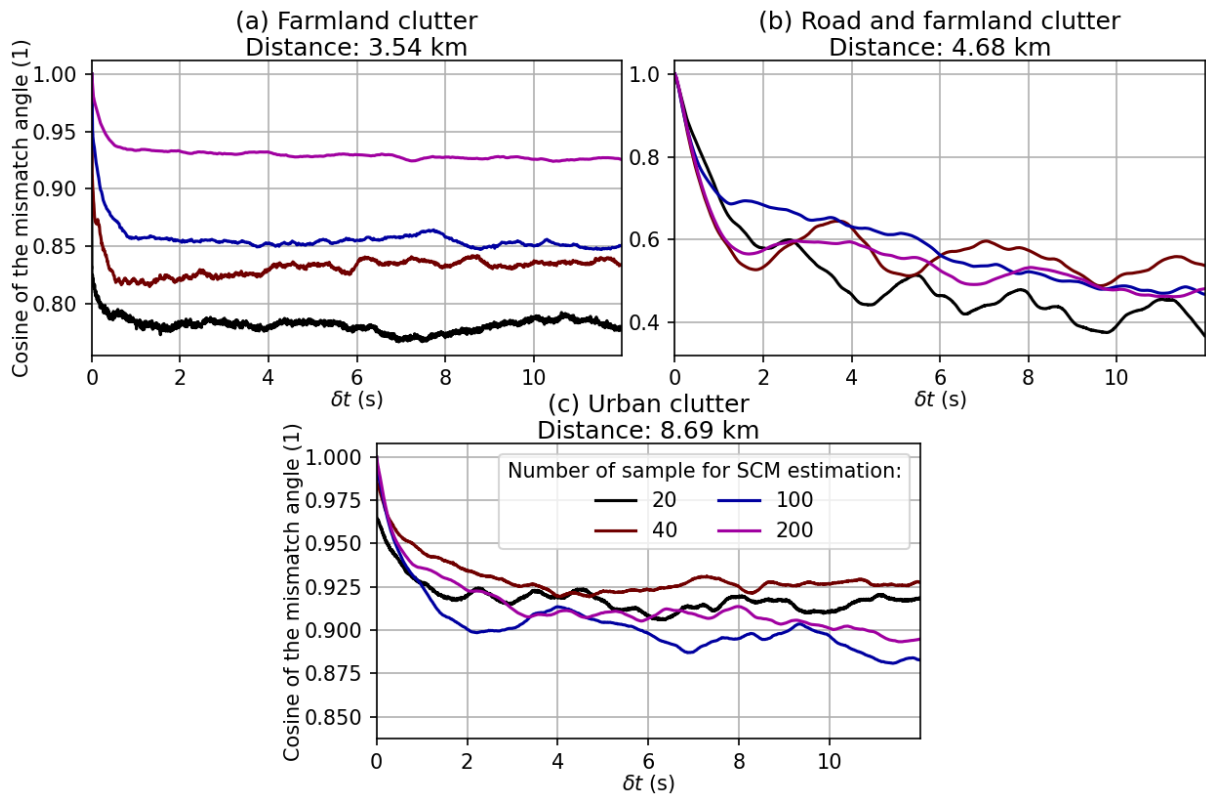


Figure 4.36: Cosine of the mismatch angle with different number of samples for the SCM estimates. There is no Doppler integration, the total integration time are 4 ms, 8 ms, 20 ms and 40 ms.

With a higher number of samples, Figure 4.36(a) shows decreased mismatch angle between the covariance matrices for the Farmland clutter, which matches with explanation discussed beforehand. It matches with the discussion of appendix D, which shows that the variance of the terms of the noise SCM decreases with the number of samples, implying that a high number of samples would lead to the different noise SCM being closer to the expected value and thus less mismatched. For the farmland and road clutter and the urban clutter, the number of samples for the SCM estimation doesn't seem to affect the mismatch, which suggests the quality of the SCM estimation, is good enough even with a low number of sample to accurately measure the mismatch. However, we would expect urban clutter to have a similar behavior to the farmland clutter as they both have a negative CNR so they should behave as noise. Nonetheless, it is possible that the underlying structure of the clutter covariance matrix (which has lower value than the noise covariance matrix due to the low CNR) is more conducive to low mismatch, which is plausible as the mismatch of this clutter covariance matrix is low even for high CNR.

We emphasize that this behavior forces us to adapt the detection scheme with clutter compared to noise. On the one hand, noise is stable during time and its covariance matrices have near zero mismatch angle between themselves, as they are very stable. On the other hand, this is not the case for clutter, which shows instability, and its esti-

mation needs to be frequent whereas noise estimation can be less frequent as noise is stable with time.

Furthermore, these results show that it is important to have a long enough Doppler integration time to measure a covariance matrix that is mainly representative of clutter and not noise. It implies a further constraint on the Doppler integration time. However this constraint should be met when we minimize the effective rank of the covariance matrix, as a noise covariance matrix has an effective rank close to N_{chan} which maximizes the effective rank.

4.4.8 . Summary of the clutter range cell analysis

Farmland clutter

Parameter	Value
Distance	3.54 km
Span CNR	14.5 dB
Effective-rank	1.63 ± 0.32
Log-eigenvalues (normalized)	$(0 \pm 2.4, -10.7 \pm 2.3, -16.1 \pm 1.7, -19.4 \pm 1.1)$
Mismatch decay time constant	1.35 s
Mismatch angle asymptotic cosine	0.52

Table 4.3: Summary of the farmland clutter extracted with a 10ms Doppler integration time. The log-eigenvalues are normalized with the median of the highest eigenvalue.

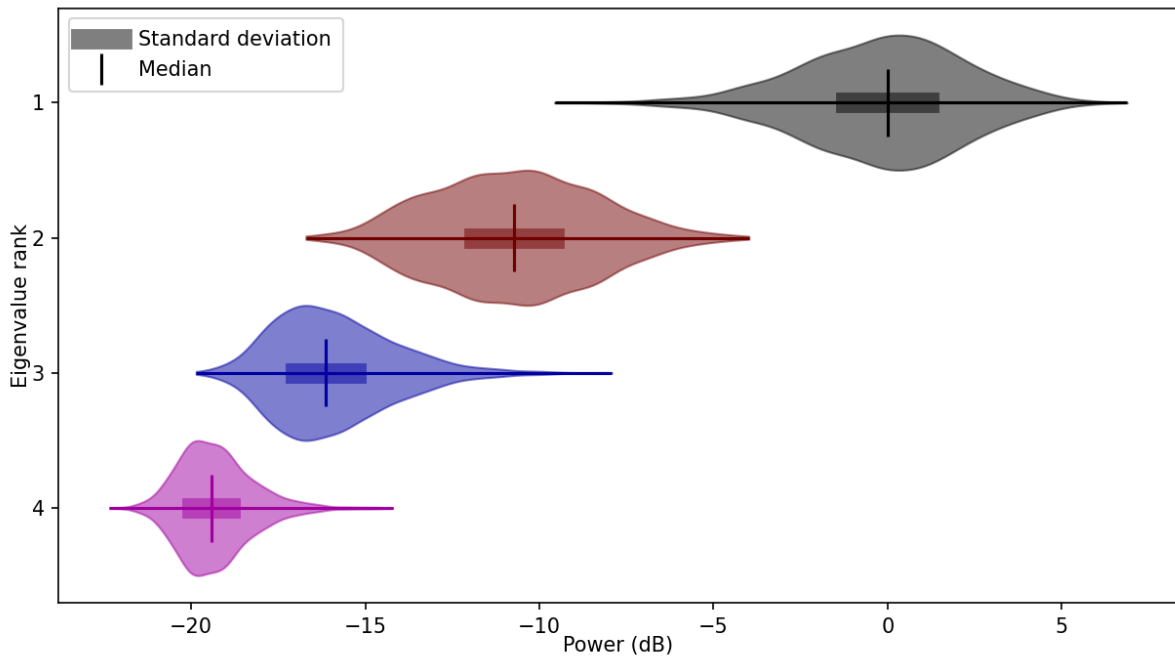


Figure 4.37: Violin plot of the eigenvalue distribution of the farmland clutter, with the median and standard deviation of each distribution outlined. The log-eigenvalues are normalized with the median of the highest eigenvalue.

Farmland and road clutter

Parameter	Value
Distance	4.68 km
Span CNR	19.4 dB
Effective-rank	1.22 ± 0.14
Log-eigenvalues (normalized)	$(0 \pm 2.2, -16.7 \pm 2.1, -22.0 \pm 1.4, -24.9 \pm 0.9)$
Mismatch decay time constant	3.68 s
Mismatch angle asymptotic cosine	0.77

Table 4.4: Summary of the farmland and road clutter extracted with a 10ms Doppler integration time. The log-eigenvalues are normalized with the median of the highest eigenvalue.

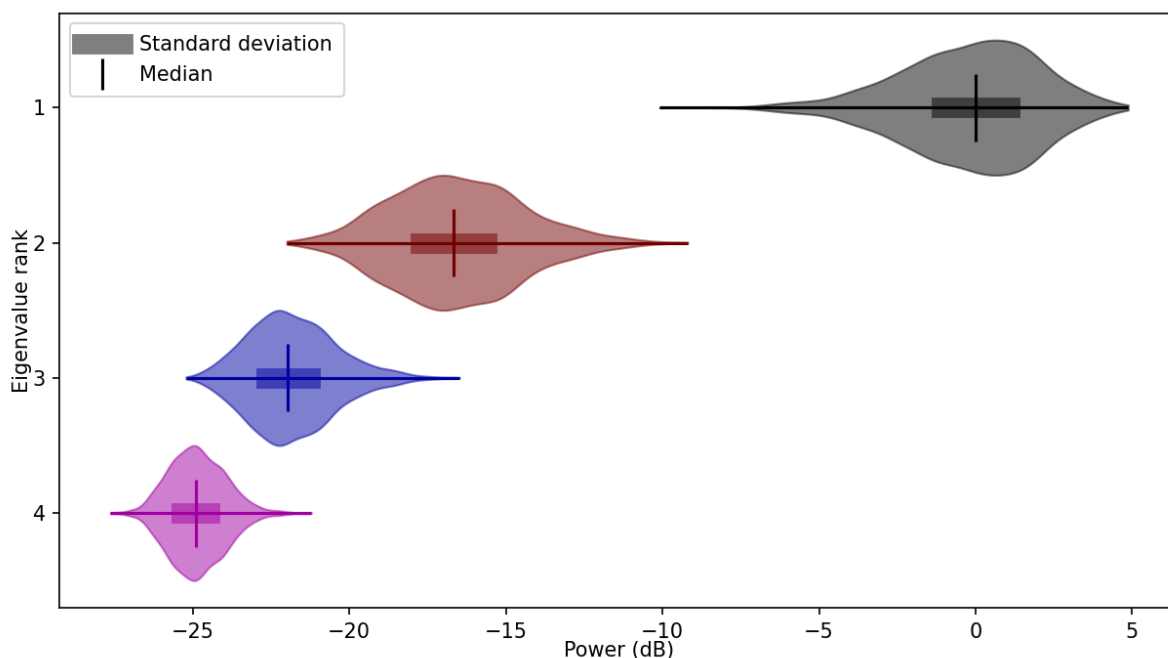


Figure 4.38: Violin plot of the eigenvalue distribution of the farmland clutter, with the median and standard deviation of each distribution outlined. The log-eigenvalues are normalized with the median of the highest eigenvalue.

Urban clutter

Parameter	Value
Distance	8.6g km
Span CNR	12.2 dB
Effective-rank	1.38 ± 0.23
Log-eigenvalues (normalized)	$(0 \pm 2.5, -15.6 \pm 1.0, -17.3 \pm 0.6, -18.8 \pm 0.6)$
Mismatch decay time constant	7.53 s
Mismatch angle asymptotic cosine	0.80

Table 4.5: Summary of the urban clutter extracted with a 10ms Doppler integration time. The log-eigenvalues are normalized with the median of the highest eigenvalue.

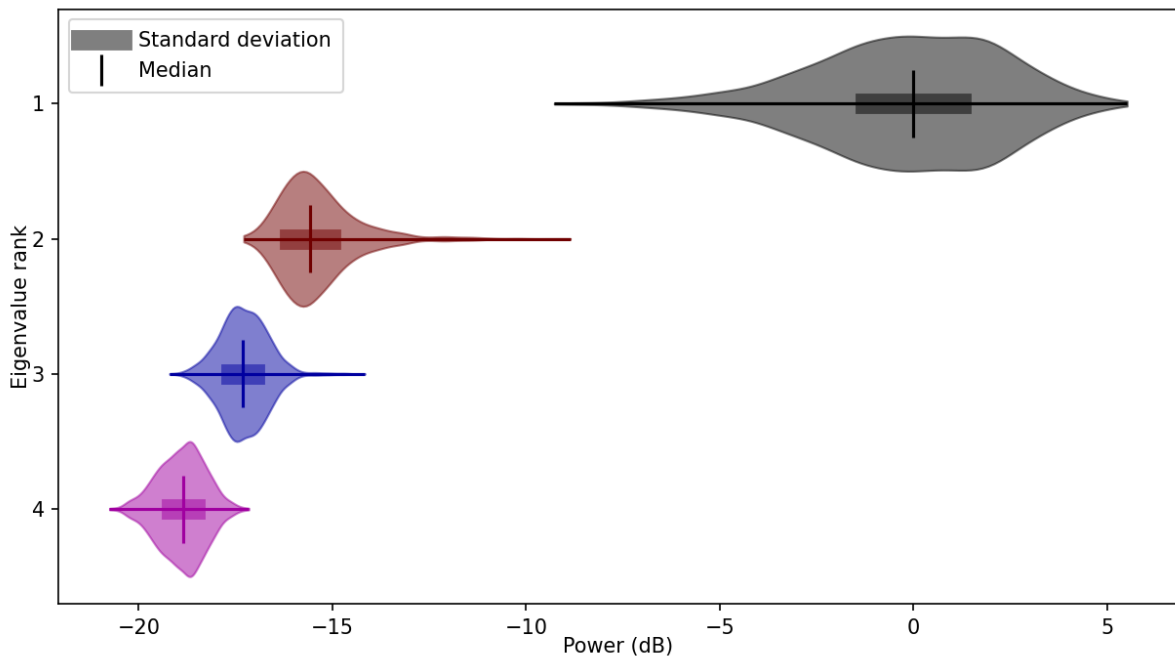


Figure 4.39: Violin plot of the eigenvalue distribution of the farmland clutter, with the median and standard deviation of each distribution outlined. The log-eigenvalues are normalized with the median of the highest eigenvalue.

Chapter 5 |

Evaluation of detectors for low-grazing endo-clutter detections

In this part we establish the performances of polarimetric detectors for low-grazing endo-clutter detection. We present the detectors we use to assess the gain of polarimetric detection in the clutter, and study their properties; we show the effective-rank of the covariance matrix of the polarimetric clutter affects the performances, and that a low effective-rank is desirable for most polarimetric detectors. We also show that a low mismatch angle between the clutter estimation of the detector and the actual clutter in the cells under test enhance the detections for the detectors using covariance matrix as a clutter filter (namely srML and P-SIRV), and does not impact the performances (with the hypothesis made, constant target and no model for the eigenvectors) of those using the polarimetric power (span and EVa). Finally, we describe a hybrid simulation process to test the detectors with the clutter data measured during the measurement campaign as well as the UAV data extracted from this same campaign. This hybrid simulation allows us to estimate the performances of the polarimetric detector as well as mono-polarimetric detectors. This comparison shows that polarimetric detectors have better performances than the monopolarimetric detectors for endo-clutter detections in a low-grazing geometry. In addition we show, with this method, that even power based detectors are sensitive to the mismatch. We propose to use the hybrid simulation method to adaptively estimate the best detector for the clutter range cells under investigation.

5.1 . Detection framework

As outlined in part 2.5, a good detector needs to be adaptive to fit different types of clutter or noise. This is achieved by using \mathbf{R}^C , the covariance matrix of the clutter and noise in the cell we are testing for a target, in the detector to adjust the output level. Adjusting the output level aims at keeping the False Alarm Rate as stable as possible whatever the properties of the clutter are. Unfortunately, we cannot estimate \mathbf{R}^C as we only estimate \mathbf{R} (based on \mathbf{X} , see equation 5.3.1) which might contain target data. We need to use secondary data to estimate \mathbf{R}^C (Figure 5.1).

As explained in 4.4.5, the clutter range cells next to the tested clutter cell are likely to have different properties so we cannot estimate the covariance matrix of the range cell under test with data from neighbouring clutter range cell. Therefore we use neighbouring data on the time axis as shown in Figure 4.25, meaning the secondary data are measured in the same range cell as \mathbf{X}_i , at a previous time, this set is $\{\mathbf{X}^E_i\}_{i \in [0, N-1]}$. $\{\mathbf{X}^E_i\}_i$ are clutter data with a the covariance matrix \mathbf{R}^E , therefore, we have: $\{\mathbf{X}^E_i\}_i \sim$

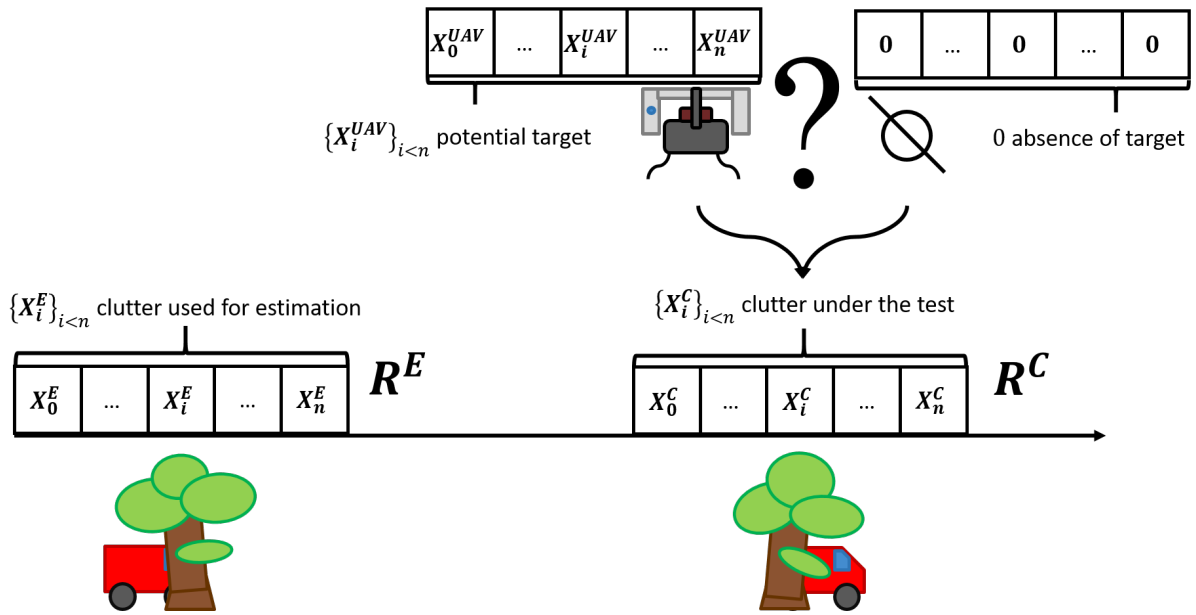


Figure 5.1: Representation of the clutter and the detector test.

$\mathcal{CN}(0, \mathbf{R}^E)$. We write the different SCM estimates:

$$\bar{\mathbf{R}} = \frac{1}{N} \sum_{i=0}^{N-1} \mathbf{X}_i \mathbf{X}_i^H \quad (5.1.1)$$

$$\overline{\mathbf{R}^E} = \frac{1}{N} \sum_{i=0}^{N-1} (\mathbf{X}^E_i) (\mathbf{X}^E_i)^H \quad (5.1.2)$$

$$\overline{\mathbf{R}^C} = \frac{1}{N} \sum_{i=0}^{N-1} (\mathbf{X}^C_i) (\mathbf{X}^C_i)^H \quad (5.1.3)$$

$$\overline{\mathbf{R}^{UAV}} = \frac{1}{N} \sum_{i=0}^{N-1} (\mathbf{X}^{UAV}_i) (\mathbf{X}^{UAV}_i)^H \quad (5.1.4)$$

As the clutter under the target and the clutter used for estimation are mismatched we define the SCR according to $\overline{\mathbf{R}^E}$ as the radar operator cannot measure $\overline{\mathbf{R}^C}$. We write:

$$SCR = \frac{\sqrt{\text{Trace}(\overline{\mathbf{R}^{UAV}})}}{\sqrt{\text{Trace}(\overline{\mathbf{R}^E})}} \quad (5.1.5)$$

We define the couple $(\mathbf{R}^E, \mathbf{R}^C)$ as being a **Covariance Matrix Couple (CMC)** of the detection test. This CMC represents the mismatch between actual clutter matrix under the target and the matrix used to estimate the clutter properties.

5.2 . General Simulation Framework

In the following analyses, we use simulations to determine the performances of detectors. We describe the generic framework of every simulation carried out in the following parts. The goal of the simulations is to determine the performances of a detector for:

- A given SCR
- A given property Θ of the CMC. This property can be: the effective rank of both covariance matrices, the mismatch angle between the covariance matrices and eventually the time interval between the estimation covariance matrices of the couple.

We recall that the h_0 hypothesis is the "target is absent" hypothesis and the h_1 hypothesis is the "target is present" hypothesis. To test a detector for h_0 hypothesis we generate clutter data to execute a detector test without a target. To test a detector for h_1 hypothesis we generate clutter data to execute a detector test with a target. For each of these detector tests we generate a new clutter dataset. The detector tests for, a given hypothesis (h_0 or h_1), a given SCR and value a given value of Θ , is a random variable, and the output of the tests are outcomes of a random variable. To assess the performances of a detector for a SCR and Θ we need to characterize both the random variables associated with hypothesis h_0 and h_1 . The outcomes of the h_0 hypothesis tests let us assess the **Cumulative Distribution Function** (CDF) of the random variables associated with the FAR which provides the $P_{FA} - threshold$ relationship. conversely, the outcomes of the tests following the h_1 hypothesis gives the CDF of the random variables associated with detection rates which provides $P_D - threshold$ relationship.

5.3 . Testing a detector with a CMC and SCR

As explained in 5.1, a detector has two inputs: a clutter dataset used to estimate the properties of the clutter, $\{\mathbf{X}^E_i\}_i$, and a clutter dataset in which a target with a given SCR is or is not present (hypothesis h_0 or h_1):

$$\begin{cases} h_0 : \{\mathbf{X}_i\}_i = \{\mathbf{X}^C_i\}_i \\ h_1 : \{\mathbf{X}_i\}_i = \{\mathbf{X}^C_i + SCR \times \mathbf{X}^{UAV}_i\}_i \end{cases} \quad (5.3.1)$$

To test the detector we need to compute the clutter datasets corresponding to a given CMC, $(\mathbf{R}^E, \mathbf{R}^C)$:

- $\{\mathbf{X}^E_i\}_i$ is generated from \mathbf{R}^E
- $\{\mathbf{X}^C_i\}_i$ is generated from \mathbf{R}^C
- We use a synthetic or measured target polarimetric signature $\{\mathbf{X}^{UAV}_i\}_i$
- We use the SCR for which we want to test the detector

To test the h_0 hypothesis we feed to the detector the clutter datasets, $\{\mathbf{X}^E_i\}_i$ and $\{\mathbf{X}_i\}_i = \{\mathbf{X}^C_i\}_i$, excluding the target from our test, the output we get is y^{h_0} . We test the h_1 hypothesis with by feeding the detector test with $\{\mathbf{X}^E_i\}_i$ and $\{\mathbf{X}_i\}_i = \{\mathbf{X}^C_i + SCR \times \mathbf{X}^{UAV}_i\}_i$. The output of this test is y^{h_1} .

5.3.1 . Testing a detector with a value of Θ and SCR

y^{h_0} and y^{h_1} are the results we get with a single test of the detector and a specific CMC. However, using a specific CMC might introduce biases in the results. A rule of thumb used in detector tests is that in order to establish performances in terms of P_{FA} , we need at least $n_{test} > \frac{100}{P_{FA}}$ measures (this is also true for P_D) [Echard 1991]. To address these issues we need to:

1. Use different CMCs with the same value of Θ , to limit the possibility of biases in the results.
2. Do several tests per CMC to have enough outcomes to properly assess the performances.

Assuming we have m different CMCs sharing the same value of Θ , we need n tests per CMC to properly assess the P_{FA} and n' additional tests per CMC to evaluate the P_D , meeting the following conditions:

$$P_{FA} > \frac{100}{m \times n} \quad (5.3.2)$$

$$P_D > \frac{100}{m \times n'} \quad (5.3.3)$$

This condition concerns only the accuracy of the P_{FA} and P'_D estimations. In addition, the m CMCs should be representative of the parameter Θ . For instance when we simulate detection tests to establish the P_{FA} , we have y^{h_0} , an outcome the test of the detector with a specific CMC. This is the outcome of a random variable associated with the detector and value Θ of this CMC. We can index the outcomes of the simulated detection tests depending on which CMC was used for the test and which of the n tests for that specific CMC it was, $y_{j,k}^{h_0}$ is the k^{th} test of the j^{th} CMC. With this tests we obtain the set of outcomes $\{y_{j,k}^{h_0}\}_{j < m, k < n}$. We use this set of outcomes to assess the P_{FA} .

For a given SCR, and the same set of CMCs (therefore the same value of Θ) we use the exact same process to create $\{y_{j,k}^{h_1}\}_{j < m, k < n'}$ we use to assess the P_D .

5.3.2 . Assessing the P_{FA} – threshold and P_D – threshold from the set of detector test outcomes

We want to obtain the P_{FA} – threshold from the set of outcomes $\{y_{j,k}^{h_0}\}_{j < m, k < n}$. For any given threshold, some elements of the set of outcomes will be inferior to that value and some will be superior. The proportion of values in the set superior to the threshold is the P_{FA} .

$$P_{FA}(threshold) = \frac{\text{Card}\left(\left\{y_{j,k}^{h_0} > threshold\right\}_{i,j}\right)}{\text{Card}\left(\left\{y_{j,k}^{h_0}\right\}_{i,j}\right)} \quad (5.3.4)$$

Similarly for the $P_D - threshold$ relationship we have:

$$P_D(threshold) = \frac{\text{Card}\left(\left\{y_{j,k}^{h_1} > threshold\right\}_{i,j}\right)}{\text{Card}\left(\left\{y_{j,k}^{h_1}\right\}_{i,j}\right)} \quad (5.3.5)$$

These two relationships allow us to fully characterize the performances of our detector for a given SCR and value of Θ .

5.3.3 . Assessing the performances of detector for different values of Θ and different SCR

The method explained in the previous part can be used for any value of the SCR and Θ . We can sample the (SCR, Θ) space to assess how our detectors behave in a wide variety of situations and for various target levels.

5.3.4 . Global parameters of the radar data and detectors

We recall that when real data are used the Doppler integration time is 10 ms, the range resolution is 15 m. The multilook number N is 50. The detector used are the multilook srML, the multilook span, the multilook P-SIRV and the EVa detector describer in 2.6.

5.4 . Influence of the effective rank on the detectors

In 4.4.4, we measured the effective rank of the clutter cells at each range as a function of the Doppler integration time. The effective rank is a continuous generalization of the discrete concept of the rank of the matrix (the number of non-zero eigenvalues) and is a measure of the degree of freedom of the phenomenon we represent with our covariance matrix. In this part, we determine the influence of the effective rank of the covariance matrix of the clutter on the polarimetric detectors performances. We show an influence of the effective rank on the performances and an interest in its minimization for most polarimetric detectors, especially those using the structure of the covariance matrix to filter the clutter. We do not make physical hypothesis on the polarimetric signature of the clutter.

5.4.1 . Simulation procedure

The simulation process described in 5.3.1 test detectors for two parameters, Θ and SCR. In this part, the matrices of the CMC are identical $\mathbf{R}^E = \mathbf{R}^C$ and Θ is the effective rank of the matrices. To test the influence of the effective rank we create clutter cells with various effective ranks. We must therefore create bins of covariance matrix couples sharing similar effective rank. We use the Metropolis-Hastings algorithm [Metropolis et al. 1953; Hastings 1970] to create 16 bins of matrix couples. Each bin contains matrices with an effective rank comprised between two boundary values. The bins uniformly sample the log of the effective ranks, meaning the boundary of the i^{th}

bin is given by $1 + (N_{chan} - 1)^{\frac{i}{n}} < e - rank < 1 + (N_{chan} - 1)^{\frac{i+1}{n}}$, with i going from 0 to $n - 1$; N_{chan} is the dimension of the problem, here we have 4 polarization states, so $N_{chan} = 4$. We fill each bin with the same number of samples by rejecting any matrix that exhibits an effective rank included in a bin already full.

To generate each matrix we first generate a vector of eigenvalue, $\Lambda = (\lambda_i)_{0 \leq i \leq 4}$, with each λ_i being uniformly distributed between 0 and 1:

$$\lambda_i = \mathcal{U}(0, 1) \quad (5.4.1)$$

We define $L = \text{diag}(\Lambda)$ with:

$$\text{diag}(\Lambda) = \begin{cases} l_{i,j} = x_i & \text{if } i = j \\ l_{i,j} = 0 & \text{if } i \neq j \end{cases} \quad (5.4.2)$$

We then generate a transfer matrix of an Hermitian matrix. We generate a 4×4 Hermitian matrix, $\mathbf{A} = (z_{ij} + z_{ij}^*)$, with $z_{ij} \sim \mathcal{CN}(0, 1)$, \mathcal{CN} being the complex normal distribution. The eigendecomposition of \mathbf{A} gives its transfer matrix \mathbf{U} . $\mathbf{R}^C = \mathbf{U}\mathbf{L}\mathbf{U}^{-1}$ is the covariance matrix of the clutter cell.

Since the covariance matrices are not biased toward any polarization, and we make no physical assumption on the target signature, the target used in those simulations has a constant signature in only one polarization $\mathbf{X}^{UAV}_i = (1, 0, 0, 0)$, with no loss of generality. We then compute the $P_{FA} - threshold$ and $P_D - threshold$ relationships according to the part 5.3.1.

5.4.2 . Simulation parameters

To run the simulation we create 16 bins with each $m = 2^{10}$ CMC, and we make $n = 2^{10}$ P_{FA} tests per CMC to estimate the $P_{FA} - threshold$ relationship. Which means we have $m \times n = 2^{20}$ tests per value of the effective rank. We can assess performances for a P_{FA} as low as $P_{FA} = 10^{-4} > \frac{100}{2^{20}}$. We assess the $P_D - threshold$ relationship with $n' = 1$ test per CMC, we have $m \times n' = 2^{10}$ tests to assess the $P_D - threshold$ relationship for each SCR, we measure a P_D as low as $P_D = 10^{-1} > \frac{100}{2^{20}}$. The reason why the lowest accurate P_D is lower, is that a detector with a P_D lower than 0.1 is not of interest, it allows to spare computing time. This is especially important since the estimation of the $P_D - threshold$ relationship has to be computed for each SCR.

5.4.3 . Simulation results

Figure 5.2 presents the probability of detection for each detector for a probability of false alarm of 10^{-4} as a function of the SCR and the effective rank. The performances of every detector are influenced by the effective rank of the covariance matrices. The performance of the span detector is the least affected by the effective rank of the clutter covariance matrix. The span performances (as represented by the P_D at a given P_{FA}) decrease with the effective rank, which means that span is better suited to high effective rank clutter (clutter similar to polarimetric white noise).

The span detector is identical to the srML with $\overline{\mathbf{R}^E} \propto I_4$, which is the case of the covariance matrix with effective rank 4 clutter in its own basis (Figure 5.3(d) shows that ML and span have near identical performances for clutter of effective rank 4). However, it is not true for a clutter with an effective rank inferior to 4, as the span does not filter any polarimetric backscattering process, it does not filter the dominant one, leading to

reduced performances as this process masks the targets in the detection test. However the loss of performances between the ideal case, effective rank of 4, and the worst cases, effective rank of 1, is low, it represents at most a loss of 1.8 dB of equivalent SCR.

All the other tested detectors exhibit an opposite behavior; they have better performances for low effective ranks than for high effective ranks. This is expected as the power of the clutter is concentrated in a smaller proportion of the total polarimetric space, thus, a larger portion of power of the target is in the orthogonal space of the clutter and thus not filtered.

For srML, the relationship between the performances and the effective rank for a given SCR is monotonous. The srML detector consistently outperforms the other detectors. Decreasing the effective rank results in better or equal performances. Between an effective rank of 1 and 4 the loss of equivalent SCR is substantial and represents 5.5 dB. In addition the worst SCR (worst means highest, since we want to be able to make detection at the lowest possible SCR) at which a P_D of 1 is attained is -0.5 dB which is the best SCR (conversely best means lowest) at which span attains a P_D of 1.

EVa and P-SIRV performances are not monotonous and while they exhibit performances similar to srML for the extreme values of the effective rank, their worst performances are not found for an effective rank of 4 but for effective ranks between 3 and 4.

5.4.4 . conclusion

When $\mathbf{R}^E = \mathbf{R}^C$ the effective rank impacts the performances of the polarimetric detectors: a minimal effective rank improves the performances of all the polarimetric detectors but the span. Figure 5.3 srML is the best detector in these simulations. However, the covariance matrices are not based on a physical modelling, and are not meant to be representative of a real clutter.

In the simulations we present in the rest of this part we use real data either in part (when we simulate to test the influence of the mismatch angle we use the measured eigenvalues) or in whole. Using real data means we have extracted the clutter with Doppler processing. Therefore we use the Doppler integration time that minimizes the effective rank. As shown in 4.4.4, the Doppler processing time influences the effective rank, and, in particular, a Doppler processing time of 10 ms minimizes the effective rank for a large number of polarimetric clutter range cells. Thus, we choose to use this Doppler processing time for the real data we use in the following simulations. This choice undermines the performances of the span detector over the other detectors, which could gain up to 2 dB of equivalent SCR if the effective rank was maximized. This decision of advantaging the other polarimetric detectors is justified by the fact that they can expect a greater improvement from the minimization of the effective rank than the improvement the span can get if we maximise the effective rank. In addition, we note that noise covariance matrix should have an effective rank of 4, thus maximizing the effective rank with integration time would most probably result in minimizing the CNR, essentially defeating the role of clutter in our study, by trying to detect the target against noise.

5.5 . Robustness of detectors with the covariance matrices mismatch

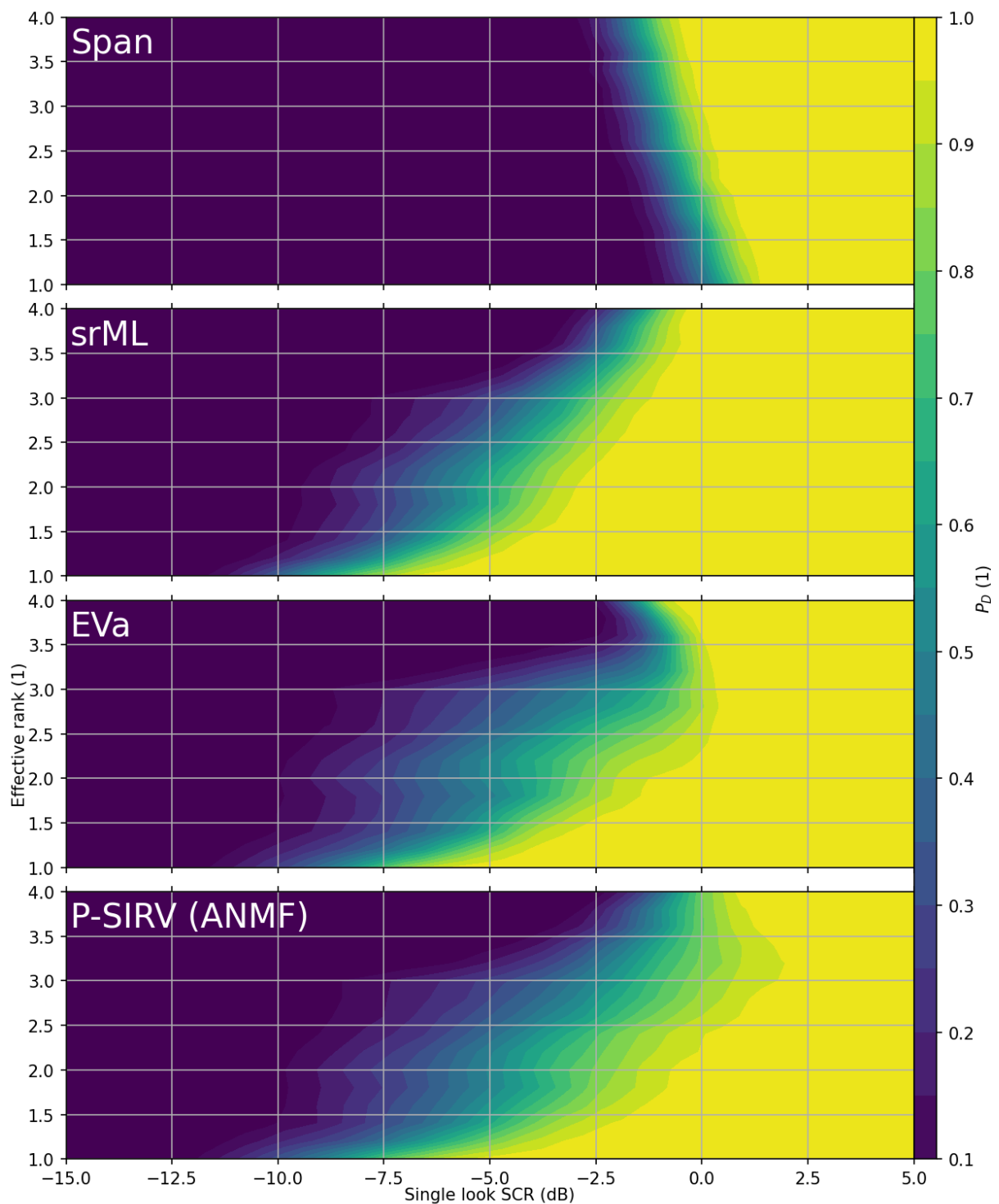


Figure 5.2: Probability of Detection (P_D) for the polarimetric detectors for a $P_{FA} = 10^{-4}$, as a function of the single look SCR of the target and the Effective rank of the covariance matrices of the CMC. 50 multilooks.

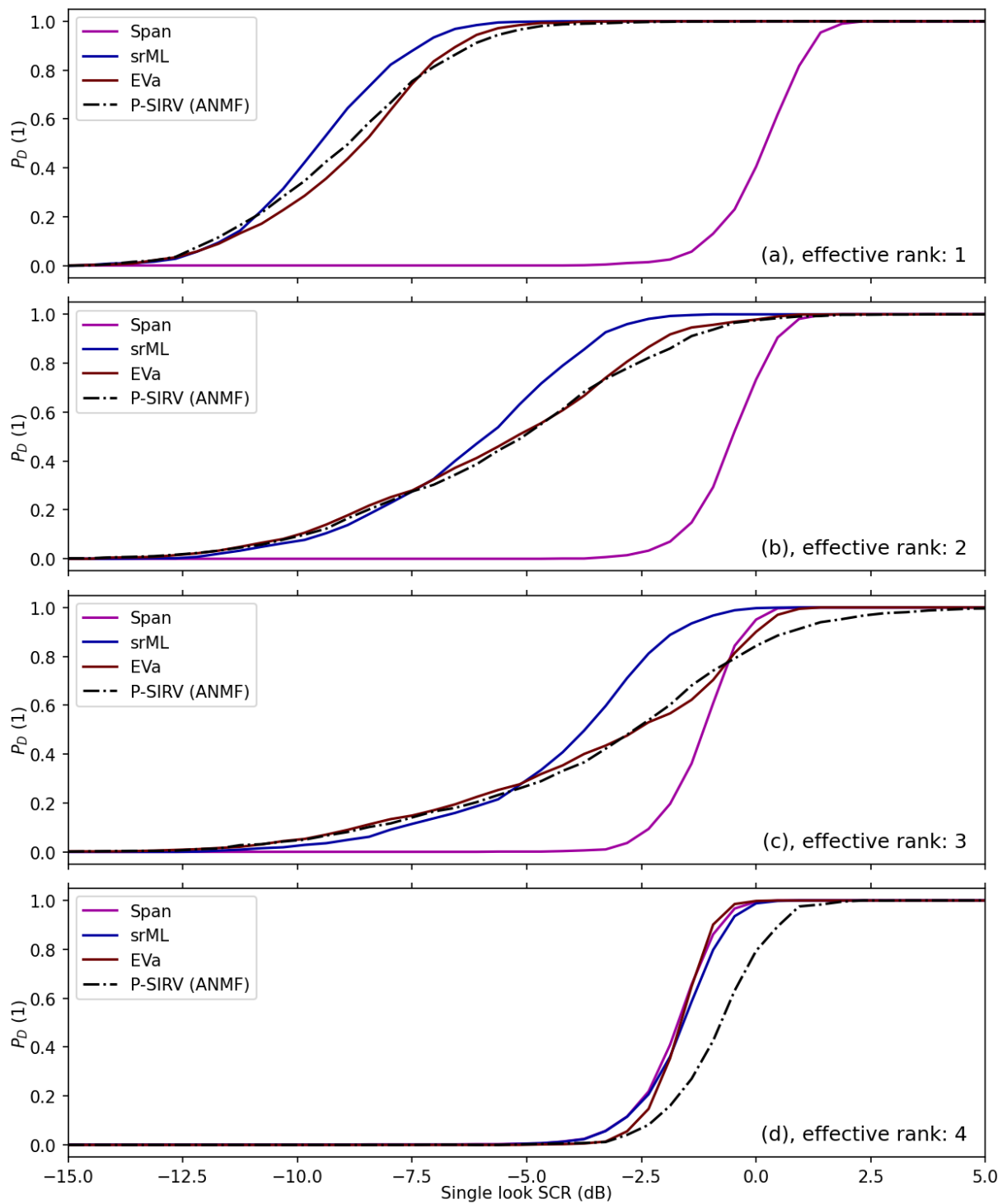


Figure 5.3: $P_D - SCR$ relationship for the polarimetric detectors for a $P_{FA} = 10^{-4}$, for the effective ranks of whole number effective rank of the CMC. 50 multilooks.

In 4.4.7 we introduced the mismatch angle as a metric to measure the misalignment between covariance matrices representing the polarimetric clutter properties. In this part, we assess the impact of the mismatch angle on the performances of the polarimetric detectors. We model the mismatch for a given eigenvalues distribution and the mismatch angle. We show a strong influence of the mismatch angle on performances for the P-SIRV and srML detectors, whereas the span and EVa detectors seem to have performances that are not correlated with the mismatch angle. The method presented in this part is the subject of a communication at the International Radar Conference 2022 in Edinburgh [Rozel et al. 2022a].

5.5.1. Generating the covariance matrix couples with mismatch

As we mentioned in 4.4.7 clutter cells at a given range have stationary eigenvalue distributions during time. As \mathbf{R}^E and \mathbf{R}^C are at the same range in our framework, they have the same eigenvalue distributions. The analysis of 4.4.7 points out that each eigenvalue of the covariance matrix is distributed with a log-normal distribution parametrized by the mean and standard deviation of the associated normal distribution.

Using the simulation process described in 5.3, we test detectors for two parameters, Θ and SCR. In this part Θ represents the cosine of the mismatch angle between the two matrices of the CMC, \mathbf{R}^E and \mathbf{R}^C . We recall that the cosine of the mismatch angle is given by:

$$\Theta = \cos\theta = \frac{\langle \mathbf{R}^E, \mathbf{R}^C \rangle}{\|\mathbf{R}^E\| \|\mathbf{R}^C\|} \quad (5.5.1)$$

\mathbf{R}^E and \mathbf{R}^C are the covariance matrices used to generate both clutters. \mathbf{R}^E gives us $\{\mathbf{X}^E_i\}_i$ the clutter dataset that the detector uses for the estimation of the clutter properties while \mathbf{R}^C is used to generate $\{\mathbf{X}^C_i\}_i$ the clutter dataset of the CUT.

We have $\tilde{\Lambda}$ the vector of with the mean of the four distributions, $\tilde{\Lambda} = (\tilde{\lambda}_i)_{i<4}$ and $\tilde{\sigma}$ the vector of the standard deviations $\tilde{\sigma} = (\tilde{\sigma}_i)_{i<4}$. For \mathbf{R}^E and \mathbf{R}^C we generate Λ^E and Λ^C their eigenvalue vector. We have:

$$\Lambda^E = (\lambda^E_i)_{i<4} \quad (5.5.2)$$

$$\Lambda^C = (\lambda^C_i)_{i<4} \quad (5.5.3)$$

With:

$$\lambda^E_i, \lambda^C_i = \text{lognormal}(\tilde{\lambda}_i, \tilde{\sigma}_i^2) \quad (5.5.4)$$

We define $\mathbf{L}^E = \text{diag}(\Lambda^E)$ and $\mathbf{L}^C = \text{diag}(\Lambda^C)$, and we generate transfer matrices \mathbf{U}^E and \mathbf{U}^C in the same way as defined in 4.3.1.

We then have:

$$\mathbf{R}^E = \mathbf{U}^E \mathbf{L}^E (\mathbf{U}^E)^{-1} \quad (5.5.5)$$

$$\mathbf{R}^C = \mathbf{U}^C \mathbf{L}^C (\mathbf{U}^C)^{-1} \quad (5.5.6)$$

This gives us one CMC. This CMC has a mismatch angle θ . We use the Metropolis-Hastings algorithm to have CMC in bins according to the cosine of their mismatch angle. A CMC in the i^{th} bin has its mismatch angle meeting the following condition:

$$\frac{i}{n} < \cos\theta < \frac{i+1}{n} \quad (5.5.7)$$

with n different bins. To favor CMC with a mismatch angle close to 0 - which are very rare with this sampling method - we use a resampling method detailed in appendix F. The matrices generated with this method follow the clutter properties as far as power is concerned, which means that their power can fluctuate as the power of the polarimetric clutter, and the CMC are rated according to their mismatch angle.

5.5.2 . Simulation parameters

To generate the bins of CMCs we need to use eigenvalues distributions, we use the eigenvalues distributions from the clutter cells presented in 4.4.8. These distributions are computed with the empirical SCM estimates in the corresponding range cells.

The we have the following eigenvalue distribution for the three clutter cells:

Clutter	Eigenvalue mean ($\hat{\Lambda}$, in dB)	Eigenvalue standard deviation ($\tilde{\sigma}$, in dB)
Farmland	(0, -10.7, -16.1, -19.4)	(2.4, 2.3, 1.7, 1.1)
Farmland and road	(0, -16.7, -22.0, -24.9)	(2.2, 2.1, 1.4, 0.9)
Urban	(0, -15.6, -17.3, -18.8)	(2.5, 1.0, 0.6, 0.6)

We run the simulation with parameters identical to the one we used in 4.3.2.1. I.e. 16 bins with each $m = 2^{10}$ CMCs, and $n = 2^{10}$ PFA tests per CMC, therefore we have $m \times n = 2^{20}$ tests per value of the mismatch angle. We measure P_{FA} as low as $P_{FA} = 10^{-4} > \frac{100}{2^{20}}$. We have $n' = 1$ test per CMC, therefore we have $m \times n' = 2^{10}$ tests we measure P_D as low as $P_D = 10^{-1} > \frac{100}{2^{10}}$.

5.5.3 . Results according to covariance matrix eigenvalue distributions

The results are presented in Figure 5.4, 5.5 and 5.6. These figures present the P_D for a P_{FA} of 10^{-4} as a function of SCR and the mismatch angle of the SCR. We can make several observations common to the three clutter. The performances of the P-SIRV and srML detectors correlate with the mismatch angle. All other parameters being equals, the higher the mismatch angle the lower the P_D is. conversely, the performances of span and EVa do not correlate with the mismatch angle.

This shows that for given eigenvalue distributions, the eigenvectors play an important role in filtering the clutter, thanks to its estimated covariance matrix, for P-SIRV and srML. However span and EVa seem to have stable performances even in case of strong mismatch. With Figure 5.7, 5.8 and 5.9, we see that in the range of expected mismatch (a cosine of the mismatch angle between 1 and the asymptotic mismatch measured in 4.4.7, Figure 4.35), the equivalent SCR losses varied 4 between 7 dB. However for farmland clutter and farmland and road clutter the performances of srML are better than those of span and EVa for all mismatch angles in the expected range, which suggests that for these two clutters, they are the best detector to use, even with the SCR losses associated with mismatch. For urban clutter the EVa outperforms the other detectors for all mismatch angles except angles lower 15° which makes it a good detector for this clutter type.

For farmland clutter and farmland and road clutter span and EVa perform similarly.

5.5.4 . Conclusion

This simulation show that the mismatch angle plays an important role in the performances of the srML and P-SIRV. Important gains of performances are obtainable with closely matched CMC when using these detectors.

The performances of the polarimetric detectors presented vary with the eigenvalue distributions used in the simulations. For the farmland clutter, the srML detector outperforms the other detectors for almost every mismatch angle, which means they are the best detectors to use in this case. Conversely, for urban clutter the EVa detector outperforms all the other detectors for all mismatch angles but 0 (cosine of 1) which means it is the best detector for this case. However, for the road and farmland no detector consistently outperforms the others for every mismatch angle. These simulations give a link between the mismatch angle and the performances of the detectors. We propose a method to then project these results on the mismatch angle measured on the real data of those clutter range cells.

5.5.5 . Assessing the best performing detector

Framework

For each clutter range cell, we established $\bar{D}(\delta t)$ in 4.4.7. $\bar{D}(\delta t)$ gives the value of $\cos\theta$, the polarimetric mismatch between two covariance matrices estimated at different times, and δt , the time interval separating the matrices. $\bar{D}(\delta t)$ gives us an estimation of the mismatch between the clutter under the target and the clutter estimated for the detector test. For given P_{FA} and P_D , we can write the minimum SCR needed for a detection as a function of $\cos\theta$, the cosine of the mismatch angle. Given these relationships we can estimate the SCR as a function of the time interval δt for each detectors. We expect that the minimum SCR required to a make a detection for a given P_{FA} and P_D will increase with the time interval.

Results

Figure 5.10, 5.11 and 5.12 present the minimum SCR for a detection with $P_{FA} = 10^{-4}$ and $P_D = 0.95$, for each clutter.

Farmland clutter We see that for the farmland clutter the srML consistently outperforms the other detectors for all time intervals. They have identical performances. For time interval greater than 4 s, approximately thrice the decay time of the exponential fit on $\bar{D}(\delta t)$ in 4.4.7 and Figure 4.35 (1.35 s), the SCR is stable for all detectors. EVa and span have mostly constant performances with time, as their performances were mostly independent from the mismatch.

These results suggest we should use the srML in this clutter range cell. Moreover to maximize the performance we should make covariance matrix estimation as frequently as possible to eliminate the effect of the decay of the cosine of the mismatch angle. If we do not minimize the mismatch, with frequent estimations the srML can loose up to 2.5 dB of equivalent SCR

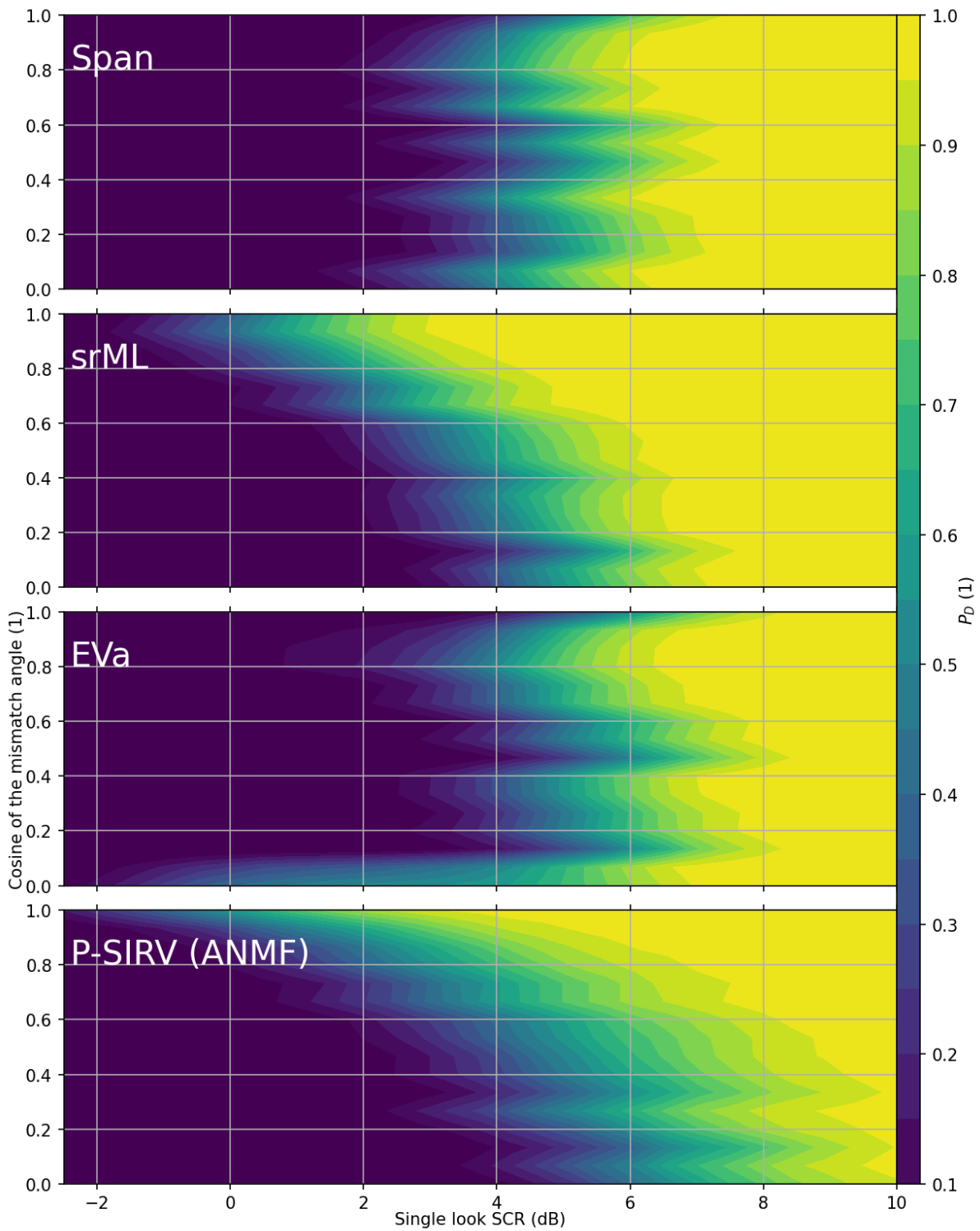


Figure 5.4: Performances of the polarimetric detectors as a function of the SCR and cosine of the mismatch angle for a P_{FA} of 10^{-4} for the farmland clutter.

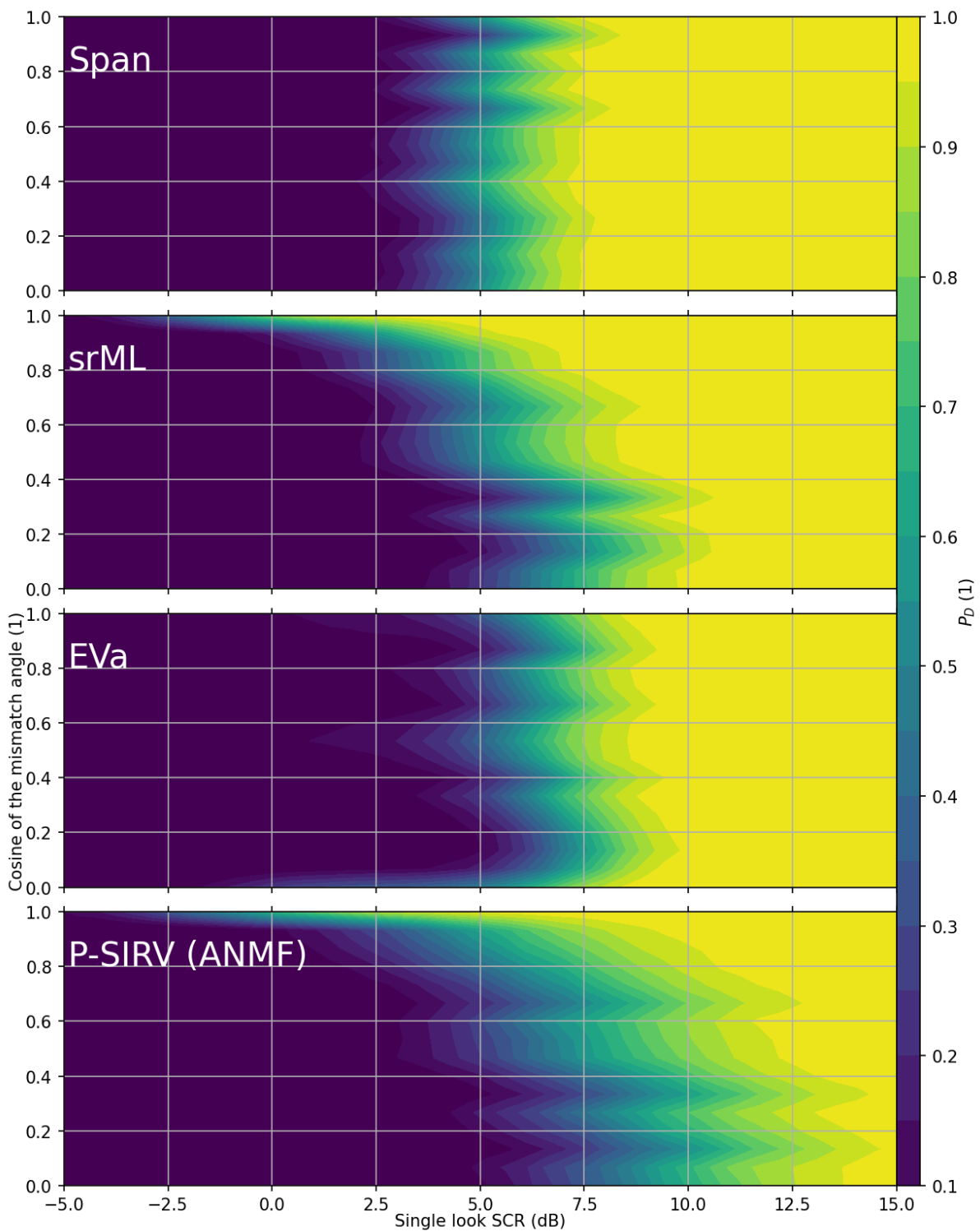


Figure 5.5: Performances of the polarimetric detectors as a function of the SCR and cosine of the mismatch angle for a P_{FA} of 10^{-4} for the farmland and road clutter.

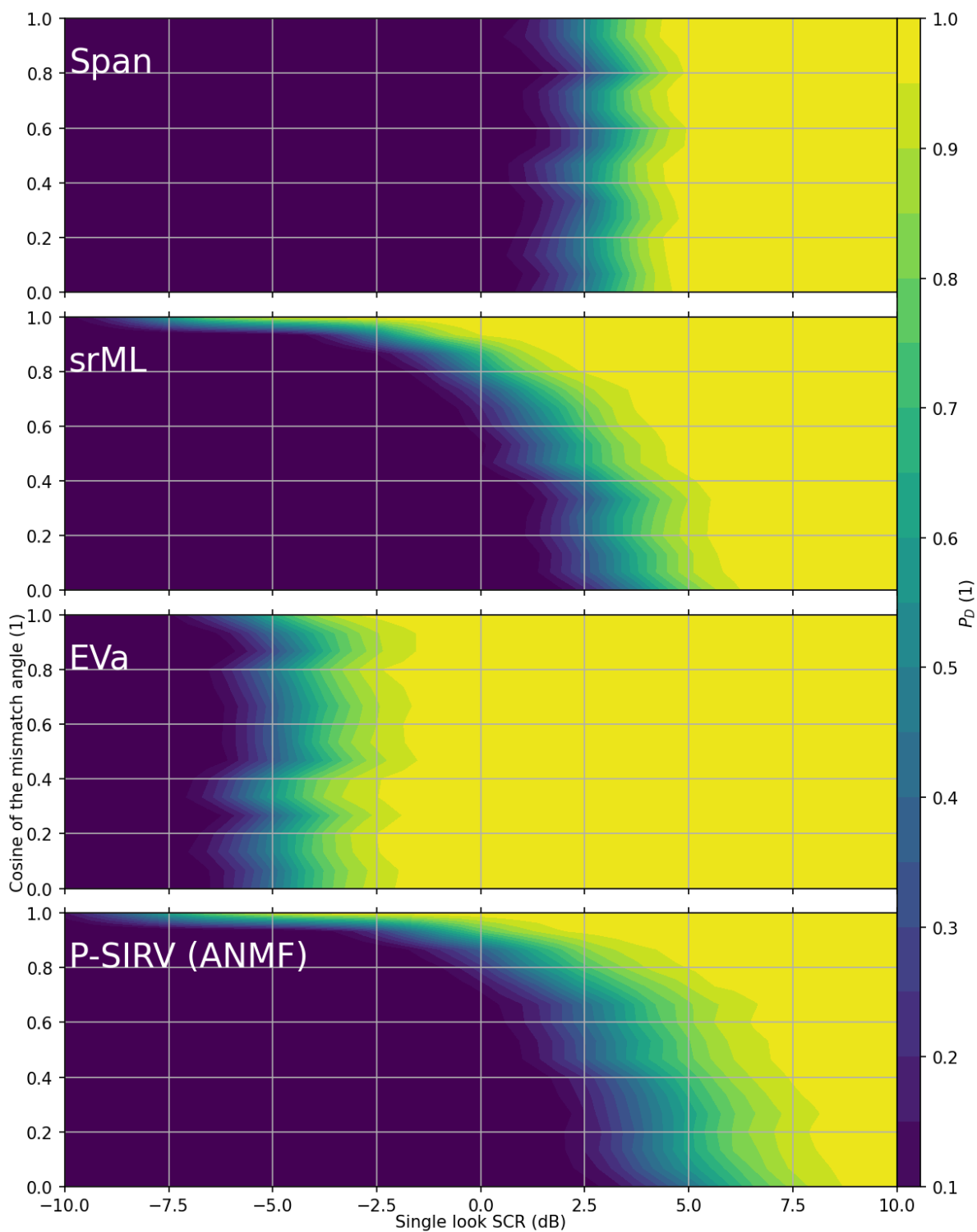


Figure 5.6: Performances of the polarimetric detectors as a function of the SCR and cosine of the mismatch angle for a P_{FA} of 10^{-4} for the urban clutter.

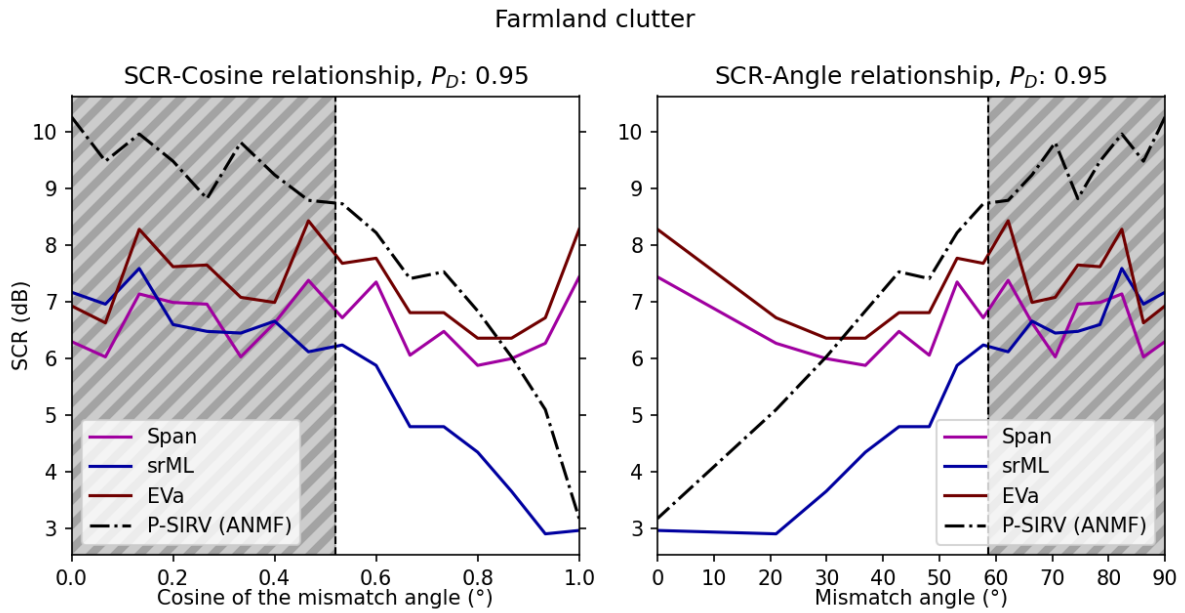


Figure 5.7: Performances of the polarimetric detectors for a P_{FA} of 10^{-4} and P_D of 0.95 for the farmland clutter. It shows the SCR needed to achieve a P_D of 0.95 with a P_{FA} of 10^{-4} as a function of mismatch angle (and its cosine).

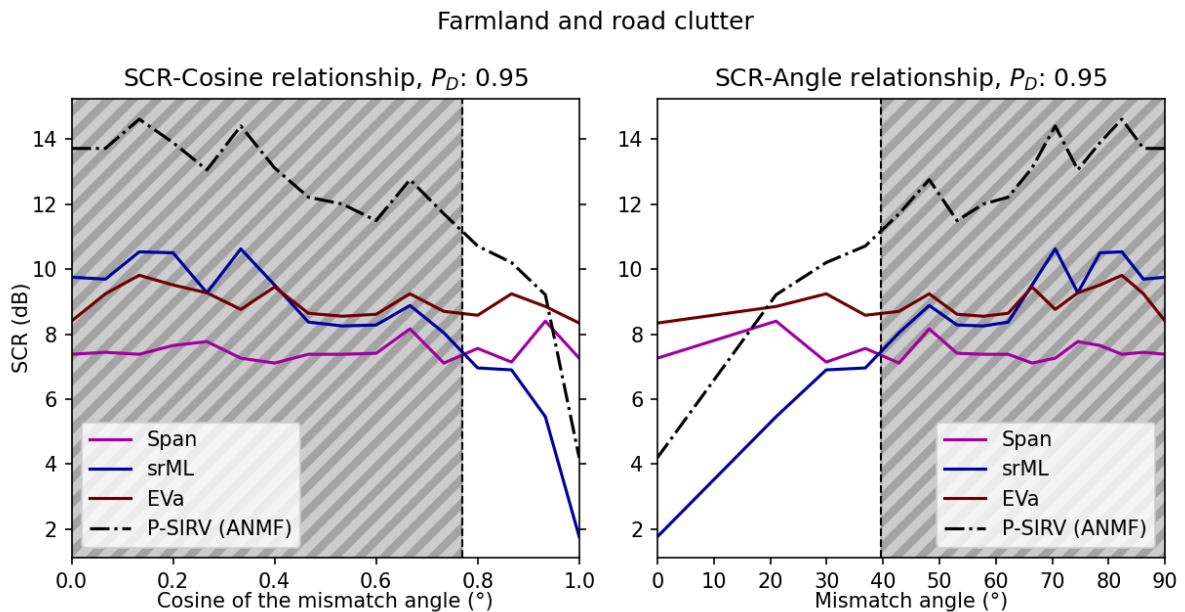


Figure 5.8: Performances of the polarimetric detectors for a P_{FA} of 10^{-4} and P_D of 0.95 for the farmland and road clutter. It shows the SCR needed to achieve a P_D of 0.95 with a P_{FA} of 10^{-4} as a function of mismatch angle (and its cosine).

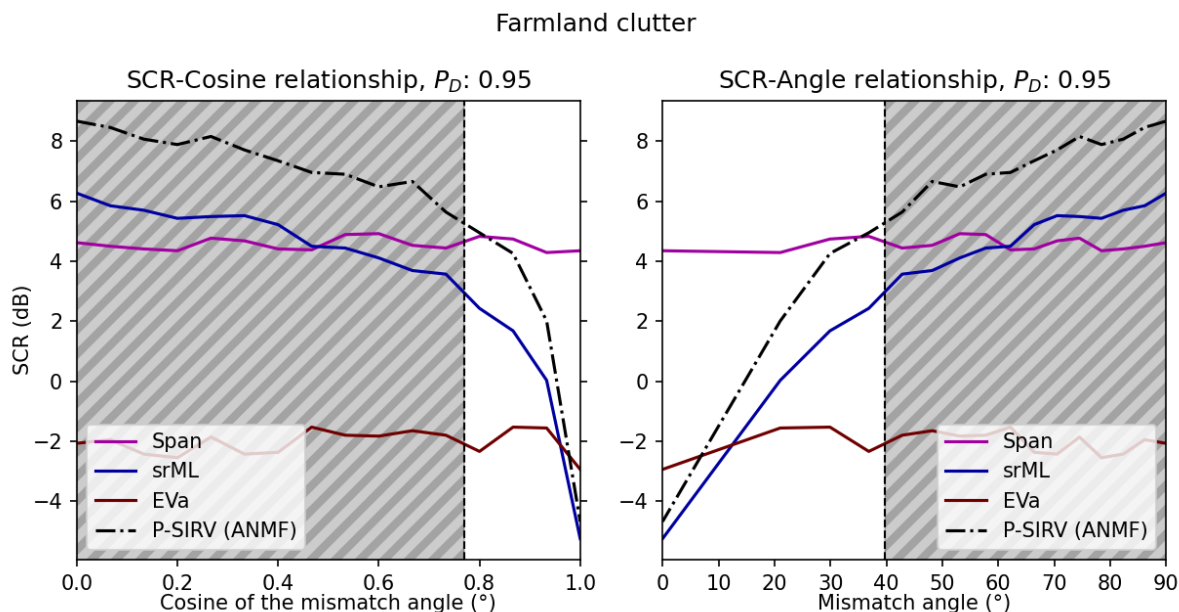


Figure 5.9: Performances of the polarimetric detectors for a P_{FA} of 10^{-4} and P_D of 0.95 for the urban clutter. It shows the SCR needed to achieve a P_D of 0.95 with a P_{FA} of 10^{-4} as a function of mismatch angle (and its cosine).

Farmland and road clutter In the farmland and road clutter, we again see that the srML outperform the other detectors for all time intervals. However, for time intervals greater than 3.5 s, the span performance converges with the performances of the srML. For time intervals in excess of 4 s, approximately equal to the decay time measured in Figure 4.35 (3.68 s), the performances of the detectors are stable.

Similarly to the results of the farmland clutter, the results for the farmland and road clutter show that we should use the srML. Reducing the time interval between the detection and the estimation of the SCM will also lead to better performances in this clutter range cell. In this range cell the effect of the mismatch on the srML is a loss of equivalent SCR up to 3 dB.

Urban clutter In the urban clutter, EVa outperforms every other detectors for every possible time intervals. For low time intervals srML and EVa have roughly the same performances, but as time intervals increase the performance gap widens. The performances of the detectors stabilize for time intervals greater than approximately 8 s which corresponds with the decay time measured in Figure 4.35.

In urban clutter the detection scheme we should adopt is different, as the EVa detector outperforms the other detectors. As the performances of EVa are not affected by the time interval between the estimation and the detection, we can make unfrequent estimations and expect good performances. This scheme provides advantages as less frequent estimations are less constraining for processing units and avoid the risk of using secondary data polluted by an undetected target.

5.5.6 . Conclusion

The study of expected performances of the different detectors as a function of the time interval allows us to choose the detection scheme for the studied clutter cells.

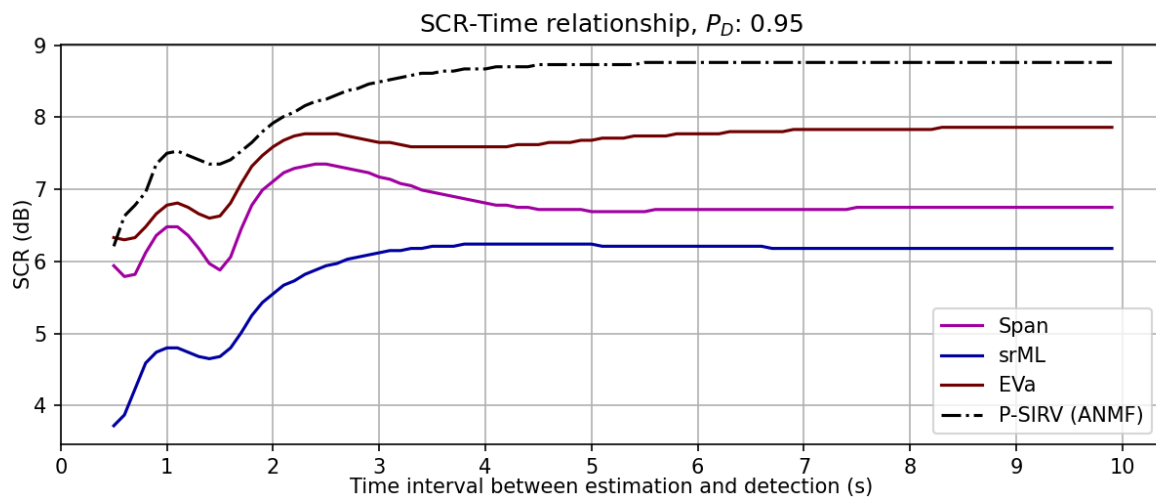


Figure 5.10: Extrapolation of the performances for the farmland clutter.

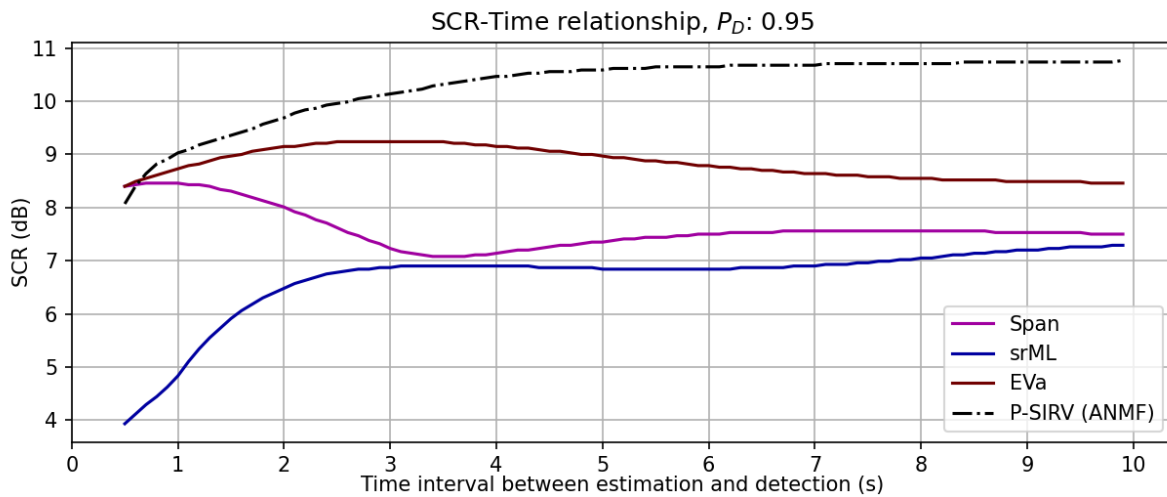


Figure 5.11: Extrapolation of the performances for the farmland and road clutter.

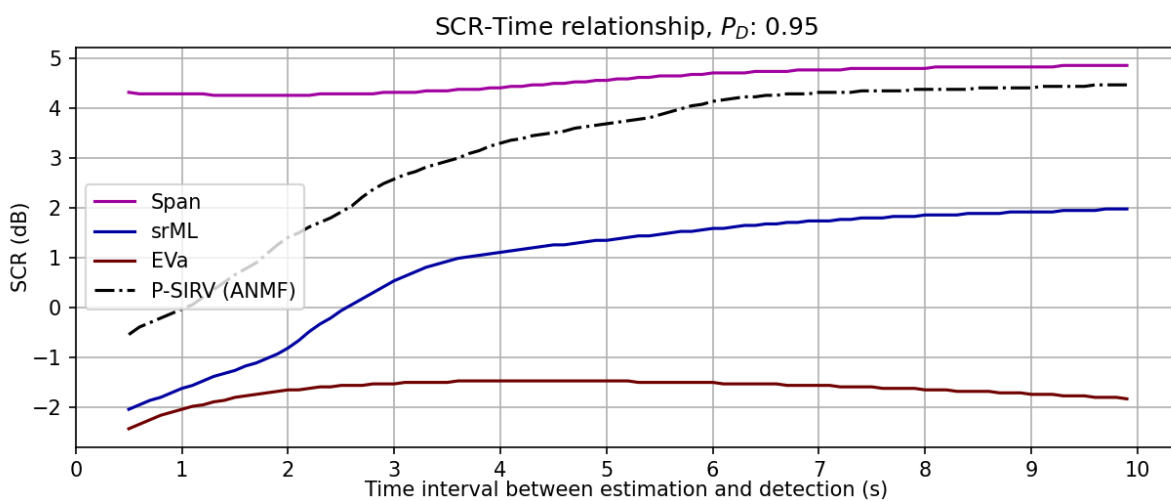


Figure 5.12: Extrapolation of the performances for the urban clutter.

Either a detection scheme relying on a detector that is affected by mismatch (srML) and frequent estimation of the clutter in order to minimize the mismatch, or using a detector independent from mismatch (Eva in our case), allowing for less frequent estimations.

Moreover we notice that the predicted performances of all the detectors stabilize after 4 to 8 s. For the farmland clutter it corresponds to three times the decay time measured in 4.4.7, which means the stabilization of the performances is mainly due to the stabilization of the mismatch. Whereas, for the urban clutter and for the farmland and road clutter, the stabilization occurs for time interval comparable to the measured decay time, which means that there is further stabilization due to SCR-Cosine relationship shown in Figure 5.8 and 5.9. We see that the SCR-Cosine relationship stabilizes for greater cosines (lower mismatch) for this clutter range cells.

In these simulations we ensured that the eigenvalues of the covariance matrices were based on the empirical properties of the clutter studied, however the eigenvectors were purely synthetic and did not use any empirical model. To check if the results hold with the actual eigenvectors and eigenvalues of the clutter tested we propose an hybrid simulation method.

5.6 . Hybrid simulations

In this part, we compare the performances of the polarimetric detectors as well as the mono-polarimetric detectors. The simulation we present do not use any parametric model for the clutter or the target. The model used for the clutter data is based on estimated SCMs from the clutter data of the measurement campaign described in 4.2. These SCMs are used to generate new clutter data, identically distributed to the real clutter. The target data are extracted from the same measurement campaign using the method described in appendix G. The SCR is changed in order to simulate for different SCR. These simulations allow us to avoid any bias linked to an unfaithful model of either the clutter or the target, and the method used provides a potential framework for the adaptive evaluation of detectors.

5.6.1 . Working principle

In the simulations we present in this part, the CMC is composed of two SCMs measured in a range cell of the clutter of the measurement campaign. For a given range cell we have $\mathbf{R}^E = \bar{\mathbf{R}}(t)$, with $\bar{\mathbf{R}}(t)$ the SCM estimate of the clutter cell at the time t . \mathbf{R}^C is SCM estimates measured at ulterior time $\mathbf{R}^C = \bar{\mathbf{R}}(t + \delta t)$. The parameter in Θ in these simulations is δt , the time interval between the two SCMs estimates. To form the bins of CMC, we select a range cell. For this range cell we compute the SCM estimates for different times and create the CMC with the couples sharing the right value of δt .

The ideal method would consist in using directly the clutter datasets measured with the measurement campaign. Unfortunately the duration of the measurement, 825 seconds, mean that we have at most 1650 non-overlapping clutter datasets, which would allow at most the measurement of a $P_{FA} < \frac{100}{1650}$, which is not a realistic value for any radar operation (With a 2 Hz refresh rate, the operator would experience a false alarm every 50 seconds per range cell).

To address this issue we generate additional clutter cell with the SCM estimates, hence $\mathbf{R}^E = \bar{\mathbf{R}}(t)$ and $\mathbf{R}^C = \bar{\mathbf{R}}(t + \delta t)$ as we recall that the CMC $(\mathbf{R}^E, \mathbf{R}^C)$ is used to

generate the two clutter datasets used in the detector tests.

As for the target used in the detector test, we use parts of the UAV signature extracted from measurement campaign (part 4.2). For a clutter dataset we use the same target in all the detector tests to ensure the detectors are always tested in the same conditions. Each set of test aimed at determining the P_D is repeated for several extracts of the polarimetric signature of the UAV.

5.6.2 . Simulation parameters

The values of tested δt in second are:

$$\{0.5, 1, 2, 3, 4, 5, 6, 7, 8, 9, 10, 20, 30, 40, 50\} \quad (5.6.1)$$

These values are chosen in a pseudo logarithmic way to investigate a large portion of the parameter space at a lower computational cost.

Each bin has $m = 2^{10}$ CMCs measured over 562 seconds (\mathbf{R}^E are measured other 512 seconds and \mathbf{R}^C are measured over 512 seconds as well, but with an offset going from 0.5 s to 50 s compared to \mathbf{R}^E). We do $n = 2^{10}$ P_{FA} tests per CMC, therefore we have $m \times n = 2^{20}$ tests per value of δt . We measure P_{FA} as low as $P_{FA} = 10^{-4} > \frac{100}{2^{20}}$. We have $n' = 1$ test per CMC and per target, therefore we have $m \times n' = 2^{10}$ tests per target signature, we measure P_D as low as $P_D = 10^{-1} > \frac{100}{2^{10}}$. We test the detectors for 120 different target signatures randomly selected in the extracted target signal.

5.6.3 . Simulation results

The clutters used to run the detector tests we present in this part are the clutter cells presented in 4.2. A summary of the properties of these clutters is found in 4.4.8. Figure 5.13, 5.14 and 5.15 give an overview of the results obtained for the 3 different clutters and each results. For each clutter and detector they show the P_D with $P_{Fa} = 10^{-4}$ as a function of the SCR and the time interval. Good performance of a detector is its ability to attain high P_D at low SCR. The P_D value is the median of the P_D values obtained for each the detector tests over the different target signals tested.

Link between time and performances

Figure 5.16, 5.17 and 5.18 show the minimum SCR necessary to have $P_D \geq 0.95$ with $P_{FA} = 10^{-4}$ as a function of the time interval for each polarimetric detector. The line corresponds to the median P_D over the different target signals used for the test. The upper and lower bounds represent the upper limit of the first and third quartiles, they show the variability of the performances of the detector with the target.

The performances of every polarimetric detector roughly correlates with the time interval, except for EVa in the urban clutter. The best performance is always (except for EVa in the urban clutter) for a time interval 0.5 s, the shortest possible (Figure 5.16, 5.17 and 5.18).

The two peaks present at 7 and 9 seconds are present because of parasitic frequency detected in the radar signal around 1/8 Hz.

These results are different from the one we obtained with the previous simulation framework, in which the mismatch was modeled with the mismatch angle and the data were synthetic. With this framework EVa and span performances were independant from the mismatch angle and thus independant from time interval (see 5.5.5). This

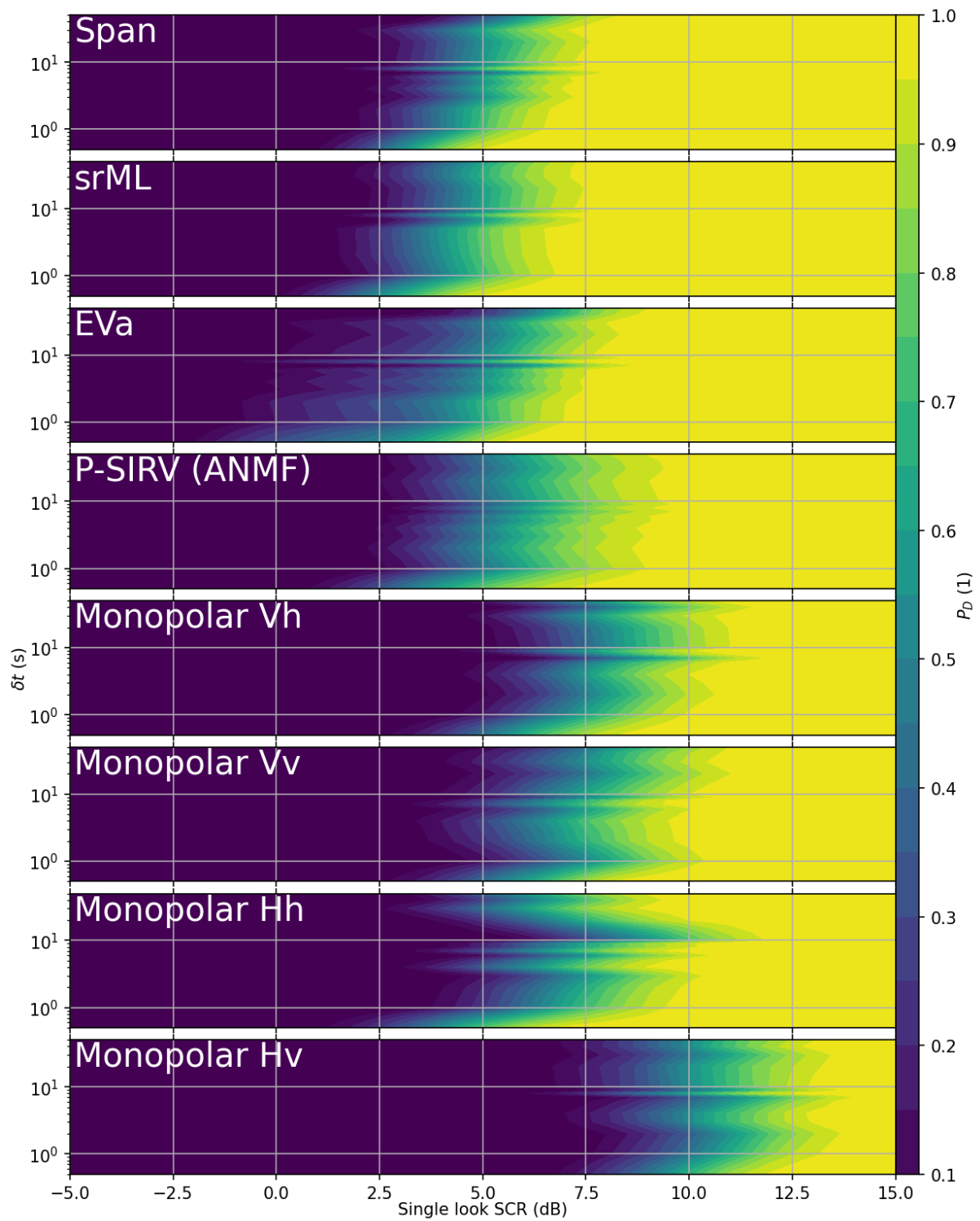


Figure 5.13: Performances of each detector for the farmland clutter with $P_{FA} = 10^{-4}$.

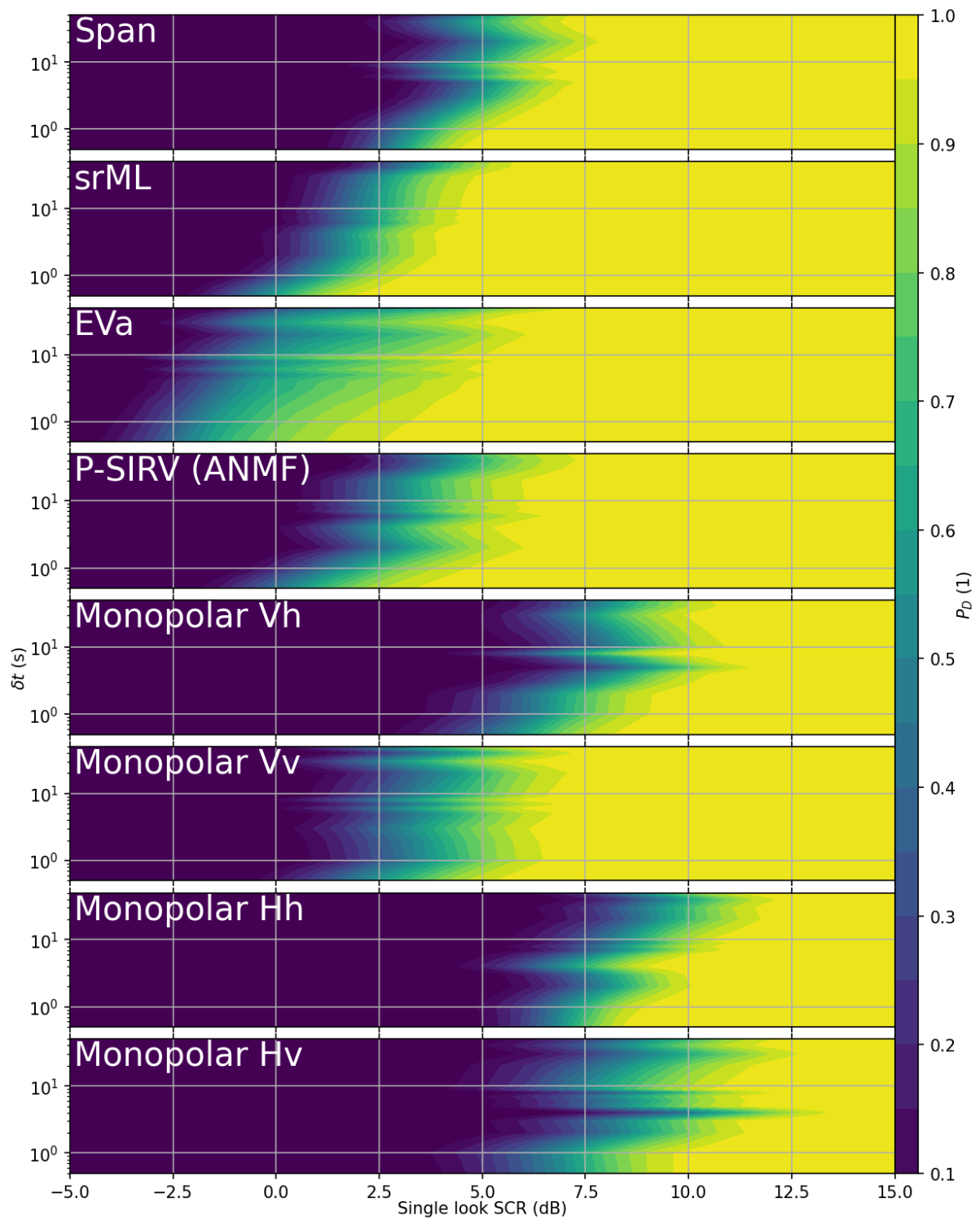


Figure 5.14: Performances of each detector for the road and farmland clutter with $P_{FA} = 10^{-4}$.

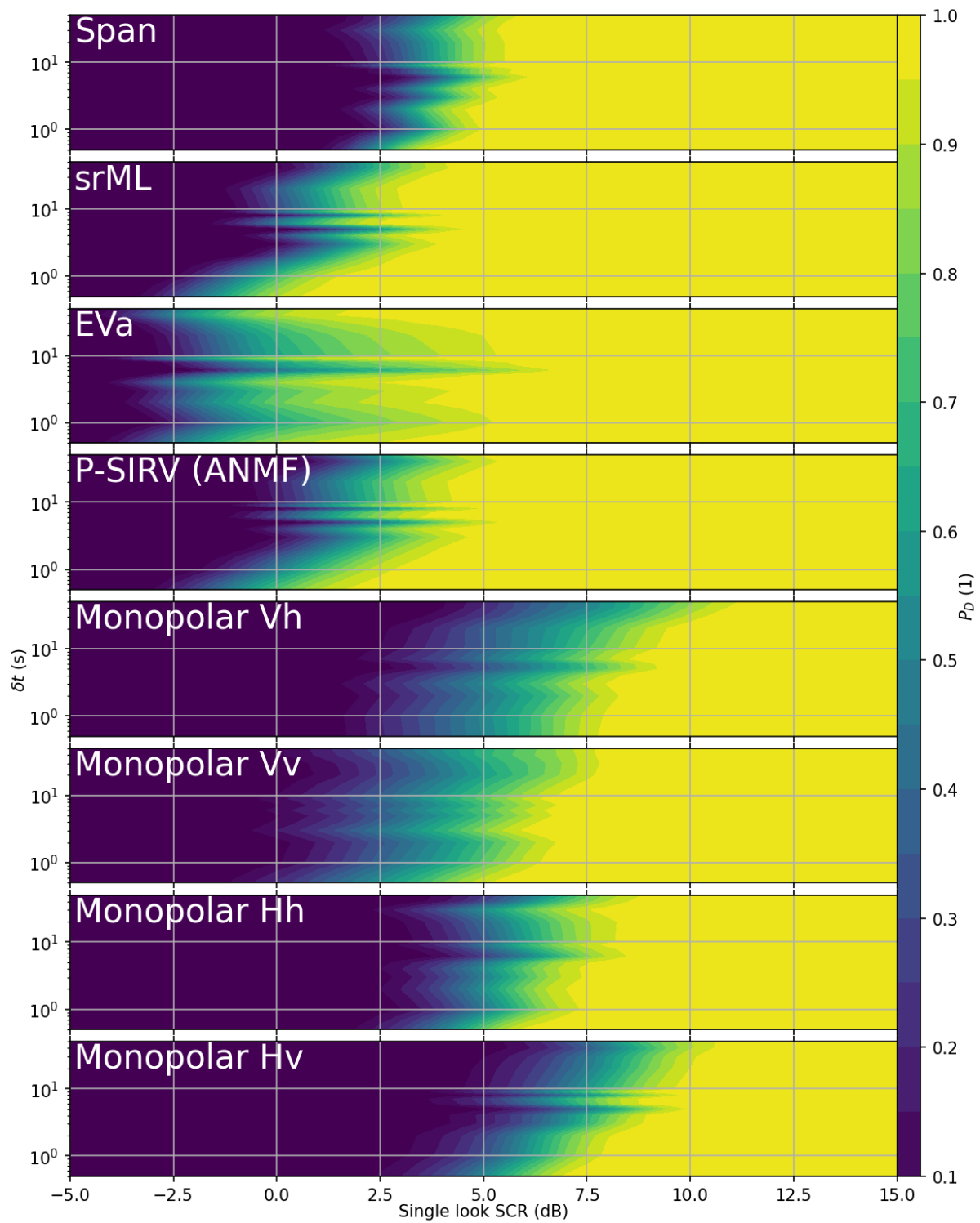


Figure 5.15: Performances of each detector for the urban clutter with $P_{FA} = 10^{-4}$.

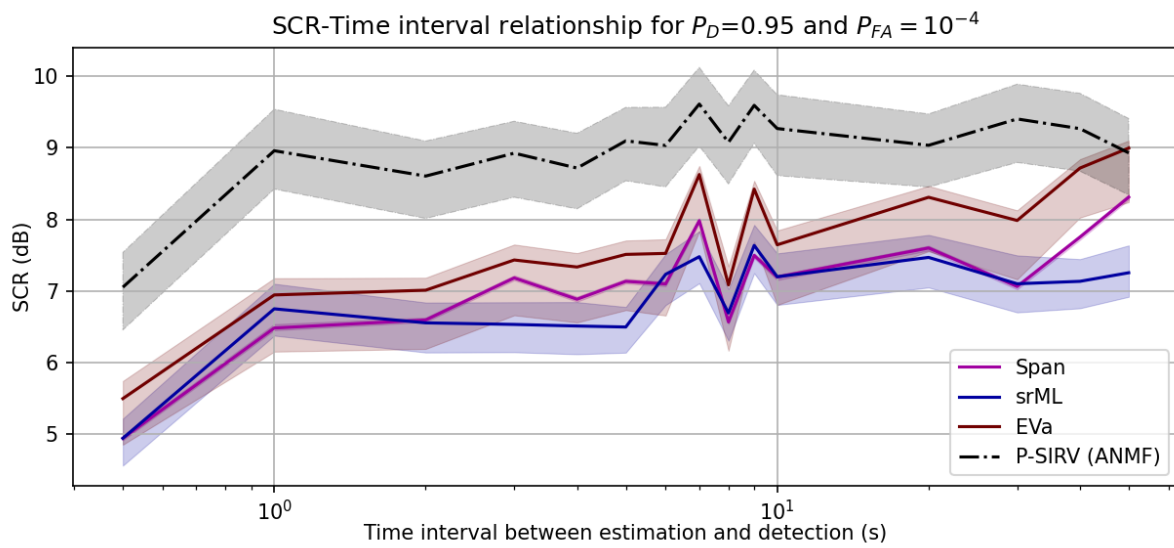


Figure 5.16: Performances of each detector for the farmland clutter with $P_{FA} = 10^{-4}$ and $P_D = 0.95$.

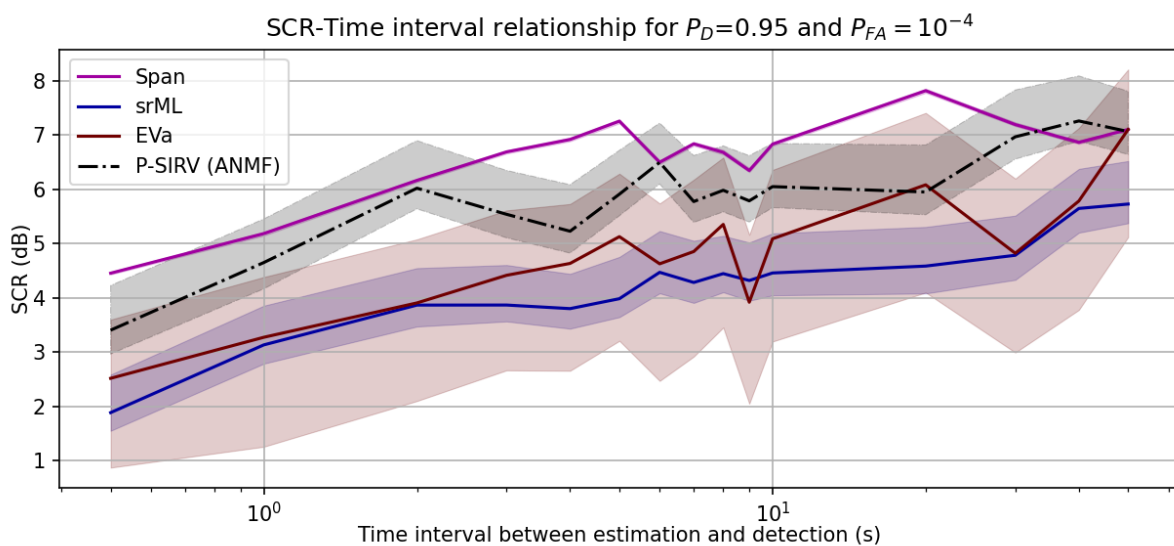


Figure 5.17: Performances of each detector for the road and farmland clutter with $P_{FA} = 10^{-4}$ and $P_D = 0.95$.

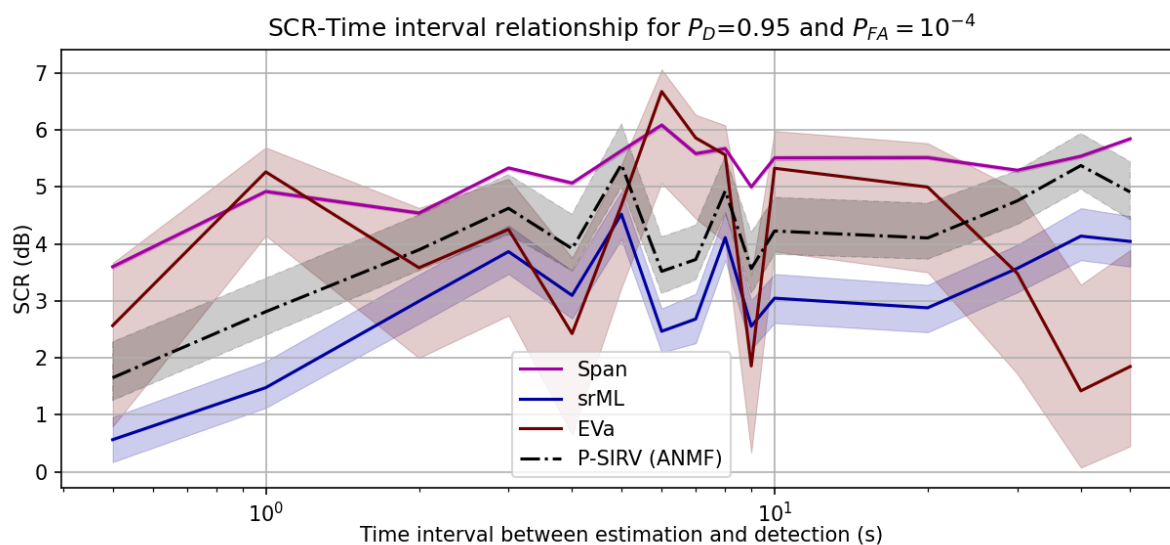


Figure 5.18: Performances of each detector for the urban clutter with $P_{FA} = 10^{-4}$ and $P_D = 0.95$.

is not the case with the simulation framework described in this part. It means that even the clutter properties on which the span and EVa rely for making accurate detections change with time in the studied clutter. Furthermore the EVa detector has highly variable performances for farmland and road clutter as well as urban clutter. The modelization described in 5.5 is not able to fully explain the behavior of EVa, as the target was constant. The constant target signature is advantageous to the EVa detector, as the target is rank 1 and constant.

These results suggest that any polarimetric endo-clutter detection following the detection framework we describe should minimize the time interval between the clutter estimation and the detection test.

Comparison between mono-polarimetric and multi-polarimetric detectors

Mono-polarimetric detectors are consistently outperformed by multi-polarimetric detectors (Figure 5.13, 5.14 and 5.15). This result is expected as the main advantage of mono-polarimetric detectors is that they can be implemented on mono-polarimetric radar, which all else, being equal, will provide data with higher SNR. In our case the SNR is a lot higher than the SCR and thus not limiting. Mono-polarimetric radars do not have higher SCR than multi-polarimetric radar as explained in 2.3.1. Figure 5.19, 5.20 and 5.21 show the difference of performances between the best performing mono-polarimetric detector of each clutter and srML (which is always the best polarimetric detector or very close to the best). For a time interval of 0.5 s the loss of equivalent SCR ranges from 2 dB for farmland clutter (Figure 5.19) to 4 dB for urban clutter (Figure 5.21).

Comparison of the results between hybrid simulation and mismatch angle simulation

We compare the results obtained with the hybrid simulations described in this part to the results of the simulations using the mismatch angle (described in 5.5), in par-

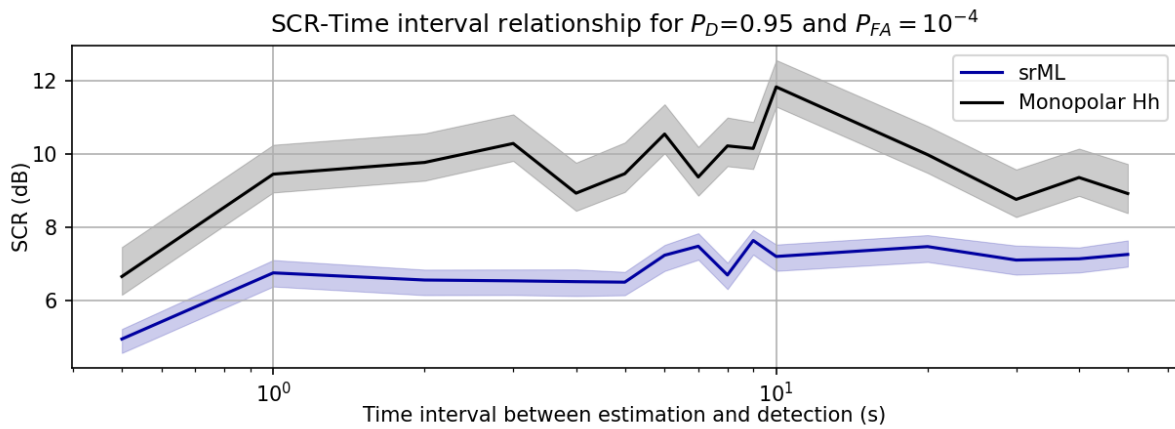


Figure 5.19: Performances of each detector for the farmland clutter for $P_{FA} = 10^{-4}$ and $P_D = 0.95$.

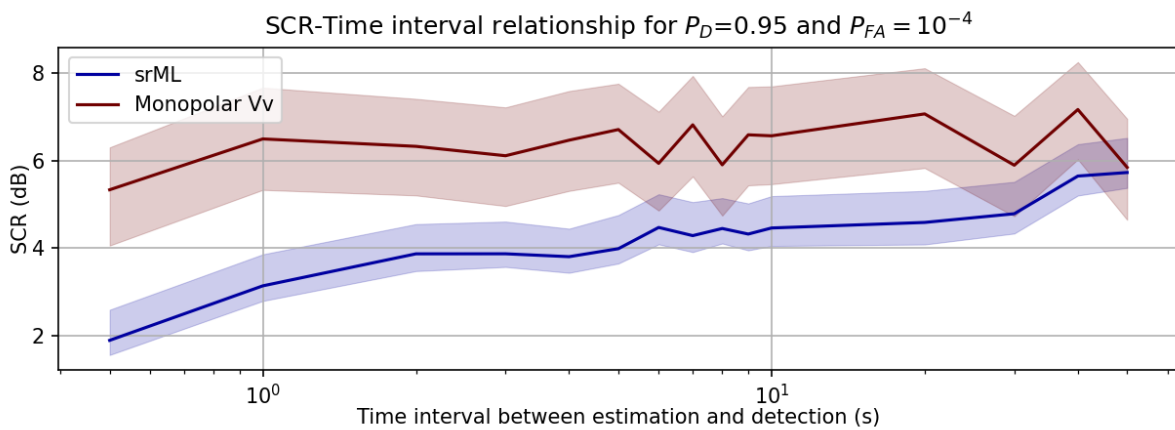


Figure 5.20: Performances of each detector for the road and farmland clutter for $P_{FA} = 10^{-4}$ and $P_D = 0.95$.

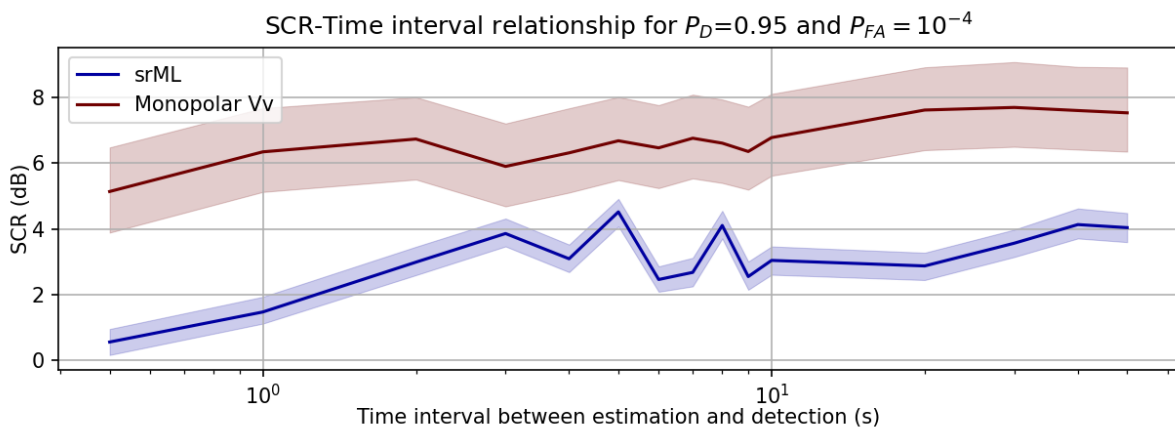


Figure 5.21: Performances of each detector for the urban clutter for $P_{FA} = 10^{-4}$.

particular the results shown in 5.5.5. We notice that the results for the srML are closely matched in farmland (Figure 5.10 for mismatch angle simulation and Figure 5.16 for hybrid simulation) and farmland and road clutter (Figure 5.11 for mismatch angle simulation and Figure 5.17 for hybrid simulation). The difference in simulated performances are within 2 dB. This is not the case for urban clutter and the other detectors. In urban clutter the performances have at least 3 dB of difference. P-SIRV was consistently underperforming in the mismatch angle simulations - with 2 to 3 dB higher SCR needed to achieve the same P_D and P_{FA} - compared to srML (Figure 5.10, 5.11 and 5.12). With the hybrid simulations, especially in farmland and road and urban clutter (Figure 5.17 and 5.18) the performance gap is smaller. The performances of span and EVa obtained with mismatch angle simulations and hybrid simulations are dissimilar. With the mismatch angle simulations, span and EVa have stable performances with regards to the time interval, less than 1 dB of variation (Figure 5.10, 5.11 and 5.12). However, with hybrid simulations the variation of performances are a lot larger, up to 5 dB (Figure 5.16, 5.17 and 5.18). This is linked with the fact that performances of EVa and span obtained hybrid simulations correlate with the time interval contrary to the ones obtained with mismatch angle simulations.

Variability of the performances with the target signal used in the detector test

As Figure 5.16, 5.17 and 5.18 show the median SCR necessary to have $P_D \geq 0.95$ with $P_{FA} = 10^{-4}$ as well as the first and third quartiles upper bound of SCR we can see how much the target signature affects the detectors performances.

Span has very consistent results over the different target signals in the detector tests. This is expected as we recall that span is used to define the SCR (see equations 5.1.5 and 2.6.3), thus, the span directly follows the SCR whichever the target polarimetric signature is. In this paragraph when we mention multi-polarimetric detector we exclude span as it behaves differently due to the SCR computation method. In farmland clutter the difference between the upper bounds of the first and third quartiles is similar for the multi-polarimetric detectors, around 1 dB (Figure 5.16). We note that the distribution of performances of EVa with respect to target signal is highly dissymmetric, as the upper limit of the third quartile is close to the median whereas the upper limit of the first quartile is almost 1 dB lower. For farmland and road clutter and urban clutter (Figure 5.17 and Figure 5.18), the upper limits of the first and third quartile are also around 1 dB apart for srML and P-SIRV. However EVa has a large dispersion of results with the target signal of the detector test, which means that the EVa detector is unpredictable and target signature dependant. This is probably due to the fact that target signal affect the eigenvalues of $\{\mathbf{X}_i\}_i$, the tested signal in inconsistent ways, depending on the respective target and clutter signature (whether or not they are "aligned"). In the theoretical simulations, the target signature was constant and, thus, necessarily rank 1, in the mismatch angle simulations (described in 5.5) it obfuscated this result and overestimated the performances of EVa.

Variability of the performances with the target clutter

These simulations show that for the same P_D , P_{Fa} , time interval and detector we can expect significantly different performances (as have shown the mismatch angle simulations). The SCR required for the same detection performances is significantly higher for

farmland clutter than road and farmland clutter and urban clutter, up to 4.5 dB more. Farmland is less favorable for endo-clutter polarimetric detections than urban clutter or farmland and road clutter. This is probably in part a consequence of its higher effective rank (as shown in 5.4) which makes it harder to filter out due to the smaller rank of the space orthogonal to the polarimetric signature of the clutter. This method is a good predictor of the performances that can be expected for a given detector in a given clutter range cell.

We note that, in the hybrid simulations, the EVa detector can achieve low P_D , around 0.2 / 0.3, at lower SCR than the other detectors (around 2 dB lower). However this fact should not influence our choice of detector since such low probabilities of detection are not useful for radar operations as $P_D = 0.3$ means that most detections are missed.

5.6.4 . Drawing conclusion from the hybrid simulations

With the results of the hybrid simulations we can draw several conclusions.

Mono-polarimetric detectors should not be used when dealing with endo-clutter detections as they are consistently outperformed by polarimetric detectors.

The time interval between the clutter estimation and the detection should be kept as low as possible to maximize polarimetric detectors performances. If we follow this rule srML is consistently the best performing detectors for desirable P_D (above 0.9), and should probably be the detectors of predilection with this detection framework, as far as the explored clutter range cells are concerned.

Span and EVa are not more robust to the covariance matrices mismatch than P-SIRV and srML detector as the results of 5.5 seemed to indicate. The strong hypothesis on the target signature made in 5.5, its constant signature leading to a rank 1 signature and a target returning a constant power to the detector are probably the cause of this discrepancy.

EVa has inconsistent performances with regards to the signals of the target, and its performances were overestimated by the mismatch angle simulations described in 5.5. This is, once more, probably due to the target modelization with a constant signature.

Finally, the hybrid simulation method is able to predict the performances of the polarimetric detectors in different clutter. This method could serve as basis for an adaptive detection scheme which could switch between detectors to better suit the encountered clutter and adapting the detection scheme to each clutter range cells. We propose performing similar simulations to those we described at the beginning of the radar operation in order to choose the best detector. This framework could be used for any detector even in non-gaussian clutter. In our 3 examples srML seems to be the one to choose but maybe this might not always be the case.

Chapter 6 |

Conclusions and perspectives

In this part we conclude this PhD thesis by summarizing the main results of this work and giving perspective on following works. In this thesis we introduce methods and metrics to characterize the clutter in low-grazing angle configuration and show that polarimetric detectors have an edge over monopolarimetric detector for the detection of endo-clutter targets in a low-grazing configuration.

6.1 . Summary

In the first part we use existing literature to outline the issues counter-UAV radars face. We first give a broad description of the working principles of a radar system. We highlight the importance of the RCS of the target in the equation of radar and introduce the concept of radar clutter and the problems it causes. Thanks to a review of the literature about counter-UAV radar, radar signature of UAVs and the classification methods, we establish the low magnitude of the RCS of UAVs as well as the presence of a micro-Doppler signature caused by the rotating blades of copter type drones (by far the most common class of consumer UAVs). The micro-Doppler signature of UAVs is very often used for classification and detection. Furthermore, this review showed that the flight domain of drones, namely low and slow, implies that they often are endo-clutter targets, and their signature and low RCS is to be compared with the signature of the clutter. The review of the literature allowed us to establish that ground clutter is different from noise. A very important difference is that it is notably coherent, and is often distributed differently from Gaussian noise. The coherency of the clutter means that the endo-clutter targets SCR behaves differently from SNR. Whereas SNR increases with transmitted power and higher integration time, SCR does not. We need to introduce additional diversity to the radar data we measure. To better separate a potentially endo-clutter target from the clutter we proposed to use polarimetric radar, as we show that polarization has proven to be a useful tool for radar classification in both imaging radar or weather radar, improving performances over non polarimetric radar. Finally we review the literature on detectors, and especially endo-clutter and polarimetric detectors showing the importance of the estimation of the signature of the environment we want to detect the target against. We then present the radar, HYCAM, used in this work. We discuss the topic of the characterization and calibration of polarimetric radar. We follow with the presentation of the measurement campaign that is used for the rest of the work of this PhD thesis. In this measurement campaign, we used HYCAM to measure a radar scene in a low-grazing geometry in which a UAV was flying along a pre-determined flight path. We follow these presentations with diverse analyses of the clutter behavior. We show, that the clutter in low-grazing angle geometry has a non-reciprocal polarimetric signature if the receive antenna for the two different received

polarizations are not colocalized. This is due to the clutter being a large collection of different backscatterers spread in different parts of the aperture of the receive antennas. It means that in the geometry we consider (separated h and v receive antennas) and for endo-clutter detection of UAVs, the clutter has four independent polarization signals. Introducing a representation of the clutter based on its SCM computed over the time axis, we addressed the polarimetric stability of the clutter using the effective rank of the SCM. We compute the effective rank of the SCM for different Doppler integration time. We found that clutter exhibits an optimal Doppler integration time that minimizes the effective ranks. We show in a later part that a low effective rank leads to increased performances of the polarimetric detectors. To minimize the effective rank for most of the clutters measured during the campaign, we can use a Doppler integration time of 10 ms. It indicates that for most low-grazing semi-urban clutter we measured, this is an ideal integration time. We then introduce a metric to measure the mismatch between two different signatures of the same clutter taken at different times. This metric is based on the angle between two matrices as we characterize the signature of the clutter with its SCM and represents the mismatch of the polarimetric signature irrespective of the variation of total power. We create a set of 3 different measured clutter, representative of the clutter types found in semi-urban areas and determine a decay time of the clutters. For two estimations of the SCM of the same clutter separated by a given time interval the mismatch grows with the time. Finally, we detail a benchmark of polarimetric detectors including a novel detector based on the eigenvalues of the SCM of the cells under test, as well as a monopolarimetric detector. We first show, as mentioned, the relationship between effective rank of the SCM of the clutter and the performances of the polarimetric detectors. For all the detectors but one (the span, based on the total polarimetric power) the performances are best for a low effective rank, the performance gain between the worst case scenario and best case scenario are equivalent to an additional 6 dB of SCR, which prompts the use of Doppler integration that minimizes the effective rank in the following simulations. We follow with simulations aimed at assessing the impact of the mismatch of the clutter estimation with the actual clutter in the cells under test on the performances of the polarimetric detectors. These simulations use randomly generated couple of covariance matrix to test the different mismatch angles. The matrices in the couple share a common eigenvalue distribution. This eigenvalue distribution is the eigenvalue distribution measured in a specific clutter. We do one simulation per clutter in our set of clutter. These simulations show that the detectors filtering the clutter with the SCM of the estimate clutter suffer an important performance losses when the mismatch angle increases, whereas span and EVA which use polarimetric power have performances that do not correlate with the mismatch angle. Finally we make hybrid simulations which use the SCM of the clutter of the clutter set to generate clutter cell identically distributed to the real clutter cell, and make detection test by injecting real target data in this clutter cell. In these tests the couple of covariance matrix are two SCMs of the same clutter cell estimated at two different times separated by a fixed time interval. The results of these simulations show that most polarimetric detectors have better performances if the clutter estimation is as close as possible to the clutter of the cells under test. This result partly corresponds to the findings of the simulation on using mismatch angle. Moreover, we find that polarimetric detectors consistently outperform the monopolarimetric detectors, and that no monopolarimetric consistently outperforms the others. It means that a detection

scheme for endo-clutter UAVs should implement polarimetric feature. However, the results of these hybrid simulation contradict the previous simulation results and show that EVa and span do have lower performances if the time interval increases. Moreover it reveals that the performances of the EVa detector depend a lot on the target signature.

The methods developed in this thesis could be used adaptively in a radar system to determine the best suited detector for a given clutter.

6.2 . Perspectives

This work gives insight on the advantages of polarimetric detections for endo-clutter drones. Several perspectives could be explored in relation with this work.

6.2.1 . Polarimetric analysis of UAV radar signature

As we have seen some detectors are very sensitive to the polarimetric signature of targets. This thesis did not analyze the polarimetric signature of UAVs. The analysis of the evolution of the polarimetric signature UAV with time should be done to allow for better designs and better performance of endo-clutter detectors.

6.2.2 . Further analyses of the polarimetric clutter

The analysis that was conducted on a set of semi-urban clutter that show different behaviors. Extending this analysis to different clutters using the tools developed in this thesis would allow for a better understanding of low-grazing polarimetric clutter. Since the studied clutter exhibits some vegetation features as well as man-made features it should exhibit some seasonality, further measurement using the effective rank and mismatch would allow to determine if polarimetric clutter is seasonal. In addition, while the clutter datasets we used for our data analysis were selected to represent important feature of semi-urban clutter, it is obvious that it cannot be considered as representing every type of ground clutter, therefore, analysis on different clutter not covered would bring a more general understanding of polarimetric clutter.

6.2.3 . Perspectives for the polarimetric detectors

Real world test for the detectors

The hybrid simulation conducted aim to be as close as possible as a real world test of the detectors while addressing the difficulty of obtaining a sufficient datasets to ensure the robustness of the results. However, we suggest that measurement campaigns featuring a more extensive ground truth, could allow for the test of the detectors on real data that would ensure a statistical robustness of the results. Such a measurement campaign would also allow for a test of the real-time detector. To achieve such a measurement campaign the use of several cooperative targets could be used to take advantage of the capabilities of radar systems to deal simultaneously with several targets. In addition, such a measurement campaign could use the metrics developed in this work to adaptively choose the best suited detector for the situation.

Adding diversity to the polarimetric detectors

To further improve the performances of the polarimetric detectors we could add more diversity to the data vectors serving as input for the detectors. In a similar fashion to STAP we could use several range and Doppler cells in the tested radar data vector in addition to polarization to enhance the performance detection of endo-clutter targets, as they might not be strictly endo-clutter but also near-clutter (in an off-grid configuration).

6.2.4 . Counter-UAV radar perspective

Classification with polarimetry

This work addresses the topic of the detection of drones in the specific context of low-grazing clutter with the large resolution cells containing many different backscatterers. Polarization has proven to be a useful tool for classification, and classification is an important topic in the context of counter-UAV radar systems as many objects share the same flight domain (mainly birds). Further investigation of the use of polarization, as an additional diversity of data in already proven classifiers using other data, such as micro-Doppler signature, could prove fruitful.

Multi-target case

Another point of concern for counter-UAV radars is the multi-target scenario in which several targets are close and can cause some disturbance in the normal operation of a radar. Counter-UAV radars are especially sensitive to this kind of problem as drones are capable of coordinated flight and can use swarming tactics. One use of polarization could be to investigate target separation in swarm scenarios, as the polarimetric signature of a cell containing several targets might be different from the polarimetric signature of a cell with a single target. As such polarization diversity could be a viable alternative to increased bandwidth or shorter PRI for increased resolution to tackle swarm scenarios.

Radar architecture, SDR and MIMO with polarimetry

Since polarization has proven to be useful for the endo-clutter detection of UAV, its integration in the architecture of counter-UAV radar is a subject of interest. In particular, the architecture of a MIMO polarimetric radar can allow for added flexibility as MIMO radar relies on added diversity of the waveforms used on the transmit size which polarization can provide. The large diversity of scenarios a counter-UAV radar can encounter also suggests that a cognitive approach to radar system is warranted, using MIMO architecture and polarization to build a multi-mode platform.

Appendices

Appendix A | Steering vectors

A steering vector is usually a phase vector that is used filter vectorised data. It generally uses a phase relationship between the different elements of the data vector. For instance, let us consider a phased array antenna with N elements (the i^{th} element is located at r_i) and an off-axis signal carried by a plane wave with \mathbf{k} its wave vector (the unitary vector normal to the wave plane and oriented in the propagation direction of the wave). The plane wave will be measured by the different elements of the array antenna at different times due to the different positions of the elements. Thus, the resulting signals will be phase shifted:

$$\mathbf{X} = (xe^{-j\mathbf{k}\cdot\mathbf{r}_1}, xe^{-j\mathbf{k}\cdot\mathbf{r}_2}, \dots, xe^{j\mathbf{k}\cdot\mathbf{r}_N}) \quad (\text{A.0.1})$$

with \mathbf{X} the collection of received signals by each antenna element, x the signal of the plane wave and $e^{-j\mathbf{k}\cdot\mathbf{r}_i}$ the phase due to the positioning of the i_{th} element of the antenna. We define S the steering vector associated with the wave vector \mathbf{k} of the incoming wave and considered array antenna:

$$\mathbf{S} = (e^{-j\mathbf{k}\cdot\mathbf{r}_1}, e^{-j\mathbf{k}\cdot\mathbf{r}_2}, \dots, e^{j\mathbf{k}\cdot\mathbf{r}_N}) \quad (\text{A.0.2})$$

We thus have:

$$\mathbf{S}^H \mathbf{X} = Nx \quad (\text{A.0.3})$$

the steering vectors S allows to measure the incoming signal with wave vector \mathbf{k} , whereas the other signals with different wave vectors are not coherently summed, and thus, are filtered.

This concept applies to any vectorised data in which the individual signals are linked predetermined phase relationship.

Appendix B | HYCAM Receive apertures

To measure the receive aperture of the two pairs of column of the receive antenna of HYCAM used in the measurement campaign we organized a measurement campaign in a field with an unobstructed view of HYCAM to ensure a free propagation towards the radar. During this campaign, we transmitted a pure frequency waveform with a horn antenna and a synthesizer to measure the reception aperture of a single element of the receiving antenna for both polarizations (Figure B.1).

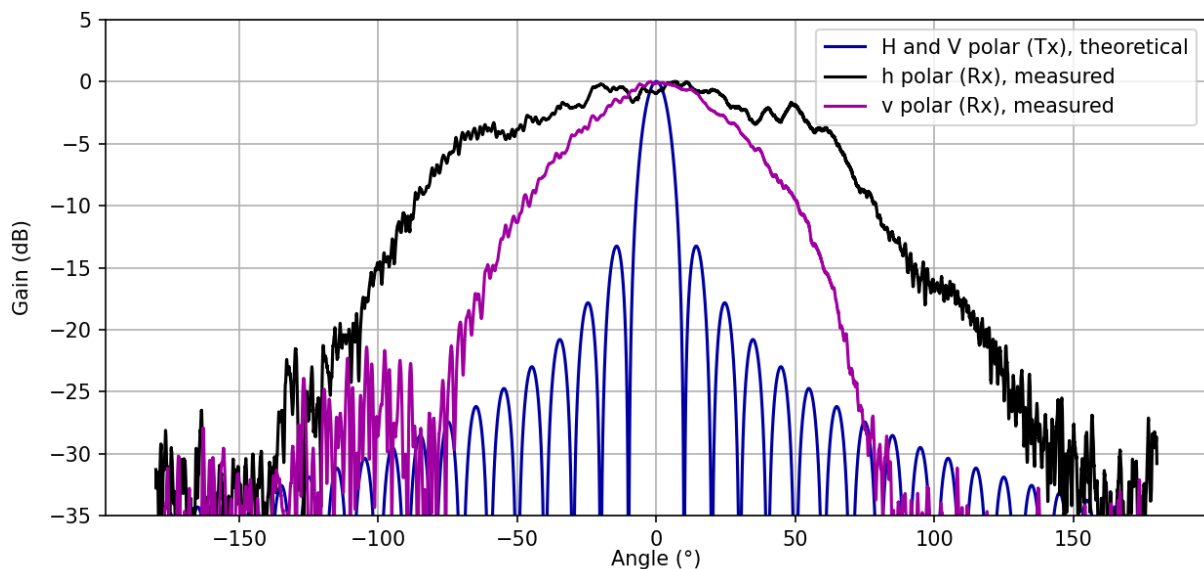


Figure B.1: HYCAM theoretical transmit aperture and measured receive aperture in both polarizations.

The measured diagram for h and v polarization turned out to be different with one being twice as large as the other one.

Appendix C | Link between CNR and maximum correlation rate

We recall that for two different signals we have the covariance given by:

$$\sigma_{XY} = \frac{1}{N} \sum_{i=1}^N (X_i - \bar{X}) (Y_i - \bar{Y}) \quad (\text{C.0.1})$$

We write:

$$\sigma_{XX} = \sigma_X^2 \quad (\text{C.0.2})$$

And the correlation is given by:

$$\rho = \frac{\sigma_{XY}}{\sqrt{\sigma_X^2 \sigma_Y^2}} \quad (\text{C.0.3})$$

We have two clutter identical clutter signals with different noise factor:

$$X = C + N_0 \quad (\text{C.0.4})$$

$$Y = C + N_1 \quad (\text{C.0.5})$$

We define their CNR $CNR_0 = \frac{\sigma_C^2}{\sigma_{N_0}^2}$ and $CNR_1 = \frac{\sigma_C^2}{\sigma_{N_1}^2}$

We have:

$$\sigma_{XY} = \sigma_{CC} + \sigma_{CN_0} + \sigma_{CN_1} + \sigma_{N_0N_1} = \sigma_C^2 \quad (\text{C.0.6})$$

as C is uncorrelated with N_0 and N_1 and N_0 and N_1 are themselves uncorrelated.

$$\rho = \frac{\sigma_{XY}}{\sqrt{\sigma_X^2 \sigma_Y^2}} = \frac{\sigma_C^2}{\sqrt{\sigma_C^2 + \sigma_{N_0}^2} \sqrt{\sigma_C^2 + \sigma_{N_1}^2}} \quad (\text{C.0.7})$$

$$\rho = \frac{\sqrt{\frac{\sigma_C^4}{\sigma_{N_0}^2 \sigma_{N_1}^2}}}{\sqrt{\frac{\sigma_C^2}{\sigma_{N_0}^2} + 1} \sqrt{\frac{\sigma_C^2}{\sigma_{N_1}^2} + 1}} \quad (\text{C.0.8})$$

$$\rho = \frac{\sqrt{CNR_0 CNR_1}}{\sqrt{(CNR_0 + 1)(CNR_1 + 1)}} \quad (\text{C.0.9})$$

Appendix D | Noise analysis

D.1 . Noise measurement

We measure the noise on the measurement campaign data used in this thesis. The noise covariance matrix is:

$$\mathbf{R}_{noise} = \begin{pmatrix} \sigma_{Hh}^2 & 0 & 0 & 0 \\ 0 & \sigma_{Vh}^2 & 0 & 0 \\ 0 & 0 & \sigma_{Hv}^2 & 0 \\ 0 & 0 & 0 & \sigma_{Hv}^2 \end{pmatrix} \quad (\text{D.1.1})$$

Where $\sigma_{\alpha\beta}^2$ is the noise variance of the $\alpha\beta$ channel. As the noise on each channel is independant, which means the non diagonal terms are null. In addition the signal of Hv and Vv (conversely Hh and Vh) are measured on the same physical channel at different time as only the transmit polarization changes. Therefore they should be identically distributed as the noise depends does not depend on the transmit channel, but only on the enviromnt and receive channel. Therefore we have $\sigma_{Hh}^2 = \sigma_{Vh}^2 = \sigma_h^2$ and $\sigma_{Hv}^2 = \sigma_{Vv}^2 = \sigma_v^2$. Therefore giving us the following covariance matrix :

$$\mathbf{R}_{noise} = \begin{pmatrix} \sigma_h^2 & 0 & 0 & 0 \\ 0 & \sigma_h^2 & 0 & 0 \\ 0 & 0 & \sigma_v^2 & 0 \\ 0 & 0 & 0 & \sigma_v^2 \end{pmatrix} \quad (\text{D.1.2})$$

To measure σ_h^2 and σ_v^2 we use a doppler range cell at speed $9.5\text{m} \cdot \text{s}^{-1}$. We compute the mean covariance matrix over the whole measurement duration (836 s) using the same parameters as in the rest of the thesis (10 ms Doppler integration time). This SCM is computed over 83600 samples. In Figure D.1, the covariance matrix exhibits the expected behavior being diagonal with two distinct values on the diagonal, one for σ_h^2 and one for σ_v^2 .

D.2 . Consideration on the noise estimation with N samples

The eigenvalues of D.1.2 are $\{\sigma_h^2, \sigma_h^2, \sigma_v^2, \sigma_v^2\}$. However, the value of the SCM depends on the number of samples, we recall that expression of the terms of the SCM estimated with N samples is:

$$\overline{\mathbf{R}_{noise}} = \left(\frac{1}{N} \sum_{i=0}^{N-1} x_{\alpha\beta,i} x_{\alpha'\beta',i}^* \right)_{\alpha\beta, \alpha'\beta' \in \{Vh, Vv, Hh, Hv\}} \quad (\text{D.2.1})$$

We have the element-wise expected value given by:

	Hv	Vv	Hh	Vh
Hv	0.77 dB	-25.46 dB	-24.23 dB	-22.59 dB
Vv	-25.46 dB	0.79 dB	-21.38 dB	-27.54 dB
Hh	-24.23 dB	-21.38 dB	2.15 dB	-20.64 dB
Vh	-22.59 dB	-27.54 dB	-20.64 dB	2.17 dB

Figure D.1: Noise polarimetric covariance matrix.

$$\left| \mathbb{E} \left(\frac{1}{N} \sum_{i=0}^{N-1} x_{\alpha\beta,i} x_{\alpha'\beta',i}^* \right) \right| = \begin{cases} \frac{1}{N} N \sigma_{\alpha\beta}^2 = \sigma_{\beta}^2 & \text{if } \alpha\beta = \alpha'\beta' \\ 0 & \text{if } \alpha\beta \neq \alpha'\beta' \end{cases} \quad (\text{D.2.2})$$

$$\left(\left| \mathbb{E} \left(\frac{1}{N} \sum_{i=0}^{N-1} x_{\alpha\beta,i} x_{\alpha'\beta',i}^* \right) \right| \right)_{\alpha\beta, \alpha'\beta'} = \begin{pmatrix} \sigma_v^2 & 0 & 0 & 0 \\ 0 & \sigma_v^2 & 0 & 0 \\ 0 & 0 & \sigma_h^2 & 0 \\ 0 & 0 & 0 & \sigma_h^2 \end{pmatrix} \quad (\text{D.2.3})$$

and the element-wise variance given by:

$$\left| \text{Var} \left(\frac{1}{N} \sum_{i=0}^{N-1} x_{\alpha\beta,i} x_{\alpha'\beta',i}^* \right) \right| = \begin{cases} \frac{2}{N} \sigma_{\beta}^4 & \text{if } \alpha\beta = \alpha'\beta' \\ \frac{1}{N} \sigma_{\beta}^4 & \text{if } \beta = \beta' \\ \frac{1}{N} \sigma_{\beta}^2 \sigma_{\beta'}^2 & \text{if } \beta \neq \beta' \end{cases} \quad (\text{D.2.4})$$

$$\left(\left| \text{Var} \left(\frac{1}{N} \sum_{i=0}^{N-1} x_{\alpha\beta,i} x_{\alpha'\beta',i}^* \right) \right| \right)_{\alpha\beta, \alpha'\beta'} = \frac{1}{N} \begin{pmatrix} 2\sigma_v^4 & \sigma_v^4 & \sigma_v^2 \sigma_h^2 & \sigma_v^2 \sigma_h^2 \\ \sigma_v^4 & 2\sigma_v^4 & \sigma_v^2 \sigma_h^2 & \sigma_v^2 \sigma_h^2 \\ \sigma_v^2 \sigma_h^2 & \sigma_v^2 \sigma_h^2 & 2\sigma_h^4 & \sigma_h^4 \\ \sigma_v^2 \sigma_h^2 & \sigma_v^2 \sigma_h^2 & \sigma_h^4 & 2\sigma_h^4 \end{pmatrix} \quad (\text{D.2.5})$$

Thus, non-diagonal terms are non-zero and it affects the eigenvalues. An 'estimation noise' is introduced on all terms by the estimation, as a variance inversely proportional to the number of samples used in the estimation. We expect that the higher the value of N is, the closer the eigenvalues should be to the actual noise of the channels. We compute the mean eigenvalues over the measurement duration as a function of samples used to estimates the SCM for the cell under consideration in D.1. We compare this with the expected simulated results with D.2.3 and D.2.5. Figure D.2 shows the evolution of the eigenvalues with the number of samples, we see that simulation and measurement match well. The simulation results are obtained by generating noise vector using the

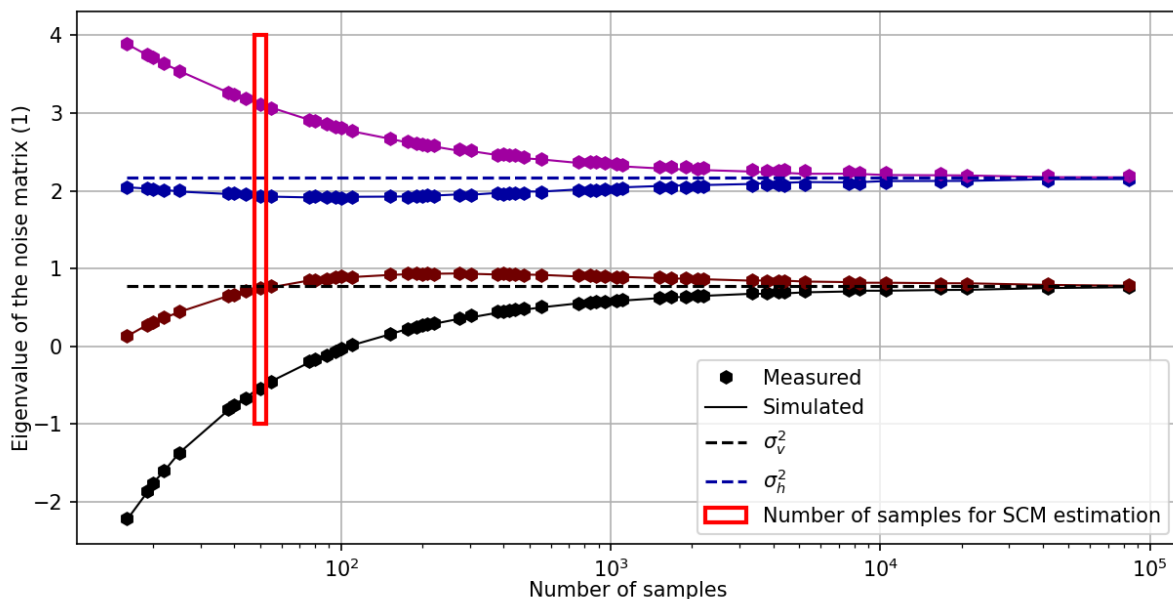


Figure D.2: Measured and simulated eigenvalues for different numbers of samples used in the SCM estimation. The rectangle outlines the number of samples used in this thesis when estimating SCM.

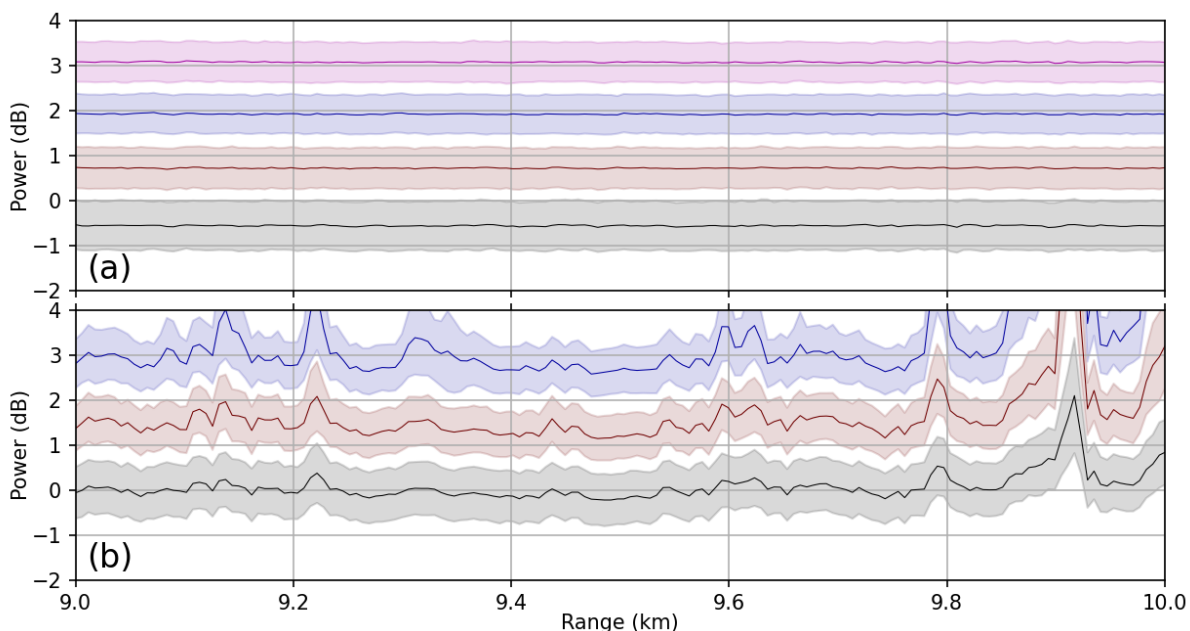


Figure D.3: Mean eigenvalues for ranges from 9 to 10 km for Doppler cell of speed $8 \text{ m} \cdot \text{s}^{-1}$ (a) and $0 \text{ m} \cdot \text{s}^{-1}$ (b) (clutter cells, excerpt from Figure 4.28b, the highest eigenvalue is above 4 dB and thus hidden). The mean eigenvalues of (a) correspond to noise covariance matrix eigenvalues. We see the lowest noise eigenvalue is -0.5 dB.

asymptotic estimate of the covariance matrix and then computing the SCM estimates with these generated noise vectors. We see that the last eigenvalue is below the lowest noise value. This means that even an eigenvalue corresponding to clutter signal can be lower than the noise floor as measured by the asymptotic estimate of the noise covariance matrix. However, if a signal is to be considered as clutter signal, it should always be higher than the last noise eigenvalue measured using the same number of samples in the estimation of both the noise and clutter covariance matrices. Figure D.3 shows example of noise and clutter eigenvalue distributions. In this example, the last clutter eigenvalue is lower than the noise floor (0.8 dB) but higher than the last noise eigenvalue (-0.5 dB).

Appendix E | Relative angle between two matrices of identical eigenvalue distributions and identical eigenvectors

We want to measure the expected value of the angle between two covariance matrices sharing the same lognormal eigenvalue distribution and the exact same eigenvectors. We measure this expected value for each of the clutter under consideration (See 4.4.8). For each clutter we use the measured lognormal distributions of each eigenvalues to generate a pair of eigenvalue vectors. The eigenvectors we use to generate the matrices are the columns of I_4 the identity matrix of dimension 4. We use the Monte-Carlo algorithm and generates 10^6 pairs of vectors of eigenvalues to have 10^6 pairs of covariance matrices per studied clutter. We can compute the cosine of the mismatch angle for each pair of covariance matrix. The mean cosine is the expected value of the cosine of the mismatch angle for the eigenvalues distributions under consideration.

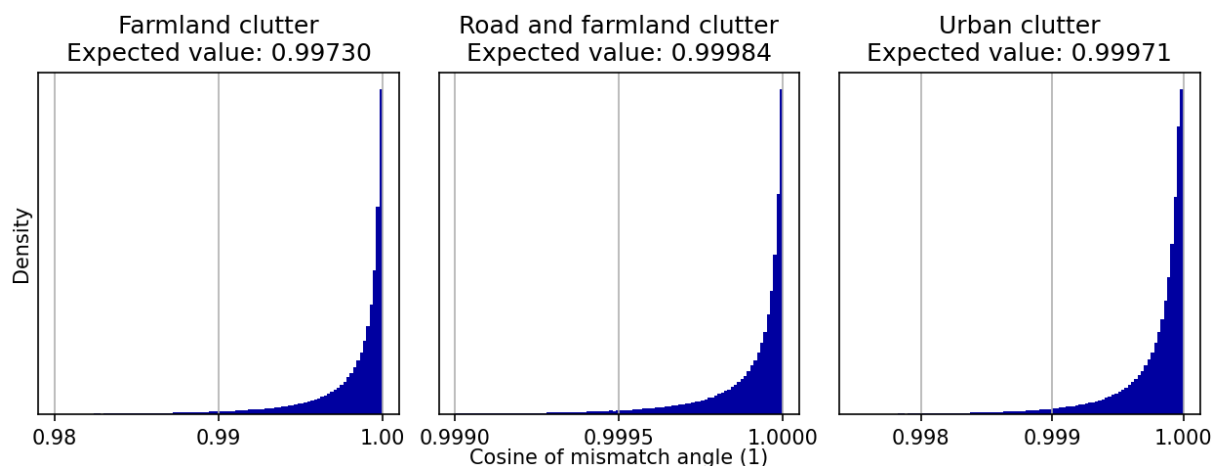


Figure E.1: Distribution of mismatch angles obtained between matrices sharing the same eigenvectors and the same eigenvalue distributions.

Figure E.1 shows the distributions of cosines for the 3 clutter under investigation. We see the cosine distributions are stacked close to 1. The expected value are shown in Table E.1.

Clutter	Cosine expected value	Corresponding angle (°)
Farmland	0.99730	4.2
Farmland and road	0.99984	1.2
Urban	0.99971	1.4

Table E.1: Cosine expected values and corresponding angles.

Appendix F | Resampling to favor mismatch angle of 0°

To favor angles close to 0° we follow the normal eigenvalue generation process described in 5.5.1. We generate both eigenvalue vectors as follows

$$\mathbf{\Lambda}^E = (\lambda^E_i)_{i < 4} \quad (\text{F.0.1})$$

$$\mathbf{\Lambda}^C = (\lambda^C_i)_{i < 4} \quad (\text{F.0.2})$$

With:

$$\lambda^E_i, \lambda^C_i = \text{lognormal}(\tilde{\lambda}_i, \tilde{\sigma}_i^2) \quad (\text{F.0.3})$$

Then we define $\mathbf{L}^E = \text{diag}(\mathbf{\Lambda}^E)$ and $\mathbf{L}^C = \text{diag}(\mathbf{\Lambda}^C)$. However to favor a mismatch angle close to 0° we generate a unique transfer matrix for the couple $\mathbf{U} = \mathbf{U}^E = \mathbf{U}^C$. We thus have:

$$\mathbf{R}^E = \mathbf{U} \mathbf{L}^E \mathbf{U}^{-1} \quad (\text{F.0.4})$$

$$\mathbf{R}^C = \mathbf{U} \mathbf{L}^C \mathbf{U}^{-1} \quad (\text{F.0.5})$$

As both of the matrices of the CMC share the same eigenvectors and eigenvalue distributions the cosine of the mismatch angle is close to 1 (the expected value of the cosines for the clutter under consideration with this kind of resampling can be found in appendix E).

Appendix G | UAV signature extraction

As for clutter, no general model for of UAV polarimetric signature of UAVs is not described in the litterature. Thus, we measure the dynamic signature of the UAV used in the measurement campaign. The flight data of the UAV were recorded in a log file. With the log data and the radar position, we compute the distance between the radar and the UAV. We convert the GPS coordinates of both the UAV and the radar in the **World Geodetic System (WGS) 84 Earth Centered - Earth Fixed (ECEF)** coordinate system. The ECEF is a coordinate systems using cartesian coordinates centered on the center of the earth, allowing us to compute the Euclidian distance between the UAV and the radar system:

$$d = \sqrt{(x_{UAV} - x_{radar})^2 + (y_{UAV} - y_{radar})^2 + (z_{UAV} - z_{radar})^2} \quad (\text{G.0.1})$$

The distance obtained with the log data, as shown on a map in Figure 4.15 (we cleaned the log data before this step), is then visually fitted to the radar data of the of the UAV flight to ensure an accurate positioning of the vehicle (Figure G.1). We compute the trace of the covariance matrices (computed on 500 ms of data, with a 10 ms Doppler processing) for the 4 central doppler-range cells (at every range):

$$\text{Tr}(\overline{\mathbf{R}}(t, d, v)) = \sum_{i=0}^3 \overline{R_{ii}}(\overline{\mathbf{R}}(t, d, v)) \quad (\text{G.0.2})$$

With v being the velocity of the Doppler-range cell and $\overline{R_{ii}}$ the element of the i^{th} column and row of the $\mathbf{R}(t, d, v)$ matrix. This is the total polarimetric power. We compute it in decibels and sum the doppler signals:

$$P_{dB}(t, d) = \sum_{v \neq 0} \text{Tr}(\overline{\mathbf{R}}(t, d, v)) \Big|_{dB} \quad (\text{G.0.3})$$

This gives a waterfall visualization of the trajectory of the UAV that can be fitted with the log data

By taking the differential of the log data over both the time and distance axes, we compute the speed of the UAV relative to the radar. We show the UAV in the Doppler-range space over time (Figure G.2).

With these positions we extract the UAV position during time. Since the measurement of the clutter were computed with a 10 ms Doppler processing we need to extract the UAV signature with the same integration time. We use the knowledge of the UAV relative speed to compute the Doppler processed data for its specific velocity with the appropriate Doppler steering vector (Equation G.0.4).

$$\mathbf{X}_{Dop}(t, d_{UAV}, v_{UAV}) = \sum_{k=0}^{N_{pulses}} \mathbf{X}_{PC}(t + 2k \times PRI, d_{UAV}) \times e^{2i\pi \left(\frac{v_{UAV}}{v_{amb}} \frac{k}{N_{pulses}} \right)} \quad (\text{G.0.4})$$

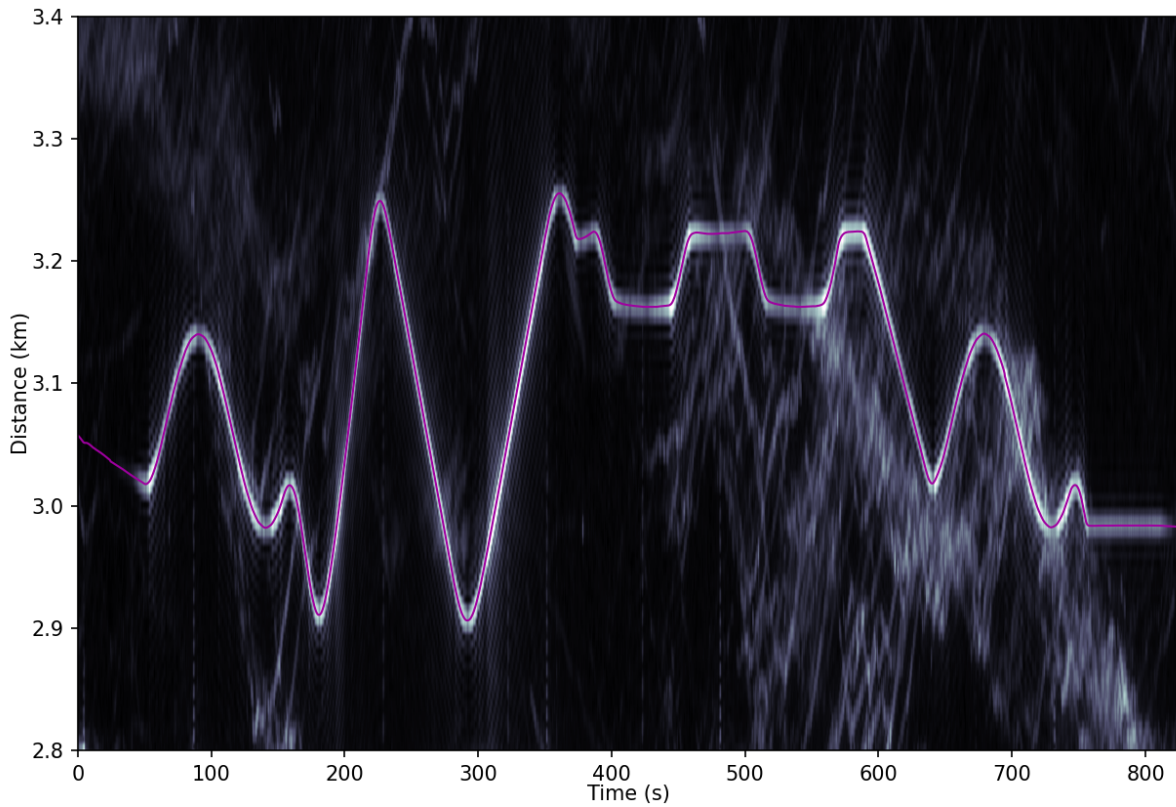


Figure G.1: Log data visually fitted on the radar data. The other visible "tracks" are birds that were flying during the measurement campaign.

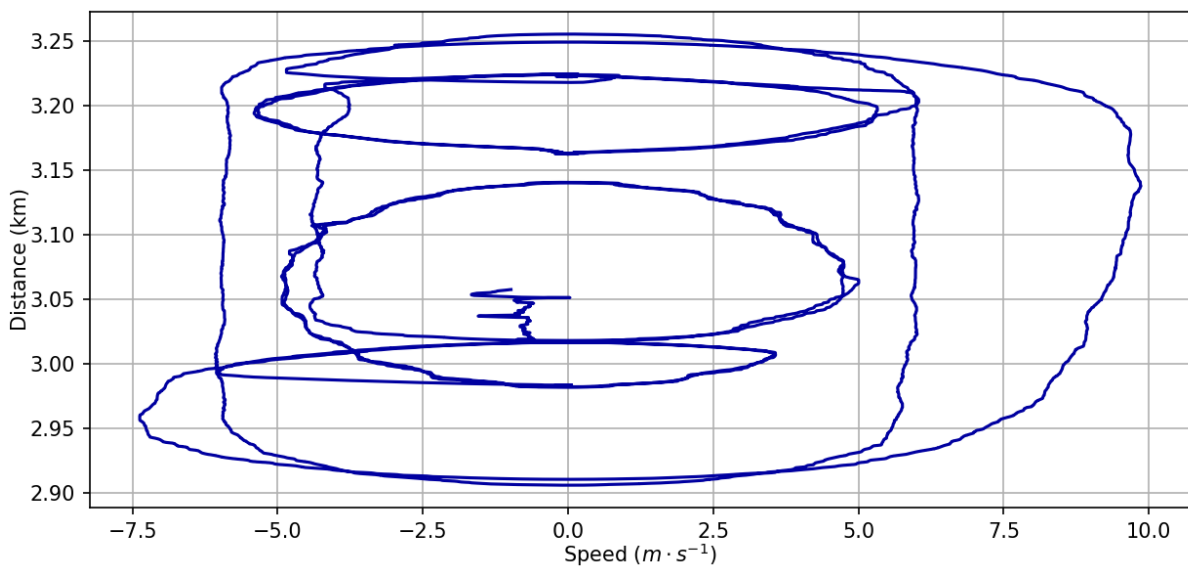


Figure G.2: Position of the UAV in the Doppler-range space.

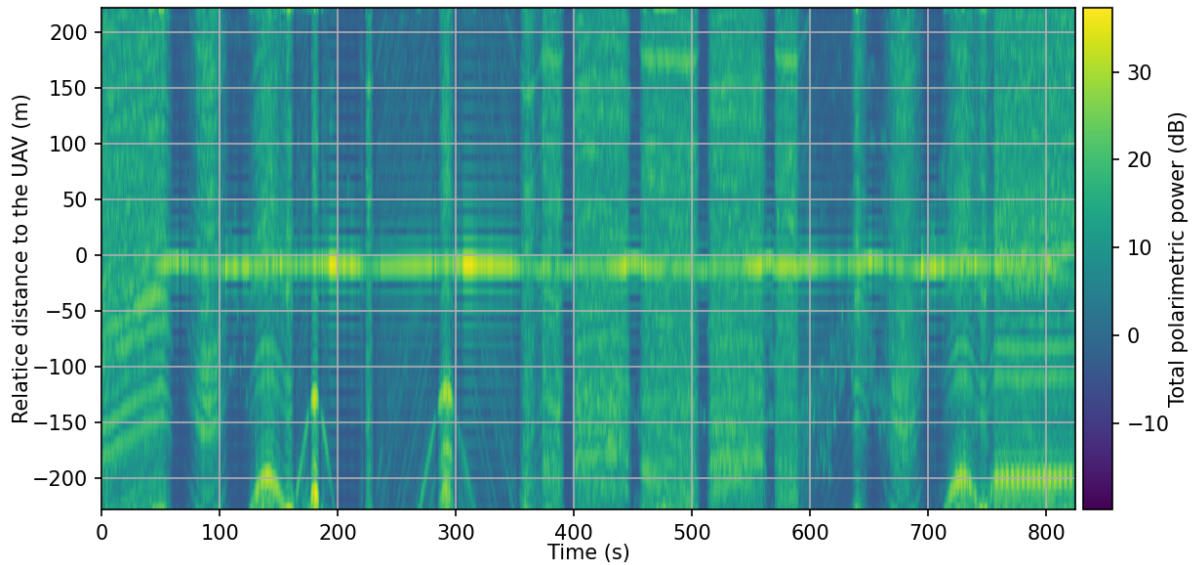


Figure G.3: UAV signal and neighbouring range cells after extraction.

Where $\mathbf{X}_{Dop}(t, d, v)$ is the radar signal in all four polarisation at time t , distance d and filtered at speed v over N_{pulses} , $\mathbf{X}_{PC}(t, d)$ is the radar signal from the pulse-culse compression at distance d and time t . v_{amb} is the ambiguous speed associated with PRI , the PRI of the measurement as defined in 2.1.1.

Figure G.3 show the signal of the UAV signal and neighbouring range cells after extraction. The final step for the signature extraction is to manually remove the parts where the UAV is in the clutter or has a SNR too low (we chose a minimum SNR of 30 dB), and to keep only the central range cells.

Appendix H | Maximum Likelihood detector for unknown amplitude and steering vector for each look

We write the likelihood ratio as follows:

$$LR = \frac{p(\mathbf{Y}|h_1)}{p(\mathbf{Y}|h_0)} = \prod_{i=0}^{N-1} \frac{p(\mathbf{X}_i|h_1)}{p(\mathbf{X}_i|h_0)} \quad (\text{H.o.1})$$

with $\mathbf{Y} = \{\mathbf{X}_i\}_{i \in [1, N]}$
The logarithm of LR is:

$$\log LR \propto \sum_{i=0}^{N-1} \log \frac{p(\mathbf{X}_i|h_1)}{p(\mathbf{X}_i|h_0)} \quad (\text{H.o.2})$$

with

$$p(\mathbf{X}_i|h_1) = \frac{1}{\pi^{N_{chan}} \|\mathbf{R}^E\|} e^{-(\mathbf{X}_i - A_i \mathbf{S}_i)^H \mathbf{R}^{E-1} (\mathbf{X}_i - A_i \mathbf{S}_i)} \quad (\text{H.o.3})$$

and

$$p(\mathbf{X}_i|h_0) = \frac{1}{\pi^{N_{chan}} \|\mathbf{R}^E\|} e^{-\mathbf{X}_i^H \mathbf{R}^{E-1} \mathbf{X}_i} \quad (\text{H.o.4})$$

thus, we have:

$$\log LR \propto \sum_{i=0}^{N-1} A_i^* \mathbf{S}_i^H \mathbf{R}^{E-1} \mathbf{X}_i + A_i \mathbf{X}_i^H \mathbf{R}^{E-1} \mathbf{S}_i - \|A_i\| \mathbf{S}_i^H \mathbf{R}^{E-1} \mathbf{S}_i \quad (\text{H.o.5})$$

To maximize $\log LR$ over the A_i imply that $\log LR$ match the following condition:

$$\frac{\partial (\log LR)}{\partial A_i} = 0 \quad (\text{H.o.6})$$

Which gives us the **Polarimetric GLRT (P-GLRT)** (the polarimetric adaptation of the GLRT), namely:

$$\max_{\substack{\{\mathbf{A}_i\}_{i \in [0..N-1]} \\ \{\mathbf{S}_i\}_{i \in [0..N-1]}}} \log LR = \max_{\{\mathbf{S}_i\}_{i \in [0..N-1]}} \sum_{i=0}^{N-1} \frac{\|\mathbf{S}_i^H \mathbf{R}^{E-1} \mathbf{X}_i\|^2}{\mathbf{S}_i^H \mathbf{R}^{E-1} \mathbf{S}_i} \quad (\text{H.o.7})$$

$$\max_{\{S_i\}_{i \in [0..N-1]}} \sum_{i=0}^{N-1} \frac{\|S_i^H R^{E-1} X_i\|^2}{S_i^H R^{E-1} S_i} = \sum_{i=0}^{N-1} \max_{\{S_i\}_{i \in [0..N-1]}} \frac{\|S_i^H R^{E-1} X_i\|^2}{S_i^H R^{E-1} S_i} \quad (\text{H.o.8})$$

with the Cauchy-Schwarz inequality we have:

$$\|S_i^H R^{E-1} X_i\|^2 \leq (S_i^H R^{E-1} S_i) (X_i^H R^{E-1} X_i) \quad (\text{H.o.9})$$

the equality is met for:

$$S_i = \gamma_i X_i \quad (\text{H.o.10})$$

thus:

$$\max_{\substack{\{A_i\}_{i \in [0..N-1]} \\ \{S_i\}_{i \in [0..N-1]}}} \log LR = \sum_{i=0}^{N-1} \|X_i^H R^{E-1} X_i\| \quad (\text{H.o.11})$$

$$\sum_{i=0}^{N-1} \|X_i^H R^{E-1} X_i\| \underset{h_1}{\overset{h_0}{\leq}} \eta_0 \quad (\text{H.o.12})$$

Equation H.o.12 describes the ML detector with the hypothesis that the S_i and A_i are different for each look.

Bibliography

Bibliography

- Acoustic mirror* (June 2022). en. Page Version ID: 1092137748. url: https://en.wikipedia.org/w/index.php?title=Acoustic_mirror&oldid=1092137748 (visited on 11/28/2022).
- Aldowesh, Abdulrazaq, Tareq Alnuaim, and Adel Alzogaiby (Apr. 2019). "Slow-Moving Micro-UAV detection with a small scale Digital Array Radar". In: *2019 IEEE Radar Conference (RadarConf)*. ISSN: 2375-5318, pp. 1–5.
- Bailey, Johnson, Armando Marino, and Vahid Akbari (Jan. 2021). "Comparison of Target Detectors to Identify Icebergs in Quad-Polarimetric L-Band Synthetic Aperture Radar Data". en. In: *Remote Sensing* 13.9, p. 1753. url: <https://www.mdpi.com/2072-4292/13/9/1753> (visited on 10/21/2021).
- Bell, M.R. and R.A. Grubbs (Jan. 1993). "JEM modeling and measurement for radar target identification". In: *IEEE Transactions on Aerospace and Electronic Systems* 29.1, pp. 73–87.
- Biallawons, Oliver, Jens Klare, and Lars Fuhrmann (June 2018). "Improved UAV Detection with the MIMO Radar MIRA-CLE Ka using Range-Velocity Processing and TDMA Correction Algorithms". In: *2018 19th International Radar Symposium (IRS)*. ISSN: 2155-5753, pp. 1–10.
- Billingsley, J. Barrie (2002). *Low-angle radar land clutter: measurements and empirical models*. en. OCLC: ocm46935969. Norwich, N.Y. : Stevenage, UK: William Andrew Pub. : SciTech Pub. ; Institution of Electrical Engineers.
- Birch, Gabriel Carisle, John Clark Griffin, and Matthew Kelly Erdman (July 2015). *UAS Detection Classification and Neutralization: Market Survey 2015*. English. Tech. rep. SAND2015-6365. Sandia National Lab. (SNL-NM), Albuquerque, NM (United States). url: <https://www.osti.gov/biblio/1222445> (visited on 05/02/2022).
- Black Hornet PRS Datasheet* (2022). English. url: <https://flir.netx.net/file/asset/15326/original/attachment> (visited on 03/07/2022).
- Blake, S. (Nov. 1988). "OS-CFAR theory for multiple targets and nonuniform clutter". en. In: *IEEE Transactions on Aerospace and Electronic Systems* 24.6, pp. 785–790. url: <http://ieeexplore.ieee.org/document/18645/> (visited on 02/14/2020).
- Blanter, Ya M. and M. Buttiker (Sept. 2000). "Shot Noise in Mesoscopic Conductors". en. In: *Physics Reports* 336.1-2. arXiv:cond-mat/9910158, pp. 1–166. url: <http://arxiv.org/abs/cond-mat/9910158> (visited on 09/28/2022).
- Boerner, W.-M., M. El-Arini, Chung-Yee Chan, and P. Mastoris (Mar. 1981). "Polarization dependence in electromagnetic inverse problems". In: *IEEE Transactions on Antennas and Propagation* 29.2, pp. 262–271.
- Brandes, Edward A., Alexander V. Ryzhkov, and Dusan S. Zrnica (Mar. 2001). "An Evaluation of Radar Rainfall Estimates from Specific Differential Phase". EN. In: *Journal of Atmospheric and Oceanic Technology* 18.3, pp. 363–375. url: https://journals.ametsoc.org/view/journals/atot/18/3/1520-0426_2001_018_0363_aeorre_2_0_co_2.xml (visited on 05/05/2022).

- Bringi, V N and V Chandrasekar (2001). "POLARIMETRIC DOPPLER WEATHER RADAR: Principles and applications". en. In: p. 664.
- Brooks, Daniel A., Olivier Schwander, Frederic Barbaresco, Jean-Yves Schneider, and Matthieu Cord (June 2018). "Temporal Deep Learning for Drone Micro-Doppler Classification". In: *2018 19th International Radar Symposium (IRS)*. ISSN: 2155-5753, pp. 1–10.
- Carretero, M. Vizcarro i, R. I. A. Harmanny, and R. P. Trommel (Oct. 2019). "Smart-CFAR, a machine learning approach to floating level detection in radar". en. In: p. 4.
- Carretero-Moya, Javier, Javier Gismero-Menoyo, Álvaro Blanco-del Campo, and Alberto Asensio-Lopez (Apr. 2010). "Statistical Analysis of a High-Resolution Sea-Clutter Database". In: *IEEE Transactions on Geoscience and Remote Sensing* 48.4, pp. 2024–2037.
- Chaturvedi, Sudhir Kumar, Raj Sekhar, Saikat Banerjee, and Hutanshu Kamal (Sept. 2019). "Comparative Review Study of Military and Civilian Unmanned Aerial Vehicles (UAVs)". en. In: *INCAS BULLETIN* 11.3, pp. 183–198. url: http://bulletin.incas.ro/files/chaturvedi_sekhar_banerjee_kamal_vol_11_iss_3.pdf (visited on 02/02/2022).
- Choi, Byunggil and Daegun Oh (Oct. 2018). "Classification of Drone Type Using Deep Convolutional Neural Networks Based on Micro- Doppler Simulation". In: *2018 International Symposium on Antennas and Propagation (ISAP)*, pp. 1–2.
- Chung, Shen Shou Max and Shih-Chung Tuan (2021). "EFFICACY OF AN S-SHAPED AIR INLET ON THE REDUCTION OF FRONT BISTATIC RADAR CROSS SECTION OF A FIGHTER ENGINE". en. In: *Progress In Electromagnetics Research B* 92, pp. 193–211. url: <http://www.jpier.org/PIERB/pier.php?paper=21060803> (visited on 03/07/2022).
- Circular (2007). en. Circular.
- Cloude, S.R. and E. Pottier (Mar. 1996). "A review of target decomposition theorems in radar polarimetry". In: *IEEE Transactions on Geoscience and Remote Sensing* 34.2, pp. 498–518.
- (Jan. 1997). "An entropy based classification scheme for land applications of polarimetric SAR". In: *IEEE Transactions on Geoscience and Remote Sensing* 35.1, pp. 68–78.
- Collett, Edward (2005). *Field Guide to Polarization*. en. Google-Books-ID: 5lJwcCsLbLsC. Society of Photo Optical.
- Conte, E., M. Lops, and G. Ricci (Apr. 1995). "Asymptotically optimum radar detection in compound-Gaussian clutter". In: *IEEE Transactions on Aerospace and Electronic Systems* 31.2, pp. 617–625.
- Dale, Holly, Chris Baker, Michail Antoniou, Mohammed Jahangir, and George Atkinson (May 2021). "A Comparison of Convolutional Neural Networks for Low SNR Radar Classification of Drones". In: *2021 IEEE Radar Conference (RadarConf21)*. ISSN: 2375-5318, pp. 1–5.
- Dale, Holly, Chris Baker, Michail Antoniou, Mohammed Jahangir, George Atkinson, and Stephen Harman (Jan. 2022). "SNR-dependent drone classification using convolutional neural networks". en. In: *IET Radar, Sonar & Navigation* 16.1, pp. 22–33. url: <https://onlinelibrary.wiley.com/doi/10.1049/rsn2.12161> (visited on 04/29/2022).
- Davidson, G., H. D. Griffiths, and S. Ablett (Feb. 2004). "Analysis of high-resolution land clutter". en. In: *IEE Proceedings - Vision, Image and Signal Processing* 151.1, pp. 86–91. url: https://digital-library.theiet.org/content/journals/10.1049/ip-vis_20040303 (visited on 06/10/2022).

- De Maio, A., G. Alfano, and E. Conte (Jan. 2004). "Polarization diversity detection in compound-Gaussian clutter". In: *IEEE Transactions on Aerospace and Electronic Systems* 40.1, pp. 114–131.
- De Maio, Antonio and Giuseppe Ricci (Dec. 2001). "A polarimetric adaptive matched filter". en. In: *Signal Processing* 81.12, pp. 2583–2589. url: <https://www.sciencedirect.com/science/article/pii/S0165168401001505> (visited on 09/15/2021).
- Death From Above* (Feb. 2017). *Death From Above: The Drone Bombs of the Caliphate*. en-GB. url: <https://www.bellingcat.com/news/mena/2017/02/10/death-drone-bombs-caliphate/> (visited on 03/11/2022).
- Drozdowicz, Jędrzej, Maciej Wielgo, Piotr Samczynski, Krzysztof Kulpa, Jarosław Krzonkalla, Maj Mordzonek, Marcin Bryl, and Zbigniew Jakielaszek (May 2016). "35 GHz FMCW drone detection system". In: *2016 17th International Radar Symposium (IRS)*. ISSN: 2155-5753, pp. 1–4.
- Duk, Vichet, Luke Rosenberg, and Brian Wai-Him Ng (June 2017). "Target Detection in Sea-Clutter Using Stationary Wavelet Transforms". In: *IEEE Transactions on Aerospace and Electronic Systems* 53.3, pp. 1136–1146.
- Echard, J.D. (Mar. 1991). "Estimation of radar detection and false alarm probability". In: *IEEE Transactions on Aerospace and Electronic Systems* 27.2, pp. 255–260.
- Ezuma, Martins, Chethan Kumar Anjinappa, Mark Funderburk, and Ismail Guvenc (Feb. 2022). "Radar Cross Section Based Statistical Recognition of UAVs at Microwave Frequencies". In: *IEEE Transactions on Aerospace and Electronic Systems* 58.1, pp. 27–46.
- Farrouki, A. and M. Barkat (2005). "Automatic censoring CFAR detector based on ordered data variability for nonhomogeneous environments". en. In: *IEE Proceedings - Radar, Sonar and Navigation* 152.1, p. 43. url: https://digital-library.theiet.org/content/journals/10.1049/ip-rsn_20045006 (visited on 09/03/2020).
- Finn, H M and R S Johnson (1968). "ADAPTIVE DETECTION MODE WITH THRESHOLD CONTROL AS A FUNCTION OF SPATIALLY SAMPLED CLUTTER-LEVEL ESTIMATES". en. In: *RCA REVIEW*, p. 51.
- Frankford, Mark T., Kyle B. Stewart, Ninoslav Majurec, and Joel T. Johnson (Apr. 2014). "Numerical and experimental studies of target detection with MIMO radar". In: *IEEE Transactions on Aerospace and Electronic Systems* 50.2, pp. 1569–1577.
- Freeman, A. and S.L. Durden (May 1998). "A three-component scattering model for polarimetric SAR data". en. In: *IEEE Transactions on Geoscience and Remote Sensing* 36.3, pp. 963–973. url: <http://ieeexplore.ieee.org/document/673687/> (visited on 07/22/2022).
- Fuhrmann, L., O. Biallawons, J. Klare, R. Panhuber, R. Klenke, and J. Ender (June 2017). "Micro-Doppler analysis and classification of UAVs at Ka band". en. In: *2017 18th International Radar Symposium (IRS)*. Prague, Czech Republic: IEEE, pp. 1–9. url: <https://ieeexplore.ieee.org/document/8008142/> (visited on 04/29/2022).
- Gersone, Fabiola, Alessio Balleri, Chris J Baker, and Mohammed Jahangir (Sept. 2018). "Simulations of L-band Staring Radar Moving Target Integration Efficiency". In: *2018 IEEE Conference on Antenna Measurements Applications (CAMA)*, pp. 1–4.
- Giuli, D. (Feb. 1986). "Polarization diversity in radars". In: *Proceedings of the IEEE* 74.2, pp. 245–269.
- Goodman, N. R. (1963). "Statistical Analysis Based on a Certain Multivariate Complex Gaussian Distribution (An Introduction)". In: *The Annals of Mathematical Statistics* 34.1, pp. 152–177. url: <https://www.jstor.org/stable/2991290> (visited on 11/29/2022).

- Guay, Rudy, Germain Drolet, and Joey R. Bray (2017). "Measurement and modelling of the dynamic radar cross-section of an unmanned aerial vehicle". en. In: *IET Radar, Sonar & Navigation* 11.7, pp. 1155–1160. url: <https://onlinelibrary.wiley.com/doi/abs/10.1049/iet-rsn.2016.0520> (visited on 01/12/2022).
- Gérard, Julien (Feb. 2022). "Drone recognition with Deep Learning". en. PhD thesis. Université Paris-Saclay. url: <https://tel.archives-ouvertes.fr/tel-03640378> (visited on 09/15/2022).
- Hansen, V. (1973). *Constant false alarm rate processing in search radars*. en. url: <https://www.semanticscholar.org/paper/Constant-false-alarm-rate-processing-in-search-Hansen/b9f381e35d0cc467d022f6661a4b477f0ba78d8f> (visited on 09/17/2020).
- Harman, Stephen (Sept. 2015). "A comparison of staring radars with scanning radars for UAV detection: Introducing the Alarm™ staring radar". In: *2015 European Radar Conference (EuRAD)*, pp. 185–188.
- (May 2017). "Analysis of the radar return of micro-UAVs in flight". In: *2017 IEEE Radar Conference (RadarConf)*. ISSN: 2375-5318, pp. 1159–1164.
- Harmanny, R. I. A., J. J. M. de Wit, and G. Prémel Cabic (Oct. 2014). "Radar micro-Doppler feature extraction using the spectrogram and the cepstrogram". In: *2014 11th European Radar Conference*, pp. 165–168.
- Hastings, W. K. (Apr. 1970). "Monte Carlo sampling methods using Markov chains and their applications". In: *Biometrika* 57.1, pp. 97–109. url: <https://doi.org/10.1093/biomet/57.1.97> (visited on 09/05/2022).
- Hein, Achim (2004). *Processing of SAR Data*. en. Signals and Communication Technology. Berlin, Heidelberg: Springer Berlin Heidelberg. url: <http://link.springer.com/10.1007/978-3-662-09457-0> (visited on 04/22/2022).
- Herschfelt, Andrew, Craig R. Birtcher, Richard M. Gutierrez, Yu Rong, Hanguang Yu, Constantine A. Balanis, and Daniel W. Bliss (May 2017). "Consumer-grade drone radar cross-section and micro-Doppler phenomenology". In: *2017 IEEE Radar Conference (RadarConf)*. ISSN: 2375-5318, pp. 0981–0985.
- History of radar* (July 2022). en. Page Version ID: 1097805662. url: https://en.wikipedia.org/w/index.php?title=History_of_radar&oldid=1097805662 (visited on 07/21/2022).
- Hoffmann, Folker, Matthew Ritchie, Francesco Fioranelli, Alexander Charlish, and Hugh Griffiths (May 2016). "Micro-Doppler based detection and tracking of UAVs with multistatic radar". In: *2016 IEEE Radar Conference (RadarConf)*. ISSN: 2375-5318, pp. 1–6.
- Honeywell RQ-16 T-Hawk* (Dec. 2021). en. Page Version ID: 1061425338. url: https://en.wikipedia.org/w/index.php?title=Honeywell_RQ-16_T-Hawk&oldid=1061425338 (visited on 03/07/2022).
- Hu, Cheng, Yixuan Wang, Rui Wang, Tianran Zhang, Jiong Cai, and Meiqin Liu (Feb. 2019). "An improved radar detection and tracking method for small UAV under clutter environment". en. In: *Science China Information Sciences* 62.2, p. 29306. url: <http://link.springer.com/10.1007/s11432-018-9598-x> (visited on 04/25/2022).
- Jahangir, Mohammed (May 2015). "Target centric wide-area 3-D surveillance using a non-scanning multibeam receiver array". In: *2015 IEEE Radar Conference (RadarCon)*. ISSN: 2375-5318, pp. 0652–0657.
- Jahangir, Mohammed and Chris Baker (Oct. 2016). "Persistence surveillance of difficult to detect micro-drones with L-band 3-D holographic radar™". In: *2016 CIE International Conference on Radar (RADAR)*, pp. 1–5.

- Jahangir, Mohammed, Chris J Baker, and Gordon A Oswald (May 2017). "Doppler characteristics of micro-drones with L-Band multibeam staring radar". In: *2017 IEEE Radar Conference (RadarConf)*. ISSN: 2375-5318, pp. 1052-1057.
- Jay, Emmanuelle, Jean Philippe Ovarlez, David Declercq, and Patrick Duvaut (June 2003). "BORD: bayesian optimum radar detector". en. In: *Signal Processing* 83.6, pp. 1151-1162. url: <https://linkinghub.elsevier.com/retrieve/pii/S0165168403000343> (visited on 04/25/2022).
- Jiang, Wen, Yulin Huang, and Jianyu Yang (July 2016). "Automatic Censoring CFAR Detector Based on Ordered Data Difference for Low-Flying Helicopter Safety". en. In: *Sensors* 16.7, p. 1055. url: <http://www.mdpi.com/1424-8220/16/7/1055> (visited on 02/14/2020).
- Kang, Ki-Bong, Jae-Ho Choi, Byung-Lae Cho, Jung-Soo Lee, and Kyung-Tae Kim (Oct. 2021). "Analysis of Micro-Doppler Signatures of Small UAVs Based on Doppler Spectrum". In: *IEEE Transactions on Aerospace and Electronic Systems* 57.5, pp. 3252-3267.
- Keane, John F and Stephen S Carr (2013). "A Brief History of Early Unmanned Aircraft". en. In: *JOHNS HOPKINS APL TECHNICAL DIGEST* 32.3, p. 14.
- Kelly, E.J. (Mar. 1986). "An Adaptive Detection Algorithm". en. In: *IEEE Transactions on Aerospace and Electronic Systems* AES-22.2, pp. 115-127. url: <http://ieeexplore.ieee.org/document/4104190/> (visited on 05/16/2022).
- Khristenko, A. V., M. O. Konovalenko, M. E. Rovkin, V. A. Khlusov, A. V. Marchenko, A. A. Sutulin, and N. D. Malyutin (June 2017). "A system for measurement of electromagnetic wave scattered by small UAVs". In: *2017 International Siberian Conference on Control and Communications (SIBCON)*. ISSN: 2380-6516, pp. 1-5.
- Kim, Byung Kwan, Hyun-Seong Kang, and Seong-Ook Park (Jan. 2017). "Drone Classification Using Convolutional Neural Networks With Merged Doppler Images". In: *IEEE Geoscience and Remote Sensing Letters* 14.1, pp. 38-42.
- Kim, Sangin, Yeong-Hoon Noh, Jinhyo Lee, Jongwon Lee, Jin-Soo Choi, and Jong-Gwan Yook (2019). "Electromagnetic Signature of a Quadcopter Drone and Its Relationship With Coupling Mechanisms". In: *IEEE Access* 7, pp. 174764-174773.
- Klare, Jens, Oliver Biallowons, and Delphine Cerutti-Maori (June 2017). "UAV detection with MIMO radar". In: *2017 18th International Radar Symposium (IRS)*. ISSN: 2155-5753, pp. 1-8.
- Kwag, Young-Kil, In-Sang Woo, Ho-Young Kwak, and Young-Ho Jung (Oct. 2016). "Multi-mode SDR radar platform for small air-vehicle Drone detection". In: *2016 CIE International Conference on Radar (RADAR)*, pp. 1-4.
- Leonardi, Mauro, Gianluca Ligresti, and Emilio Piracci (May 2022). "Drones Classification by the Use of a Multifunctional Radar and Micro-Doppler Analysis". en. In: *Drones* 6.5, p. 124. url: <https://www.mdpi.com/2504-446X/6/5/124> (visited on 06/10/2022).
- Li, Chenchen J. and Hao Ling (2017). "An Investigation on the Radar Signatures of Small Consumer Drones". In: *IEEE Antennas and Wireless Propagation Letters* 16, pp. 649-652.
- Li, Tengmingyang, Biyang Wen, Yingwei Tian, Ziyang Li, and Sijie Wang (Jan. 2019). "Numerical Simulation and Experimental Analysis of Small Drone Rotor Blade Polarimetry Based on RCS and Micro-Doppler Signature". In: *IEEE Antennas and Wireless Propagation Letters* 18.1, pp. 187-191.

- Liang, Cang, Ning Cao, Xiaokai Lu, and Youjie Ye (Sept. 2018). "UAV Detection Using Continuous Wave Radar". In: *2018 IEEE International Conference on Information Communication and Signal Processing (ICICSP)*, pp. 1–5.
- Liu, Hongping and V. Chandrasekar (Feb. 2000). "Classification of Hydrometeors Based on Polarimetric Radar Measurements: Development of Fuzzy Logic and Neuro-Fuzzy Systems, and In Situ Verification". EN. In: *Journal of Atmospheric and Oceanic Technology* 17.2, pp. 140–164. url: https://journals.ametsoc.org/view/journals/atot/17/2/1520-0426_2000_017_0140_cohbop_2_0_co_2.xml (visited on 05/05/2022).
- Lord Rayleigh, John William Strutt (1879). "XXXI. Investigations in optics, with special reference to the spectroscope". In: *The London, Edinburgh, and Dublin Philosophical Magazine and Journal of Science* 8.49, pp. 261–274. eprint: <https://doi.org/10.1080/14786447908639684>. url: <https://doi.org/10.1080/14786447908639684>.
- Lupidi, Alberto, Christian Greiff, and Stefan Brüggewirth (n.d.). "Polarimetric Radar Technology for European Defence Superiority - the PolRad Project". en. In: (), p. 5.
- Martinez, Michael (Apr. 2019). "UAS Detection, Classification, and Tracking in Urban Terrain". In: *2019 IEEE Radar Conference (RadarConf)*. ISSN: 2375-5318, pp. 1–6.
- Mathys, G. and J.O. Stenflo (Apr. 1986). "Sectropolarimetry of magnetic stars". In: *Astronomy & Astrophysics* 168, pp. 184–196.
- Meslot, Vincent, Vincent Corretja, Stephane Kemkemian, Jean-Michel Quellec, Richard Montigny, and Christian Cochin (May 2016). "Polarisation influence on sea clutter properties and radar detection performance in X-band for low-grazing angles". en. In: *2016 IEEE Radar Conference (RadarConf)*. Philadelphia, PA: IEEE, pp. 1–5. url: <http://ieeexplore.ieee.org/document/7485250/> (visited on 04/25/2022).
- Metropolis, Nicholas, Arianna W. Rosenbluth, Marshall N. Rosenbluth, Augusta H. Teller, and Edward Teller (June 1953). "Equation of State Calculations by Fast Computing Machines". In: *The Journal of Chemical Physics* 21.6, pp. 1087–1092. url: <https://aip.scitation.org/doi/abs/10.1063/1.1699114> (visited on 09/05/2022).
- Moisseev, D., C. Unal, H. Russchenberg, and L. Ligthart (May 2000). "Doppler polarimetric ground clutter identification and suppression for atmospheric radars based on co-polar correlation". In: *13th International Conference on Microwaves, Radar and Wireless Communications. MIKON - 2000. Conference Proceedings (IEEE Cat. No.00EX428)*. Vol. 1, 94–97 vol.1.
- Morris, Peter Joseph Basil and K. V. S. Hari (June 2021). "Detection and Localization of Unmanned Aircraft Systems Using Millimeter-Wave Automotive Radar Sensors". In: *IEEE Sensors Letters* 5.6, pp. 1–4.
- Northrop Grumman RQ-4 Global Hawk* (Mar. 2022). en. Page Version ID: 1075609186. url: https://en.wikipedia.org/w/index.php?title=Northrop_Grumman_RQ-4_Global_Hawk&oldid=1075609186 (visited on 03/07/2022).
- Novak, L.M., M.B. Sechtin, and M.J. Cardullo (Mar. 1989). "Studies of target detection algorithms that use polarimetric radar data". In: *IEEE Transactions on Aerospace and Electronic Systems* 25.2, pp. 150–165.
- Ochodnický, Ján, Zdenek Matousek, Marián Babjak, and Ján Kurty (May 2017). "Drone detection by Ku-band battlefield radar". In: *2017 International Conference on Military Technologies (ICMT)*, pp. 613–616.
- Oh, Beom-Seok, Xin Guo, Fangyuan Wan, Kar-Ann Toh, and Zhiping Lin (Feb. 2018). "Micro-Doppler Mini-UAV Classification Using Empirical-Mode Decomposition Features". In: *IEEE Geoscience and Remote Sensing Letters* 15.2, pp. 227–231.

- Park, Hyung-Rae, Jian Li, and Hong Wang (Jan. 1995). "Polarization-space-time domain generalized likelihood ratio detection of radar targets". en. In: *Signal Processing* 41.2, pp. 153–164. url: <https://www.sciencedirect.com/science/article/pii/S016516849400097J> (visited on 09/15/2021).
- Pascal, F., J-P. Ovarlez, P. Forster, and P. Larzabal (Sept. 2004). "Constant false alarm rate detection in Spherically Invariant Random Processes". In: *2004 12th European Signal Processing Conference*, pp. 2143–2146.
- Pastina, D., P. Lombardo, V. Pedicini, and T. Bucciarelli (May 2000). "Adaptive polarimetric target detection with coherent radar". In: *Record of the IEEE 2000 International Radar Conference [Cat. No. 00CH37037]*, pp. 93–97.
- Patel, Jarez S., Francesco Fioranelli, and David Anderson (2018a). "Review of radar classification and RCS characterisation techniques for small UAVs or drones". en. In: *IET Radar, Sonar & Navigation* 12.9, pp. 911–919. url: <https://onlinelibrary.wiley.com/doi/abs/10.1049/iet-rsn.2018.0020> (visited on 01/12/2022).
- (Sept. 2018b). "Review of radar classification and RCS characterisation techniques for small UAVs or drones". en. In: *IET Radar, Sonar & Navigation* 12.9, pp. 911–919. url: <https://onlinelibrary.wiley.com/doi/10.1049/iet-rsn.2018.0020> (visited on 04/25/2022).
- Poitevin, Pierre, Michel Pelletier, and Patrick Lamontagne (Oct. 2017). "Challenges in detecting UAS with radar". In: *2017 International Carnahan Conference on Security Technology (ICCST)*. ISSN: 2153-0742, pp. 1–6.
- Poullin, Dominique (2016). "UAV detection and localization using passive DVB-T radar MFN and SFN". en. In: p. 10.
- Poullin, Dominique, Philippe Dorey, and Abigael Taylor (2022). "Potential of Passive DVB-T Radar Component Against Illegal UAV Flights". In: *AI, Computer Science and Robotics Technology*. url: <https://doi.org/10.5772/acrt.07>.
- Radar Based Non-Cooperative Target Recognition (NCTR) in the Low Airspace and Complex Surfaces environments* (2021). Anglais.
- Rahman, Samiur and Duncan A. Robertson (2020). "Classification of drones and birds using convolutional neural networks applied to radar micro-Doppler spectrogram images". en. In: *IET Radar, Sonar & Navigation* 14.5, pp. 653–661. url: <https://onlinelibrary.wiley.com/doi/abs/10.1049/iet-rsn.2019.0493> (visited on 04/29/2022).
- Rahman, Samiur and Duncan Alexander Robertson (Feb. 2019). "In-flight RCS measurements of drones and birds at K-band and W-band". en. In: *IET Radar, Sonar & Navigation* 13.2, pp. 300–309. url: <https://onlinelibrary.wiley.com/doi/10.1049/iet-rsn.2018.5122> (visited on 04/25/2022).
- Research and Technology Organization and RTO Sensors and Electronics Technology Panel (SET) Symposium Sensors and Electronics Technology Panel (2004). *Target identification and recognition using RF systems: papers presented at the RTO Sensors and Electronics Technology Panel (SET) symposium held in the Banner Hall at the Defence Museum, Akershus Frotress in Oslo, Norway on 11-13 October 2004 = Reconnaissance et identification de cibles ?? l'aide des syst??mes RF*. en. OCLC: 254244124.
- Ritchie, Matthew, Francesco Fioranelli, Hervé Borrión, and Hugh Griffiths (2017). "MULTI-STATIC MICRO-DOPPLER RADAR FEATURES EXTRACTION FOR CLASSIFICATION OF UNLOADED/LOADED MICRO-DRONES". en. In: p. 21.
- Ritchie, Matthew, Francesco Fioranelli, Hugh Griffiths, and Borge Torvik (Oct. 2015). "Micro-drone RCS analysis". In: *2015 IEEE Radar Conference*, pp. 452–456.

- Ritchie, Matthew, Francesco Fioranelli, Hugh Griffiths, and Børge Torvik (May 2016). "Monostatic and bistatic radar measurements of birds and micro-drone". In: *2016 IEEE Radar Conference (RadarConf)*. ISSN: 2375-5318, pp. 1–5.
- Roy, Olivier and Martin Vetterli (Sept. 2007). "The effective rank: A measure of effective dimensionality". In: *2007 15th European Signal Processing Conference*, pp. 606–610.
- Rozel, Milan, Philippe Brouard, and H el ene Oriot (2022). "Polarimetric Adaptive Processing and Eigenvalue Detector for Counter UAVs radar". In: *NATO STO Review-The Journal of the NATO Science and Technology Organization*, SET-273.
- Rozel, Milan, Pierre Bruneel, Philippe Brouard, and H el ene Oriot (2022a). "Influence of covariance matrix mismatch on polarimetric detectors for low-grazing endo-clutter detection". English. In: *IET Conference Proceedings*, 178–183(5). url: <https://digital-library.theiet.org/content/conferences/10.1049/icp.2022.2312>.
- Rozel, Milan, Nicolas Gonalves, Alec Reygrobellet, and Pierre Bruneel (2022b). "Construction of a Radar Cross-Section Database Using ADS-B Data from the OpenSky Network". In: *Engineering Proceedings* 28.1. url: <https://www.mdpi.com/2673-4591/28/1/4>.
- Ryzhkov, A. V. and D. S. Zrnic (Oct. 1998). "Discrimination between Rain and Snow with a Polarimetric Radar". EN. In: *Journal of Applied Meteorology and Climatology* 37.10, pp. 1228–1240. url: https://journals.ametsoc.org/view/journals/apme/37/10/1520-0450_1998_037_1228_dbrasw_2.0.co_2.xml (visited on 05/05/2022).
- Sachidananda, M. and D. S. Zrnic (Dec. 1987). "Rain Rate Estimates from Differential Polarization Measurements". EN. In: *Journal of Atmospheric and Oceanic Technology* 4.4, pp. 588–598. url: https://journals.ametsoc.org/view/journals/atot/4/4/1520-0426_1987_004_0588_rrefdp_2_0_co_2.xml (visited on 05/05/2022).
- Sarabandi, K., Y. Oh, and F.T. Ulaby (Oct. 1992). "Performance characterization of polarimetric active radar calibrators and a new single antenna design". In: *IEEE Transactions on Antennas and Propagation* 40.10, pp. 1147–1154.
- Sayama, S. and H. Sekine (July 2001). "Weibull, log-Weibull and K-distributed ground clutter modeling analyzed by AIC". In: *IEEE Transactions on Aerospace and Electronic Systems* 37.3, pp. 1108–1113.
- Schleher, D. C. (Nov. 1976). "Radar Detection in Weibull Clutter". In: *IEEE Transactions on Aerospace and Electronic Systems* AES-12.6, pp. 736–743.
- Schleiss, Marc, Jonas Olsson, Peter Berg, Tero Niemi, Teemu Kokkonen, S oren Thorn-dahl, Rasmus Nielsen, Jesper Ellerb ak Nielsen, Denica Bozhinova, and Seppo Pulkkinen (June 2020). "The accuracy of weather radar in heavy rain: a comparative study for Denmark, the Netherlands, Finland and Sweden". English. In: *Hydrology and Earth System Sciences* 24.6, pp. 3157–3188. url: <https://hess.copernicus.org/articles/24/3157/2020/> (visited on 05/05/2022).
- Schroder, Arne, Matthias Renker, Uwe Aulenbacher, Axel Murk, Urs Boniger, Roland Oechslin, and Peter Wellig (Oct. 2015). "Numerical and experimental radar cross section analysis of the quadrocopter DJI Phantom 2". In: *2015 IEEE Radar Conference*, pp. 463–468.
- Schr oder, Arne, Uwe Aulenbacher, Matthias Renker, Urs B oniger, Roland Oechslin, Axel Murk, and Peter Wellig (Oct. 2016). "Numerical RCS and micro-Doppler investigations of a consumer UAV". en. In: ed. by Karin U. Stein and Ric H. M. A. Schleijsen. Edinburgh, United Kingdom, p. 999704. url: <http://proceedings.spiedigitallibrary.org/proceeding.aspx?doi=10.1117/12.2241298> (visited on 04/25/2022).

- Schüpbach, Christof, Christian Patry, Francois Maasdorp, Urs Böniger, and Peter Wellig (May 2017). "Micro-UAV detection using DAB-based passive radar". In: *2017 IEEE Radar Conference (RadarConf)*. ISSN: 2375-5318, pp. 1037–1040.
- Sedivy, Pavel and Ondrej Nemeč (2021). "Drone RCS Statistical Behaviour". en. In: p. 18.
- Sekine, M., S. Ohtani, T. Musha, T. Irabu, E. Kiuchi, T. Hagsawa, and Y. Tomita (July 1981). "Weibull-Distributed Ground Clutter". In: *IEEE Transactions on Aerospace and Electronic Systems* AES-17.4, pp. 596–598.
- Shackle, Samira (Dec. 2020). "The mystery of the Gatwick drone". en-GB. In: *The Guardian*. url: <https://www.theguardian.com/uk-news/2020/dec/01/the-mystery-of-the-gatwick-drone> (visited on 03/07/2022).
- Shannon, Claude E (1948). "A mathematical theory of communication". In: *The Bell system technical journal* 27.3, pp. 379–423.
- Shnidman, D.A. (July 1999). "Generalized radar clutter model". In: *IEEE Transactions on Aerospace and Electronic Systems* 35.3, pp. 857–865.
- Shrader, W. (May 1973). "Radar Technology Applied to Air Traffic Control". In: *IEEE Transactions on Communications* 21.5, pp. 591–605.
- Skolnik, M. I. (1970). "RADAR HANDBOOK". In: url: <https://trid.trb.org/view/49654> (visited on 02/02/2022).
- Smith, M.E. and P.K. Varshney (1997). "VI-CFAR: a novel CFAR algorithm based on data variability". en. In: *Proceedings of the 1997 IEEE National Radar Conference*. Syracuse, NY, USA: IEEE, pp. 263–268. url: <http://ieeexplore.ieee.org/document/588317/> (visited on 04/25/2022).
- Sun, Hongbo, Beom-Seok Oh, Xin Guo, and Zhiping Lin (Dec. 2019). "Improving the Doppler Resolution of Ground-Based Surveillance Radar for Drone Detection". In: *IEEE Transactions on Aerospace and Electronic Systems* 55.6, pp. 3667–3673.
- SYAC UAV (Oct. 2022). en. Page Version ID: 1117052715. url: https://en.wikipedia.org/w/index.php?title=SYAC_UAV&oldid=1117052715 (visited on 11/28/2022).
- Titin-Schnaider, C. and S. Attia (Dec. 2003). "Calibration of the MERIC full-polarimetric radar: theory and implementation". en. In: *Aerospace Science and Technology* 7.8, pp. 633–640. url: <https://www.sciencedirect.com/science/article/pii/S1270963803000737> (visited on 03/20/2023).
- Tong, Hui, V. Chandrasekar, K. R. Knupp, and James Stalker (Oct. 1998). "Multiparameter Radar Observations of Time Evolution of Convective Storms: Evaluation of Water Budgets and Latent Heating Rates". EN. In: *Journal of Atmospheric and Oceanic Technology* 15.5, pp. 1097–1109. url: https://journals.ametsoc.org/view/journals/atot/15/5/1520-0426_1998_015_1097_mroote_2_0_co_2.xml (visited on 05/05/2022).
- Torvik, Børge, Karl Erik Olsen, and Hugh Griffiths (Sept. 2016). "Classification of Birds and UAVs Based on Radar Polarimetry". In: *IEEE Geoscience and Remote Sensing Letters* 13.9, pp. 1305–1309.
- Tragl, K. (Sept. 1990). "Polarimetric radar backscattering from reciprocal random targets". In: *IEEE Transactions on Geoscience and Remote Sensing* 28.5, pp. 856–864.
- Trim, Richard M (Dec. 2002). "A Brief History of the Development of Radar in Great Britain up to 1945". en. In: *Measurement and Control* 35.10, pp. 299–301. url: <https://doi.org/10.1177/002029400203501003> (visited on 05/31/2022).
- Trunk, G.V. (Sept. 1978). "Range Resolution of Targets Using Automatic Detectors". In: *IEEE Transactions on Aerospace and Electronic Systems* AES-14.5, pp. 750–755.

- Unmanned aerial vehicle* (Mar. 2022). en. Page Version ID: 1075752170. url: https://en.wikipedia.org/w/index.php?title=Unmanned_aerial_vehicle&oldid=1075752170 (visited on 03/07/2022).
- Wakabayashi, H., T. Matsuoka, K. Nakamura, and F. Nishio (Nov. 2004). "Polarimetric Characteristics of sea ice in the sea of Okhotsk observed by airborne L-band SAR". In: *IEEE Transactions on Geoscience and Remote Sensing* 42.11, pp. 2412–2425.
- Wang, Yanting and V. Chandrasekar (Oct. 2010). "Quantitative Precipitation Estimation in the CASA X-band Dual-Polarization Radar Network". EN. In: *Journal of Atmospheric and Oceanic Technology* 27.10, pp. 1665–1676. url: https://journals.ametsoc.org/view/journals/atot/27/10/2010jtecha1419_1.xml (visited on 05/05/2022).
- Ward, James (1995). "SPACE-TIME ADAPTIVE PROCESSING FOR AIRBORNE RADAR". en. In: p. 6.
- Ward, KD (1982). "A radar sea clutter model and its application to performance assessment". In: *Proc. IEE Conf. Radar-82*.
- Ward, K.D., C.J. Baker, and S. Watts (1990). "Maritime surveillance radar. Part 1: Radar scattering from the ocean surface". en. In: *IEE Proceedings F Radar and Signal Processing* 137.2, p. 51. url: <https://digital-library.theiet.org/content/journals/10.1049/ip-f-2.1990.0009> (visited on 05/17/2022).
- Waters, Nick (Feb. 2017). *Death From Above: The Drone Bombs of the Caliphate*. en-GB. url: <https://www.bellingcat.com/news/mena/2017/02/10/death-drone-bombs-caliphate/> (visited on 03/11/2022).
- (Jan. 2022). *Myanmar's Rebels Get Resourceful With Improvised Drones*. en-GB. url: <https://www.bellingcat.com/news/2022/01/20/myanmars-rebels-get-resourceful-with-improvised-drones/> (visited on 03/11/2022).
- Weiss, M. (Jan. 1982). "Analysis of Some Modified Cell-Averaging CFAR Processors in Multiple-Target Situations". In: *IEEE Transactions on Aerospace and Electronic Systems* AES-18.1, pp. 102–114.
- Wit, J. J. M. de, R. I. A. Harmanny, and P. Molchanov (Oct. 2014). "Radar micro-Doppler feature extraction using the Singular Value Decomposition". In: *2014 International Radar Conference*. ISSN: 1097-5764, pp. 1–6.
- Yaacoub, Jean-Paul, Hassan Noura, Ola Salman, and Ali Chehab (Sept. 2020). "Security analysis of drones systems: Attacks, limitations, and recommendations". In: *Internet of Things* 11, p. 100218. url: <https://www.ncbi.nlm.nih.gov/pmc/articles/PMC7206421/> (visited on 03/04/2022).
- Yamaguchi, H. (Oct. 2002). "Target detection in ground clutter with W-band stepped frequency polarimetric radar system". In: *RADAR 2002*. ISSN: 0537-9989, pp. 258–262.
- Yamaguchi, Y., T. Moriyama, M. Ishido, and H. Yamada (Aug. 2005). "Four-component scattering model for polarimetric SAR image decomposition". In: *IEEE Transactions on Geoscience and Remote Sensing* 43.8, pp. 1699–1706.
- Yamaguchi, Yoshio, Akinobu Sato, Wolfgang-Martin Boerner, Ryoichi Sato, and Hiroyoshi Yamada (June 2011). "Four-Component Scattering Power Decomposition With Rotation of Coherency Matrix". In: *IEEE Transactions on Geoscience and Remote Sensing* 49.6, pp. 2251–2258.
- Zhu, Lingzhi, Shuning Zhang, Huichang Zhao, Si Chen, Dongxu Wei, and Xiangyu Lu (2019). "Classification of UAV-to-Ground Vehicles Based on Micro-Doppler Signatures Using Singular Value Decomposition and Deep Convolutional Neural Networks". In: *IEEE Access* 7, pp. 22133–22143.

Zikidis, Konstantinos, Alexios Skondras, and Charisios Tokas (n.d.). "Low Observable Principles, Stealth Aircraft and Anti-Stealth Technologies". en. In: (), p. 37.